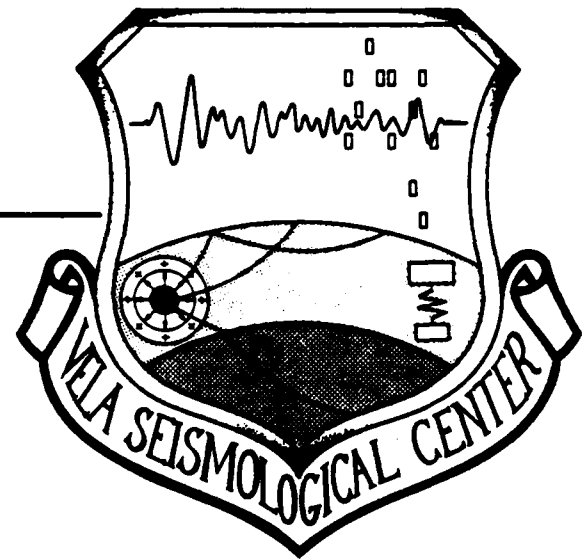


Ap-A 133 574

12  
VSC-TR-83-12

SURFACE WAVE PATH  
CORRECTIONS, DETERMINISTIC  
DISCRIMINATION AND BODY WAVE  
ATTENUATION



W. E. Farrell  
J. L. Stevens  
J. M. Savino  
B. Shkoller  
L. B. Bache

S-CUBED  
P. O. Box 1620  
La Jolla, California 92038

October 1982

OCT 14 83

SEMIANNUAL TECHNICAL REPORT

Approved for Public Release,  
Distribution Unlimited

Monitored by:

VELA Seismological Center  
312 Montgomery Street  
Alexandria, Virginia 22314

DTIC FILE COPY

83 10 12 15 3

AFTAC Project Authorization No. VT/0701/B/PMP

ARPA Order No. 2551, Program Code No. 1A10

ARPA Order No. 4406, Program Code No. 2A10

ARPA Order No. 4435, Program Code No. 2A10

Effective Date of Contract: 1 April 1981

Contract Expiration Date: 30 September 1982

Amount of Contract: \$1,004,347.00

Contract No. F8606-80-C-0016

Principal Investigator and Phone No.

Dr. John M. Savino, (714) 453-0060, Ext. 453

Mr. John R. Murphy, (703) 476-5197

Project Scientist and Phone No.

Mr. Brian W. Barker, (202) 325-7581

This research was supported by the Advanced Research Projects Agency of the Department of Defense and was monitored by AFTAC/VSC, Patrick Air Force Base, Florida 32925, Under Contract No. F08606-80-C-0016.

The views and conclusions contained in this document are those of the authors and should not be interpreted as necessarily representing the official policies, either expressed or implied, of the Advanced Research Projects Agency, the Air Force Technical Applications Center, or the U. S. Government.

S3 Project No. 11143

## Unclassified

SECURITY CLASSIFICATION OF THIS PAGE (When Data Entered)

REPORT DOCUMENTATION PAGE		READ INSTRUCTIONS BEFORE COMPLETING FORM
1. REPORT NUMBER VSC-TR-83-12	2. GOVT ACCESSION NO. <i>A133574</i>	3. RECIPIENT'S CATALOG NUMBER
4. TITLE (and Subtitle)  SURFACE WAVE PATH CORRECTIONS, DETERMINISTIC DISCRIMINATION AND BODY WAVE ATTENUATION	5. TYPE OF REPORT & PERIOD COVERED Semiannual Technical Report	
7. AUTHOR(s) W. E. Farrell, J. L. Stevens, J. M. Savino, B. Shkoller, L. B. Bache	6. PERFORMING ORG. REPORT NUMBER SSS-R-83-5776	
9. PERFORMING ORGANIZATION NAME AND ADDRESS S-CUBED P.O. Box 1620 La Jolla, California 92038	10. PROGRAM ELEMENT, PROJECT, TASK AREA & WORK UNIT NUMBERS ARPA Ord. #2551, Pro.C. #1A10 ARPA Ord. #4406, Pro.C. #2A10 ARPA Ord. #4435, Pro.C. #2A10	
11. CONTROLLING OFFICE NAME AND ADDRESS VELA Seismological Center 312 Montgomery Street Alexandria, Virginia 22314	12. REPORT DATE October 1982	
14. MONITORING AGENCY NAME & ADDRESS (if different from Controlling Office)	13. NUMBER OF PAGES 170	
16. DISTRIBUTION STATEMENT (of this Report)  Approved for Public Release, Distribution Unlimited.	15. SECURITY CLASS. (of this report) Unclassified	
17. DISTRIBUTION STATEMENT (of the abstract entered in Block 20, if different from Report)		
18. SUPPLEMENTARY NOTES		
19. KEY WORDS (Continue on reverse side if necessary and identify by block number) Surface Wave dispersion Seismic spectra Seismic Research Observatories Multivariate discrimination Nuclear explosion seismograms Deterministic seismic discrimination Narrowband filtering Seismic attenuation (t-star)		
20. ABSTRACT (Continue on reverse side if necessary and identify by block number) Rayleigh waves from the Eastern Kazakh test site recorded at Seismic Research Observatory receivers have been analysed for phase-velocity dispersion, group velocity dispersion and spectral amplitude. Linear inversion theory has been used to interpret these data as arising from waves propagating in plane-layered earth models. This yields the mean shear velocity and attenuation over each path as well as the moment of the source. Using the path models, synthetic seismograms have been calculated for use in more refined estimates of source type and source strength. →(Continued)		

Unclassified

SECURITY CLASSIFICATION OF THIS PAGE(When Data Entered)

(Continued)

Multivariate linear discrimination has been used to distinguish synthetic body wave spectra of explosions from synthetic body wave spectra of earthquakes. The same algorithm with no modification is highly successful at distinguishing the body wave spectra for real events. High frequency attenuation of the spectra for real data causes the deterministic discriminant to be biased. It is shown how the bias is used to infer  $t^*$ . The attenuation parameter,  $t^*$ , has been calculated for Kazakh-SRO and NTS-SRO paths for several score underground explosions. For NTS sources,  $t^*$  is about 0.8. For Kazakh sources  $t^*$  ranges between 0.2 and 0.8.

(Source attenuation).



Unclassified

SECURITY CLASSIFICATION OF THIS PAGE(When Data Entered)

## TABLE OF CONTENTS

<u>Section</u>	<u>Page</u>
I. INTRODUCTION AND SUMMARY . . . . .	1
1.1 INTRODUCTION. . . . .	
1.2 SUMMARY . . . . .	2
II. SURFACE WAVE ANALYSIS PACKAGE. . . . .	4
2.1 WHAT IS A PATH CORRECTION? . . . . .	4
2.2 HOW TO MAKE A PATH CORRECTION . . . . .	5
2.2.1 Recovery of Phase and Group Velocities and Spectral Amplitudes. . . . .	8
2.2.2 Inversion for Earth Structures . . .	17
2.2.3 Generation of Synthetic Seismograms and Excitation Functions . . . . .	23
2.3 SHAGAN RIVER-SRO PATH CORRECTIONS . . . .	26
III. AUTOMATIC DISCRIMINATION . . . . .	77
3.1 DETERMINISTIC DISCRIMINATION . . . . .	77
3.1.1 Theoretical Source Models. . . . .	80
3.1.2 Spectral Scaling. . . . .	81
3.1.3 Discriminating Theoretical Spectra. . . . .	85
3.2 EFFECT OF ATTENUATION . . . . .	95
3.2.1 Constant $t^*$ Model . . . . .	95
3.2.2 Effect of $t^*$ on the Deterministic Discriminant . . . . .	98
3.2.3 Definition of the Discriminant Bias. . . . .	100
3.2.4 Classification of Isolated Events . . . . .	103

TABLE OF CONTENTS (Continued)

<u>Section</u>		<u>Page</u>
3.3 APPLICATION OF DETERMINISTIC DISCRIMINATION TO SELECTED AI DATA . . . . .		105
3.3.1 Station KAAO . . . . .		106
3.3.2 Station CHTO . . . . .		109
3.3.3 Station RKON . . . . .		111
3.3.4 Station BFAK . . . . .		113
3.3.5 Other Stations . . . . .		113
3.3.6 Conclusions . . . . .		117
3.4. ESTIMATING $t^*$ FROM SRO RECORDINGS OF EXPLOSIONS . . . . .		118
3.4.1 Data Set . . . . .		119
3.4.2 Feature Extraction . . . . .		123
3.4.3 $t^*$ . . . . .		126
3.4.4 Conclusions . . . . .		132
REFERENCES . . . . .		135
APPENDIX A . . . . .		139
APPENDIX B . . . . .		141
APPENDIX C . . . . .		154

## LIST OF ILLUSTRATIONS

<u>Figure</u>		
	<u>Page</u>	
1. East Kazakh shear velocity structure used for synthetic seismogram . . . . .	7	
2. Synthetic seismogram (top) for the fundamental mode Rayleigh wave made using East Kazakh structure (Figure 1) and dispersion curves (bottom) . . . . .	9	
3. Form summarizing inputs and outputs for surface wave analysis package . . . . .	10	
4. Group velocity curve obtained by narrow band filtering the synthetic seismogram in Figure 2 . . . . .	11	
5. Phase-matched filter output for synthetic seismogram . . . . .	13	
6. Phase velocities estimated by TELVEL for synthetic seismogram . . . . .	14	
7. Final group velocities obtained for synthetic seismogram by iterative application of phase-matched filter . . . . .	16	
8. Shear velocity structure obtained by inverting dispersion curves produced by TELVEL from the synthetic seismogram, together with linearized data fit . . . . .	20	
9. Final model obtained using a DF of 6.0 and a single discontinuity (compare with Figure 1) together with data fit . . . . .	22	
10. Q structure and data fit obtained using a DF of 2.5 . . . . .	24	
11. Synthetic seismogram generated using the structure output by INVERT, together with phase and group velocity dispersion curves. . . . .	27	
12. Seismograms recorded at SRO stations for Shagan River explosion number 318, December 2, 1979 . . . . .	29	
13. Seismograms recorded at SRO stations for Shagan River explosion number 312, November 29, 1978 . . . . .	30	

LIST OF ILLUSTRATIONS (Continued)

<u>Figure</u>		<u>Page</u>
14.	Seismograms recorded at SRO stations for Shagan River explosion number 313, June 23, 1979 . . . . .	31
15.	Path 1: SHAGAN-KONO . . . . .	35
16.	Path 2: SHAGAN-SHIO . . . . .	41
17.	Path 3: SHAGAN-SHIO . . . . .	47
18.	Path 4: SHAGAN-SHIO . . . . .	53
19.	Path 5: SHAGAN-ANTO . . . . .	59
20.	Path 6: SHAGAN-CHTO . . . . .	65
21.	Path 7: SHAGAN-KAAO . . . . .	71
22.	Block diagram of automatic discrimination procedure. . . . .	78
23.	A handful of numerical models is expanded to give a much larger training set using magnitude scaling laws . . . . .	82
24.	For an earthquake and explosion of equal moment, the corner frequency of the latter exceeds the former because the velocity-stress parameters (D) are different . . . . .	84
25.	Scaled body wave spectra for a collection of numerical earthquakes and explosions covering the magnitude range $3 < m_b < 6$ . . . . .	86
26.	The synthetic spectra are scaled and then classified using the Fisher discriminant. . . . .	87
27.	The Fisher discriminant accurately separates the explosion spectrums from the earthquake spectrums when quadratic scaling (see Figure 25) is used . . . . .	91
28.	When cubic scaling is used, the jackknife produces this discriminant distribution . . . . .	94

LIST OF ILLUSTRATIONS (Continued)

<u>Figure</u>		<u>Page</u>
29.	When deterministic weights are applied to real data, the discriminants are biased positive because of attenuation. . . . .	96
30.	Synthetic weights applied to KAAO spectra effectively separate the two event types . . . . .	108
31.	Synthetic weights applied to CHTO spectra give five misclassified events and $t^* = 0.45$ . . . . .	110
32.	Synthetic weights applied to RKON spectra produce two misclassified events, but the missed explosion is clearly anomalous . . . . .	112
33.	Synthetic weights applied to BFAK spectra give one misclassified explosion and numerous misclassified earthquakes . . . . . . . . .	114
34.	Typical SRO recordings of Kazakh explosions, arranged with smallest apparent $t^*$ at the top . . . . . . . . . . .	124
35.	The spectral integral, $d$ , for a suite of KAZAKH and NTS explosions differs from the values obtained for a collection of numerical explosions because of attenuation . . . . .	127
36.	$t^*$ estimates obtained from body wave spectra spanning two frequency intervals . . . . .	131
37.	Comparison between $t^*$ obtained by Lundquist and Samowitz (1982, Figure 7, Page 30) from analysis of the relative receiver function and $t^*$ obtained in this study for SRO recordings of KAZAKH explosions . . . . . . . . . . .	133

## LIST OF TABLES

<u>Table</u>		<u>Page</u>
1.	Estimated $\Psi_\infty$ . . . . . . . . . . . . . . . . .	32
2.	Time Domain Amplitudes Comparison . . . . . . .	34
3.	Event Information for Kazakh Explosions . . . . .	120
4.	Event Information for NTS Explosions . . . . .	122
5.	$t^*$ Calculation for Kazakh Events. . . . . . .	129
6.	$t^*$ Calculation for NTS Events. . . . . . .	130

## I. INTRODUCTION AND SUMMARY

### 1.1 INTRODUCTION

During the past six months research efforts at S-CUBED under contract F08606-80-C-0016 have focused on automatic discrimination and surface wave path corrections. This report summarizes the major accomplishments achieved to date on these two topics.

The objective of the automatic discrimination effort is to design, code and test a computer program which analyzes seismograms automatically and then classifies them as either explosion-like or earthquake-like, with associated misclassification probabilities. The coding and implementation of the program for automatic discrimination is following the approach used previously for "Automatic Seismic Signal Processing Research" (VT/0704). The on-line code consists of two modules. One performs feature selection and produces as its output a file of discriminants (or features) for each input seismogram. The second module statistically combines the features at each station to perform individual station classifications and then polls all stations to form a network consensus as to the character of an event.

In order to test the Automatic Discrimination code, we have been assembling an expanded collection of Area of Interest (AI) seismograms and processing them in a manner similar to the original VELA Seismological Center (VSC) sponsored AI experiment. The objective of this evaluation is to determine the effectiveness of the various discriminants with respect to availability and type of data, source size, propagation path and station properties.

The objective of the surface wave path corrections effort is to develop computer software for the VSC seismic system to invert observed surface waves for path structure and attenuation, and to provide Green's functions for moment tensor inversion for selected paths. This task has been largely completed and an S-CUBED Topical Report, written by Stevens, et al. (1982) and submitted to VSC during this reporting period, gives a fairly complete description of

the surface wave analysis package. The report also serves as a user's guide for the software package which was made operational at the Seismic Research Center (SRC) during the past six months. The reader is referred to appendices to the report by Stevens, et al. (1982) which contains file formats, sign conventions, an explanation of some of the algorithms used in the programs, and definitions of output quantities.

In brief, the method adopted in the surface wave analysis package uses dispersion to obtain the travel path structure which, in turn, is used to estimate the moment of an explosion source and path attenuation. The technique was originally used by Bache, et al. (1978) to estimate the moment and yield of NTS events. The basic algorithms used in that study were subsequently improved, extended, and simplified so that path corrections may be obtained much more easily in an interactive environment.

## 1.2 SUMMARY

The major result of the surface wave studies described in this report is the development of an interactive computer program for processing long-period seismic data and its application to the analysis of SRO recordings of East Kazakh events. The analysis interprets an observed vertical component long-period seismogram in terms of the following quantities.

1. The dispersion of the group and phase velocities.
2. The plane layered structure ( $\beta$ ,  $Q$ ) which best explains the dispersion.
3. The moment of the source.
4. The matched filter which best removes the dispersion.

In addition, a synthetic seismogram module permits the calculation and display of the seismogram caused by an explosion source in a plane layered earth model.

The conclusion from the SRO surface wave study is that, with respect to East Kazakh KONO, SHIO are excellent stations, MAJO, GRFO

are good stations, ANTO, CHTO are noisy with more multipathing than the first four, and KAA0 (distance 18 degrees) is very difficult to process. CHTO seismograms have a peculiar spectrum, with a large dip at about 20 seconds period.

The major result of the automatic discrimination studies described in this report is the development of a new multivariate body wave discriminant based upon numerical source simulations. Source identification using this method is called "deterministic" discrimination, because the definition of the discriminant depends entirely upon deterministic body wave modeling. Application of the discriminant to a modest data set shows good results. Furthermore, the method of deterministic discrimination can be used to estimate the body wave attenuation parameter,  $t^*$ , and we present  $t^*$  result for SRO recordings of NTS and East Kazakh sources.

The conclusion from the automatic discrimination study is that deterministic source models can effectively serve as training data in a multivariate discriminant. Furthermore, the deterministic discriminant can be viewed as a way of estimating the excess high frequency attenuation ( $t^*$ ) that occurs when waves propagate in the earth instead of the computer. Measurements of  $t^*$  using the new technique agree with independent studies of the same data.

## II. SURFACE WAVE ANALYSIS PACKAGE

The following is a description of the S-CUBED Surface Wave Analysis Package which is designed to obtain path corrections from observed seismograms. There are three main programs in the package. The first -- TELVEL, uses the method of phase-matched filters (Herrin and Goforth, 1977) to recover surface wave phase (C) and group (U) velocities. The second -- INVERT, inverts the phase and group velocities to obtain the earth structure for the path, and obtains an approximate Q (attenuation) structure and moment by comparing synthetic and observed spectral amplitudes. The third -- SYNSRF, uses a variety of methods (Takeuchi and Saito, 1972; Schwab and Knopoff, 1970; Harkrider, 1964, 1970) modified for high frequency stability, to synthesize surface waves.

All programs are interactive and self-contained. Every effort has been made to make them as easy to use as possible. In this report, we show the uses of the programs for making path corrections by going through an example in detail using a synthetic seismogram, and by applying the method to Shagan River -- SRO station travel paths.

### 2.1 WHAT IS A PATH CORRECTION?

A path correction is a Green's function for a given source region and source-to-receiver path. Once the Green's function is known, it may be used to generate synthetic surface waves from an arbitrary source, as observed at the receiver point, or the inverse problem may be solved: an observed seismogram may be used to estimate the strength and type of the source, usually in the form of a moment tensor.

The basic procedure used to make a path correction was outlined in an earlier report (Wang, et al., 1981). Since then the procedure has been improved by allowing simultaneous estimation of Q and moment, and by making the codes interactive and compatible.

## 2.2 HOW TO MAKE A PATH CORRECTION

To make a path correction, simply take a seismogram, use program TELVEL to obtain the Rayleigh wave phase and group velocities, then use program INVERT to find the average source-to-receiver shear velocity ( $\beta$ ) and Q structure, and finally use program SYNSRF to generate eigenfunctions for this structure, and to compute a synthetic seismogram which resembles the original seismogram. The scalar moment of the explosion is found together with the estimate of Q, and the eigenfunctions can be used to perform a moment tensor inversion for any source in the same area as the original explosion.

In practice, finding a path correction is more than a routine operation, and there are a number of ways to err during the data processing. The purpose of this section is to go through the procedure in some detail and to identify the traps which are lurking to confuse the user. Fortunately, most of the errors which can be made will show up somewhere during the processing. A bad set of phase and/or group velocities may not produce a reasonable earth model when inverted. An inaccurate inversion for shear velocity may make it impossible to determine a reasonable Q structure. If the seismogram obtained at the end of the procedure is a good match to the original (except for noise or multipathing effects, etc.), then chances are very good that the path correction has been accurately found.

The first step in making a path correction is to collect all of the information pertaining to the seismogram. The following items are required:

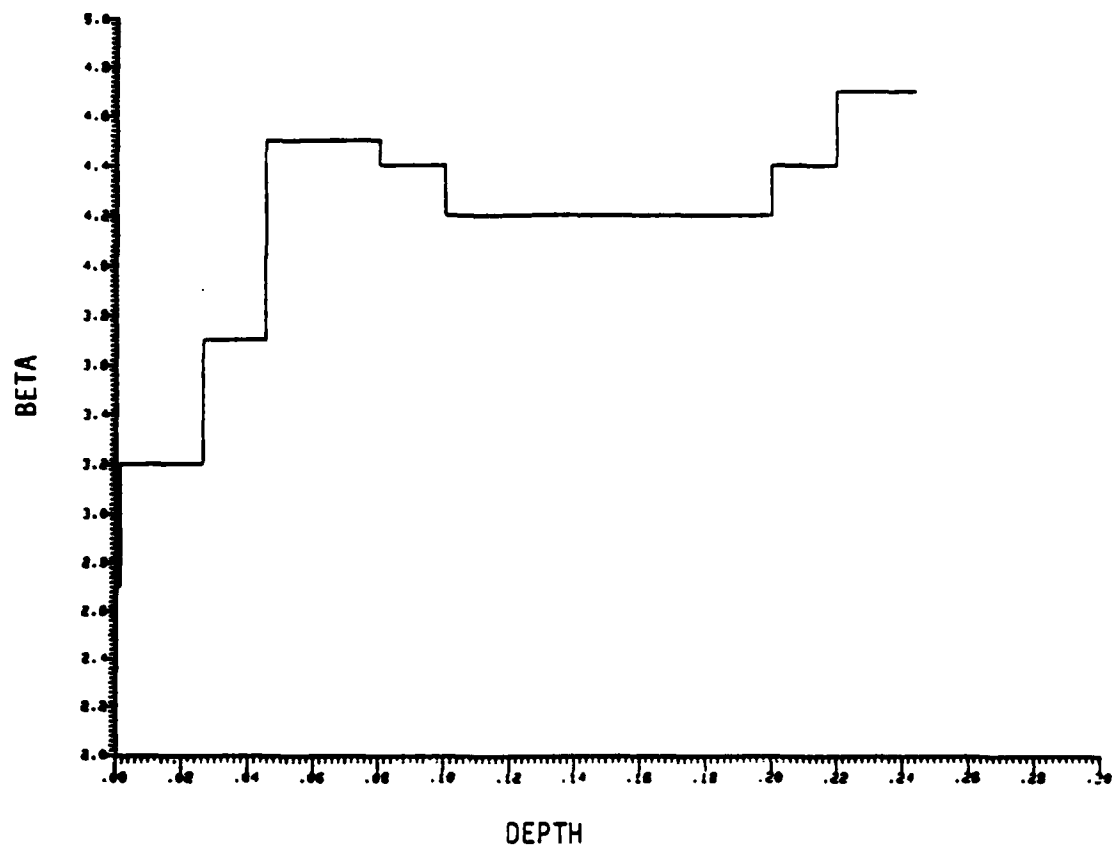
1. A seismogram sampled at evenly spaced points in REALIO format demeaned, detrended and tapered.
2. The number of points in the seismogram.
3. The sampling interval for the seismogram.
4. The time delay between the source time and the start of the seismogram.

5. The distance from the source to the receiver.
6. The instrument response expressed as a ratio of polynomials also in REALIO format.

It is very important to have an accurate estimate of source to receiver distance, and the seismogram start time. It is well worth double checking these numbers since everything that follows will be wrong if these numbers are incorrect. Of course, errors of a few seconds or a few kilometers may not result in major errors in the final results, but it is the abundant typos and minute errors that can be disastrous. The best way to be sure of timing is to compare several seismograms for the same path to be sure the times are all consistent.

Several small utility codes are available which allow the conversion of any seismograms to REALIO format as well as detrending, demeaning, etc., and which put instrument responses in the proper format (see appendices in topical report (Stevens, et al., 1982) for file formats, etc.). Instrument responses may be in polynomial form or may be tabulated instrument responses. One additional quantity is required by TELVEL -- the initial phase of the source. For an explosion (vertical component, displacement, positive up, Rayleigh wave) the initial phase is  $-3\pi/4$ . In order to illustrate the procedure we apply the entire surface wave analysis package to a synthetic seismogram. This is a useful exercise to go through before processing data for a new area, as the results help to identify certain problems in advance, and may help to identify the correct  $2\pi$  branch in the phase velocity analysis. If an approximate structure is available for an area, it should be used to make a similar test.

A synthetic seismogram was constructed (with program SYNSRF) using the structure listed and shown in Figure 1. The synthetic was computed using an SRO long-period instrument at a distance of 3000 kilometers and an explosion source with a  $\Psi_{\infty}$  (the long-period limit of the reduced velocity potential) of one cubic meter. The



THICKNESS (m)	ALPHA (m/sec)	BETA (m/sec)	RHO (Kg/m <sup>3</sup> )	Q
1100.0	5000.0	2700.0	2100.0	150.0
25000.0	5900.0	3200.0	2500.0	250.0
19000.0	6800.0	3700.0	2800.0	400.0
20000.0	8100.0	4500.0	3300.0	600.0
15000.0	8200.0	4500.0	3300.0	600.0
20000.0	8000.0	4400.0	3300.0	100.0
100000.0	7800.0	4200.0	3200.0	90.0
20000.0	8000.0	4400.0	3300.0	100.0
80000.0	8500.0	4700.0	3500.0	200.0

Figure 1. East Kazakh shear velocity structure used for synthetic seismogram.

synthetic seismogram and true phase and group velocity dispersion curves are shown in Figure 2. Figure 3 shows a form summarizing the inputs and outputs to the programs. It is useful to have a similar form available before starting the procedure.

### 2.2.1 Recovery of Phase and Group Velocities and Spectral Amplitudes

With this information in hand, the next step is to run TELVEL. The first phase of TELVEL is to apply a set of narrow-band filters to the seismogram to obtain an approximate set of group velocities. The choice of filter frequencies and filter widths (specified in terms of the filter  $Q$ ) is up to the user. From experience, a  $Q$  of 10 provides a good filter width for most data./ For long-period data, such as SRO data, 20 to 40 frequencies from 0.01 to 0.1 Hz usually produces a good group velocity curve over the reliable frequency range of data (see Figure 4). Occasionally, the program will encounter difficulties in finding a good group velocity curve. If it does, try going back and using more or fewer frequencies or a lower or higher  $Q$ . Sometimes the program will find a good set of group velocities as evidenced by the peaks on the plot, but will not recognize it (no curve will be drawn through them). If so, they can be entered by hand using the edit command. The narrow band filter is an important step in finding the group and phase velocities. Not only does it provide an initial group velocity estimate, but it may show up features such as bifurcated group velocity curves which may render the phase matched filter unstable.

The purpose of TELVEL is to improve the initial estimate of group velocity by phase matched filtering while eliminating interfering multipath arrivals, higher modes and noise, and to find the phase velocities. The phase matched filter is found by integrating the group delay found initially by narrow band filtering. When the filter is applied to the original seismogram, the true surface wave is compressed into a narrow time window. The

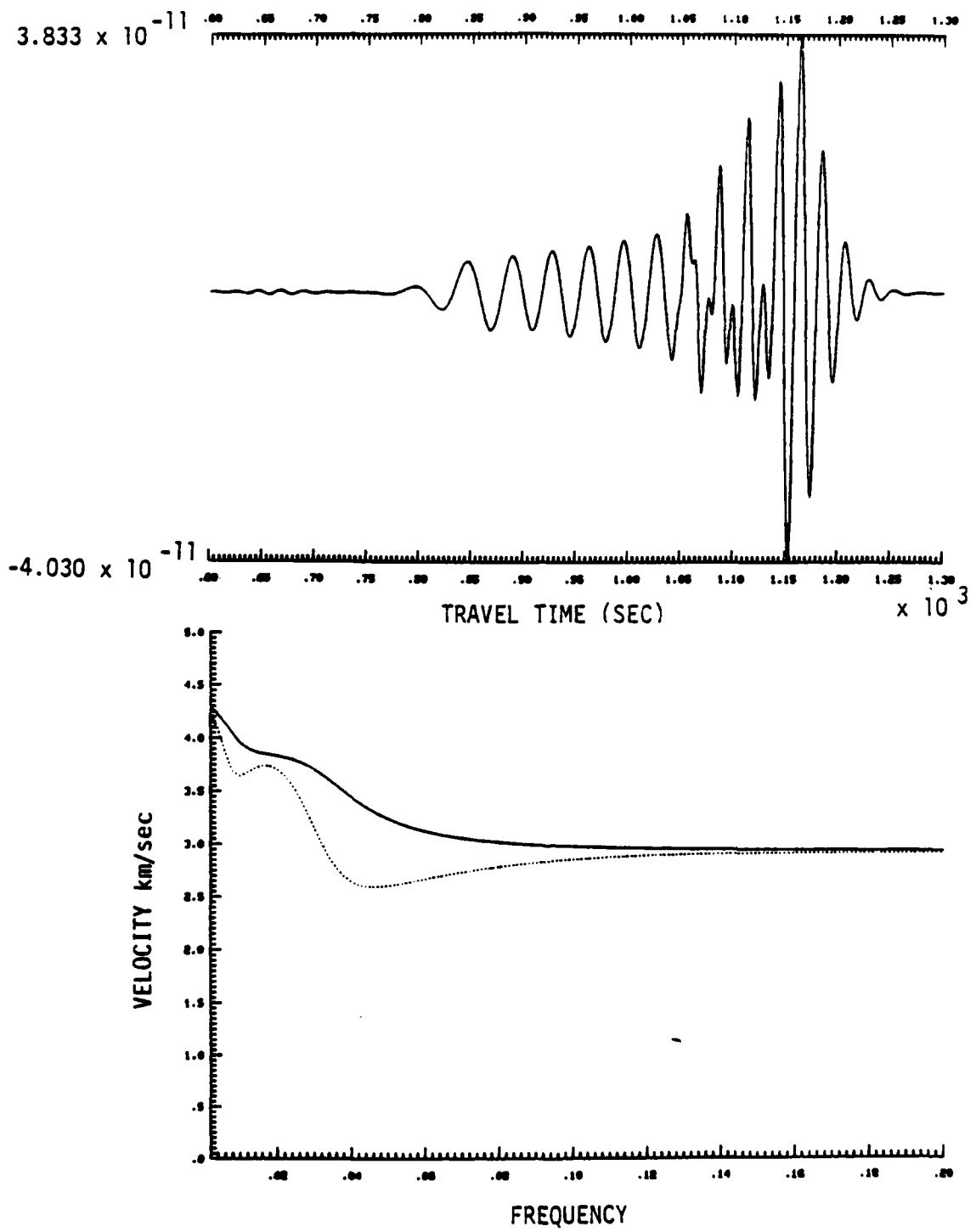


Figure 2. Synthetic seismogram (top) for the fundamental mode Rayleigh wave made using East Kazakh structure (Figure 1) and dispersion curves (bottom). Solid line is phase velocity, dashed is group velocity.

Source Location: East Kazakh  
Receiver Location: Synthetic a 3000 km  
Source Time: 0 sec  
Receiver Time: 600sec  
Delay Time: 600 sec  
Distance: 3000 km

Seismogram File: RSYN \* EKSRO  
Number of Points: 901  
 $\Delta T$ : 1.0 sec  
Instrument: SRO-LP  
Initial Phase = - 0.75

Narrow Band Filters Used  
NF, FMIN, FMAX, Q = 30, .01, .1, 10

TELVEL Output File(s): TEL \* EKSRO

Eigenfunction File for Source Region EF \* EKAZ2  
Instrument Gain (conversion to meters) 1.  
Estimated Moment =  $6.4 \times 10^{11}$  /Gain =  $6.4 \times 10^{11}$   
Estimated  $\Psi_\infty$  = .980 /Gain = .980

INVERT Output File(s): INV \* EKSRO

SYNSRF  
Frequencies Computed: 100, .002, .2

Output Files: EF \* EKSRO

Estimated  $M_s$ : 0.04  
Comments: Test on Synthetic Seismogram

#### PATH CORRECTION INFORMATION

Figure 3. Form summarizing inputs and outputs for Surface Wave Analysis Package.

SEC 6: OPTION(N-HELP) ? > L  
 GROUP VELOCITY PICKED:  
 1BX FREE CLIPV AMPL  
 1 2 3 4 5 6 7 8 9 10 11 12 13 14 15 16 17 18 19 20 21 22 23 24 25 26 27 28 29 30  
 .0165 2.656 .059  
 .0168 2.659 .183  
 .0209 2.674 .195  
 .0238 2.664 .222  
 .0263 2.593 .369  
 .0296 2.575 .449  
 .0336 2.592 .544  
 .0364 2.767 .673  
 .0393 2.674 .822  
 .0426 2.631 .944  
 .0445 2.612 1.000  
 .0469 2.607 .995  
 .0493 2.669 .915  
 .0518 2.616 .814  
 .0544 2.627 .763  
 .0570 2.641 .597  
 .0599 2.653 .566  
 .0632 2.677 .439  
 .0661 2.695 .363  
 .0690 2.712 .315  
 .0716 2.728 .276  
 .0743 2.743 .231  
 .0771 2.756 .197  
 .0800 2.769 .169  
 .0825 2.780 .145  
 .0850 2.791 .124  
 .0876 2.801 .106  
 .0904 2.809 .091  
 .0933 2.817 .078  
 SEC 6: OPTION(N-HELP) ? >

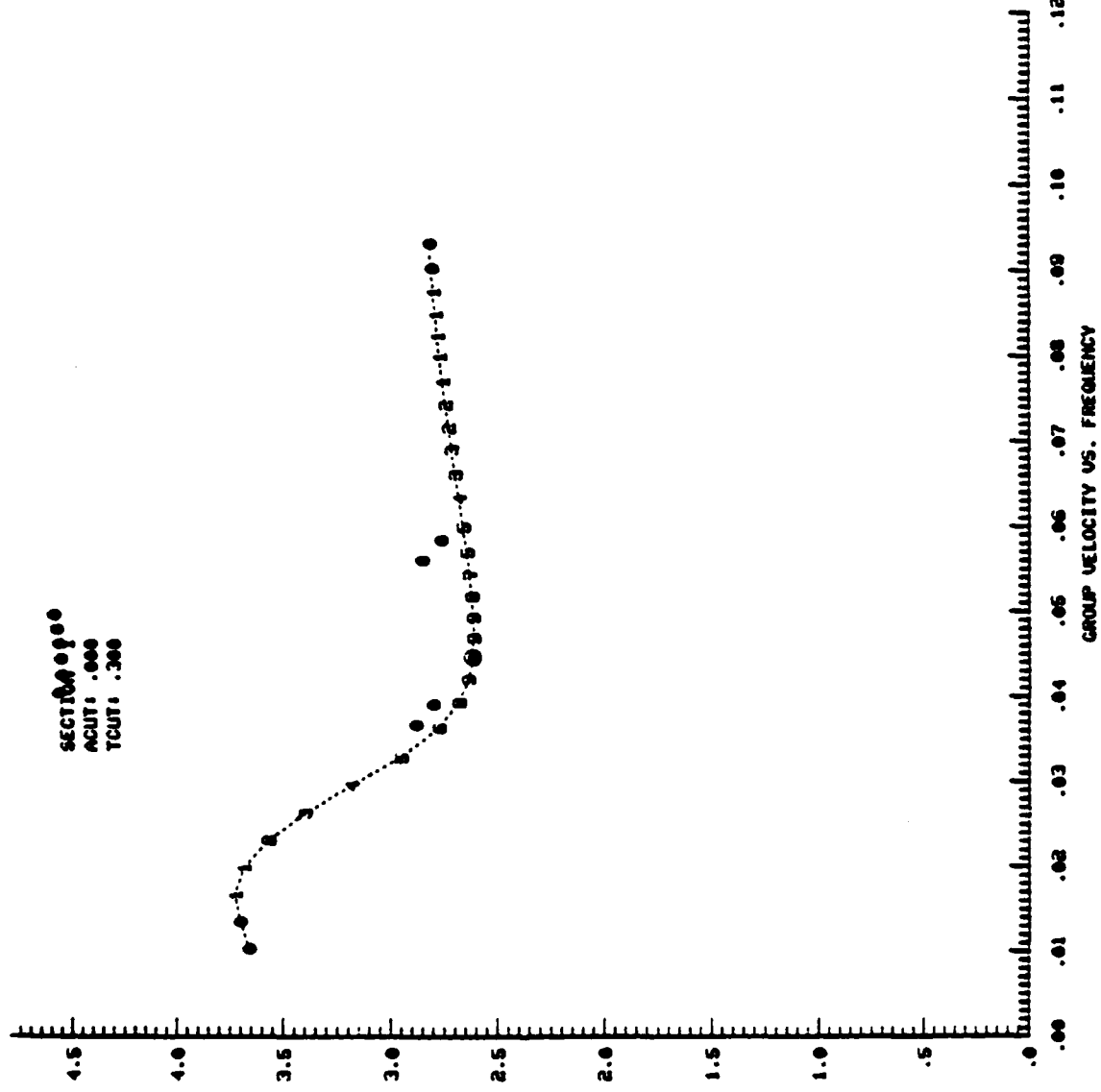


Figure 4. Group velocity curve obtained by narrow band filtering the synthetic seismogram in Figure 2.

resulting phase matched filter output is plotted by TELVEL to allow windowing of the time series (see Figure 5). It is important to choose a time window large enough to contain most of the energy in the main arrival, but small enough to eliminate most of the noise and multiple arrivals from the filter. The best way to choose the time limits is to look at the phase matched filter output and then back up to apply the appropriate time window. For long period data a time window of 50-100 seconds on each side of the main pulse is usually appropriate.

After the phase matched filter is applied to the seismogram, the filter phase is unwrapped and used to estimate the phase velocities of the Rayleigh wave. Since any multiple of  $2\pi$  may be added to the phase, there is an uncertainty introduced into the phase velocity. If  $\phi$  is the phase of the surface wave ( $\phi$  is always  $< 0$ ) then the phase velocity is given by

$$C = \frac{-2\pi fr}{\phi - \phi_0 + 2\pi n}$$

where  $r$  is the distance,  $\phi_0$  is the initial phase,  $f$  is the frequency and  $n$  is an undetermined integer. The choice of the correct value of  $n$  is often difficult. In order to help choose the correct value of  $n$ , TELVEL plots the phase velocity for a user specified value of  $n$  together with values of  $n \pm 1$  (see Figure 6). The following facts help in the choice of  $n$ .

1. The true phase velocity approaches a constant in the low frequency limit. If the phase velocity is well determined, values of  $n$  which are too small cause the phase velocity to decrease rapidly at low frequencies, while values of  $n$  which are too large cause the phase velocity to increase rapidly at low frequencies. In practice, the correct phase velocity is usually the first curve to turn upwards at low frequencies, although it is sometimes the first to turn downwards, and there is sometimes no clear choice.

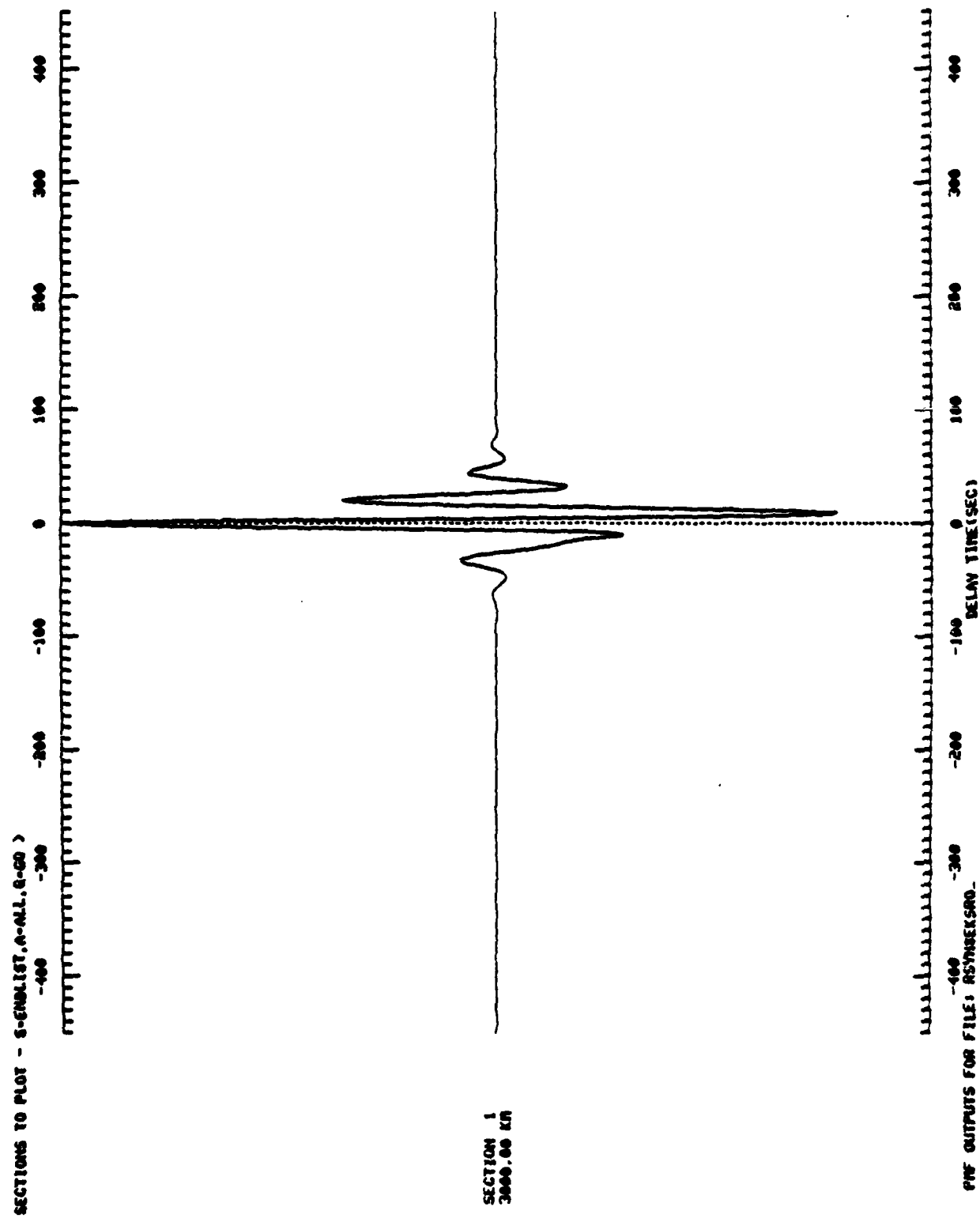


Figure 5. Phase matched filter output for synthetic seismogram. Energy is compressed to within  $\pm 100$  seconds of primary arrival time based on initial group velocity curve.

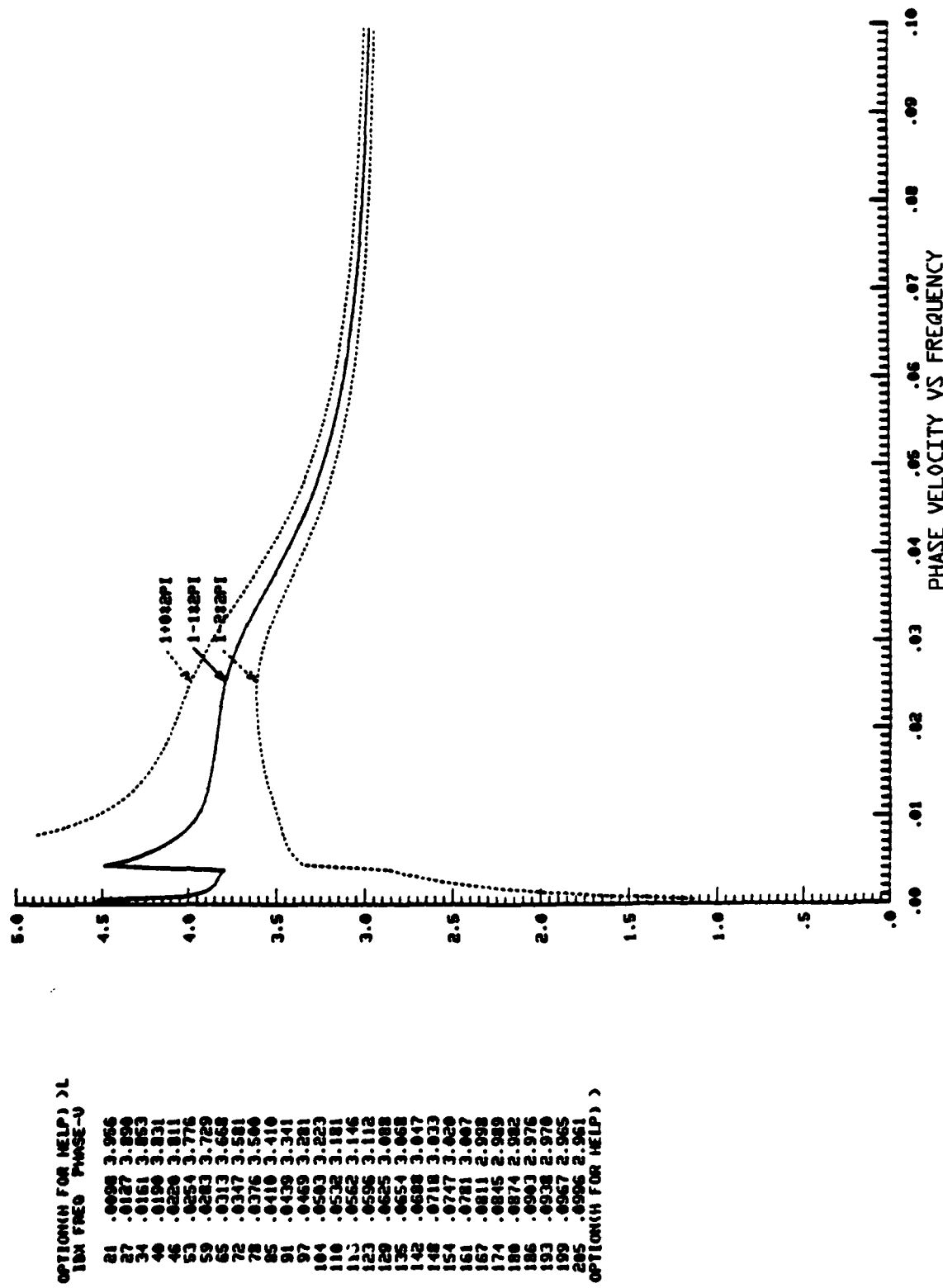


Figure 6. Phase velocities estimated by TELVEL for synthetic seismogram. Solid line is correct choice. Dashed lines differ by  $n \pm 2\pi$ .

2. The true phase velocity is not very different from the group velocity at low frequencies, and is always greater than the group velocity at the lowest accurately determined frequency.
3. The phase velocity is approximately equal to 4 km/sec in most regions of the world at frequencies between 0.01 and 0.02 Hz.

If the choice of number of  $2\pi$ 's to add to the phase is not clear, save output files for more than one value and see which one leads to a reasonable inversion model. Also, processing of another seismogram for the same path may lead to a clearer choice of phase velocity.

An iterative procedure is used to refine the group velocity estimate. Usually two or three iterations will produce stable group velocity estimates which do not change from one iteration to the next (see Figure 7). It is a good idea to save the phase velocity plot, and group velocity plot on the final iteration for future reference. The choice of  $2\pi$ 's to be added to the phase may be easier after the group velocity has converged.

The final decision to be made is the choice of frequencies to output. These do not need to be the same as the initial narrow band filter frequencies. The range of frequencies should be large enough to include all data points that are reliable, but small enough to exclude unreliable data points. Two figures obtained in the processing help to identify the appropriate range. Points on the initial narrow band filtered group velocity plot with amplitudes less than 10 to 20 per cent (indicated by 1 and 2 on the plot) of the maximum amplitude are not likely to be reliable. On the final group velocity plot, portions of the curve at the ends, which have not stabilized, are not reliable. Portions of the group velocity curve which appear odd such as those which have a rapid decrease in velocity or an unusually high velocity at low frequency or rapid oscillations at high frequency should not be used. Periods longer than the time window used are also unreliable. It is important to

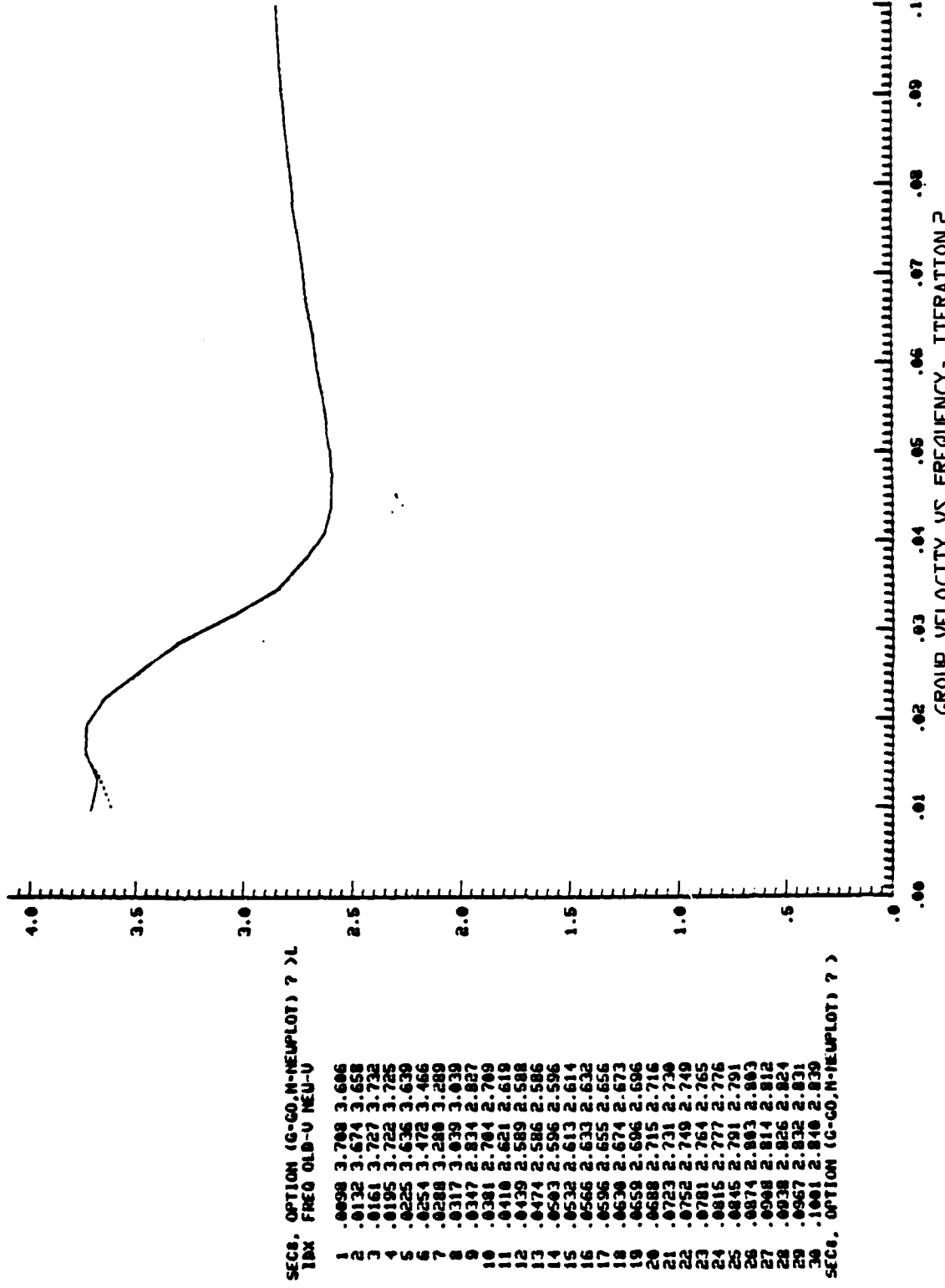


Figure 7. Final group velocities obtained for synthetic seismogram by iterative application of phase matched filter.

obtain information at low frequencies since these frequencies determine the deep structure of the earth. For most SRO station at distances of 2000 through 5000 kilometers, phase and group velocities may be reliably obtained from about 0.015 to 0.08 Hz. A convenient frequency spacing is 0.005 Hz. Phase and group velocities can almost always be obtained down to a minimum frequency of 0.02 Hz.

The output file from TELVEL contains the estimated phase and group velocities and the instrument corrected spectral amplitudes of the seismogram. The corrected amplitudes should be an improvement over the Fourier amplitudes, since they are obtained from the compressed seismogram after the removal of noise and interfering phases.

The TELVEL output file also contains a space for the standard deviation of the phase and group velocity. TELVEL does not estimate errors in the velocities, so it simply outputs default values of zero. If more than one seismogram for the same path are processed, they can be averaged to get an improved estimate of phase and group velocities and to estimate uncertainties in the data. A small utility program (AVEDAT) is available which constructs a combined file in the format of a TELVEL file.

### 2.2.2 Inversion for Earth Structure

The TELVEL output file is in the proper format to be used by the second major code -- INVERT, which inverts the phase and group velocities for the average shear velocity structure along the path, and which uses the amplitudes to estimate the Q structure of the path.

Program INVERT has been designed to require a minimum of operator input. A starting model is automatically generated from the input data. The final model is independent of the starting model, but it is important to choose a suitable range of depths appropriate for the resolution capability of the data.

Only the TELVEL output file is required for shear velocity inversion. One other file is needed for Q inversion. Assuming that

the structure of the source region is approximately known independently from previous investigations, an eigenfunction file (generated for the source region structure by program SYNSRF) will be input at this stage.

INVERT is divided into three main sections — model generation, inversion, and analysis. Most of the time the only command necessary in the model generation section is RUN which causes model generation to be performed. In the model generation section, the user can set a value of Poisson's ratio and the coefficients of Birch's law if desired. The inversion code only inverts for shear velocity while compressional velocity and density are constrained by these constants. The default values are appropriate for most of the earth and rarely need to be changed. Two features which are sometimes needed are the ability to set a discontinuity at a particular depth, and the ability to set the number of layers used in the inversion. The default number of layers is 20. A smaller number of layers will result in a faster, but less accurate inversion.

In many cases a discontinuity may be required to match the data, but its depth is not usually known in advance. The best plan is to run the inversion section and insert a discontinuity where the resulting model shows a strong velocity gradient.

The first step in the inversion is to constrain the smoothness of the model defined by the number of degrees of freedom (command DF) allowed. A small value of DF produces a smooth model while a higher value produces a better data fit. A good value to start with is a DF of 4.

The command INVERT causes the first iteration of the inversion to be performed. This command causes partial derivatives  $ac/\partial\theta$  and  $au/\partial\theta$  to be calculated from the initial (or current) model. It causes a set of matrices to be assembled from the partial derivatives, and performs a full singular value decomposition of the matrices. Finally it computes the exact nonlinear phase and group velocities for the estimated model with the DF specified initially. All of this requires quite a lot of computation and will take some computer time.

After the inversion has been performed, the command PLOT will plot the shear velocity structure while the command PLOT DATA will plot the linearized data fit.

The command DF has a new meaning after an inversion has been performed. A major advantage of the matrix decomposition is that new models for different values of DF may be generated without recomputing the matrices. Thus if the command DF 4 was given before inversion, the command DF 5 after inversion instantly produces the (linearized) model for a DF of 5. The commands PLOT and PLOT DATA again produce the model and data fit for the new DF (see Figure 8). This makes it very easy to pick the best value of DF. A second iteration can then be performed using this model as the new starting model. Usually three iterations with the same DF are sufficient for convergence.

An obvious question is how to choose the best model. The answer is to use a DF high enough to get a good data fit, but small enough to prevent oscillations of the shear velocity model, and to yield a smooth fit to the data. Usually a DF of about 5 gives a good model. With good quality data such as the SRO data a DF of 6 may be used, while less accurate data may only allow a DF of 4 (DF need not be an integer).

One other choice must often be made during inversion. It may be necessary to include a discontinuity in the model. The most common place a discontinuity is needed is at the crust-mantle boundary. The proper location for the discontinuity may be determined by the midpoint of a sharp gradient which appears in the shear velocity model. Within the inversion section a discontinuity may be added by specifying the number of the layer above the desired discontinuity, or it may be specified by depth by returning to the model generation section (this is unnecessary unless the user requests a specific depth which does not coincide with a layer boundary). If higher frequency data are available, as it may be for WWSSN instruments at distances less than 1000 kilometers, it may be necessary to include a shallow discontinuity in the upper few

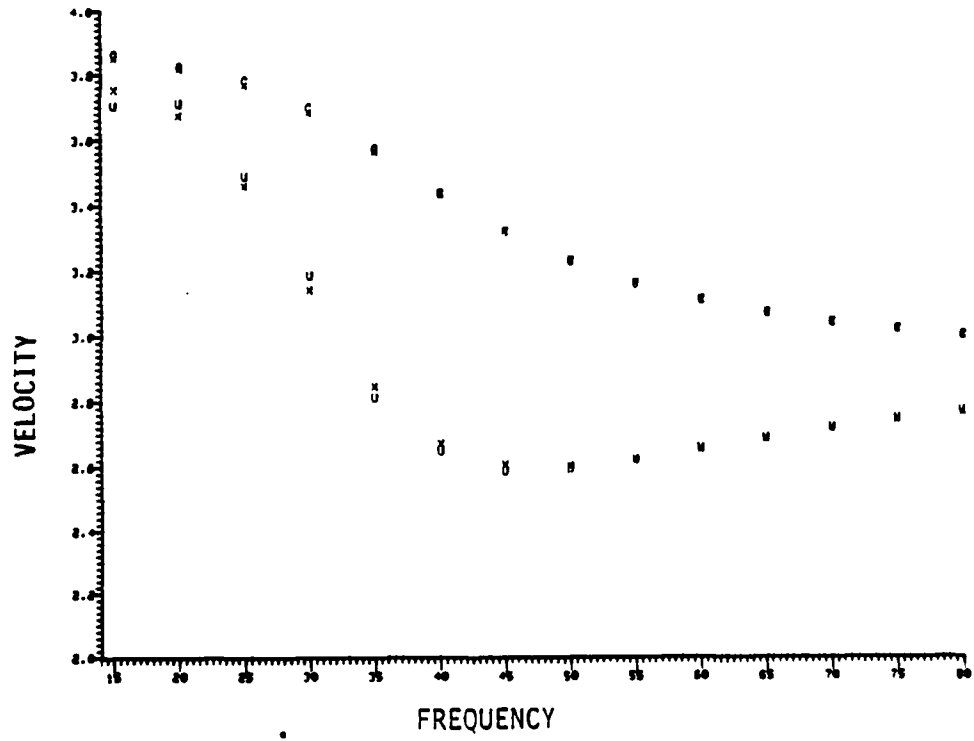
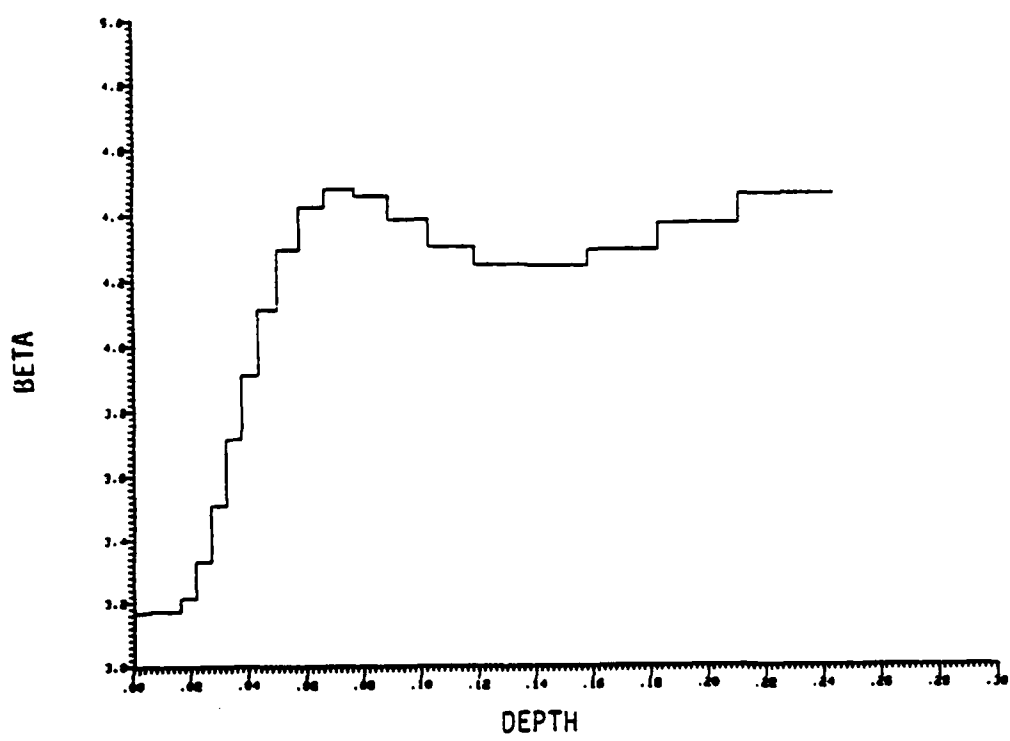


**Figure 8.** Shear velocity structure obtained by inverting dispersion curves produced by TELVEL from the synthetic seismogram, together with linearized data fit. The strong gradient from 20 to 60 km indicates a possible discontinuity. This model is shown for the second iteration using a DF of 5.0. (X) indicates synthetic data, (U) indicates estimated group velocity, (C) indicates estimated phase velocity.

kilometers. It may be difficult to define the proper depth, since the phase and group velocities may lose accuracy at the high frequencies needed to resolve shallow depths. When the presence of this layer is indicated, it is often essential. The NTS-Tucson seismograms, for example, absolutely cannot be matched without a shallow low velocity, low Q layer in the upper two kilometers (Bache, T. C., W. L. Rodi, and D. G. Harkrider (1978)).

After the last iteration has been performed, give the command END to finalize the inversion and go to the analysis section. Here you can make final plots of the model, and the true nonlinear data fit (Figure 9). You can also print the data fit, variances and spreads for the final model.

One more calculation is required to obtain the complete earth model -- the Q structure needs to be found. The program does this by computing a synthetic seismogram (actually an unattenuated synthetic spectrum) at the observed frequencies and taking the ratio with the spectrum of the filtered data. The logarithm of the ratio is equal to a constant (the moment) plus a frequency dependent attenuation coefficient. In effect the level of the spectral ratio gives the moment, while the shape of the spectral ratio as a function of frequency gives the attenuation coefficients which can be inverted for the Q structure. As mentioned before, if an eigenfunction file is available for the source region, the program will generate the synthetic spectrum using these eigenfunctions for the source region and using the inverted structure for the path. The program uses the spectral ratio and inverts for log moment and  $\beta/Q$  simultaneously.

The spectral amplitudes are never known as accurately as the phase and group velocities, so a lower DF must be used for Q inversion. The minimum possible DF is 2. A DF of 2 will produce Q proportional to  $\beta$  in all layers. An important function of the Q inversion is in fact to smooth the spectral ratios and the attenuation coefficients. It is usually necessary to use a DF between 2 and 3. Higher DF's result in unrealistic Q structures. Discontinuities are not allowed for Q inversion, and are not used even if they were used in the velocity inversion.

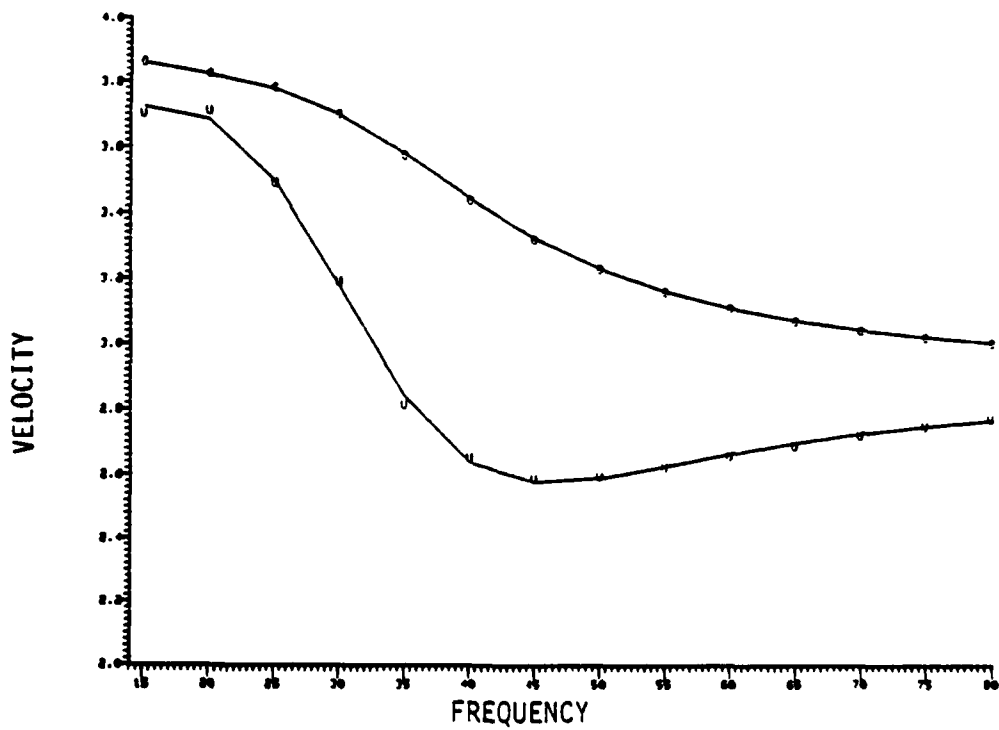
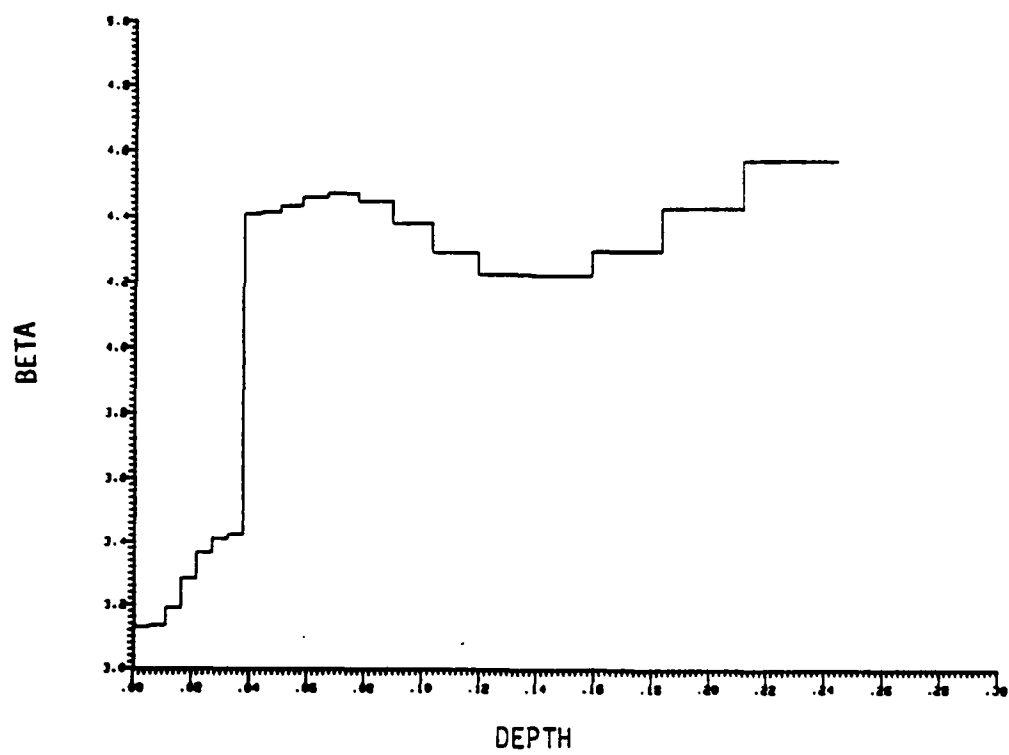


Figure 9. Final model obtained using a DF of 6.0 and a single discontinuity (compare with Figure 1) together with data fit. The intermediate layer from 30 to 50 km has been split by the single discontinuity. The dispersion curves are an excellent fit to the data.

Q inversion is linear, and takes little computer time. Matrices are formed and decomposed on the first iteration, so the best Q model may be quickly found. Again the command PLOT plots the Q model while the command PLOT DATA plots the spectral ratios and corresponding data fit. The spectral ratios should look like an upward sloping line (see Figure 10). If the data points do not have an upward slope, it means the attenuation coefficients decrease with frequency and no Q structure will fit the data. If this happens, there is probably something wrong with the inversion, or with the data.

When the Q inversion is performed, the estimated moment and  $\Psi_\infty$  of the explosion are printed out. Save these numbers, since they are not printed out again.

Since the Q inversion produces a smoothed S/Q model, it will not reveal any true discontinuities in Q in the earth. In particular, it will not usually produce a very low Q at the surface. If high frequency data have been used, it may be necessary to add a low Q layer near the surface after the inversion to reduce high frequency ringing.

Once the inversion is completed the final step is to output a structure file. The structure file is a formatted file, which is in the format of an input file to SYNSRF.

### 2.2.3 Generation of Synthetic Seismograms and Excitation Functions

The third stage of the path correction procedure is to use the program SYNSRF to generate an eigenfunction file, and to make a synthetic seismogram as the final test of the procedure.

SYNSRF is divided into four main sections. The first section requires input of a model (structure) file and a choice of frequencies for the calculation of phase velocities. The second section calculates group velocities, eigenfunctions and related parameters. The third section calculates a synthetic seismogram. The fourth section allows prints and plots of the seismogram, spectra and dispersion curves.

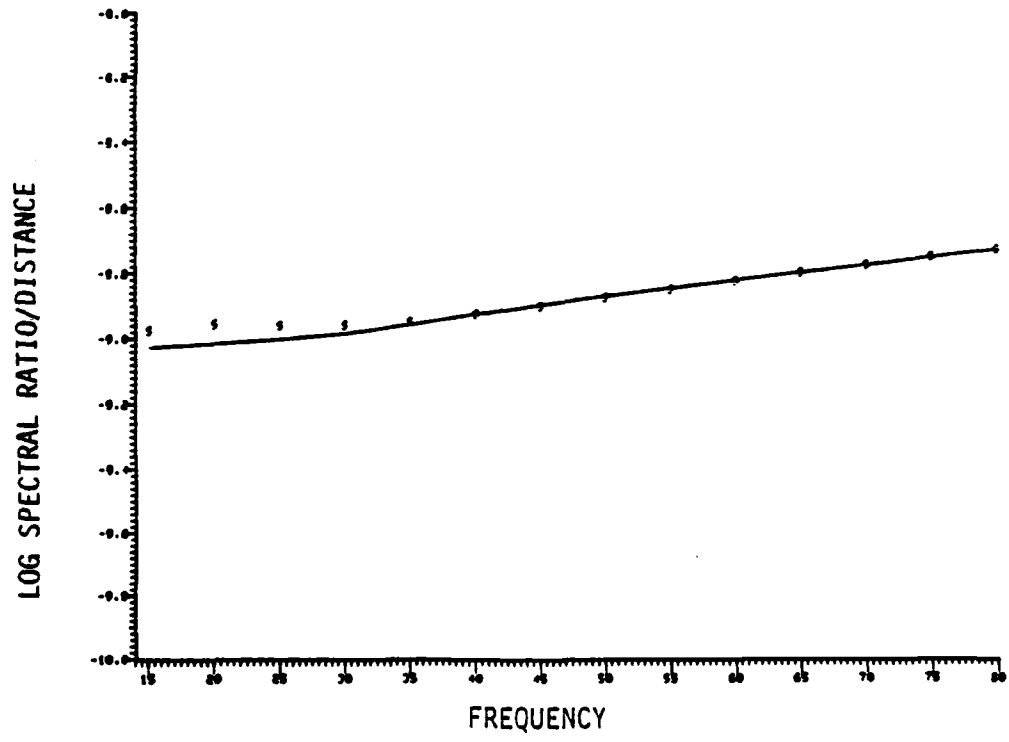
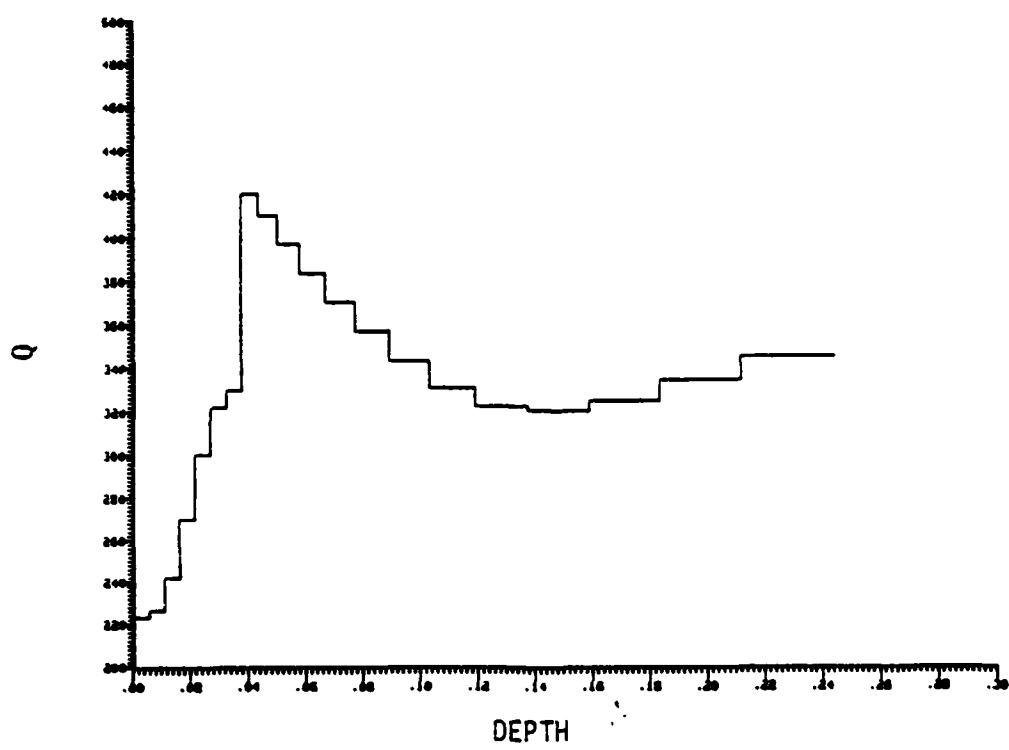


Figure 10. Q structure and data fit obtained using a DF of 2.5. The Q model is a smoothed version of the true Q model (Figure 1) while the data is the ratio of synthetic (unattenuated) to observed spectra. The moment is obtained simultaneously. For this example the moment differed by 2% from the true moment.

SYNSRF is designed to be easy to use and to make it easy to correct mistakes. If you run one of the sections and use an incorrect number, or forget to output a file, simply back up, make the change and run this section again. None of the sections is very time consuming and all previous inputs are remembered (except for output files, since they are closed after each section is run).

The essential input in part 1 of SYNSRF is the model file (the output file from INVERT). The default set of frequencies is 100 frequencies evenly spaced from .002 to .2 Hz. In most cases, this will be a good range of frequencies. For observations at close range (< 1000 km) with an instrument that does not filter out higher frequencies, it may be necessary to use frequencies from .005 to .5 Hz instead. The program is currently dimensioned to allow 100 frequencies and three modes. After the model file is read in in Part 1, the program looks through the shear velocities to estimate root search parameters (minimum and maximum phase velocities and a step size). The default values are almost always adequate, especially for the fundamental mode. If the step size chosen is too large, a root may be missed. This will show up as a glitch in the dispersion curve.

The command RUN causes dispersion curves to be calculated and leaves the program in Part 2. The only inputs needed in Part 2 are the source depth and a file name for the eigenfunction output file. The default source depth is 1 kilometer. If the structure being used is the path structure, then the source depth is irrelevant. It is necessary to specify an eigenfunction file name here. This file will be used in two ways. It will be read back in Part 3 if a separate source region is used, and it contains all of the information needed to construct the Green's function that is the final path correction.

The command RUN now causes the eigenfunctions to be generated and leaves the program in Part 3. You can make a plot of the dispersion curves (phase and group velocities) here to compare with the observations. Make this plot before reading in a new source

region eigenfunction file, since the velocities plotted are the source region velocities.

Several quantities must be input here to make a synthetic seismogram. If you are using separate source and path regions, an eigenfunction file for the source region and the eigenfunction file for the path must be read in. An instrument response must be read in, preferably using the polynomial coefficients that were in TELVEL. The distance and time window must be specified here. After the distance is set, the time window is estimated by the program using the group velocities. For the purpose of making a path correction, however, it may be preferable to use the time window of the original seismogram to make the comparison easier.

The command RUN now causes a seismogram for an explosion with a  $\Psi_\infty$  of one cubic meter to be generated, and leaves the program in Part 4. Then plots of the seismogram and spectrum may be made, a run summary may be obtained, and surface wave magnitudes may be computed.

The seismogram plotted here should look like the original seismogram (see Figure 11) after removal of noise and multipathing. The amplitude should differ from the original amplitude by a factor approximately equal to the  $\Psi_\infty$  estimated in the inversion calculation.

The last step in the procedure is to transform the eigenfunction file into a form usable by a moment tensor inversion program. A short program EXCITE turns the eigenfunction file into a formatted file using the excitation function notation of Kanamori and Given (1981). A more detailed explanation of this approach is given in Appendix 4 of the report by Stevens, et al. (1982).

### 2.3 SHAGAN RIVER-SRO PATH CORRECTIONS

In this section we describe, in brief, the processing of explosion seismograms recorded at seven SRO stations. For each path there is a description of the analysis including an estimate of

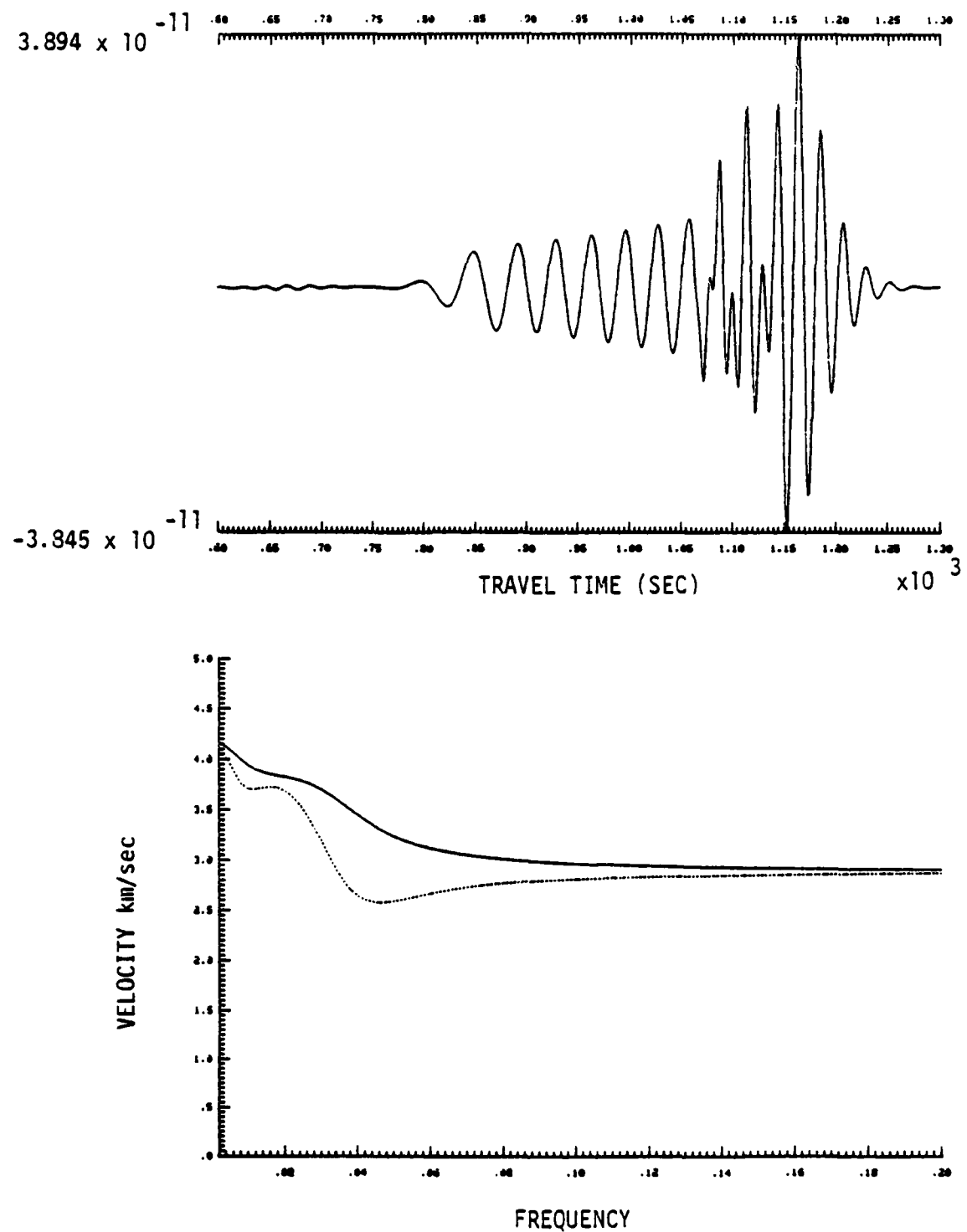


Figure 11. Synthetic seismogram generated using the structure output by INVERT, together with phase and group velocity dispersion curves. Compare with Figure 2.

confidence for each path correction, plus five figures. The first figure is a narrow band filter estimate of the group velocity for one seismogram along each path. The NBF estimate often shows up problems such as extreme multipathing, high noise level, or bifurcated group velocity curves which may cause difficulty in the data analysis. The second figure is a plot of the data fit, solid lines being the calculated phase and group velocity curves from our final structure while letters U (group velocity) and C (phase velocity) are observed data points. The third figure is a plot of shear velocity versus depth for the structure obtained by inversion, the fourth is a plot of Q versus depth, while the last figure is a listing of velocities, densities, obtained for each model. The three events processed are presumed explosions at the Shagan River test site which occurred on 2 December 1979 (No. 318), 29 November 1978 (No. 312), and 23 June 1979 (No. 313) according to the U. S. Geological Survey Preliminary Determination of Epicenters Bulletin. Event 312 is apparently a double event, in which an  $m_b$  6.0 followed an  $m_b$  5.3 by 4.0 seconds. We used the parameters appropriate for the larger event in the processing, and could see no sign of the smaller event. The seismograms are shown in Figures 12 through 14.

In addition to obtaining a velocity and Q structure for each path, we also obtain an estimate of moment for each path. By assuming a known compressional velocity and density for the source region (we used  $\alpha = 5000$  m/sec,  $\rho = 2100$  kg/m<sup>3</sup>), the result may be expressed in terms of  $\Psi_\infty$  using the relation  $M_x = 4\pi\rho\alpha^2\Psi_\infty$ . The results are listed in Table 1.

The last station is considerably less reliable than the first six for reasons that will be explained with the data. It is interesting to note that there seems to be a correlation between the estimated  $\Psi_\infty$  and the quality of the data. This may be an indication of energy lost due to scattering and non-plane layered effects along the travel path. It does not seem to result from application of the

Event: 318 Class: Ex Location: Shagan River  
Lat: 49.937 Lon: 78.817 Depth: 0.0 Rb: 6.0  
Date: 2 Dec 79 O-time: 036:04:36:57.5 Mat: 4.26

Station Delta Start time

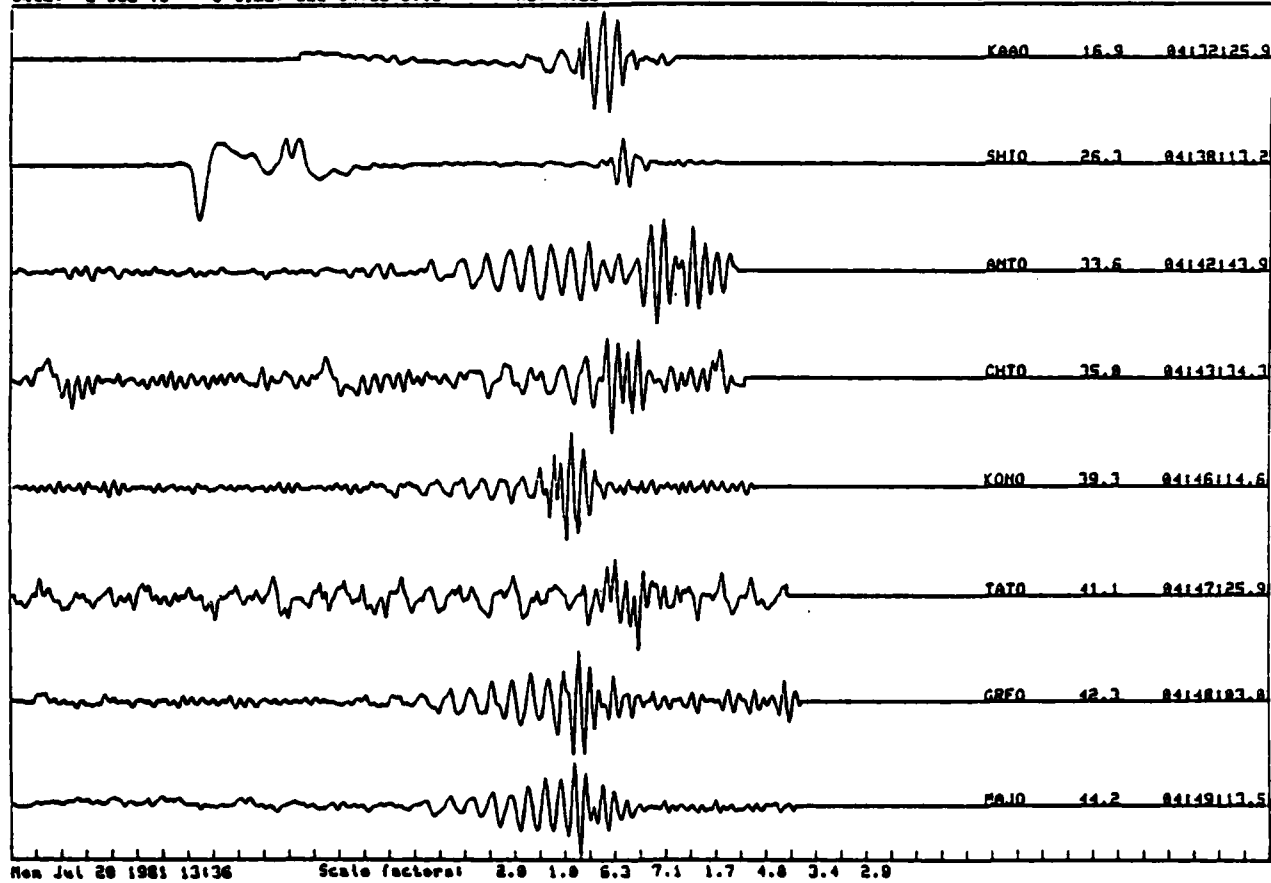


Figure 12. Seismograms recorded at SRO stations for Shagan River explosion number 318, December 2, 1979. Seismograms were processed to obtain path corrections for stations KAAO, SHIO, ANTO, CHTO, KONO, GRFO and MAJO. Before processing, a reduced time window was chosen to eliminate early arrivals and glitches and the seismograms were demeaned and detrended.

Event: 312 Class: Ex Location: Shagan River  
Lat: 49.861 Lon: 78.716 Depth: 0. Mag: 5.3  
Date: 29 Nov 78 O-time: 033704:32:58.0

Station Delta Start time

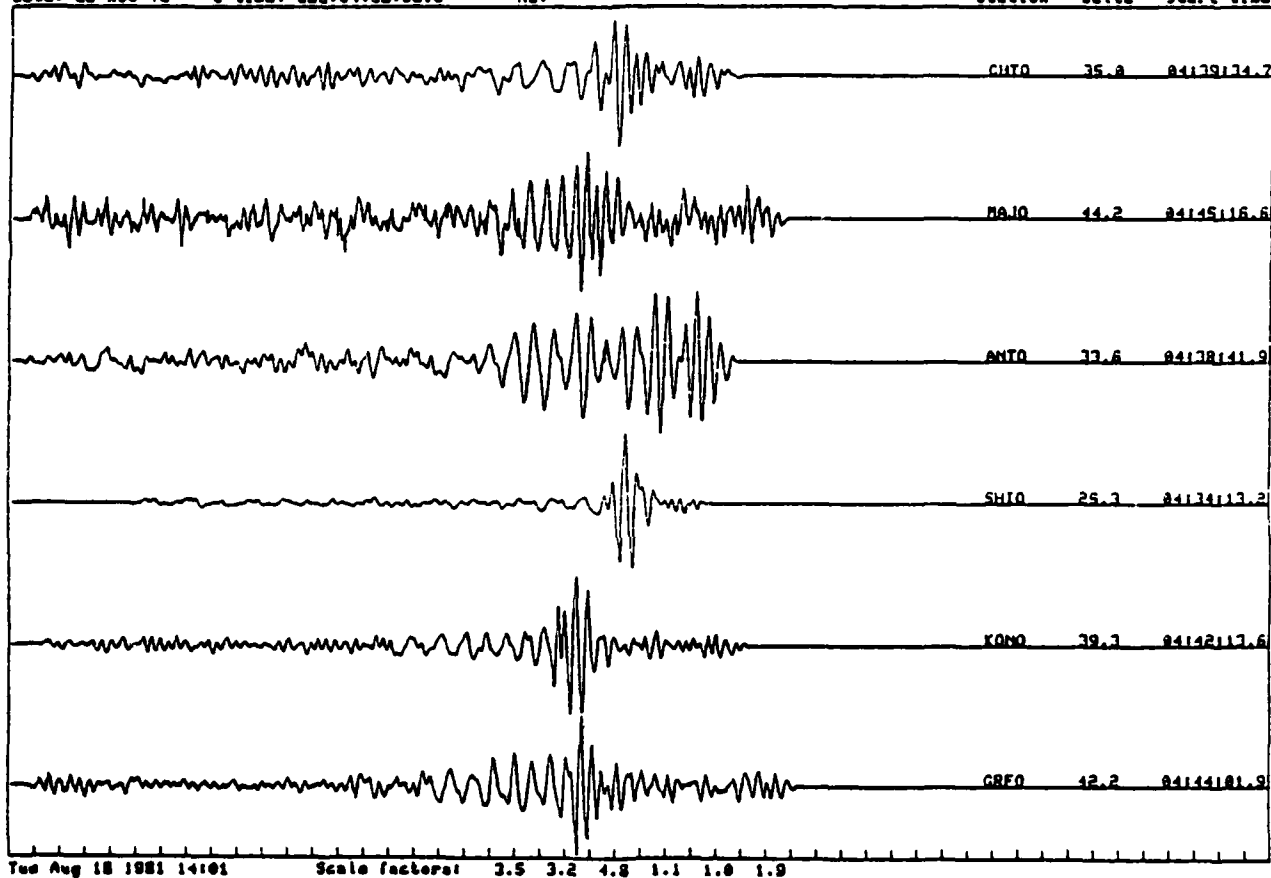


Figure 13. Seismograms recorded at SRO stations for Shagan River explosion number 312, November 29, 1978. Seismograms were processed to obtain path corrections for stations CHTO, MAJO, ANTO, SHIO, KONO, and GRFO.

Event: 313 Class: Ex Location: Shagan River  
Lat: 48.886 Lon: 78.887 Depth: 8. Mag: 6.3  
Date: 23 Jun 79 O-time: 174:02:56:57.6 Mag:

Station Delta Start time

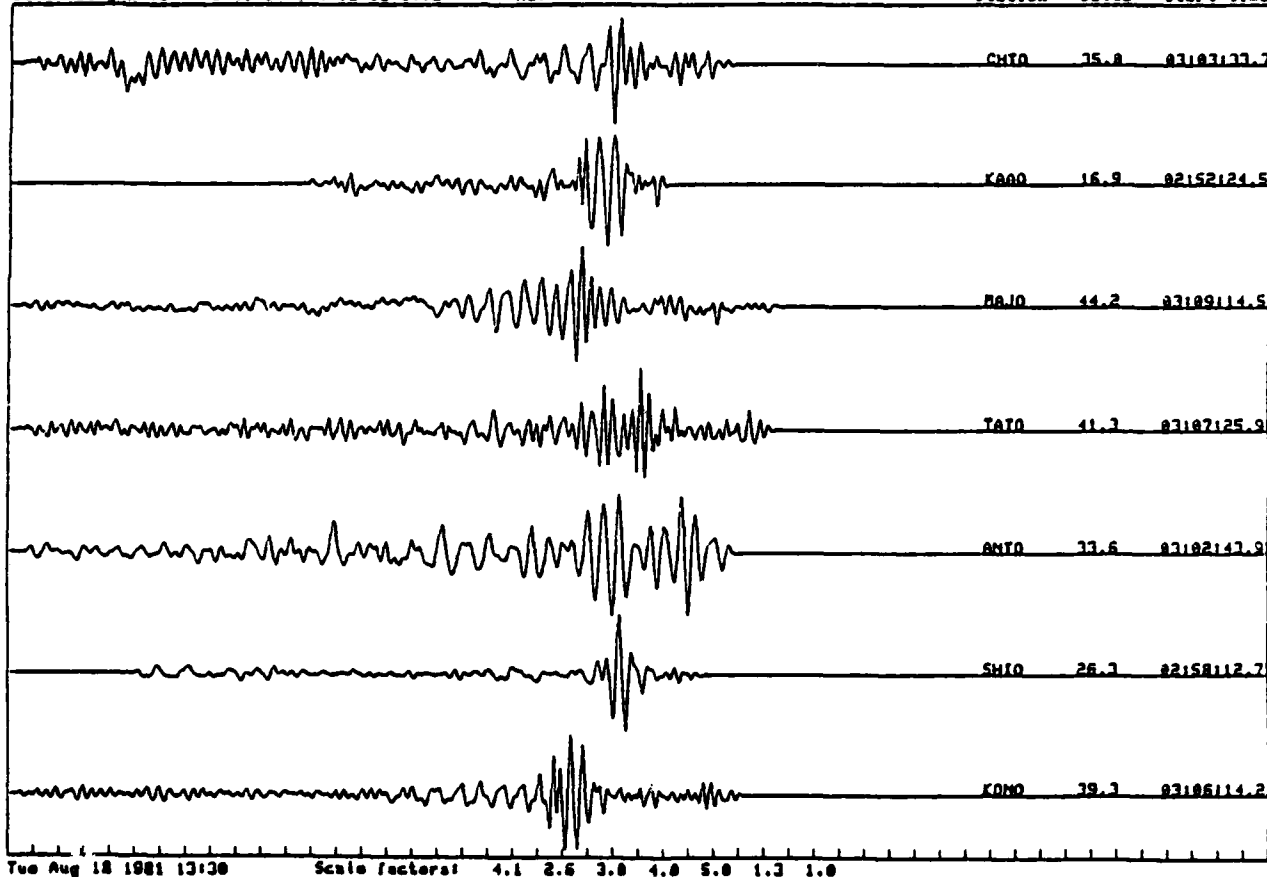


Figure 14. Seismograms recorded at SRO stations for Shagan River explosion number 313, June 23, 1979. Seismograms were processed to obtain path corrections for stations CHT0, MAJO, SHIO, and KONO. Processing of stations KAA0 and ANTO was attempted, but excessive noise and multipathing made it difficult to obtain stable group velocity curves at those stations.

Table 1  
ESTIMATED  $\psi_\infty$   
(MOMENT  $\div 6.60 \times 10^{11}$ )

<u>Station</u>	<u>Distance</u>	<u>Event No. 318</u>	<u>Event No. 312</u>	<u>Event No. 313</u>
KONO	4370	15100	9980	15000
SHIO	2926	13400	9760	13400
MAJO	4918	13000	5100	8100
GRFO	4700	11800	6700	—
ANTO	3739	10300	5440	—
CHTO	3890	7200	5000	6700
KAAO	1885	5700	—	—

phase matched filter time window since synthetic seismograms made using the estimated values of  $\psi_\infty$  are not consistently lower in amplitude than the observed seismograms based upon time domain measurements (see Table 2). Of course, the estimates of  $\psi_\infty$  also depend on the accuracy of the instrument gain. These seismograms were provided by Data Services at the Seismic Research Center (SRC) after conversion to nanometers (at 20 seconds).

In general, the processing resulted in reasonable velocity structures and Q structures for most of the stations and should provide a good estimate of the path structure and attenuation. The results are shown in Figure 15 through 21.

Table 2  
TIME DOMAIN AMPLITUDE COMPARISON

<u>STATION</u>	<u>OBSERVED/SYNTHETIC AMPLITUDES (NM)</u>		
	<u>Event No. 318</u>	<u>Event No. 312</u>	<u>Event No. 313</u>
KONO	765/725	460/479	736/720
SHIO	606/600	414/437	576/600
MAJO	371/378	134/148	248/236
GRFO	361/484	240/275	---
ANTO	192/156	94/83	143/---
CHTO	174/249	132/173	178/232
KAAO	613/305	---	282/---

Figures 15.1 through 15.5 are on the following pages.

Figure 15. Path 1: SHAGAN-KONO

Distance: 4372 km  
Azimuth: 72.6°  
Instrument: ASRO-LP  
Events Processed: 318, 312, 313

Description: This is an excellent station. A very clean group velocity curve was obtained with no evidence of multipathing or any observational problems.

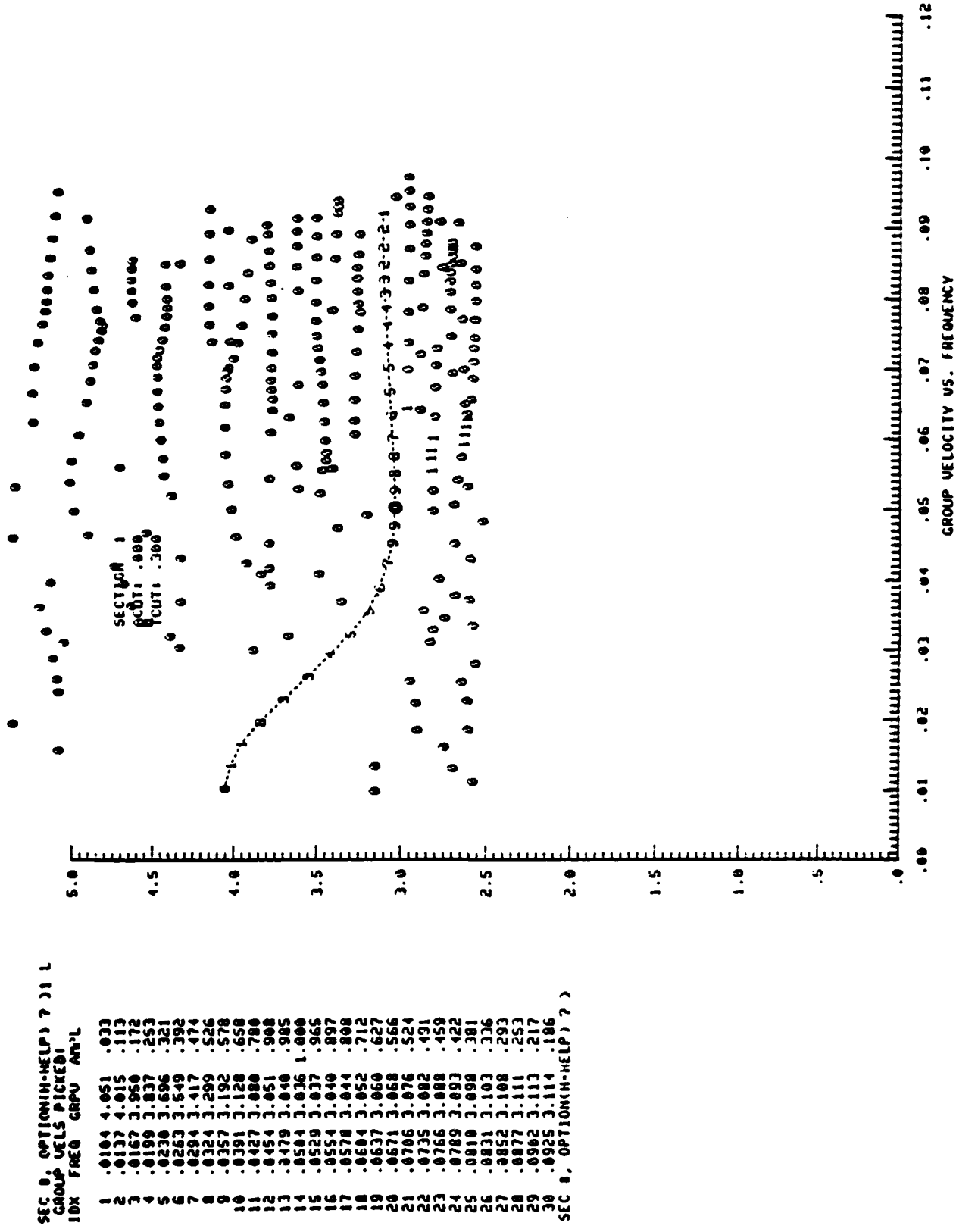


Figure 15.1.

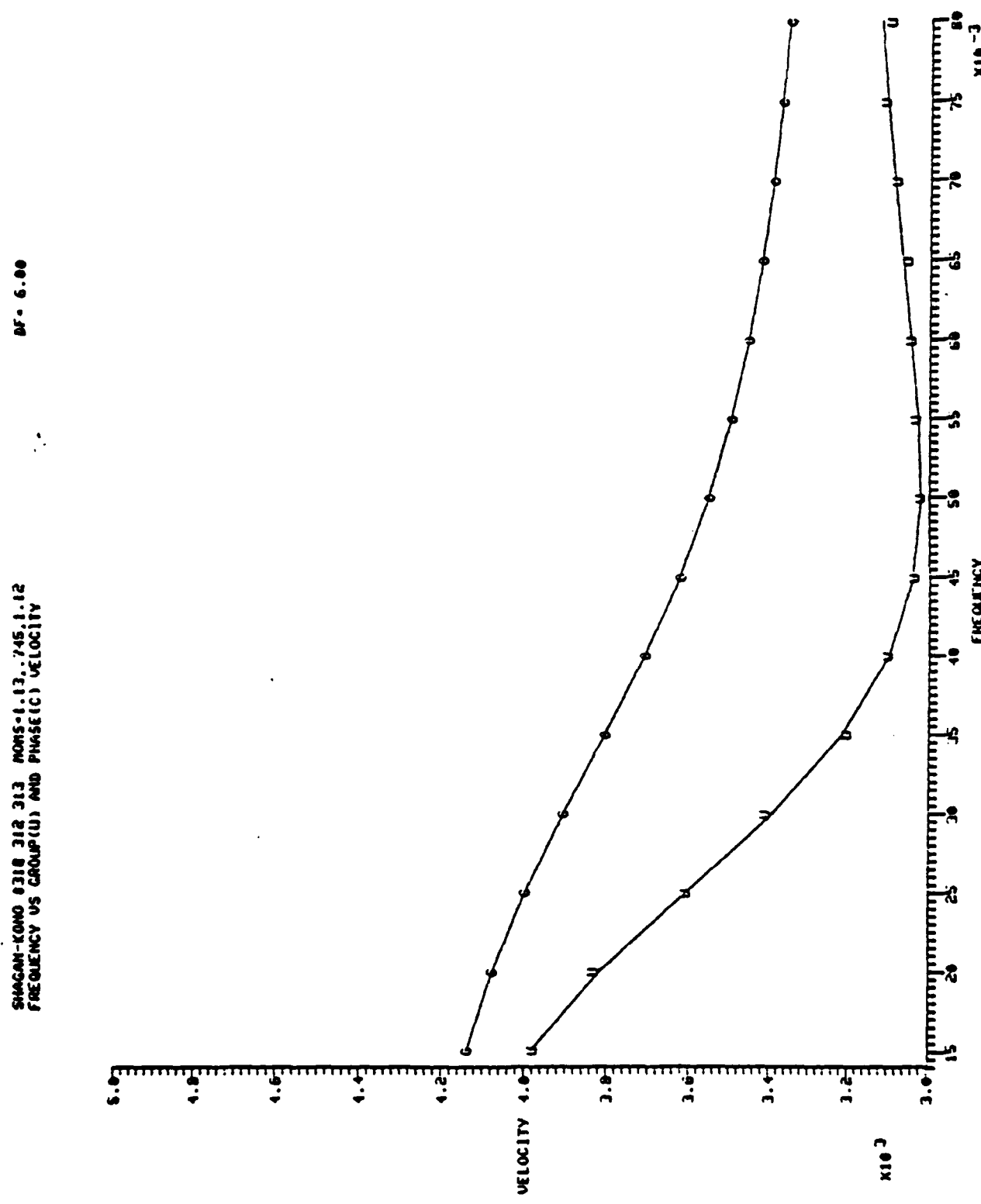


Figure 15.2.

SHAGAN-KONO 8310 312 313 M0NS-1.13.745.1.12  
CURRENT MODEL

DF = 6.00

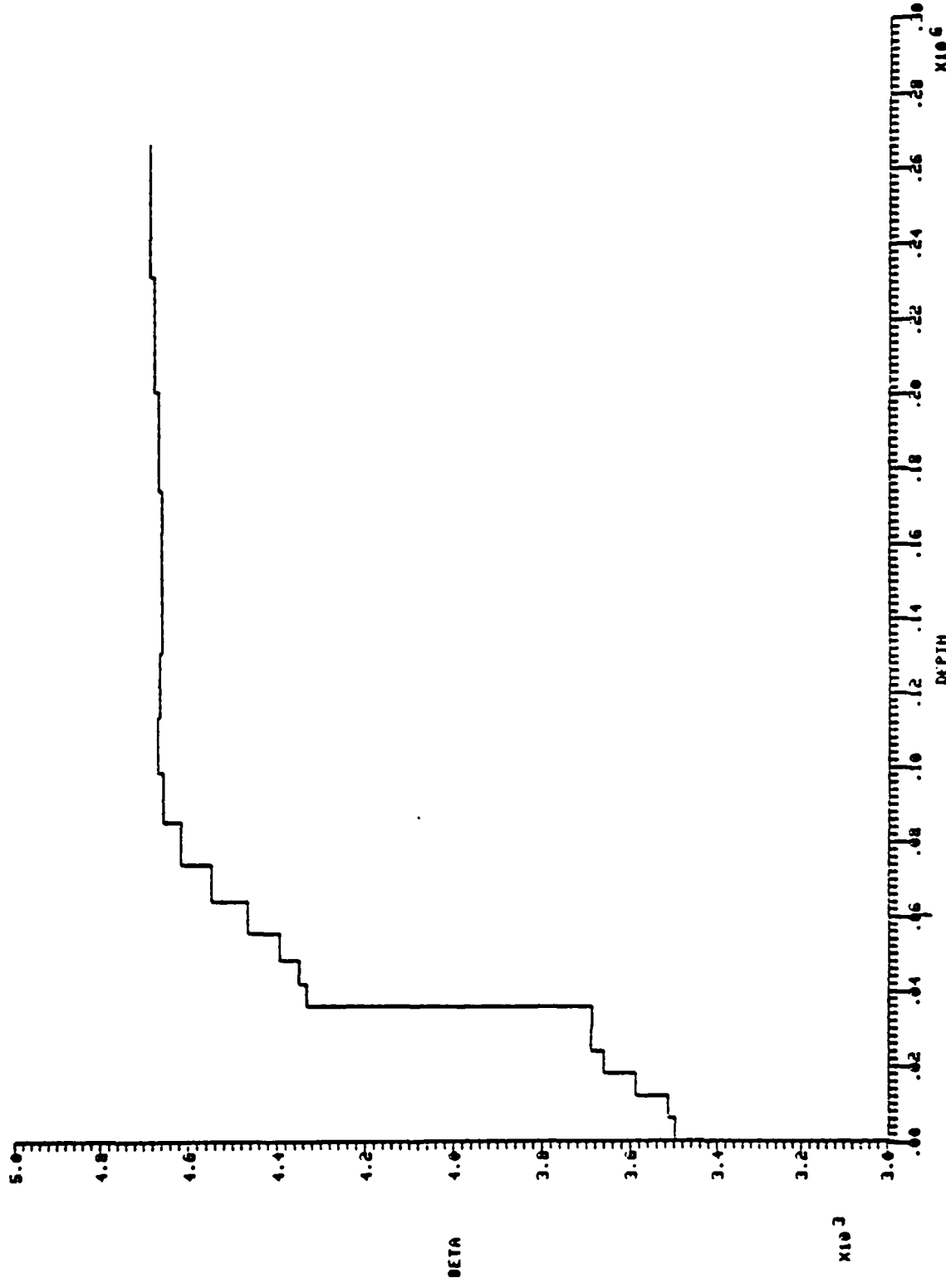


Figure 15.3.

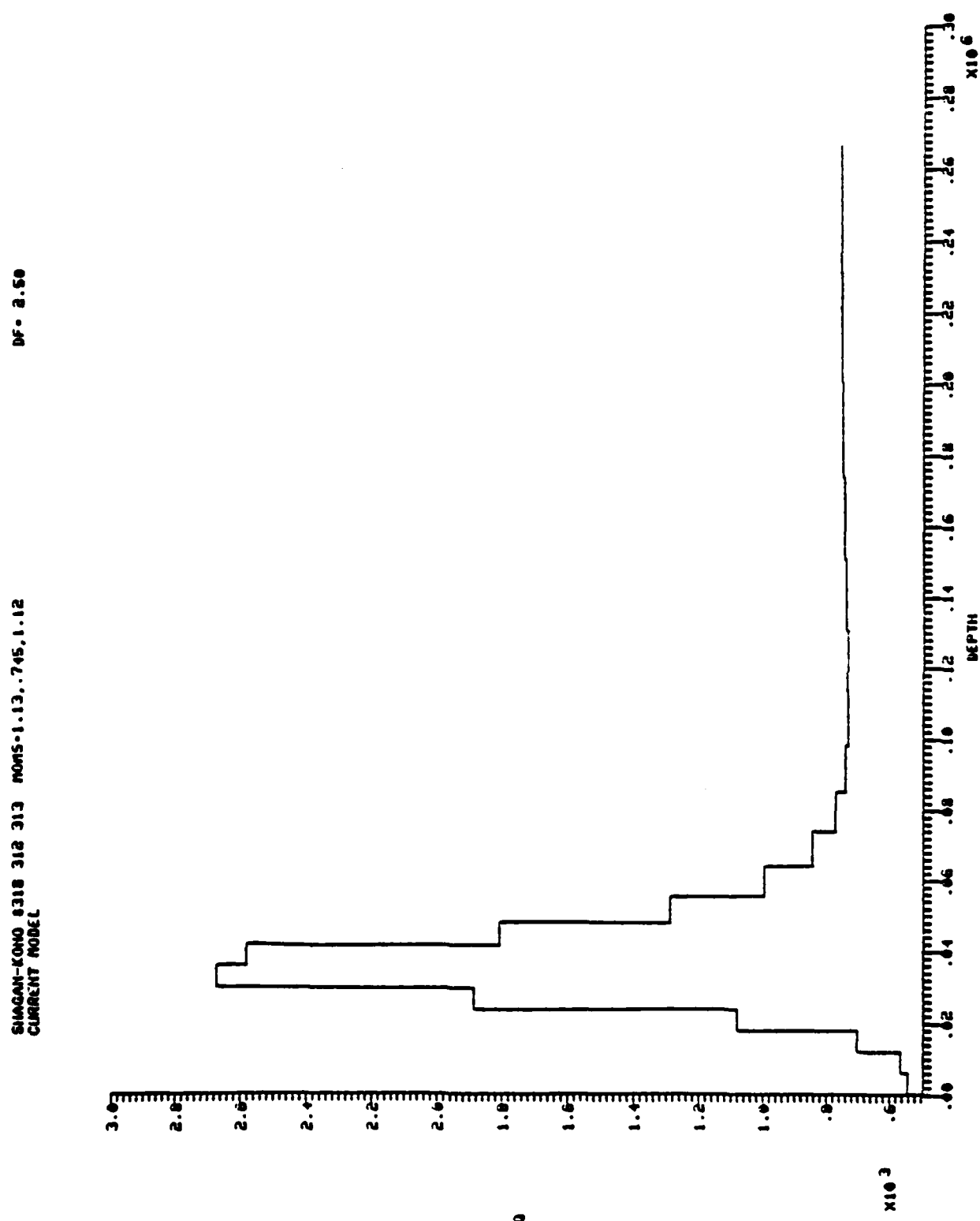


Figure 15.4

### SHAGAN-KONO STRUCTURE

I	DEPTH	THICK	ALPHA	BETA	RHO	QDM
1	5.986+003	5.985+003	6.230+003	3.497+003	2.673+003	5.429+002
2	1.197+004	5.985+003	6.260+003	3.514+003	2.684+003	5.659+002
3	1.756+004	5.985+003	6.392+003	3.538+003	2.732+003	7.035+002
4	2.394+004	5.985+003	6.522+003	3.561+003	2.789+003	1.083+003
5	2.993+004	5.985+003	6.574+003	3.690+003	2.798+003	1.568+003
6	3.591+004	5.985+003	6.569+003	3.637+003	2.797+003	2.673+003
7	4.190+004	5.985+003	7.718+003	4.332+003	1.216+003	2.532+003
8	4.832+004	6.417+003	7.750+003	4.350+003	1.227+003	1.510+003
9	5.572+004	7.400+003	7.828+003	4.394+003	1.256+003	1.251+003
10	6.425+004	8.533+003	7.956+003	4.466+003	1.303+003	9.593+002
11	7.409+004	9.840+003	8.191+003	4.547+003	1.356+003	8.473+002
12	8.544+004	1.134+004	8.224+003	4.616+003	1.400+003	7.748+002
13	9.553+004	1.308+004	8.295+003	4.656+003	1.426+003	7.431+002
14	1.136+005	1.508+004	8.314+003	4.667+003	1.434+003	7.344+002
15	1.310+005	1.740+004	8.367+003	4.663+003	1.431+003	7.355+002
16	1.511+005	2.006+004	8.297+003	4.657+003	1.427+003	7.409+002
17	1.742+005	2.313+004	8.298+003	4.658+003	1.428+003	7.462+002
18	2.069+005	2.668+004	8.311+003	4.665+003	1.422+003	7.506+002
19	2.317+005	3.077+004	8.329+003	4.675+003	1.439+003	7.533+002
20	2.672+005	3.548+004	8.347+003	4.685+003	1.445+003	7.561+002

Figure 15.5..

Figures 16.1 through 16.5 are on the following pages.

Figure 16. Path 2: SHAGAN-SHIO

Distance: 2927 km

Azimuth: 340.8°

Instrument: SRO-LP

Events Processed: 318, 312, 313

Description: This is an excellent station. There is a small branch in the group velocity curve at 0.065 Hertz, but otherwise it is very clean. The group velocities seem stable and inversion results in a reasonable structure with a relatively low Q.

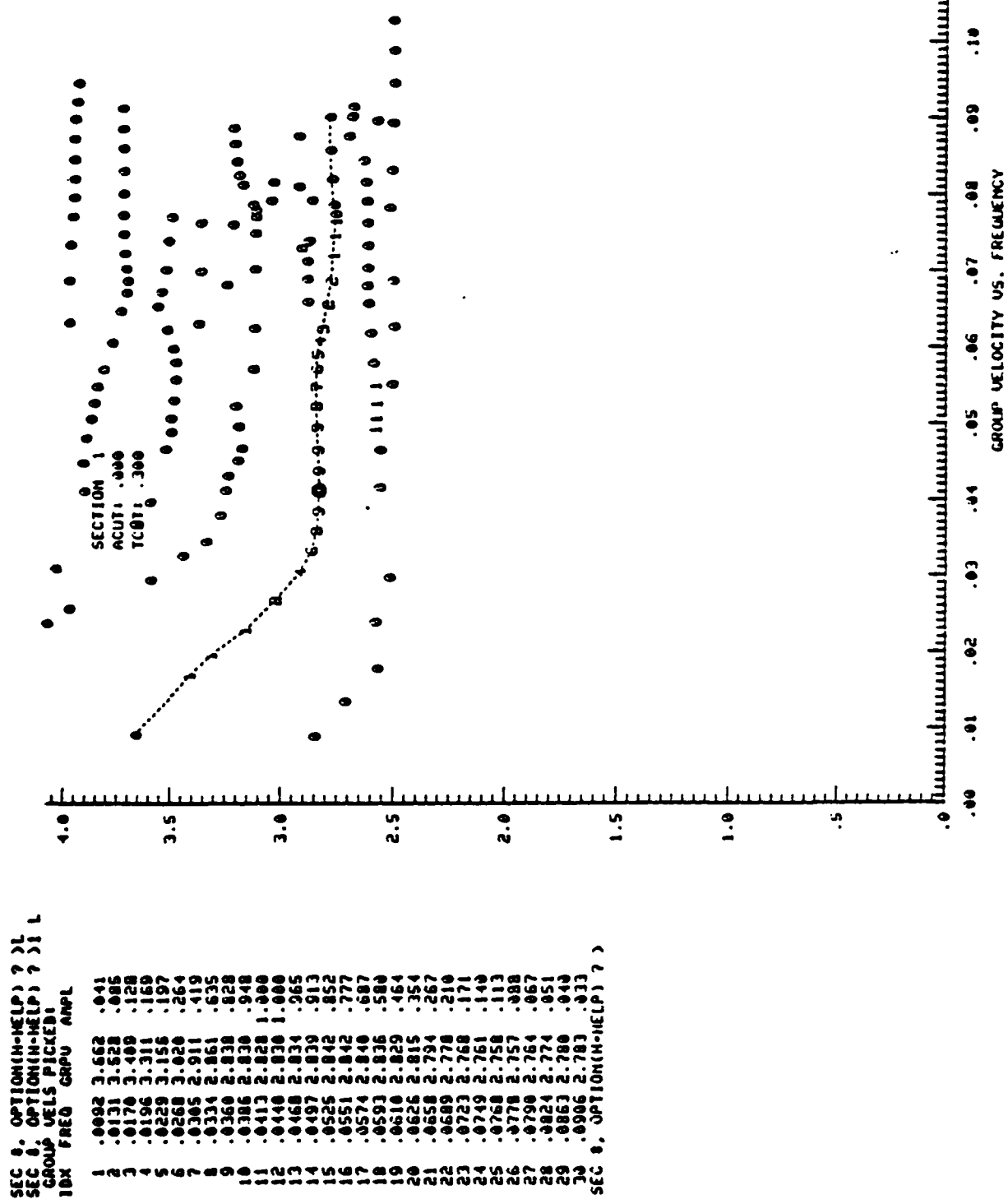


Figure 16.1.

SHACAN-SH10 0318 312 213 M05-1.10.000,1.10

MF = 5.50

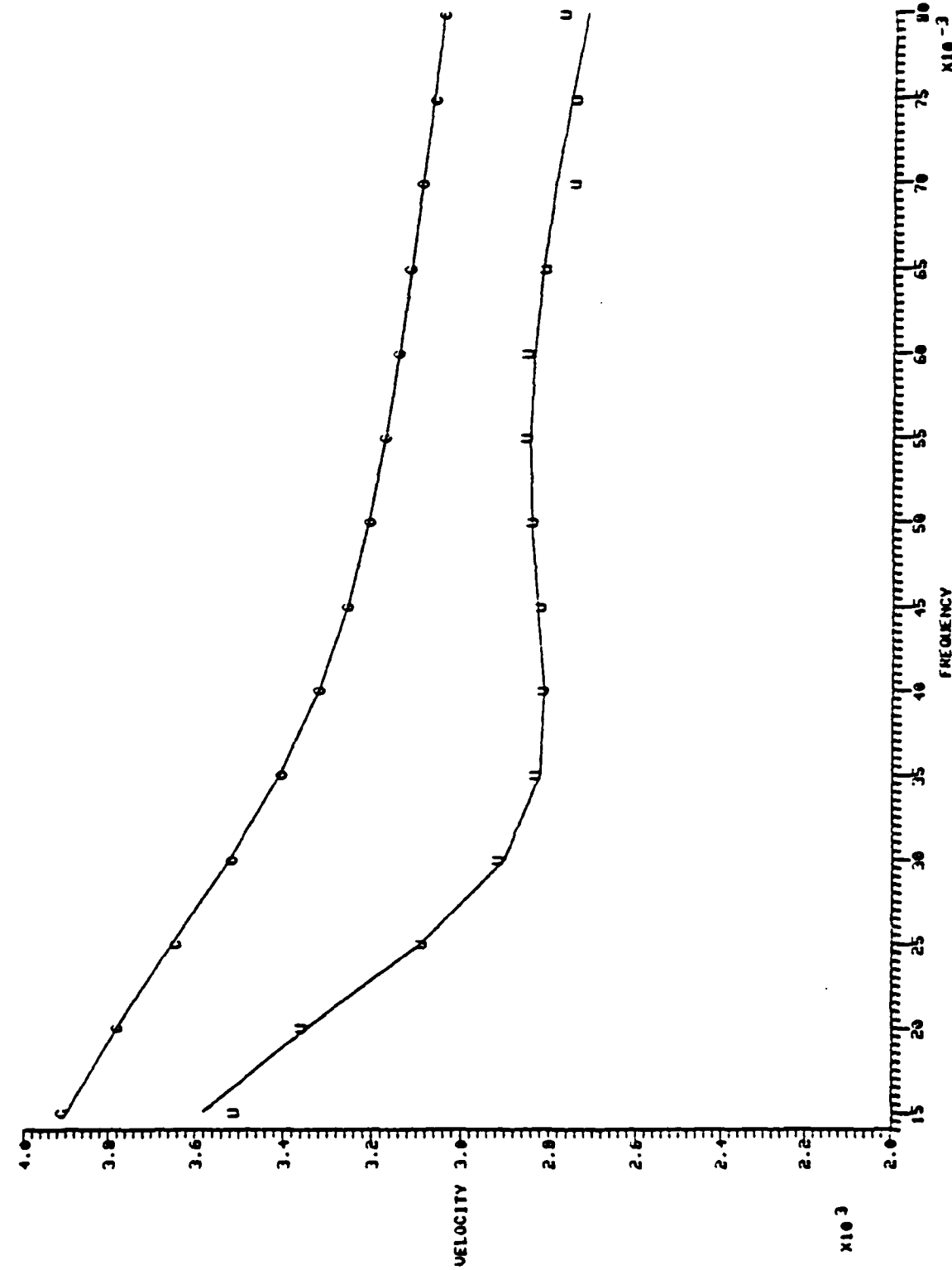


Figure 16.2.

SHAGAN-SWID 312 CTC NORM-1.10. .000.1.10  
CURRENT MODEL

DF = 5.50

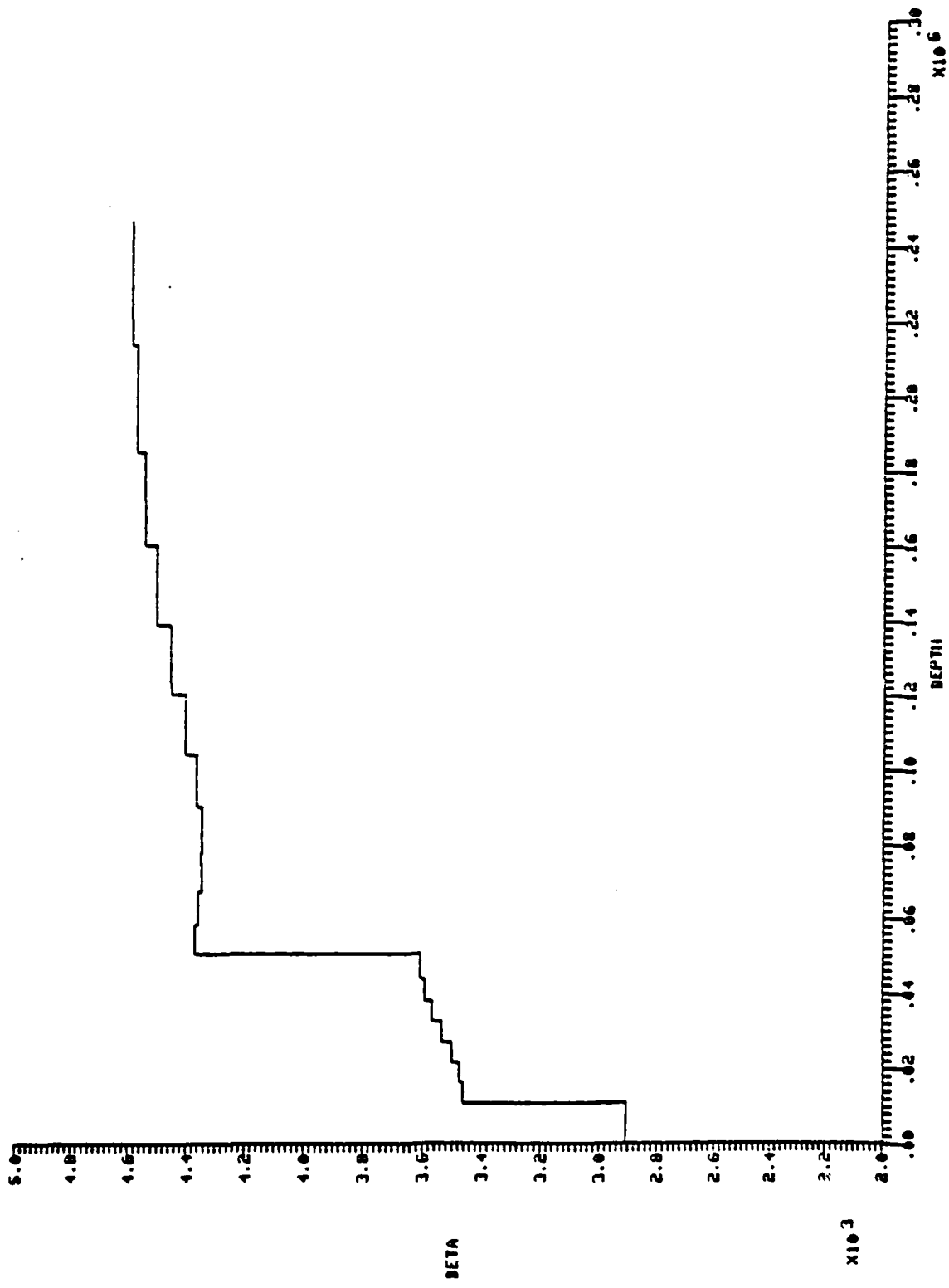
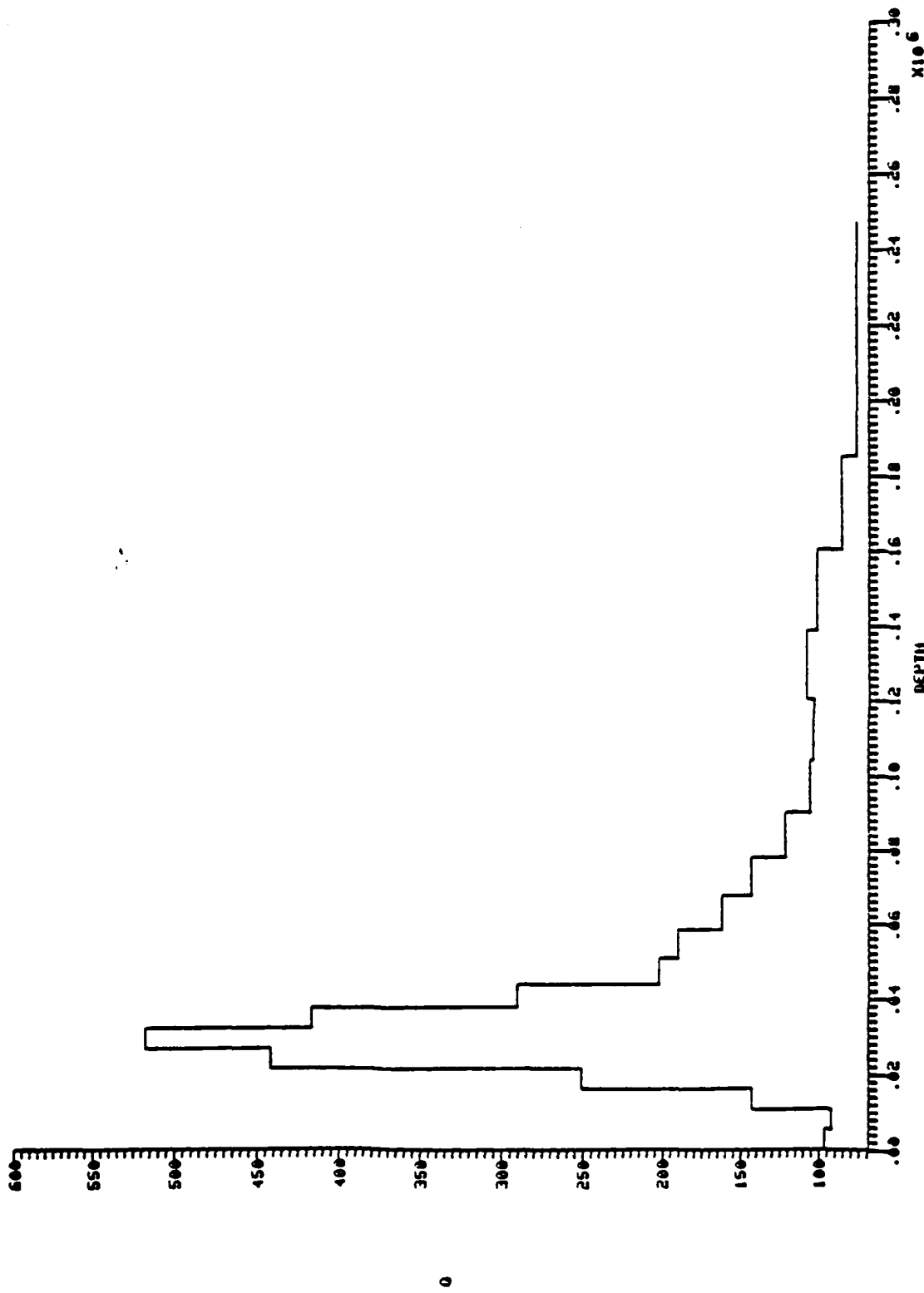


Figure 16.3.

SHANGHAI SHI 312 313 M005-1.10.0.800.1.10  
CURRENT MODEL

DF = 2.30



### SHAGAN-SHIO STRUCTURE

	DEPTH	THICK	ALPHA	BETA	RHO	QOM
1	5.434+003	5.433+003	5.179+003	2.907+003	2.290+003	9.654+001
2	5.387+004	5.433+003	5.179+003	2.905+003	2.298+003	9.221+001
3	5.639+004	5.433+003	6.171+003	3.164+003	2.652+003	1.422+002
4	6.174+004	5.433+003	6.131+003	3.175+003	2.659+003	2.511+002
5	6.717+004	5.433+003	6.237+003	3.531+003	2.675+003	4.413+002
6	3.259+004	5.433+003	6.296+003	3.534+003	2.697+003	5.170+002
7	3.394+004	5.433+003	6.353+003	3.568+003	2.718+003	4.161+002
8	4.393+004	5.394+003	6.399+003	3.592+003	2.735+003	2.906+002
9	5.974+004	6.307+003	6.426+003	3.607+003	2.745+003	2.026+002
10	5.369+004	7.362+003	7.732+003	4.363+003	3.239+003	1.906+002
11	6.768+004	9.380+003	7.764+003	4.358+003	3.233+003	1.627+002
12	7.317+004	1.348+004	7.741+003	4.345+003	3.224+003	1.435+002
13	9.328+004	1.211+004	7.737+003	4.343+003	3.223+003	1.218+002
14	1.343+005	1.399+004	7.769+003	4.361+003	3.235+003	1.053+002
15	1.204+005	1.615+004	7.837+003	4.399+003	3.259+003	1.037+002
16	1.391+005	1.866+004	7.924+003	4.448+003	3.291+003	1.083+002
17	1.606+005	2.155+004	8.319+003	4.496+003	3.322+003	1.018+002
18	5.074+004	2.489+004	8.083+003	4.537+003	3.349+003	5.649+001
19	2.143+005	2.875+004	8.133+003	4.585+003	3.367+003	7.703+001
20	2.475+005	3.320+004	8.167+003	4.584+003	3.380+003	7.703+001

Figure 16.5.

Figures 17.1 through 17.5 are on the following pages.

Figure 17. Path 3: SHAGAN-MAJO

Distance: 4911 km  
Azimuth: 307°  
Instrument: ASRO-LP  
Events Processed: 318, 312, 313

Description: This is a good station. There is clear evidence of multipathing, but the separate arrivals are removed by the phase matched filter. The group velocities differ by 0.1 km/sec at 0.02 Hertz. Processing three seismograms and averaging helps to obtain consistent results.

SEC 8. OPTIONIN-HELP1 ? >1 L  
GROUP VELS PICKED:  
IDX FREQ GRP1 AMP1

1	.0105	3.910	.305
2	.0125	3.874	.420
3	.0141	3.867	.421
4	.0165	3.674	.312
5	.0189	3.592	.263
6	.0205	3.317	.117
7	.0257	3.335	.162
8	.0283	3.314	.291
9	.0303	3.318	.464
10	.0324	3.277	.618
11	.0343	3.249	.757
12	.0363	3.225	.844
13	.0285	3.179	.911
14	.0408	3.133	.970
15	.0427	3.162	1.000
16	.0443	3.086	.974
17	.0461	3.077	.912
18	.0484	3.068	.852
19	.0510	3.057	.816
20	.0540	3.045	.809
21	.0570	3.039	.809
22	.0597	3.016	.864
23	.0613	3.007	.882
24	.0625	3.003	.864
25	.0637	3.002	.813
26	.0649	3.042	.746
27	.0661	3.002	.656
28	.0673	3.001	.566
29	.0682	3.000	.478
30	.0692	2.998	.394
31	.0703	2.993	.320
32	.0722	2.987	.258
33	.0752	2.981	.212
34	.0779	2.976	.178
35	.0808	2.972	.153
36	.0837	2.969	.133
37	.0855	2.967	.117
38	.0876	2.966	.103
39	.0888	2.966	.089
40	.0898	2.967	.077

SEC 8. OPTIONIN-HELP1 ? >

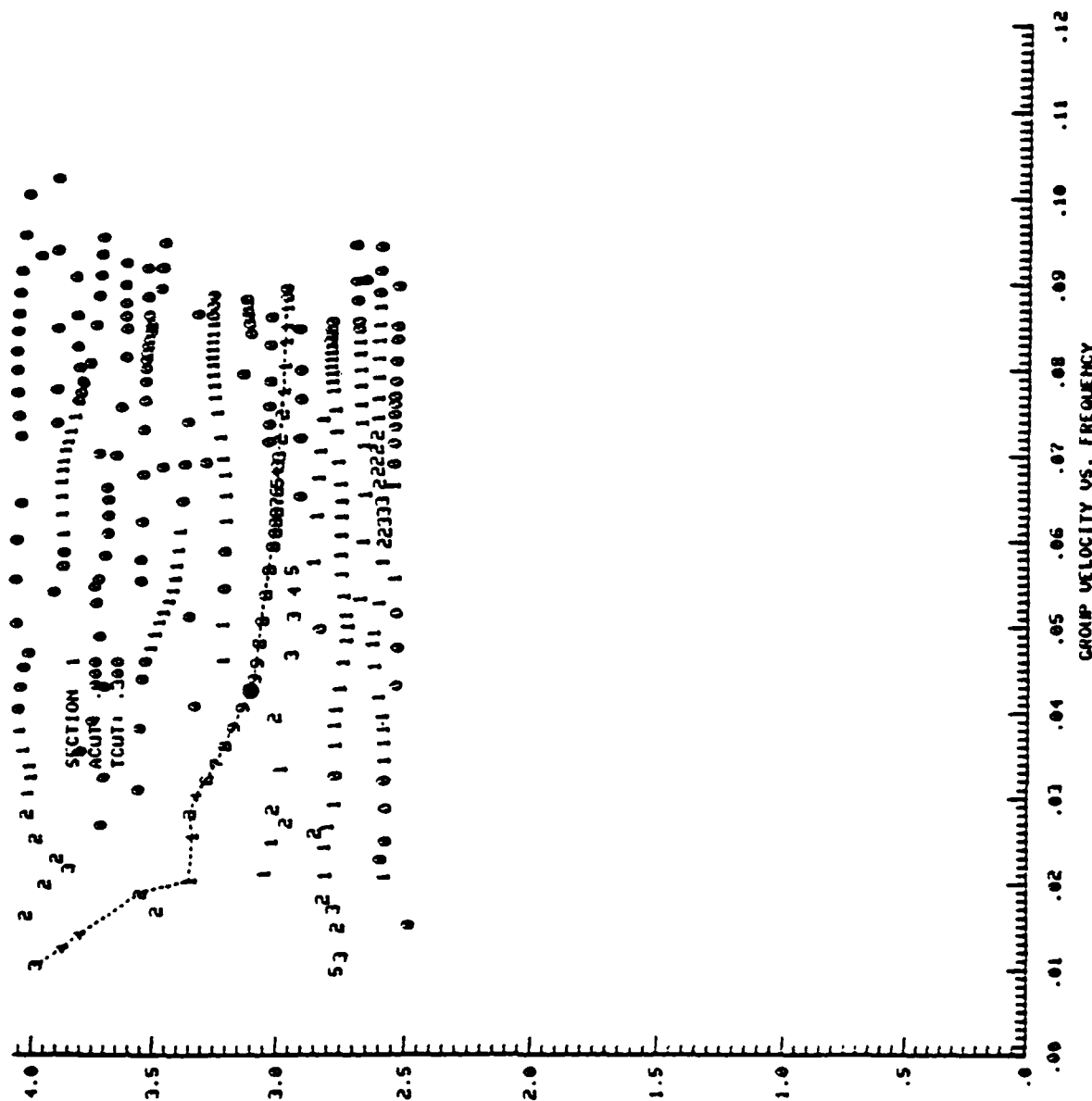


Figure 17.1.

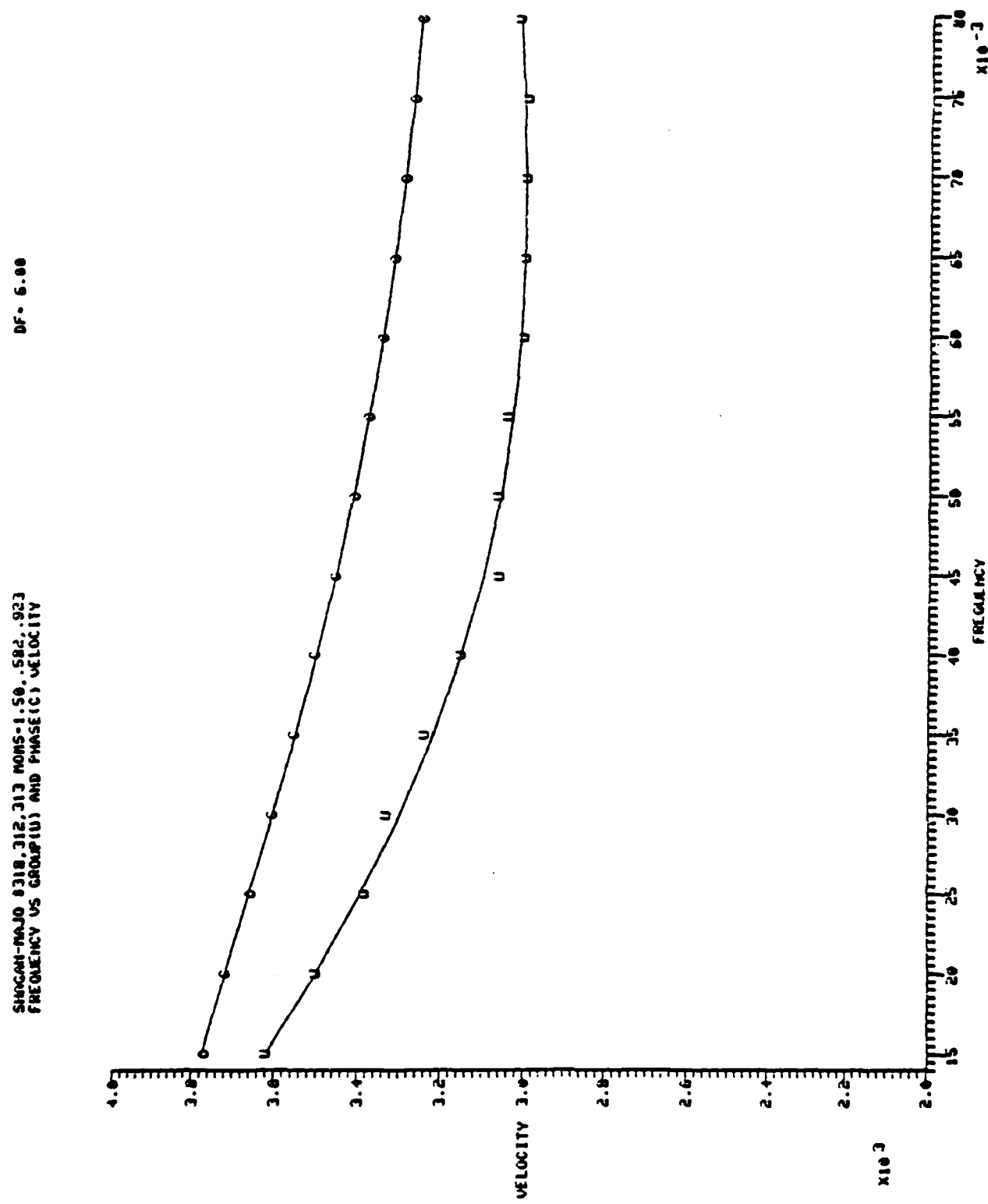


Figure 17.2.

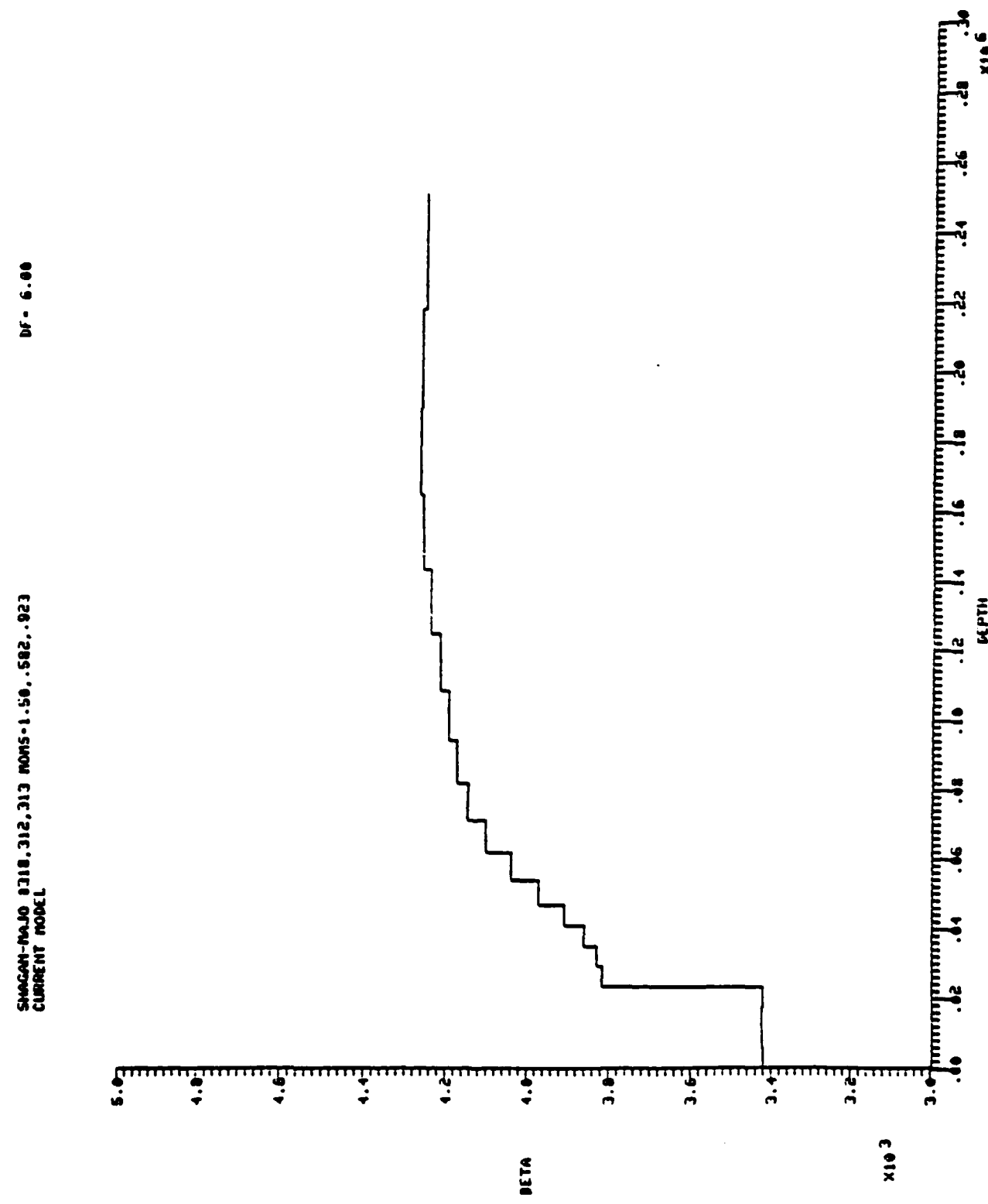
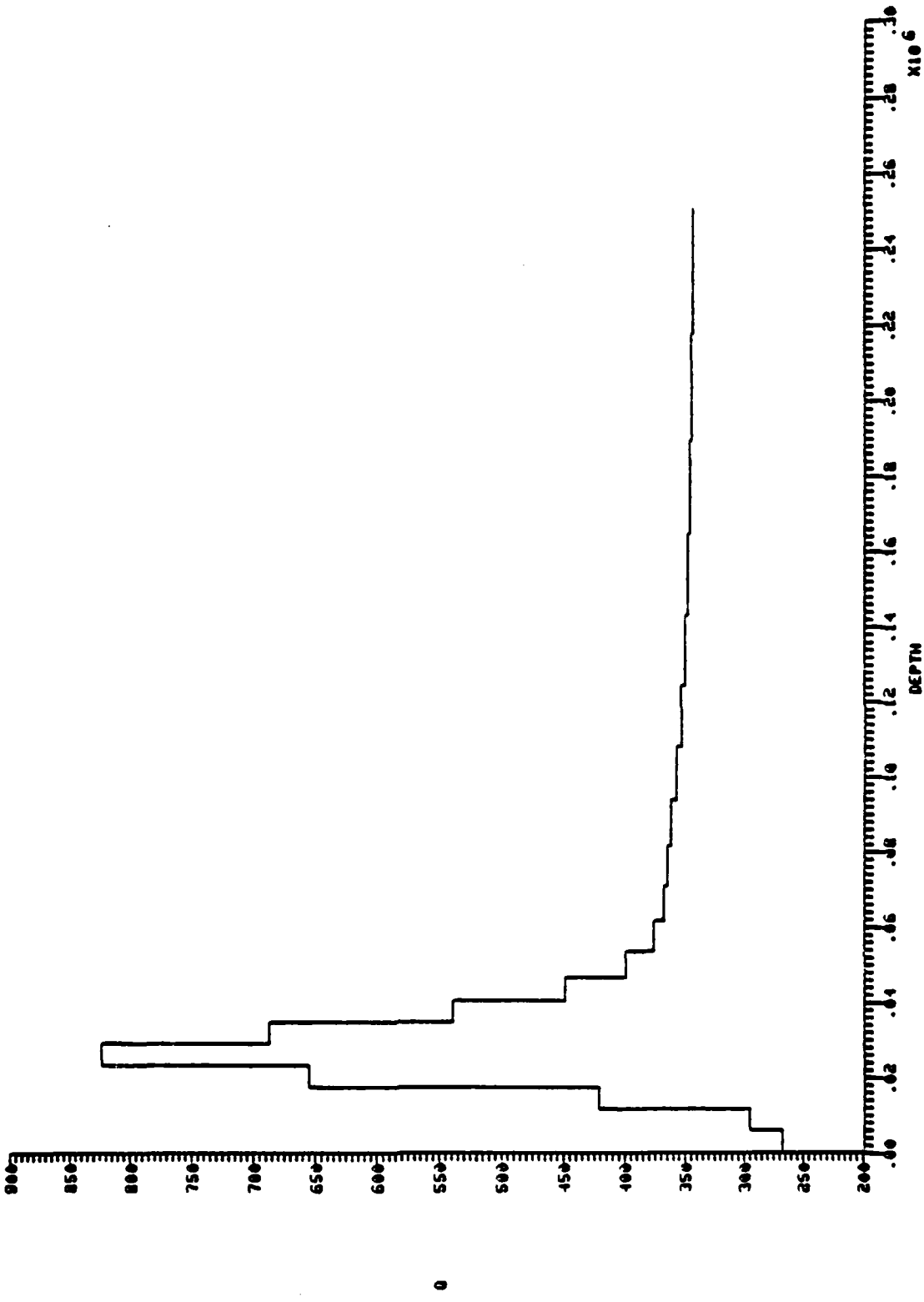


Figure 17.3.

SMAGAN-BAJO 9318, 312, 313 NOMS-1.50, .582, .923  
CURRENT MODEL

DF = 2.50



### SHAGAN-MAJO STRUCTURE

I	DEPTH	THICK	ALPHA	BETA	RHO	COM
1	5.300+003	5.799+003	6.395+003	3.421+003	2.624+003	2.674+002
2	1.150+004	5.799+003	6.098+003	3.423+003	2.625+003	2.553+002
3	1.740+004	5.799+003	6.398+003	3.423+003	2.625+003	4.214+002
4	2.320+004	5.799+003	6.093+003	3.420+003	2.623+003	6.554+002
5	2.900+004	5.799+003	6.798+003	3.816+003	2.889+003	9.236+002
6	3.480+004	5.799+003	6.323+003	3.430+003	2.889+003	6.373+002
7	4.060+004	5.799+003	6.379+003	3.461+003	2.910+003	5.359+002
8	4.671+004	6.107+003	6.964+003	3.909+003	2.941+003	4.488+002
9	5.373+004	7.025+003	7.075+003	3.971+003	2.581+003	3.999+002
10	6.182+004	8.082+003	7.197+003	4.340+003	3.026+003	3.764+002
11	7.111+004	9.298+003	7.306+003	4.101+003	3.066+003	3.682+002
12	8.181+004	1.069+004	7.385+003	4.145+003	3.054+003	3.654+002
13	9.412+004	1.230+004	7.434+003	4.173+003	3.112+003	3.625+002
14	1.083+005	1.415+004	7.468+003	4.192+003	3.125+003	3.589+002
15	1.246+005	1.623+004	7.506+003	4.213+003	3.138+003	3.536+002
16	1.413+005	1.873+004	7.548+003	4.237+003	3.154+003	3.504+002
17	1.648+005	2.155+004	7.580+003	4.255+003	3.166+003	3.481+002
18	1.896+005	2.479+004	7.595+003	4.263+003	3.171+003	3.464+002
19	2.182+005	2.852+004	7.589+003	4.260+003	3.169+003	3.448+002
20	2.510+005	3.231+004	7.572+003	4.250+003	3.162+003	3.439+002

Figure 17.5.

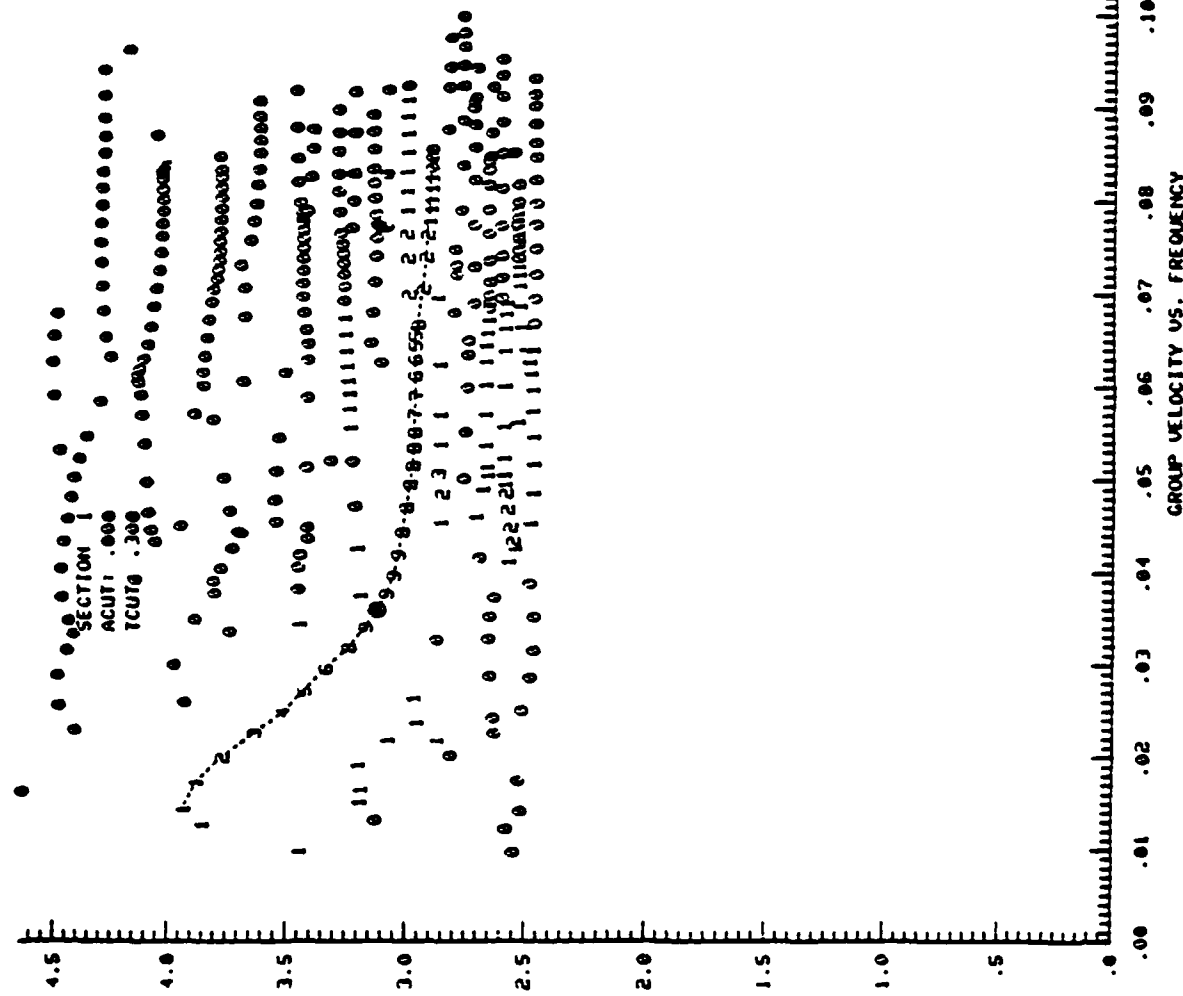
Figures 18.1 through 18.5 are on the following pages.

Figure 18. Path 4: SHAGAN-GRFO

Distance: 4699 km  
Azimuth: 62.7°  
Instrument: SRO-LP  
Events Processed: 318, 312

Description: This is a good, although somewhat noisy, station. The group velocity plot shows many distinct arrivals, but the phase matched filter seems to separate them well. The final phase and group velocities are quite consistent for the two events processed.

SEC 1. OPTIONIN-HELP1 ? 21 L  
 SEC 2. OPTIONIN-HELP1 ? 21 L  
 GROUP VELS PICKED:  
 IDX FREE GRPV ANPL



SEC 1. OPTIONIN-HELP1 ? ,  
 SEC

Figure 18.1.

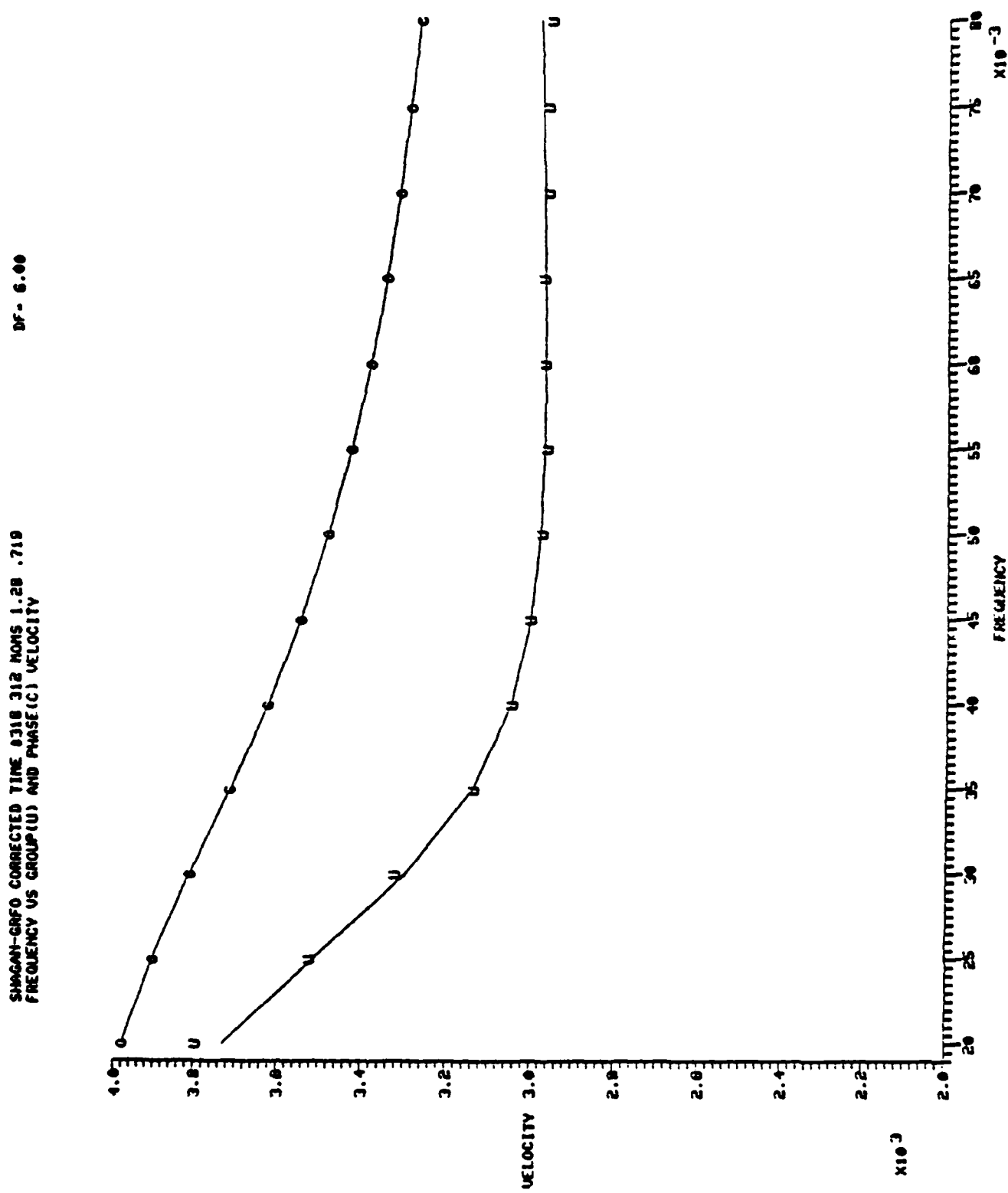


Figure 18.2.

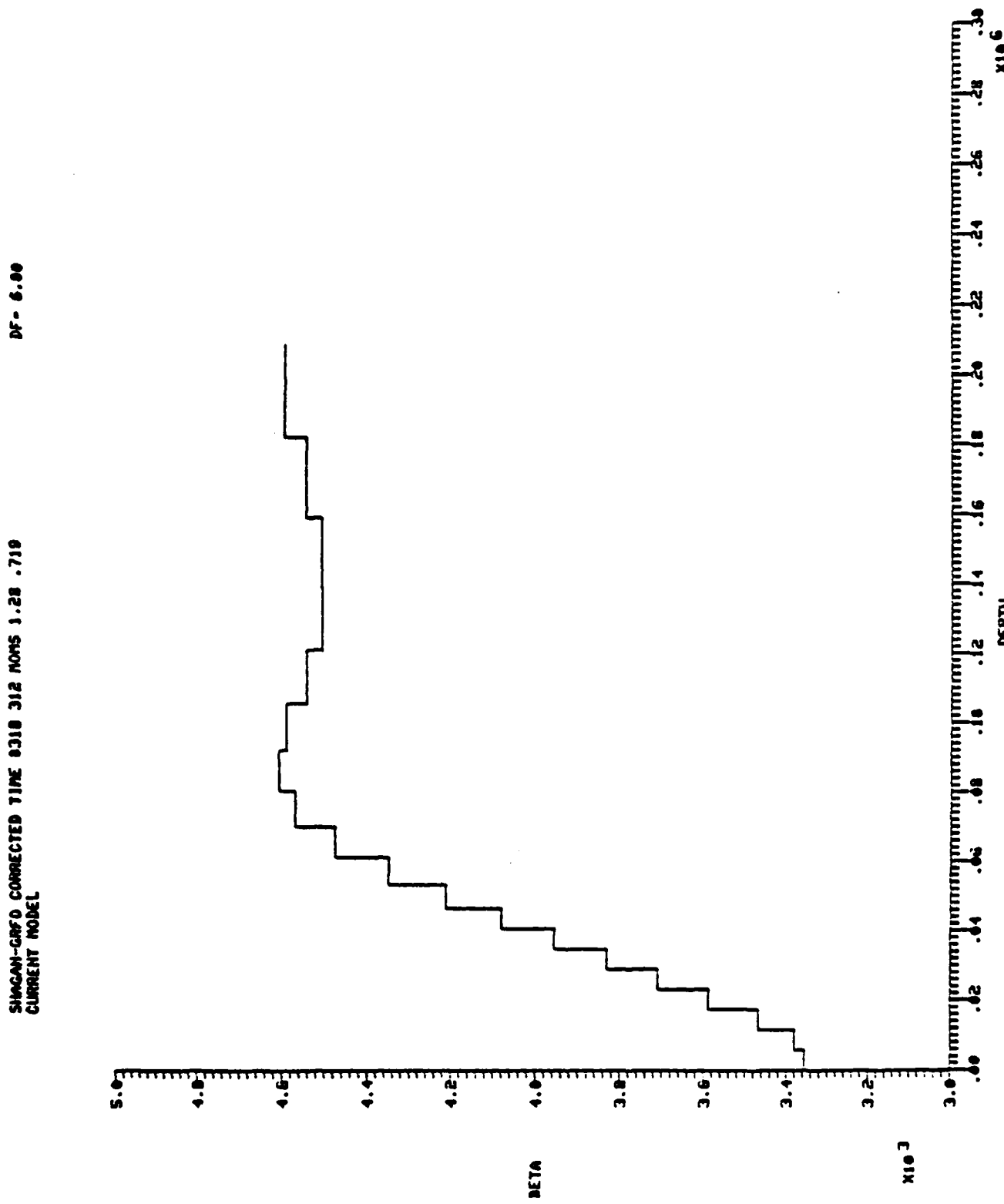


Figure 18.3.

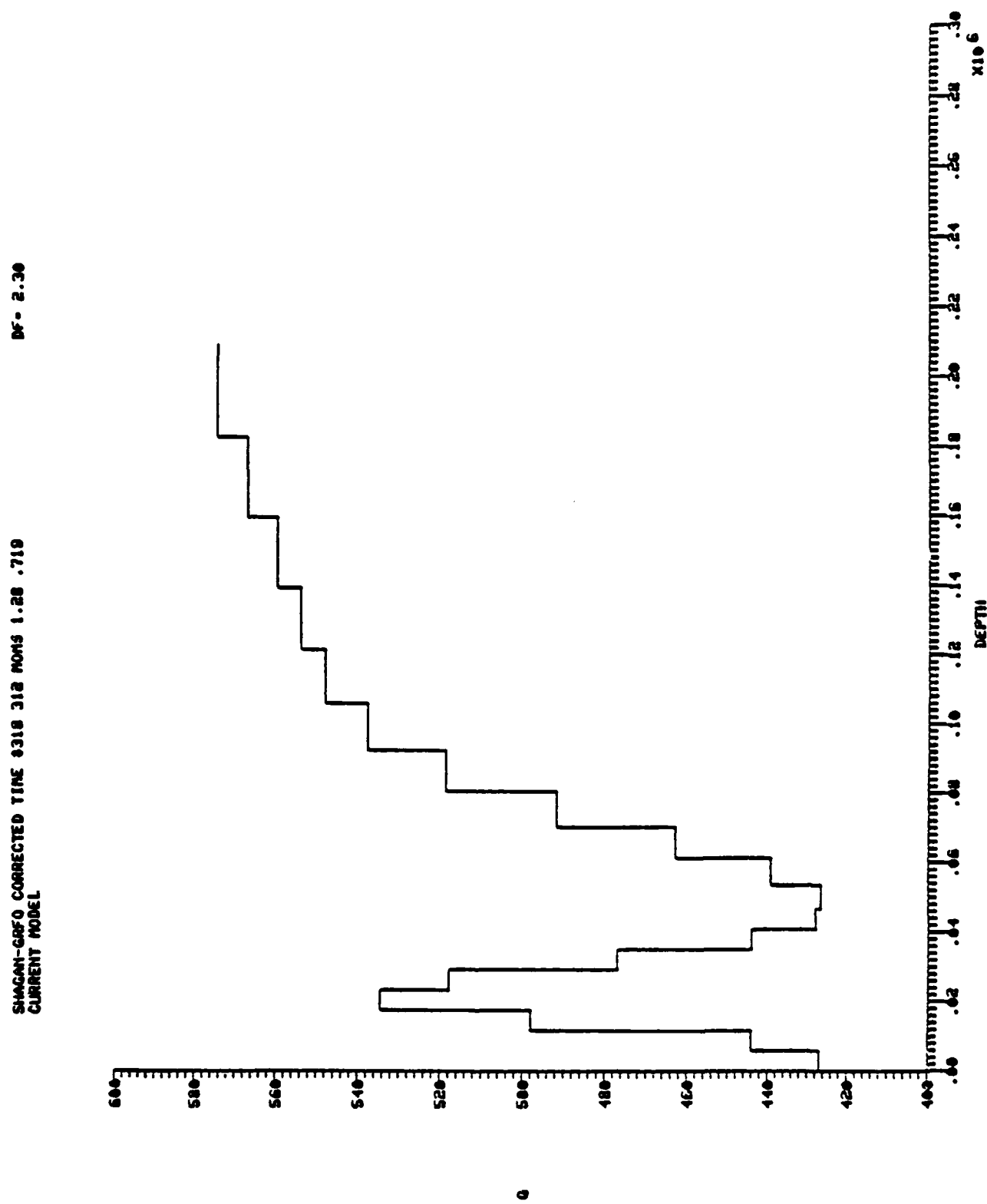


Figure 18.4

### SHAGAN-GRFO STRUCTURE

I	DEPTH	THICK	ALPHA	BETA	RHO	QDM
1	5.834+003	5.833+003	5.977+003	3.355+003	2.581+003	4.279+002
2	1.167+004	5.833+003	6.920+003	3.379+003	2.596+003	4.441+002
3	1.750+004	5.833+003	6.177+003	3.467+003	2.654+003	4.981+002
4	2.334+004	5.833+003	6.350+003	3.587+003	2.732+003	5.346+002
5	2.917+004	5.833+003	6.510+003	3.710+003	2.811+003	5.178+002
6	3.500+004	5.833+003	6.827+003	3.832+003	2.891+003	4.779+002
7	4.884+004	5.833+003	7.044+003	3.954+003	2.970+003	4.441+002
8	4.579+004	5.949+003	7.267+003	4.079+003	3.051+003	4.279+002
9	5.360+004	6.815+003	7.502+003	4.211+003	3.137+003	4.256+002
10	6.141+004	7.808+003	7.748+003	4.349+003	3.227+003	4.393+002
11	7.836+004	8.946+003	7.972+003	4.475+003	3.309+003	4.629+002
12	8.361+004	1.024+004	8.136+003	4.567+003	3.369+003	4.917+002
13	9.235+004	1.174+004	8.294+003	4.685+003	3.393+003	5.184+002
14	1.058+005	1.345+004	8.172+003	4.587+003	3.382+003	5.373+002
15	1.212+005	1.541+004	8.086+003	4.539+003	3.350+003	5.475+002
16	1.389+005	1.765+004	8.022+003	4.563+003	3.327+003	5.535+002
17	1.591+005	2.023+004	8.024+003	4.564+003	3.323+003	5.592+002
18	1.823+005	2.317+004	8.092+003	4.542+003	3.352+003	5.665+002
19	2.068+005	2.655+004	8.183+003	4.593+003	3.385+003	5.739+002

Figure 18.5.

Figures 19.1 through 19.5 are on the following pages.

Figure 19. Path 5: SHAGAN-ANTO

Distance: 3740 km  
Azimuth: 57.2°  
Instrument: SRO-LP  
Events Processed: 318, 312

Description: This is a low Q path, so the signal is small relative to noise and the data is difficult to process. There are numerous multiple arrivals on the group velocity plots. No group velocity curve could be found for Event 313. Nevertheless, fairly consistent velocities were obtained for the remaining two events from 0.02 to 0.07 Hertz, and when inverted, they produce a reasonable velocity and Q structure.

```

SEC 8. OPTIMUM-HELP? >
> 1 L
GROUP VELS PICKED
IDX FREQ GAMP ANPL
1 .000 .000 .000 .000
2 .000 .000 .000 .000
3 .0163 3.827 .211 .331
4 .0201 3.679 .311 .331
5 .0232 3.517 .465 .331
6 .0271 3.421 .692 .331
7 .0295 3.266 .993 .331
8 .0313 3.177 .987 .331
9 .0336 3.093 .779 .331
10 .0374 3.026 .657 .331
11 .0396 2.918 .569 .331
12 .0444 2.748 1.000 .331
13 .0461 2.755 .916 .331
14 .0488 2.761 .799 .331
15 .0516 2.759 .781 .331
16 .0512 2.752 .693 .331
17 .0567 2.737 .563 .331
18 .0608 2.708 .421 .331
19 .0631 2.664 .380 .331
20 .0641 2.668 .310 .331
21 .0654 2.668 .241 .331
22 .0668 2.665 .189 .331
23 .0687 2.663 .132 .331
24 .0699 2.659 .095 .331
25 .0716 2.654 .067 .331
26 .0742 2.647 .048 .331
27 .0763 2.649 .034 .331
28 .0800 2.632 .025 .331
29 .0838 2.623 .019 .331
30 .0926 2.589 .016 .331
SEC 9. OPTIMUM-HELP? >

```

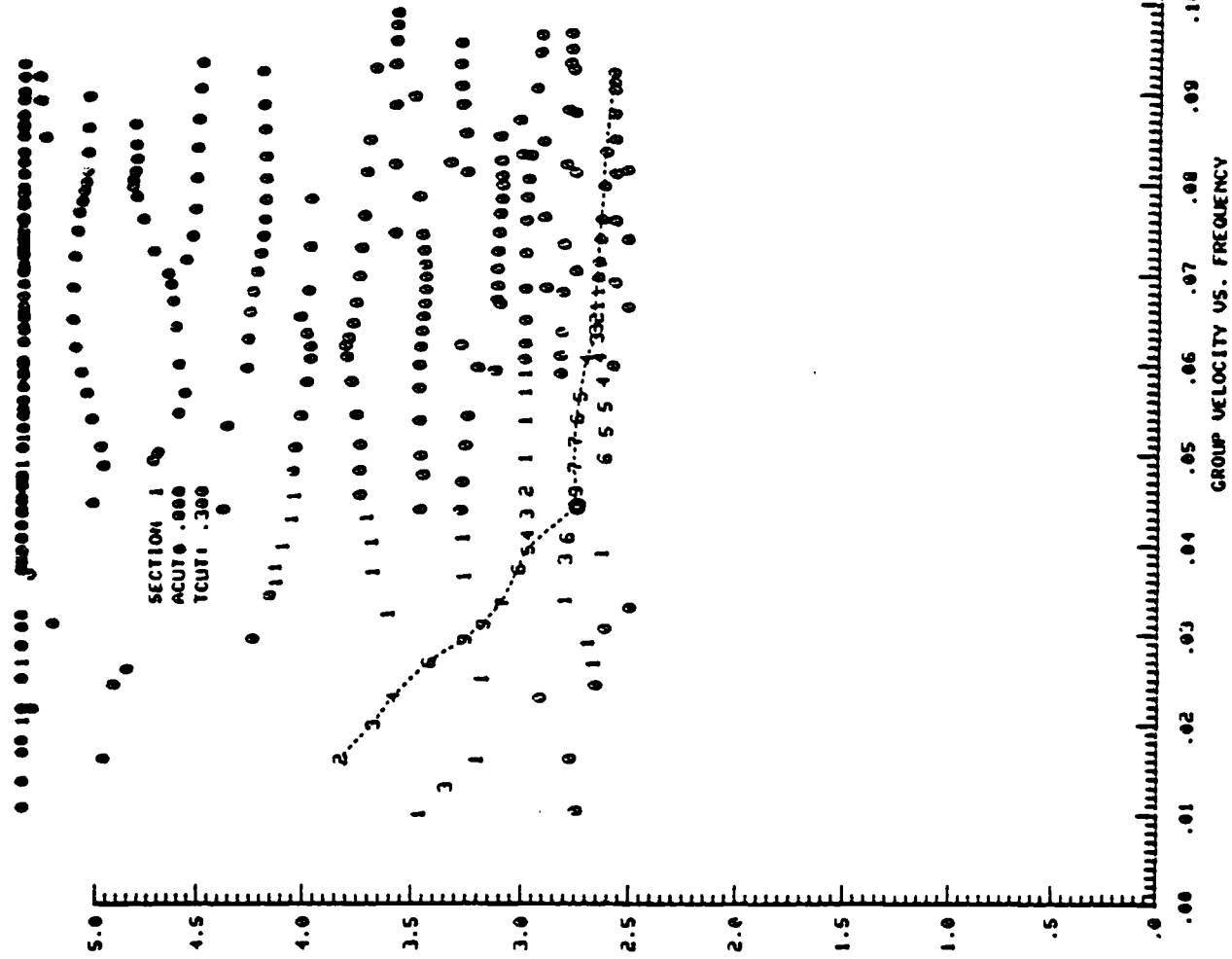


Figure 19.1.

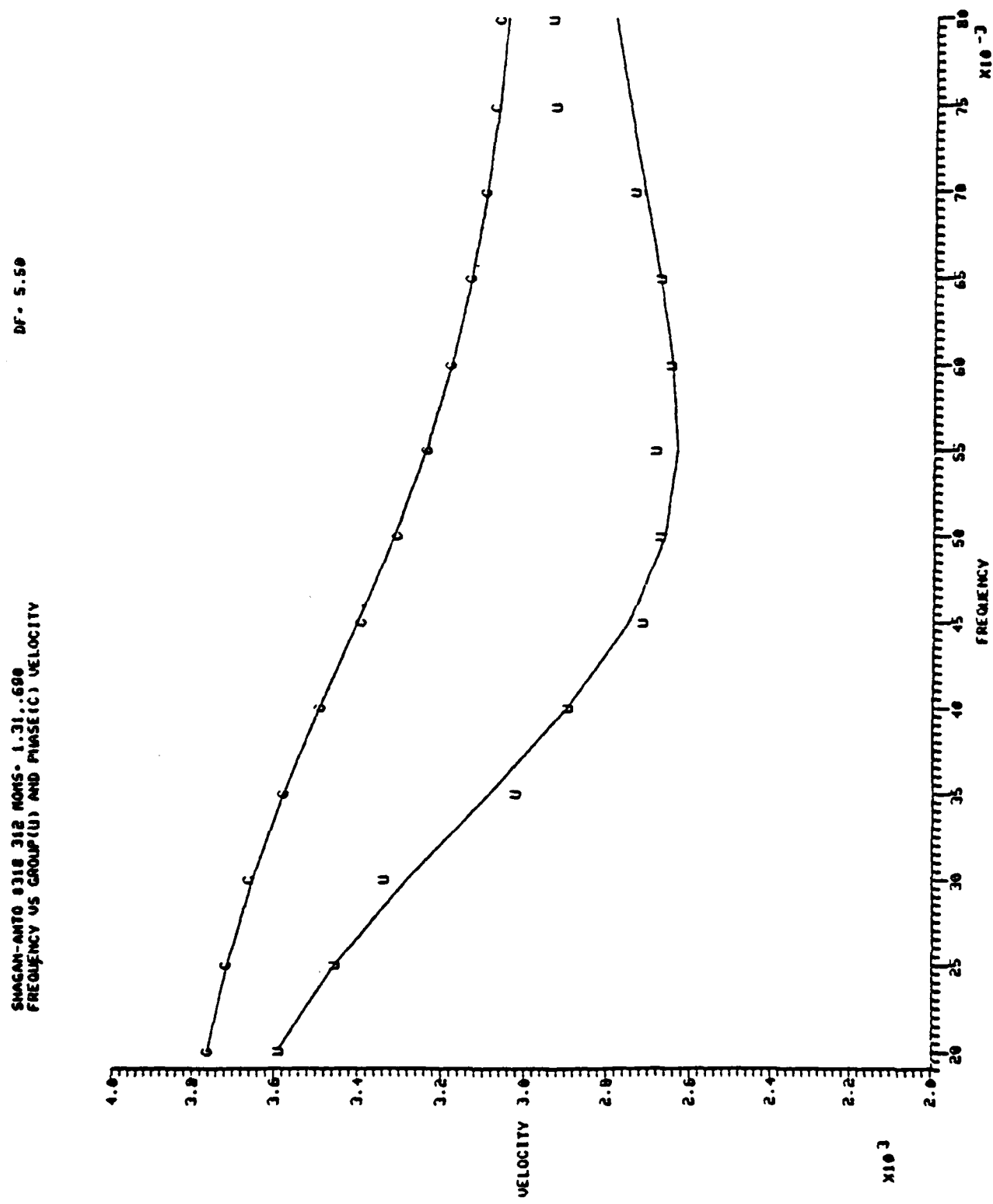
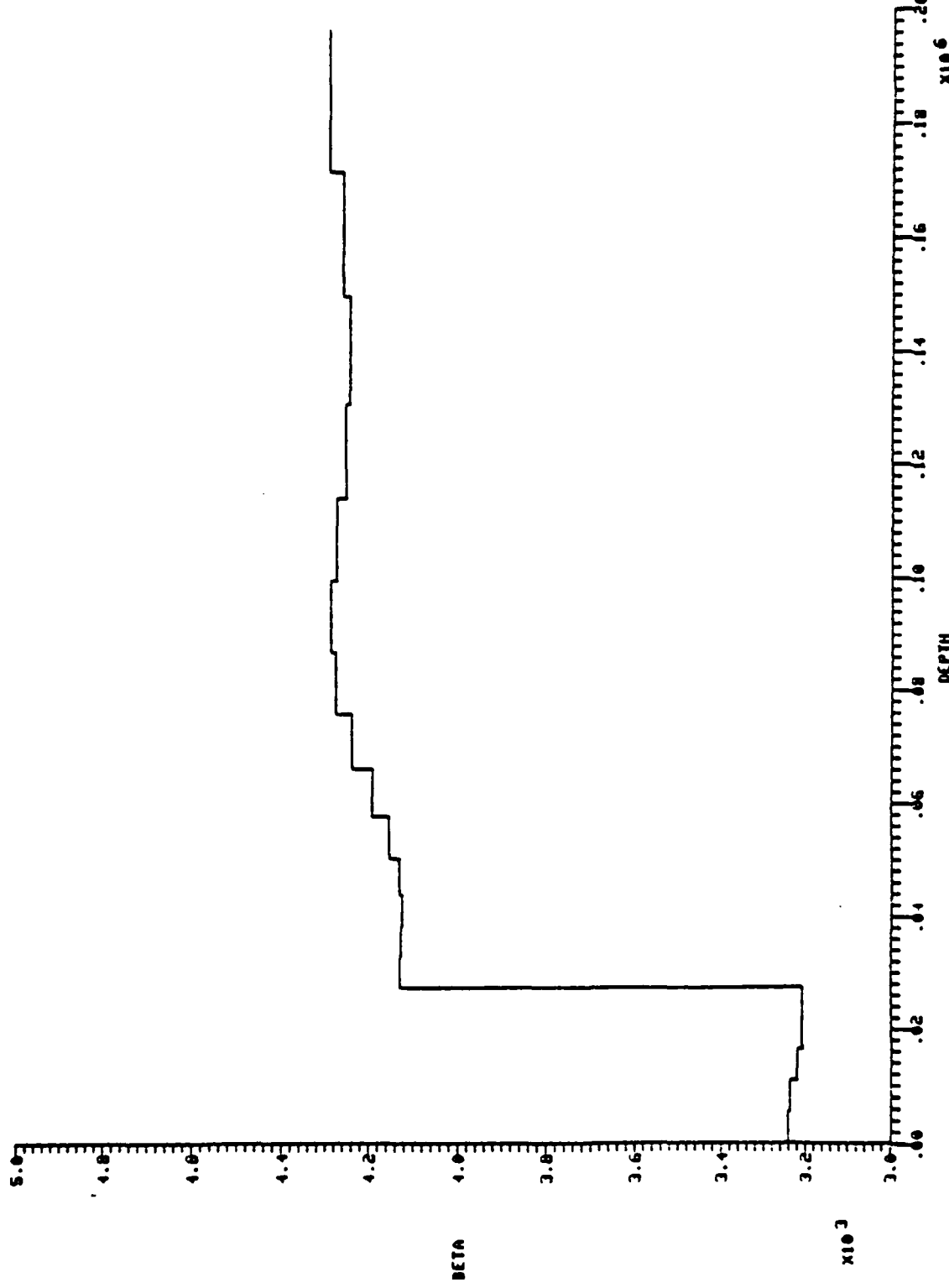


Figure 19.2.

SHAGAN-AUT 312 312 MONS-1.11.69  
CURRENT MODEL

DF = 5.50



SMOGAN-ANTO 0130 312 MONTHS - 1.31. .690

DF = 2.50

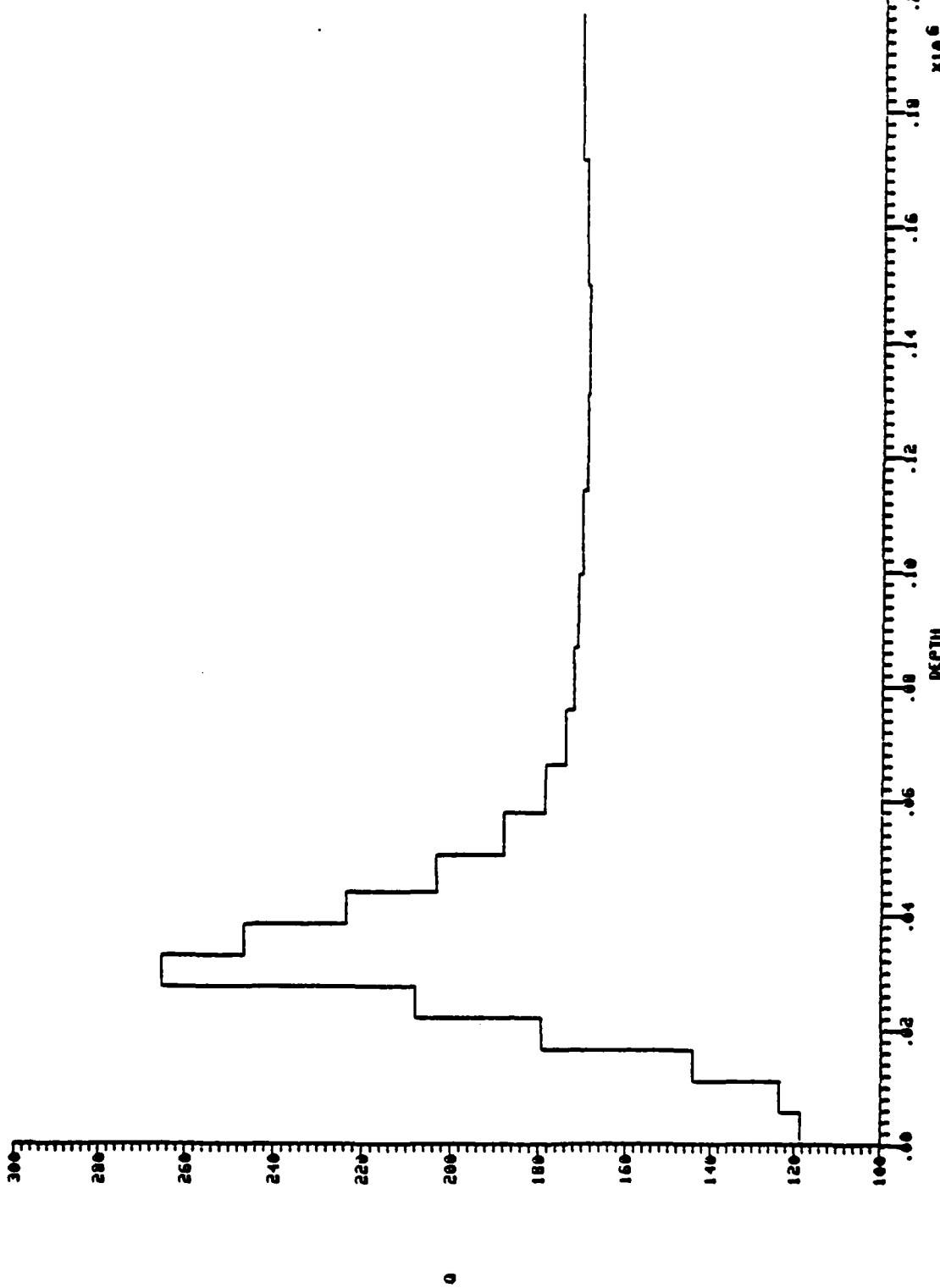


Figure 19.4

### SHAGAN-ANTO STRUCTURE

I	DEPTH	THICK	ALPHA	BETA	RHO	Q3R
1	5.480+003	5.480+003	5.772+003	3.240+003	2.506+003	1.155+002
2	1.895+004	5.480+003	5.765+003	3.236+003	2.503+003	1.236+002
3	1.644+004	5.480+003	5.735+003	3.219+003	2.492+003	1.442+002
4	2.192+004	5.480+003	5.715+003	3.208+003	2.485+003	1.794+002
5	2.740+004	5.480+003	5.713+003	3.207+003	2.485+003	2.050+002
6	3.288+004	5.480+003	7.356+003	4.129+003	3.084+003	2.652+002
7	3.836+004	5.480+003	7.351+003	4.126+003	3.082+003	2.465+002
8	4.384+004	5.600+003	7.347+003	4.124+003	3.031+003	2.237+002
9	5.038+004	6.418+003	7.358+003	4.130+003	3.054+003	2.333+002
10	5.774+004	7.355+003	7.395+003	4.151+003	3.098+003	1.390+002
11	6.617+004	8.425+003	7.465+003	4.190+003	3.123+003	1.797+002
12	7.583+004	9.660+003	7.548+003	4.237+003	3.154+003	1.741+002
13	8.650+004	1.107+004	7.613+003	4.273+003	3.177+003	1.722+002
14	9.959+004	1.268+004	7.634+003	4.285+003	3.185+003	1.712+002
15	1.141+005	1.453+004	7.611+003	4.272+003	3.177+003	1.792+002
16	1.308+005	1.666+004	7.572+003	4.250+003	3.162+003	1.692+002
17	1.499+005	1.909+004	7.557+003	4.242+003	3.157+003	1.688+002
18	1.718+005	2.188+004	7.584+003	4.257+003	3.167+003	1.593+002
19	1.968+005	2.507+004	7.639+003	4.288+003	3.187+003	1.795+002

Figure 19.5.

Figure 20.1 through 20.5 are on the following pages.

Figure 20. Path 6: SHAGAN-CHTO

Distance: 3890 km

Azimuth: 337.1°

Instrument: SRO-LP

Events Processed: 318, 312, 313

Description: This is a rather noisy station with multiple arrivals and multipathing present. Most difficult is a branch in the group velocity curve above 0.06 Hertz. This causes the group velocity from the phase matched filter to jump to the other branches. Averaging velocities for three events helped to obtain a consistent result. This station also has a large dip in the spectrum near 20 seconds period which is difficult to model with a plane-layered structure.

SEC 8, OPTION(H-HELP) ? 111  
 GROUP UEL'S PICKED  
 1BX FREE CAPU AMPL  
 1 .0105 3.569 .141  
 2 .0153 3.569 .422  
 3 .0199 3.393 .723  
 4 .0246 3.149 .939  
 5 .0293 3.034 1.066  
 6 .0333 2.976 .948  
 7 .0376 2.911 .747  
 8 .0403 2.924 .453  
 9 .0492 2.926 .412  
 10 .0568 2.894 .643  
 11 .0597 2.871 .919  
 12 .0613 2.871 .938  
 13 .0626 2.872 .739  
 14 .0632 2.876 .474  
 15 .0643 2.849 .262  
 16 .0664 2.843 .141  
 17 .0711 2.846 .079  
 18 .0788 2.848 .052  
 19 .0870 2.848 .039  
 20 .0924 2.851 .031  
 SEC 3, OPTION(H-HELP) ? 1

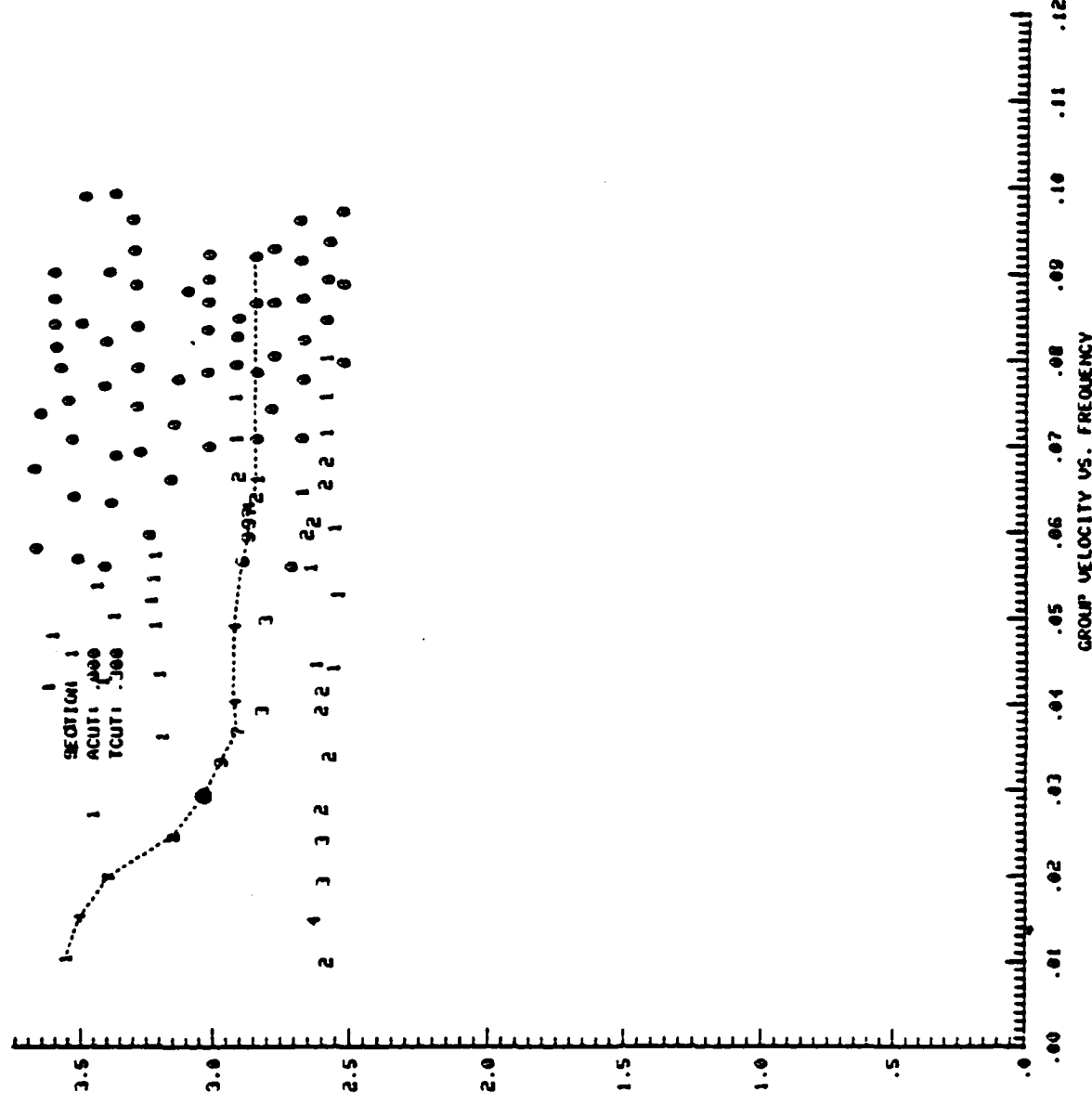


Figure 20.1.

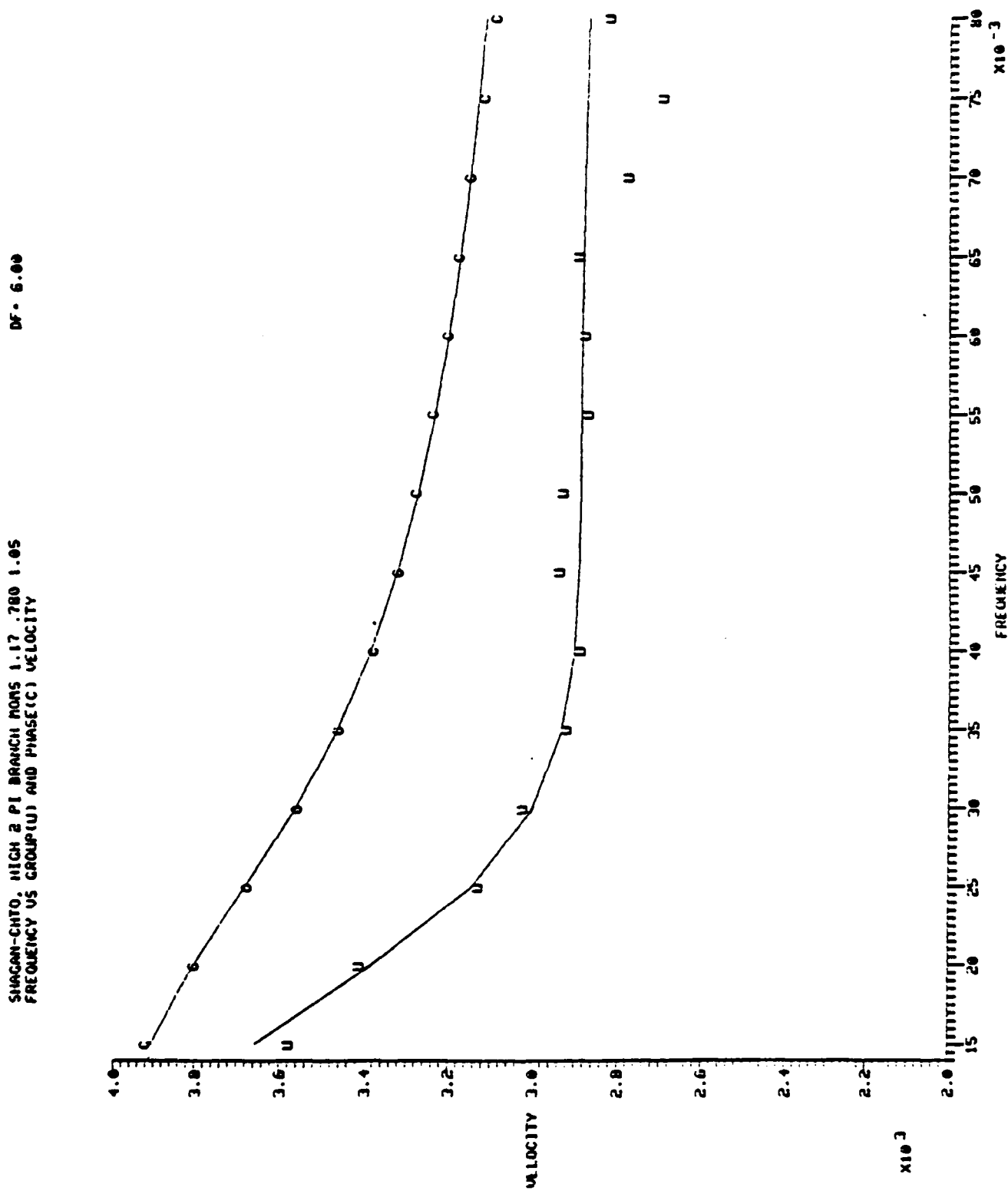
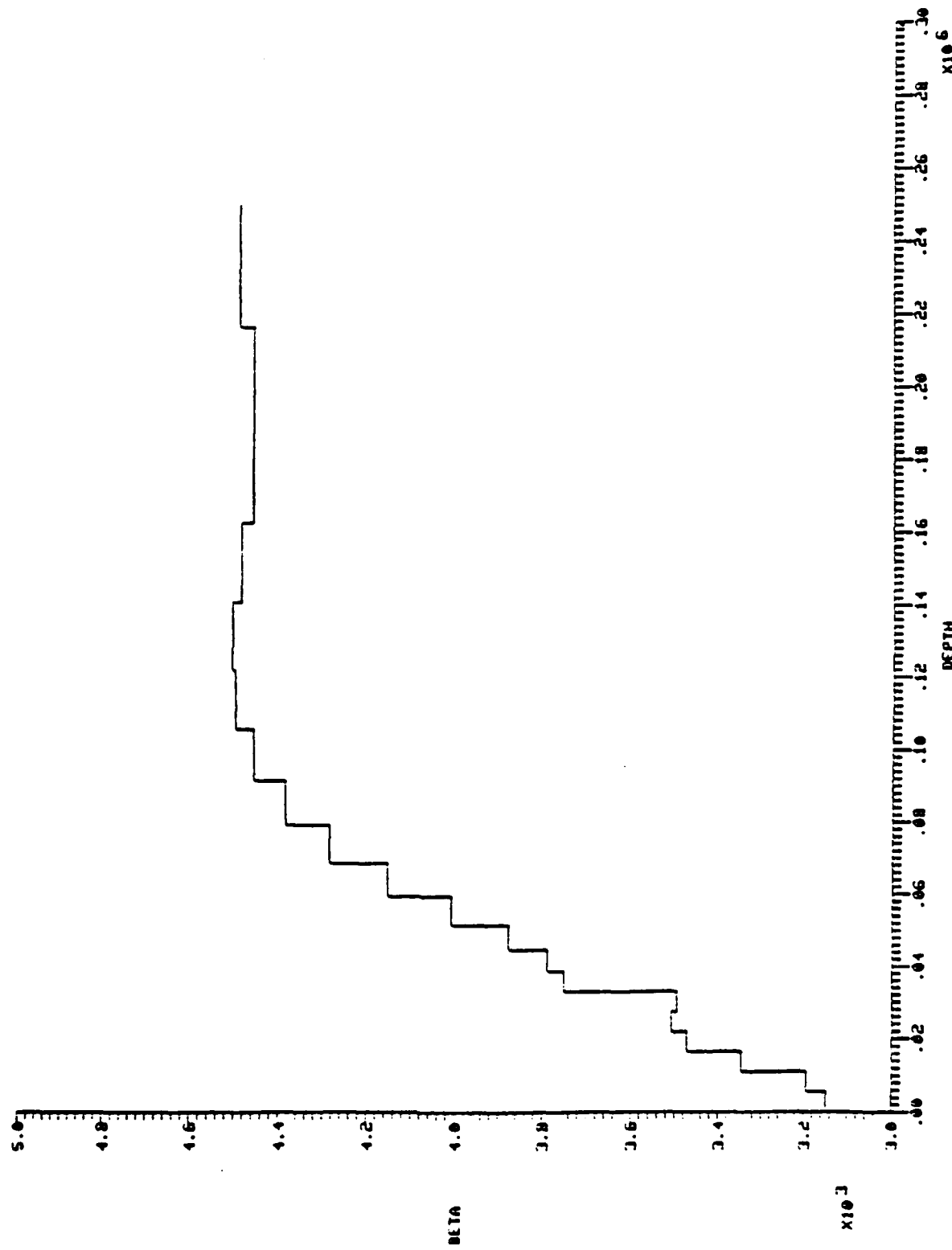


Figure 20.2.

SIAGAN-CHITO, HIGH 2 PI BRANCH ROTS 1.17 .780 1.05  
CURRENT MODEL

DF = 6.00



SHAGAN-CHTO, HIGH 2 PI BRANCH NORM 1.17 .780 1.05  
CURRENT MODEL

DF = 2.50

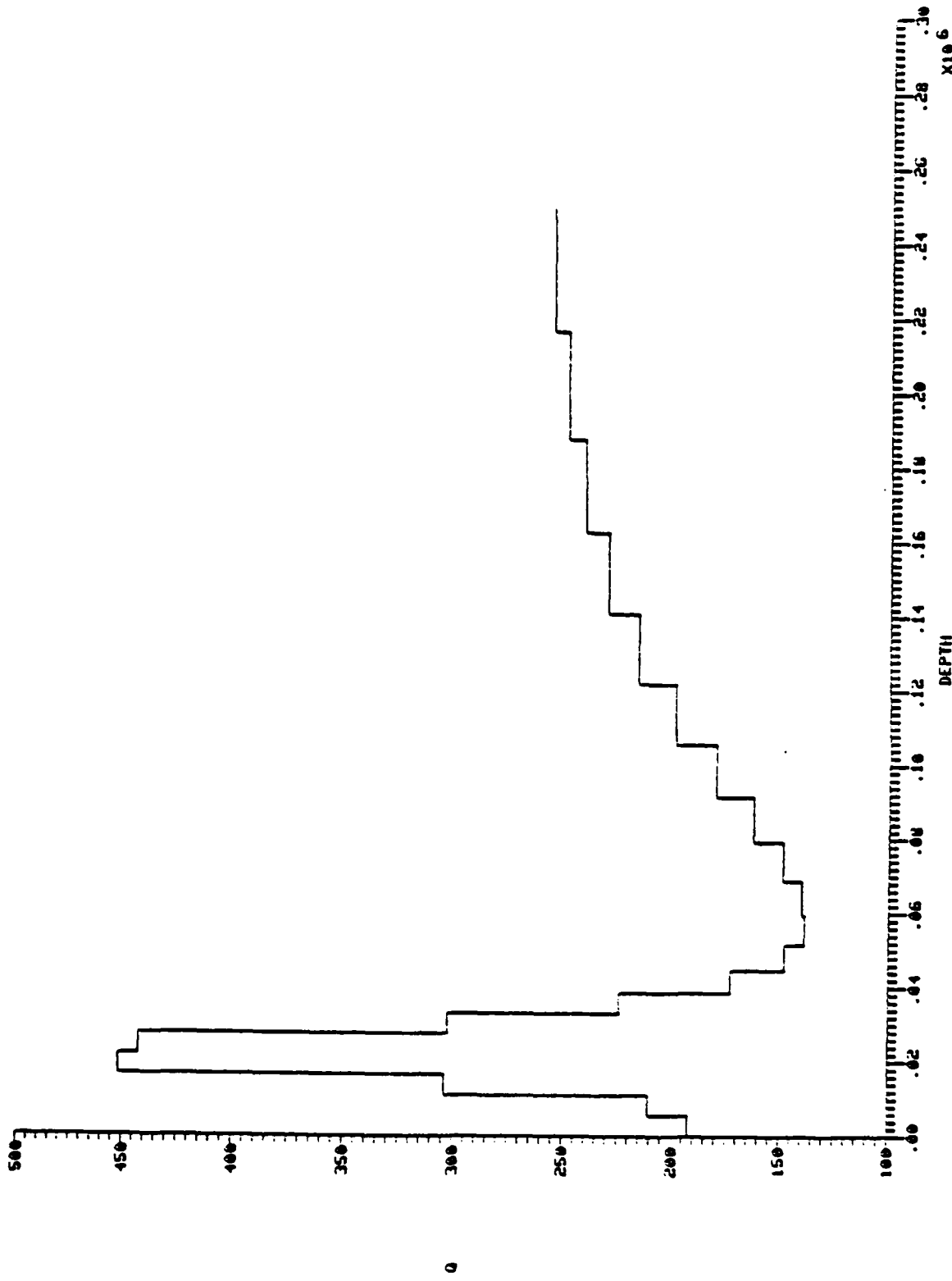


Figure 20.4

### SHAGAN-CHTO STRUCTURE

I	DEPTH	THICK	ALPHA	BETA	RHO	QGM
1	5.521+003	5.521+003	5.608+003	3.148+003	2.446+003	1.323+002
2	1.104+004	5.521+003	5.690+003	3.194+003	2.476+003	2.107+002
3	1.656+004	5.521+003	5.961+003	3.346+003	2.575+003	3.038+002
4	2.299+004	5.521+003	6.184+003	3.471+003	2.656+003	4.514+002
5	2.761+004	5.521+003	6.250+003	3.508+003	2.680+003	4.423+002
6	3.313+004	5.521+003	6.227+003	3.495+003	2.672+003	3.924+002
7	3.865+004	5.521+003	6.883+003	3.751+003	2.838+003	2.241+002
8	4.462+004	5.965+003	6.750+003	3.789+003	2.863+003	1.723+002
9	5.150+004	5.889+003	6.907+003	3.877+003	2.920+003	1.476+002
10	5.945+004	7.346+003	7.140+003	4.308+003	3.005+003	1.384+002
11	6.863+004	9.175+003	7.397+003	4.152+003	3.099+003	1.397+002
12	7.922+004	1.059+004	7.629+003	4.282+003	3.183+003	1.484+002
13	9.144+004	1.222+004	7.807+003	4.382+003	3.248+003	1.524+002
14	1.056+005	1.411+004	7.931+003	4.452+003	3.294+003	1.798+002
15	1.218+005	1.629+004	8.003+003	4.492+003	3.329+003	1.985+002
16	1.407+005	1.880+004	8.015+003	4.499+003	3.324+003	2.159+002
17	1.624+005	2.170+004	7.980+003	4.479+003	3.311+003	2.300+002
18	1.874+005	2.505+004	7.937+003	4.455+003	3.296+003	2.404+002
19	2.163+005	2.892+004	7.935+003	4.454+003	3.295+003	2.484+002
20	2.497+005	3.339+004	7.992+003	4.486+003	3.316+003	2.551+002

Figure 20.5.

Figures 21.1 through 21.5 are on the following pages.

Figure 21. Path 7: SHAGAN-KAAO

Distance: 1884 km  
Azimuth: 22.1  
Instrument: ASRO-LP  
Events Processed: 318

Description: This is a very difficult station to process because of a cleanly bifurcated group velocity curve above 0.04 Hertz. The split is quite obvious in the narrow band filter, but the phase matched filter simply cannot handle it, wanting to jump back and forth between the branches. To process this seismogram, we selected the upper group velocity curve and performed no iterations with the phase matched filter. The final result (synthetic seismogram made using the structure) is a fairly good match to the original, but we cannot express much confidence in the results. The same problem will arise in any further data processing at this station; so it should probably be avoided if possible.

SEC 8, OPTION(H-HELP) ? 2L  
 SEC 8, OPTION(H-HELP) ? 2L  
 GROUP VELS PICKED!  
 10X FREQ GRPU ANPL  
 1 .0000 .000 .000  
 2 .0138 3.787 .113  
 3 .0163 3.769 .120  
 4 .0201 3.469 .163  
 5 .0233 3.245 .274  
 6 .0268 3.166 .279  
 7 .0298 3.033 .352  
 8 .0326 2.943 .521  
 9 .0356 2.965 .755  
 10 .0393 2.894 .935  
 11 .0413 2.888 1.000  
 12 .0435 2.881 .957  
 13 .0453 2.871 .822  
 14 .0468 2.843 .630  
 15 .0494 2.803 .468  
 16 .0524 2.786 .319  
 17 .0557 2.783 .277  
 18 .0587 2.785 .226  
 19 .0605 2.746 .179  
 20 .0625 2.768 .135  
 21 .0670 2.749 .098  
 22 .0729 2.743 .096  
 23 .0786 2.736 .096  
 24 .0831 2.734 .107  
 25 .0862 2.732 .109  
 26 .0880 2.733 .111  
 27 .0891 2.727 .107  
 28 .0903 2.719 .098  
 29 .0913 2.703 .086  
 30 .0912 2.686 .074  
 SEC 8, OPTION(H-HELP) ? 2

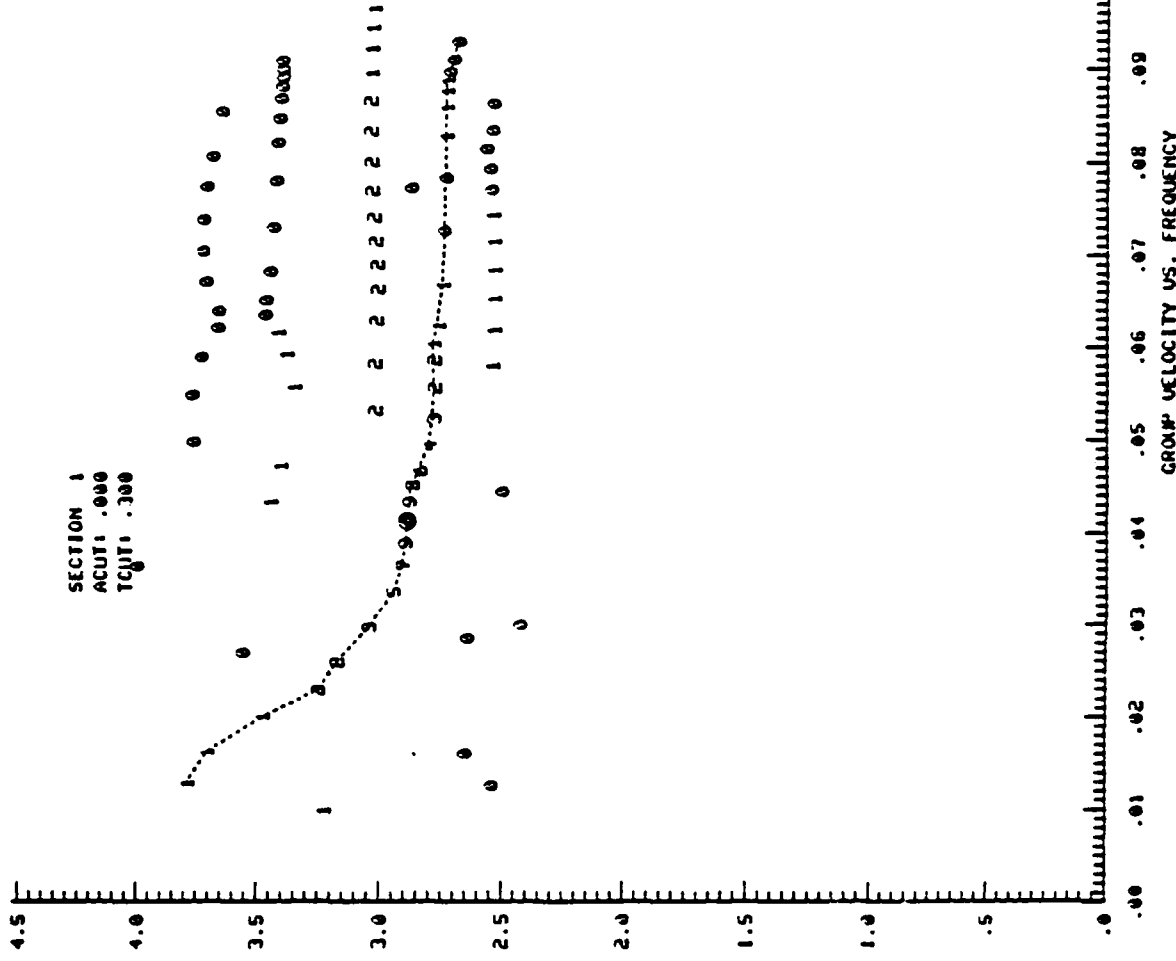
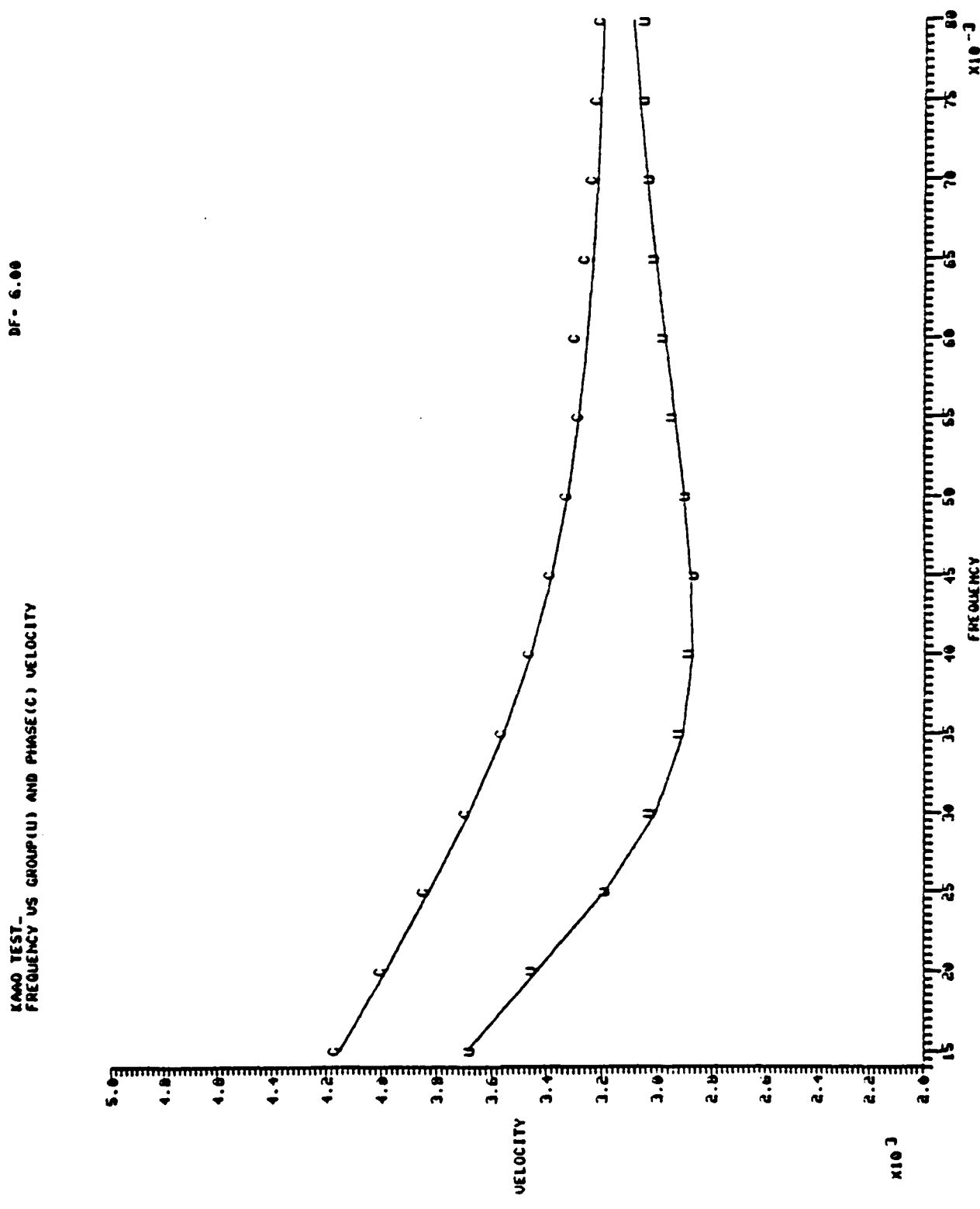
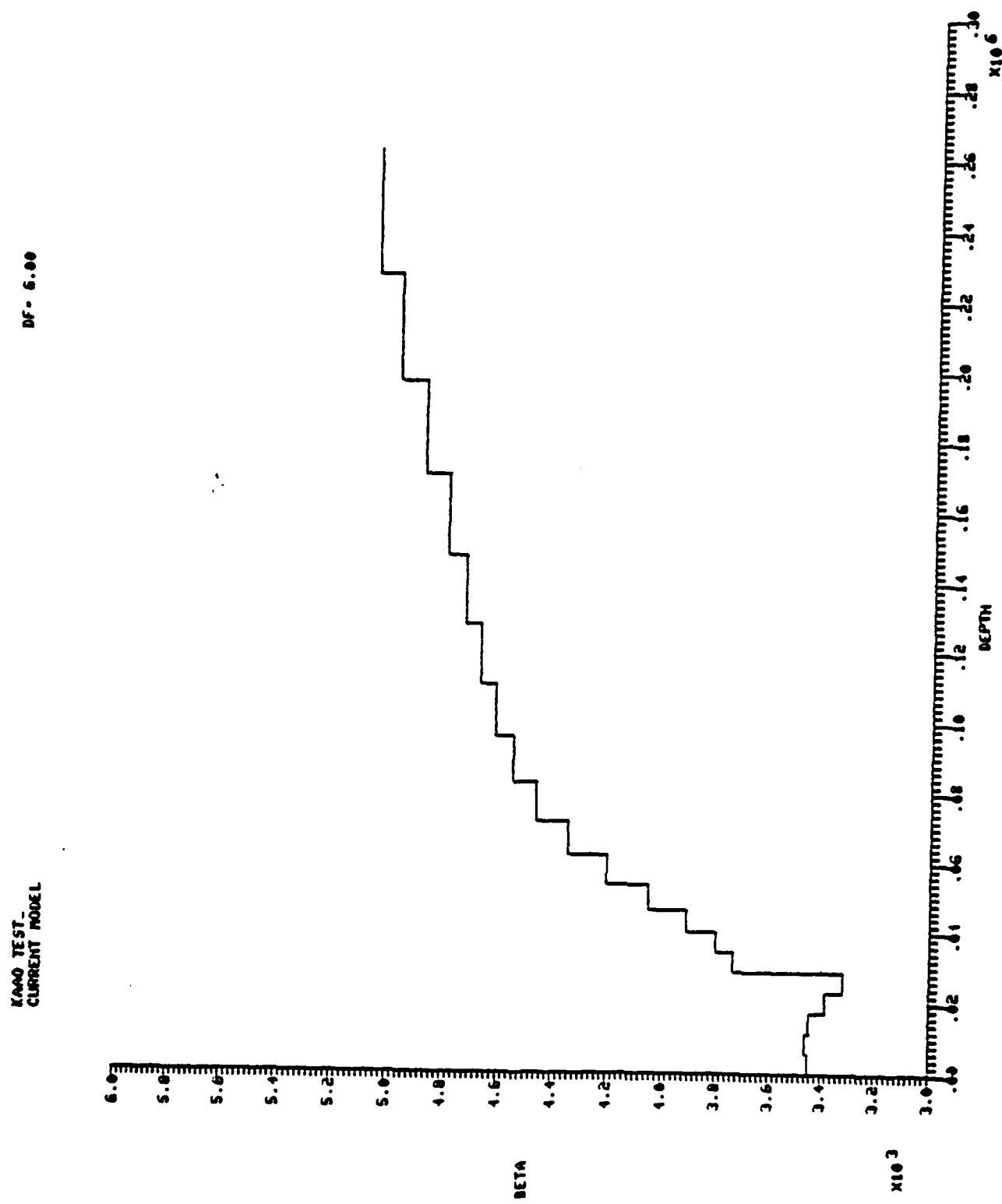


Figure 21.1





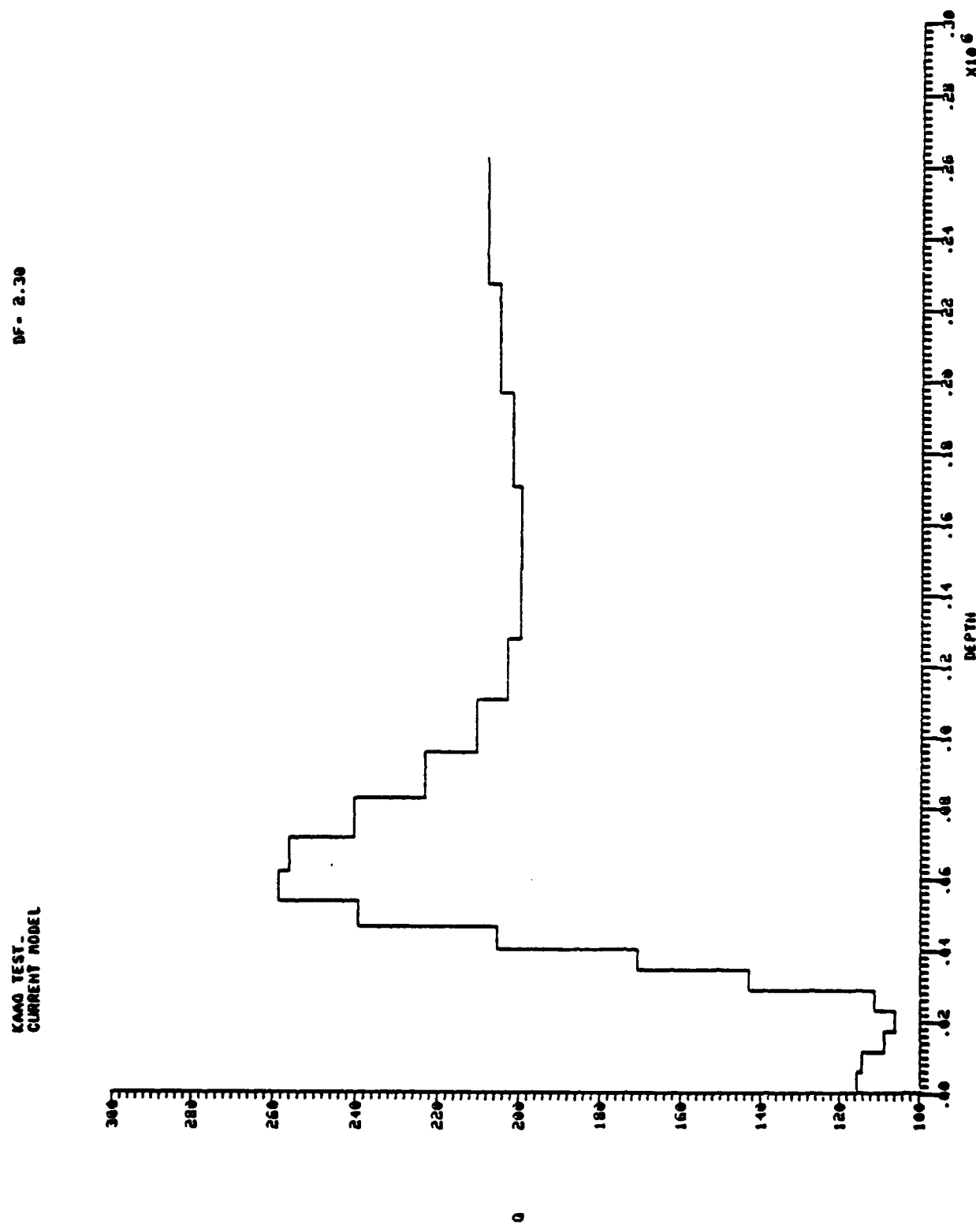


Figure 21.4

### SHAGAN-KAAO STRUCTURE

I	DEPTH	THICK	ALPHA	BETA	RHO	QDM
1	5.737+003	5.737+003	6.141+003	3.447+003	2.641+003	1.155+002
2	1.147+004	5.737+003	6.159+003	3.457+003	2.647+003	1.142+002
3	1.721+004	5.737+003	6.134+003	3.443+003	2.638+003	1.087+002
4	2.255+004	5.737+003	6.025+003	3.382+003	2.598+003	1.359+002
5	2.869+004	5.737+003	5.909+003	3.317+003	2.556+003	1.112+002
6	3.442+004	5.737+003	6.656+003	3.726+003	2.329+003	1.431+002
7	4.316+004	5.737+003	6.772+003	3.801+003	2.871+003	1.709+002
8	4.646+004	6.242+003	6.968+003	3.911+003	2.942+003	2.253+002
9	5.352+004	7.212+003	7.217+003	4.051+003	3.033+003	2.392+002
10	6.155+004	8.333+003	7.498+003	4.204+003	3.133+003	2.584+002
11	7.158+004	9.628+003	7.744+003	4.347+003	3.226+003	2.558+002
12	8.278+004	1.112+004	7.951+003	4.463+003	3.301+003	2.402+002
13	9.556+004	1.235+004	8.102+003	4.548+003	3.356+003	2.230+002
14	1.184+005	1.485+004	8.228+003	4.614+003	3.399+003	2.103+002
15	1.276+005	1.716+004	8.318+003	4.669+003	3.435+003	2.229+002
16	1.474+005	1.982+004	8.418+003	4.725+003	3.471+003	1.396+002
17	1.703+005	2.290+004	8.537+003	4.792+003	3.515+003	1.395+002
18	1.968+005	2.646+004	8.692+003	4.879+003	3.571+003	2.316+002
19	2.274+005	3.058+004	8.861+003	4.974+003	3.633+003	2.248+002
20	2.627+005	3.533+004	9.009+003	5.057+003	3.687+003	2.379+002

Figure 21.5.

### III. AUTOMATIC DISCRIMINATION

A new method for performing seismic discrimination from teleseismic body-wave data has been devised. This method has its roots in several previous methods (VFM, spectral ratio and moment/corner frequency), but it combines and unifies them into one master scheme ideally suited to automatic analysis. Furthermore, it explicitly incorporates recent results in deterministic modeling of explosion and earthquake body waves and makes allowance for absorption through path-dependent  $t^*$  operators.

For want of accessible data, this method, which we call deterministic discrimination, has not been exhaustively tested. Preliminary application to a mixed explosion/earthquake data set (Section 3.3) shows it often is as successful as the purely statistical methods. In order to apply deterministic discrimination, explicit allowance must be made for the attenuation of the spectrum due to scattering and absorption. The method for doing this, when the attenuation is modeled by a frequency-independent  $t^*$  operator is given Section 3.2. The theory is then used contrariwise (Section 3.4) to derive  $t^*$  directly from the deterministic discriminant function evaluated for a suite of NTS and Kazakh explosions.

#### 3.1 DETERMINISTIC DISCRIMINATION

Over the past several years we have developed the method for automatic discrimination outlined in Figure 22. In essence, it consists of reducing  $n$  separate recordings of a seismic event (event oriented waveform data) into  $n + 1$  discriminant numbers,  $d$ , one for each recording as well as a network average. In addition, we attach two probabilities to each  $d$ , the chance  $d$  could have come from an earthquake source  $p(d/q)$ , and the chance  $d$  could have come from an explosion source  $p(d/x)$ .

The scalars,  $d$ , are found by forming a linear combination of seismogram features as is indicated by the "classify" box in

**AUTOMATIC DISCRIMINATION**  
**EVENT ORIENTED**  
**WAVEFORM DATA**

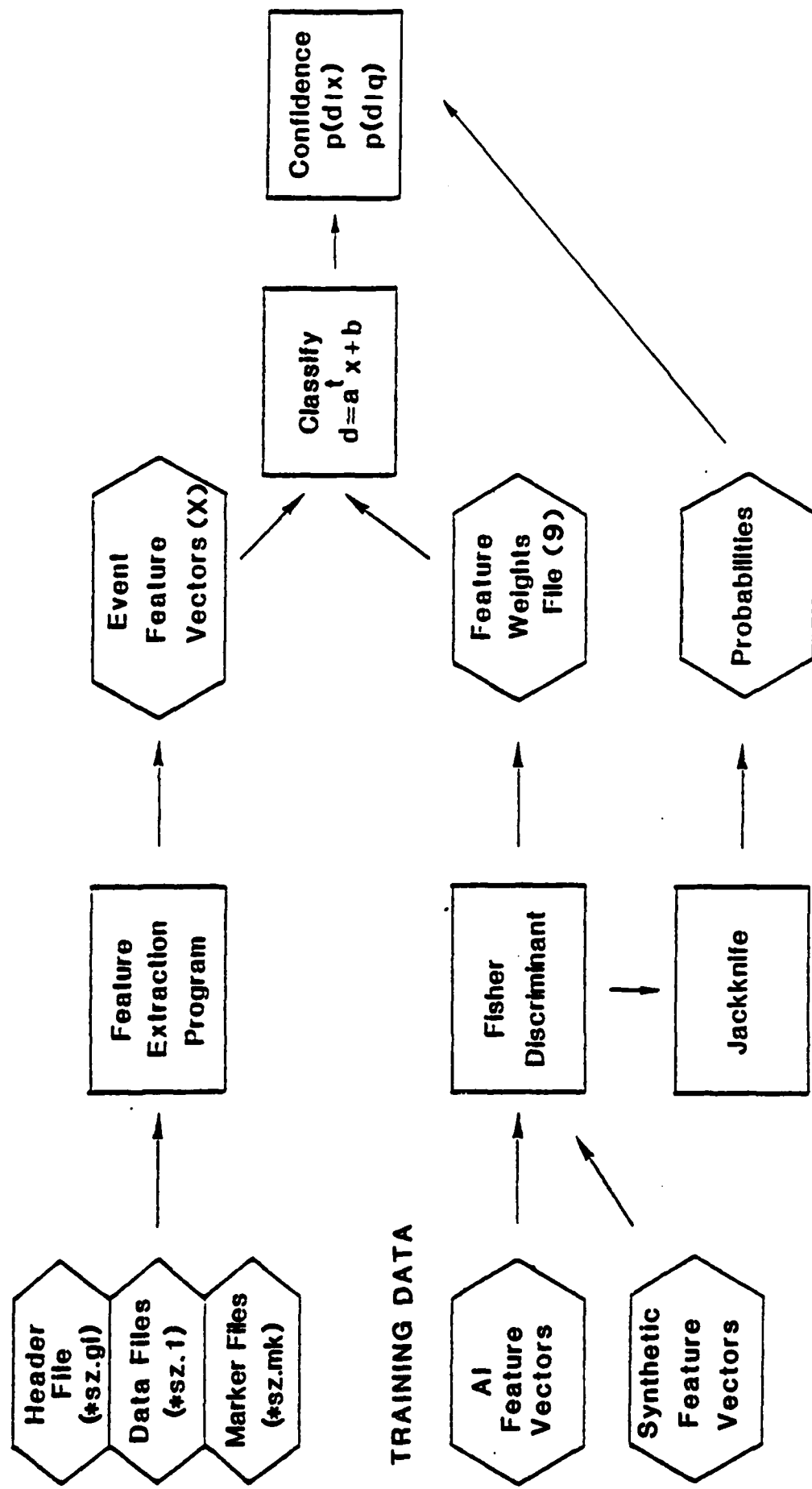


Figure 22. Block diagram of automatic discrimination procedure.

Figure 22. The linear combination is specified by a set of weights,  $a$ , and a constant,  $b$ , and they are discovered by processing training data, as is shown in the lower portion of Figure 22.

Heretofore, the training data has consisted of seismogram features calculated several years ago on a mixed collection of explosion and earthquake data assembled by VELA Seismological Center for the Discrimination Experiment. This is referred to as the "AI" data. It has always been recognized that training data exclusively based on past seismic observation has several deficiencies. Among them are:

1. For most collections of explosion and earthquake seismograms, the two populations will have different magnitude distributions.
2. Rarely, if ever, is a sufficient number of events colocated near enough that differences in path properties for both body waves and surface waves can be neglected.
3. Methods based on available training data must be applied with caution when analyzing isolated events from source regions with no historical records.

As a way of overcoming the magnitude bias, path bias and record absence limitations, and also to provide additional information about the source, deterministic discrimination uses synthetic training data, the "Synthetic Feature Vectors" shown in Figure 22.

Synthetic Feature Vectors describe properties of the seismic waves as they leave the source region, not as they impinge on function  $\{a,b\}$  derived from analysis of synthetic feature vectors purports to be universal. This is in contrast to our previous analysis of AI training data which proceeded on a station-by-station basis. To particularize the universal discriminant function to a specific path, one geophysical parameter,  $tp$ , is needed.

Statistical averaging still is important for deterministic discrimination, however, because many different kinds of events are included in the synthetic training data. These events cover a range

of source sizes, source mechanisms, and source material properties. It is recognized that path effects can blur the differences between earthquake and explosion sources, and an important part of the work described here has concentrated on this point.

Not all possible discriminants are presently testable with synthetic data, for to create such data requires models based on the physics of the excitation and propagation of seismic energy. The complexity discriminant, for example, is not sufficiently understood at present to admit theoretical calculations although a multiple rupture earthquake model might be a method of approach.

The synthetic discriminant we have studied is the shape of the teleseismic body wave spectrum over the frequency range from 0.5 to 5.0 hertz. It should also be possible to apply the concept to synthetic surface wave spectra, but here the vagaries of path dependent attenuation and dispersion require more particular information about specific source-receiver pairs than does the body wave spectrum which, according to current views, is controlled primarily by source type, source size, material properties at the source and attenuation ( $t^*$ ).

Deterministic discrimination happens in two stages. The first, or learning stage, consists of training the algorithm to recognize the difference between earthquakes and explosions based upon synthetic body wave spectra. The second stage consists of applying the taught algorithm to actual data to test its efficacy. The only communication between these two stages consists of the spectral weighting factors  $a$ . Thus we take, initially, data of known type and find the weights function which best separates their spectra. These weights are used afterwards to classify actual data.

### 3.1.1 Theoretical Source Models

Stevens and Day (1982) have described how the body wave source spectrums used in this analysis were calculated. For spectral discrimination, of course, models for both explosion sources and earthquake sources are required. Archambeau et al. (1974) developed

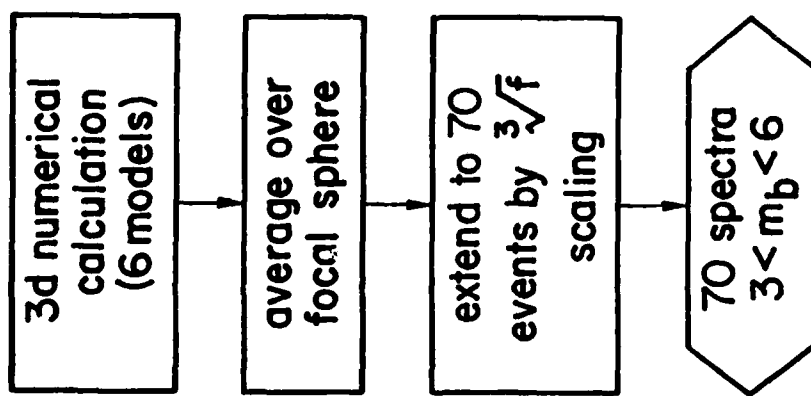
the theoretical basis behind spectral discriminants in general. Analytic approximations to explosion source spectra have been available for some time (e.g., Haskell, 1967; Mueller and Murphy, 1971; von Seggern and Blandford, 1972) and their validity tested against actual data (Filson and Frasier, 1972; Burdick, *et al.*, 1981). More complex explosion models, allowing for imperfect elasticity and nonlinear stress-strain relations, must be calculated numerically (Rimer, *et al.*, 1979). Dynamic fault models of the earthquake source are also a more recent development, and likewise rely on elaborate numerical simulations (e.g., Day, 1982a, b).

Numerical models are expensive to calculate, so only a few distinct source types are contained in the synthetic training data. Since these do not span a sufficiently large magnitude range, the few fundamental models were extended using cube-root (or, for explosions, Mueller-Murphy) scaling. It was important to extend the fundamental source models, because this ensured that within the training set there were sources with corner frequencies both greater than and less than the outer limits of the 0.4 to 5.0 Hz analysis band. Figure 23 shows the steps by which eight fundamental explosion models and six fundamental earthquake models were extended to 140 synthetic events using cube root scaling laws. The final set covered a magnitude range between approximately three and six.

### 3.1.2 Spectral Scaling

It is a property of seismic sources that the shape as well as the level of the spectrum changes with source size. Since teleseismic observations of the radiation are restricted to a relatively narrow frequency band (typically 0.5 hertz to 3.0 hertz), it is important to make a magnitude dependent scaling of the raw spectra. The scaling serves two purposes: it reduces the influence that magnitude alone might have as a "discriminant" (the magnitude bias problem), and it linearizes the difference between earthquake spectra and explosion spectra, thereby increasing the efficacy of the linear discriminant algorithm.

## EARTHQUAKE MODELS



## EXPLOSION MODELS

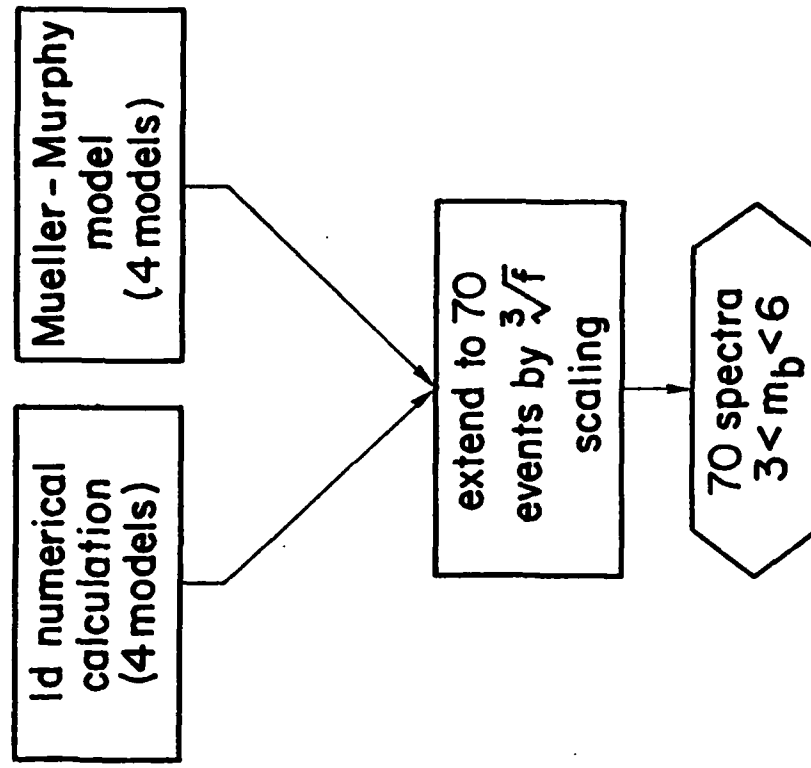


Figure 23. A handful of numerical models is expanded to give a much larger training set using magnitude scaling laws.

It should be understood that the spectral scaling rule is not meant to be a fit to any particular source or even class of sources. It is, on the contrary, meant to be ambiguous as to source type. That is, the rule should be a spectrum which is as much like a typical earthquake as it resembles a typical explosion. The fundamental consideration behind the scaling rule is that it should linearize (with respect to frequency and source size) the spectrum, without showing a preference for source type.

The concept behind the scaling used here arises from the view that, given equal moments,  $\Omega$ , an explosion source has a larger corner frequency than an earthquake source as shown in Figure 24. Since the moment can be written (Aki and Richards, 1980, Equation 14.35)

$$\Omega = Df_c^{-3} , \quad (1)$$

it can be seen that the parameter,  $D$ , is diagnostic of source type. It has, in fact, been attempted to infer  $D$  directly from recorded data by making independent measurements of  $\Omega$  and  $f_c$  (Rivers, et al., 1980). The result was not particularly successful, presumably because of the limited bandwidth accessible for analysis. Our approach has been to use synthetic modeling in order to derive  $D$  from theory rather than observation; or more specifically, to estimate that  $D$  which best separates synthetic explosion spectra and synthetic earthquake spectra of identical moment.

The method used for normalizing the spectra is based on the work of Stevens and Day (1982). In that study, spectral magnitudes were found for a variety of earthquake and explosion sources and used to evaluate the  $m_b$ : $M_s$  and VFM discrimination methods. Those results were used here to find a "reference discrimination spectrum." It was observed that a spectral magnitude curve of the form ( $\ell = f_c^{-1}$ )

$$m_b^r(f) = \log_{10} \frac{D\ell^3 f}{1 + (\ell f)^2} \quad (2)$$

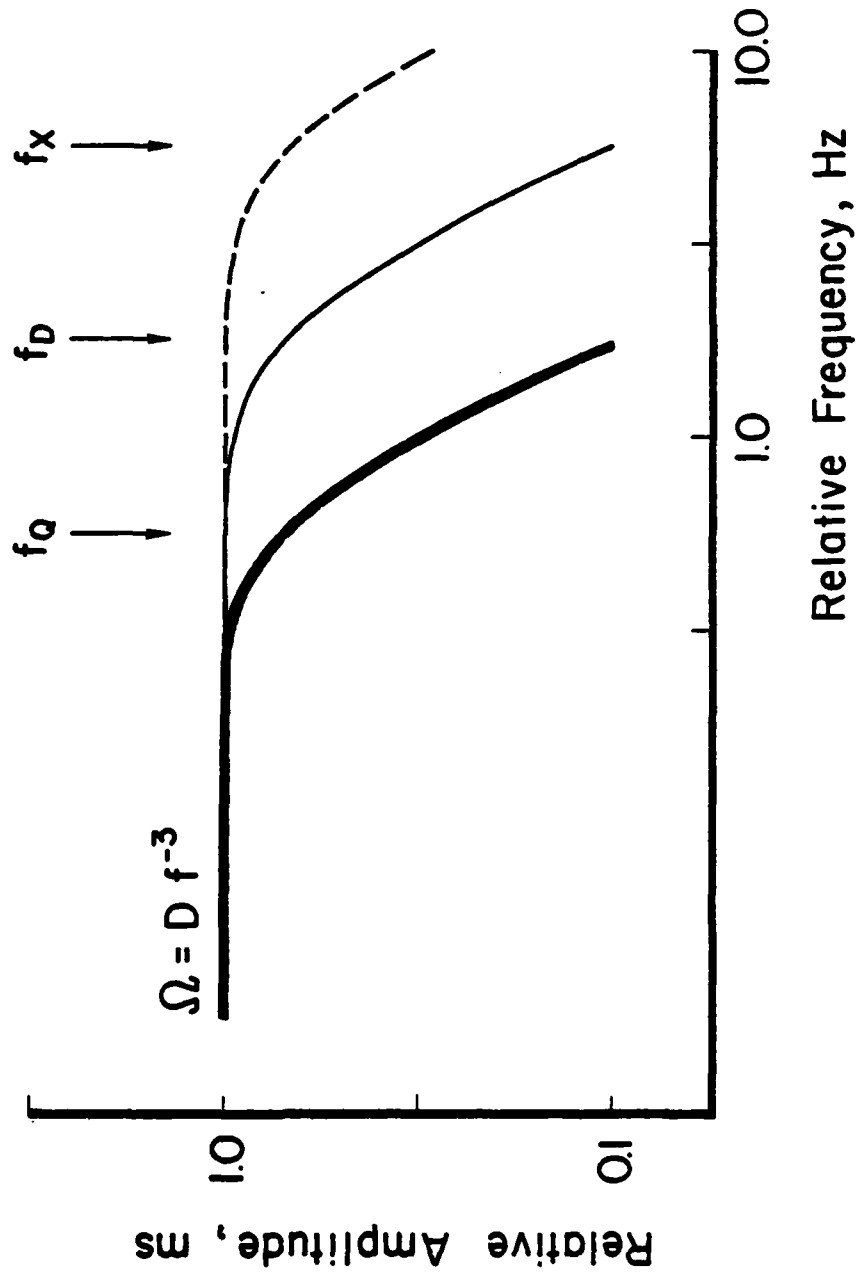


**Figure 24.** For an earthquake and explosion of equal moment, the corner frequency of the latter exceeds the former because the velocity-stress parameters ( $D$ ) are different. By estimating the corner frequency ( $f_D$ ) of a reference discrimination spectrum, it is possible to estimate the reference velocity-stress constant ( $D$ ) needed for spectral scaling. The relative frequency and relative amplitude scales are somewhat exaggerated for clarity.

with  $\log_{10} D = 5.6$  cleanly separated the earthquake and explosion spectral magnitude curves. This expression was used to scale the theoretical spectra in the following way. For each separate spectrum, the magnitude at 1 hertz ( $m_b(1)$ ) was noted. This number was used to solve Equation (2) for the scaling parameter  $\ell$ , with  $f$  fixed at 1. The reference spectrum,  $m_b^r(f)$  was then evaluated for all frequencies  $f$  and subtracted from the actual  $m_b(f)$ . The spectra used here varied in magnitude (at 1.0 hertz) from 3.0 to 6.0 and so cover the important magnitude range. The resulting normalized synthetic spectra are shown in Figure 25. Note that the normalized explosion spectra almost all increase with frequency while the earthquake spectra generally decrease. Note further, that the magnitude zone containing all spectra of a given type is typically 0.8 magnitude units wide at a given frequency, and shifts, on average, by 0.5 magnitude units as the frequency varies from 0.5 to 5.0 hertz. Both with respect to the width of the spectral band ( $\sim 0.8 m_b$ ), and with respect to the magnitude shift with frequency ( $\sim 0.5 m_b$  over 5 hz range), the normalized spectra have much less variance than the raw spectra. Equally important, the normalization has not destroyed the differences between spectra of the two different source types.

### 3.1.3 Discriminating Theoretical Spectra

The scaled theoretical spectra were classified by using the Fisher linear discriminant, as described by Farrell, et al. (1981). A flow diagram for the procedure is given in Figure 26.

It should be clear from the scaled spectra shown in Figure 25 that highly successful discrimination is almost trivially simple. For example, when  $f < 1.0$  hertz, the univariate discriminant

$$d = m_b(f) \quad (3)$$

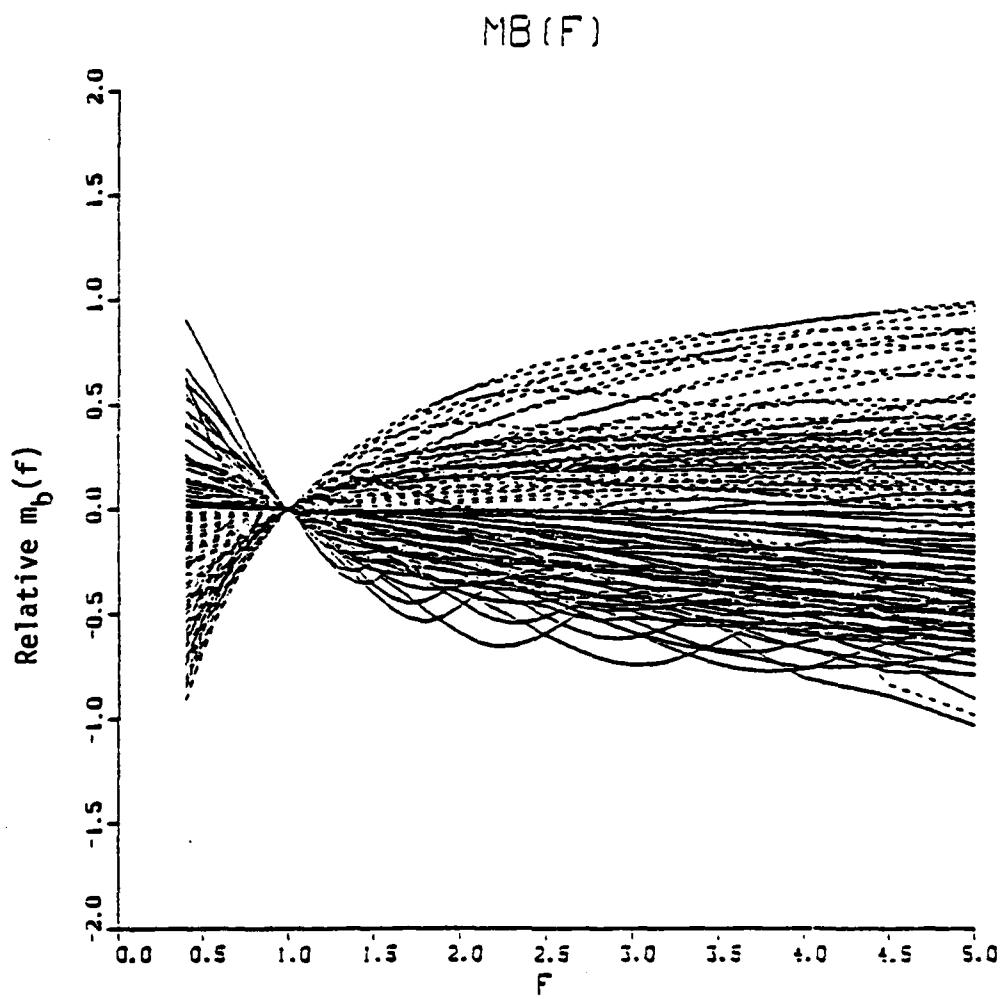


Figure 25. Scaled body wave spectra for a collection of numerical earthquakes and explosions covering the magnitude range  $3 < m_b < 6$ . Dash lines denote explosions, and solid lines denote earthquakes.

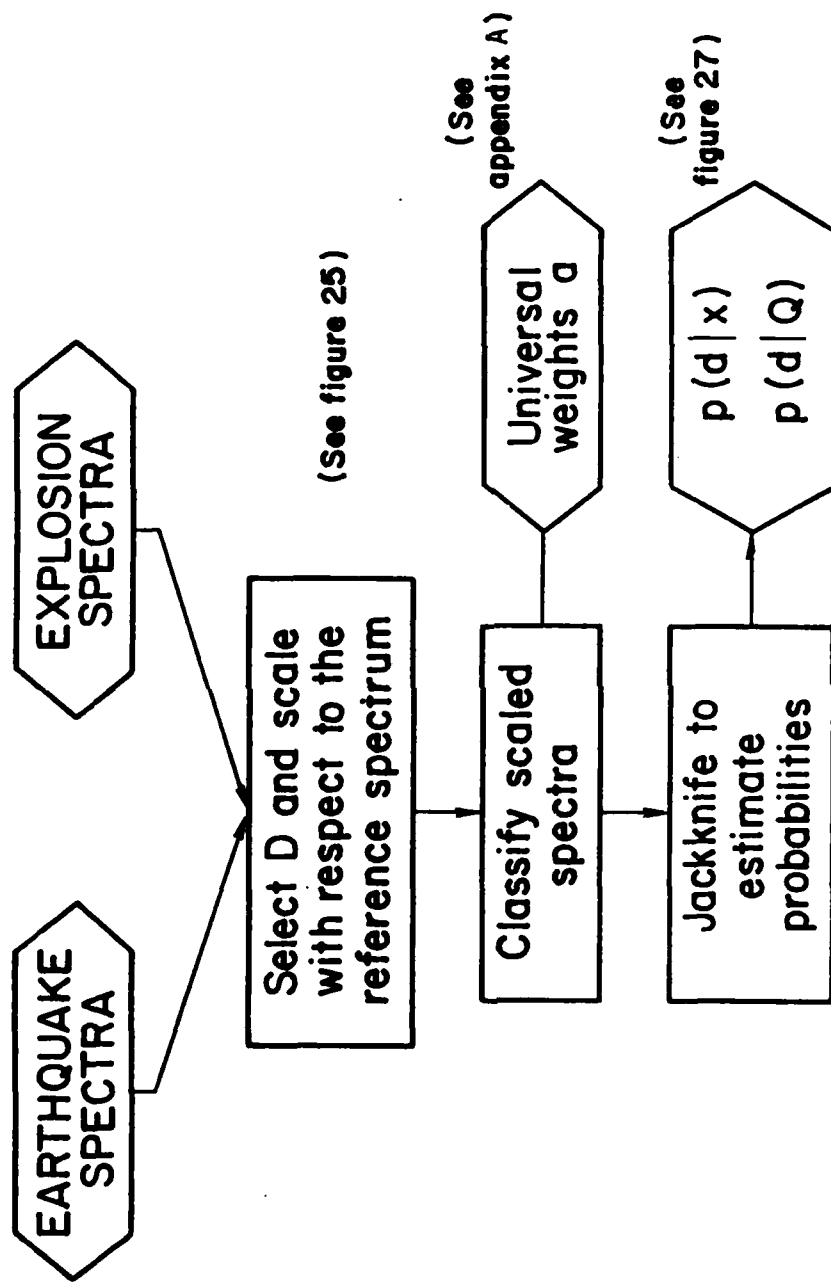


Figure 26. The synthetic spectra are scaled and then classified using the Fisher discriminant. Misclassification probabilities are estimated by a jackknife calculation.

classifies many events correctly according to the rule

$$d \begin{cases} < 0 \rightarrow \text{explosion} \\ > 0 \rightarrow \text{earthquake} \end{cases} . \quad (4)$$

Simply reversing the rule gives comparable results when  $f > 1.0$  hertz.

Even more successful is the bivariate discriminant defined for a pair of frequencies  $\{f_1, f_2; f_1 < 1.0, f_2 > 1.0\}$

$$d = m_b(f_1) - m_b(f_2) , \quad (5)$$

or, more generally,

$$d = a_1 m_b(f_1) + a_2 m_b(f_2) \quad (6)$$

with a rule similar to Equation (4). This bivariate method, in fact, was just the one developed by Savino, et al. (1980).

The multidimensional generalization of the linear discriminant given by Equation (6) and the rule given by Equation (4) is the Fisher discriminant

$$d = a \cdot m + b \quad (7)$$

where in vector notation,  $a$  is a row vector of weights,  $m$  is a column vector of normalized magnitudes, and  $b$  is a scalar constant. To within an arbitrary scale factor, the prescription for the Fisher discriminant says,

$$a = S^{-1} m^t \quad (8)$$

$$b = \frac{a \cdot (m_1 + m_2)}{2} \quad (9)$$

where  $S$  is the pooled covariance matrix,  $m_1$  is the mean vector of population 1,  $m_2$  is the mean vector of population 2, and  $a m^t$  is the transpose of  $(m_1 - m_2)$ .

In practice, the pooled covariance is often nearly singular, causing its inverse to be highly unstable. To stabilize this calculation, the inverse is damped (a method known as ridge regression in the statistics literature) by performing a singular value decomposition and suppressing eigenvalues which are less than a certain fraction of the largest eigenvalue. This leads to a slightly nonoptimum discriminant function, but one which is less sensitive to noise in the data.

The measure of damping is the number of degrees of freedom (NDF). When NDF is small, discrimination is performed on a small dimension subspace of the space spanned by all the variables. For the spectral discriminant being studied here, it is typically found that NDF ranging from 2 to 10 (40 variables) gives satisfactory results, indicating that the essential information is highly organized.

If it were reasonable to assume that the selection of synthetic events (the 140 spectra) were a random sample from two multidimensional populations of the Gaussian type with equal covariances, then standard formulas could be used to estimate misclassification probabilities. We have not followed this standard approach for several reasons:

1. There is no rational justification for adopting the multidimensional normal approximation to the probability density functions.
2. Even if there were, we cannot be confident that the available synthetic data constitutes a random sample.
3. There is no reason to assume that the covariance matrix for explosion spectra is the same as the covariance matrix for the earthquake spectra. On the contrary, the very different elements of the source physics makes it much more likely that collections of earthquake spectra are more diverse than collections of explosion spectra. Shumway and Blandford (1970) have shown, however, that

such differences may not be important for linear discriminant analyses.

Thus, the method we use to assign misclassification probabilities is the jackknife method, a linear approximation to the bootstrap (Efron, 1979, and references therein). This technique, more informatively referred to as the leave-one-out method, is simple to implement. For a sample of size  $n$ , where  $n = n_1 + n_2$  with  $n_1$  samples from population one and  $n_2$  samples from population two, Equations (8) and (9) are evaluated for all possible subsets of the available training data containing exactly  $n - 1$  samples. The set  $\{a, b\}$  is used in Equation (7), letting the datum ( $m$ ) be just that observation deleted from the  $\{a, b\}$  calculation. Thus, one pretends that each observation in turn is missing, and classifies it by the discriminant function obtained from the remaining data. Discriminants obtained in this way, we refer to as  $d^*$ .

To quantify the distribution of  $d^*$  obtained, a simple normal law is fit to the collection of each type. This yields means and variances for the two populations.

The foregoing procedure was applied to the synthetic body wave spectra yielding the results plotted in Figure 27. This figure shows the jackknifed values for  $d^*$  obtained for the earthquakes (crosses) and explosions (circles), where the symbols have been displaced vertically for clarity. Also shown are the bell-shaped probability density functions fit to each cluster.

The success of this procedure is apparent. If the rule

$$d \begin{cases} < 0 \rightarrow \text{explosion} \\ > 0 \rightarrow \text{earthquake} \end{cases} \quad (10)$$

is adopted, then only three events (one earthquake and two explosions) are misclassified. But these three events are among either the very largest or the very smallest of the synthetic collection,

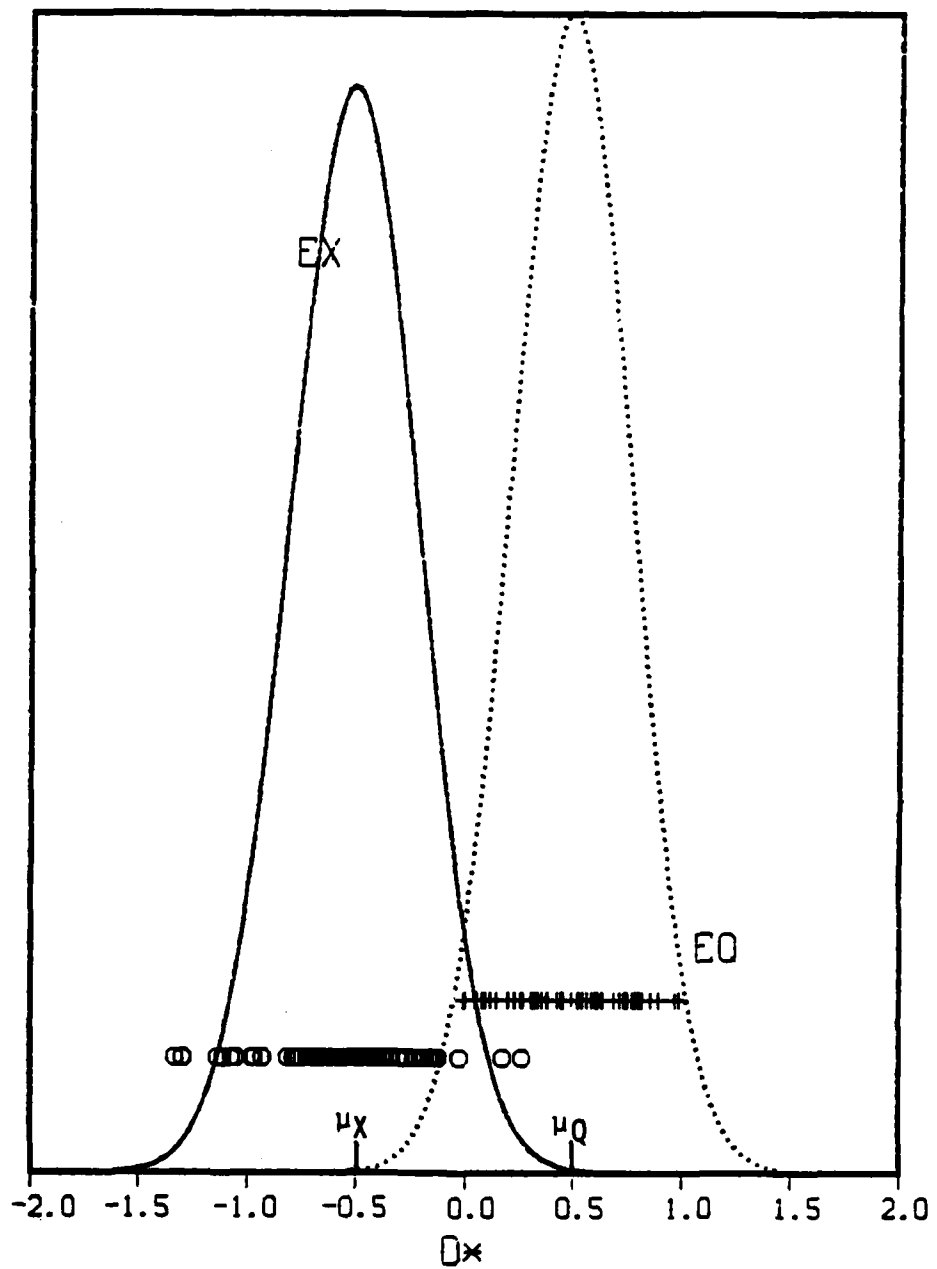


**Figure 27.** The Fisher discriminant accurately separates the explosion spectrums from the earthquake spectrums when quadratic scaling (see Figure 25) is used. The covariance matrix was highly damped for this calculation (NDF = 2.0). These jackknife results show the explosion discriminants clustered near  $\mu_X = -0.5$ , and the earthquake discriminants clustered near  $\mu_Q = +0.5$ . Compare this figure with Figure 28.

so that their corner frequencies fall outside the spectral band used for discrimination.

Equation (10) is not the only viable rule. It might be thought more hazardous to mistake an explosion for an earthquake than vice versa. In this case, these data might suggest a critical value of  $d^*$  near + 0.25. Alternatively, a rule we use subsequently when discussing real data is to choose the critical value such that equal fractions of the two types of events are misclassified. Of greater practical importance, however, is to discover the physical reasons that certain events are misclassified, for this could lead to improved discrimination methodologies. The fact that the misclassified events shown here are either very large or very small has been noted. Is there, perhaps, a more subtle residual magnitude bias hidden in the distribution of  $d^*$ ? If so, improvements in the spectral scaling law could be made. Attenuation is another effect which we elaborate on later.

With the 140 test events contained in these synthetic training data, there are 141 possible discriminant functions  $\{a,b\}$ , any or all of which might be tested against real data. One of these sets is obtained when the entire population of events is used, the others result from the separate jackknife calculations. For a homogeneous collection of training data, such as these synthetics, the differences in the numerous  $\{a,b\}$  are expected to be small, particularly when  $n$  is large. Thus, the choice ought to be unimportant, and we elect to use the set  $\{a,b\}$  obtained when all events are used. These weight factors, called deterministic weights, are tabulated in Appendix A.

It was noted previously that the judicious choice of a reference spectrum is crucial, both to linearize the data and to ameliorate possible magnitude bias. The quadratic reference spectrum defined by Equation (2) is one popular model which has some theoretical justification; but it is by no means the only reasonable choice. It is certainly the simplest model, for it contains just two parameters,  $D$  and  $f_c$ . However, theoretical studies and

experimental measurements have shown that explosions and earthquakes in some environments can have a pronounced spectral rise at the corner frequency. This resonant behavior is evidence of under-damping, an effect modeled by adding a term in the denominator which depends linearly on  $f_c$ . A cubic denominator polynomial is also often used, particularly for modeling earthquake spectra.

In a practical sense, the necessity of adopting more complex reference spectra is, at present, not convincing. This is because the data available are so band limited, the low frequencies being lost in background noise and the high frequencies being lost through attenuation. For every extra free parameter proposed in the reference spectrum model, it is necessary to provide a means of estimating it with real data.

With synthetic data this practical problem does not occur, and one alternative model which was tested but not pursued was the simple cubic model

$$m_b^r(f) = \log_{10} \left[ \frac{D \ell^3 f}{1 + (\ell f)^3} \right]. \quad (11)$$

The jackknife discrimination result obtained when this scaling law was applied to the synthetics is shown in Figure 28. Since the cubic law seems to produce perfect results, why reject it? First, the better performance is only marginal (3 events in 140), and may be accidental. Second, the cubic law did not produce better classification results than the quadratic law when tested on real data. Finally, a large slice of the  $m_b(f)$  plane is untouched by theoretical spectra of cubic shape (see Aki and Richardo, 1980 Figure 14.13), and noisy data falling up there could, perhaps, be inadvertently weighted too strongly. The most mundane reason of all is perhaps the most compelling: real data is so band-limited, and the corner zone so broad, that the asymptotic limit ( $f^{-2}$  or  $f^{-3}$ ) is irrelevant.

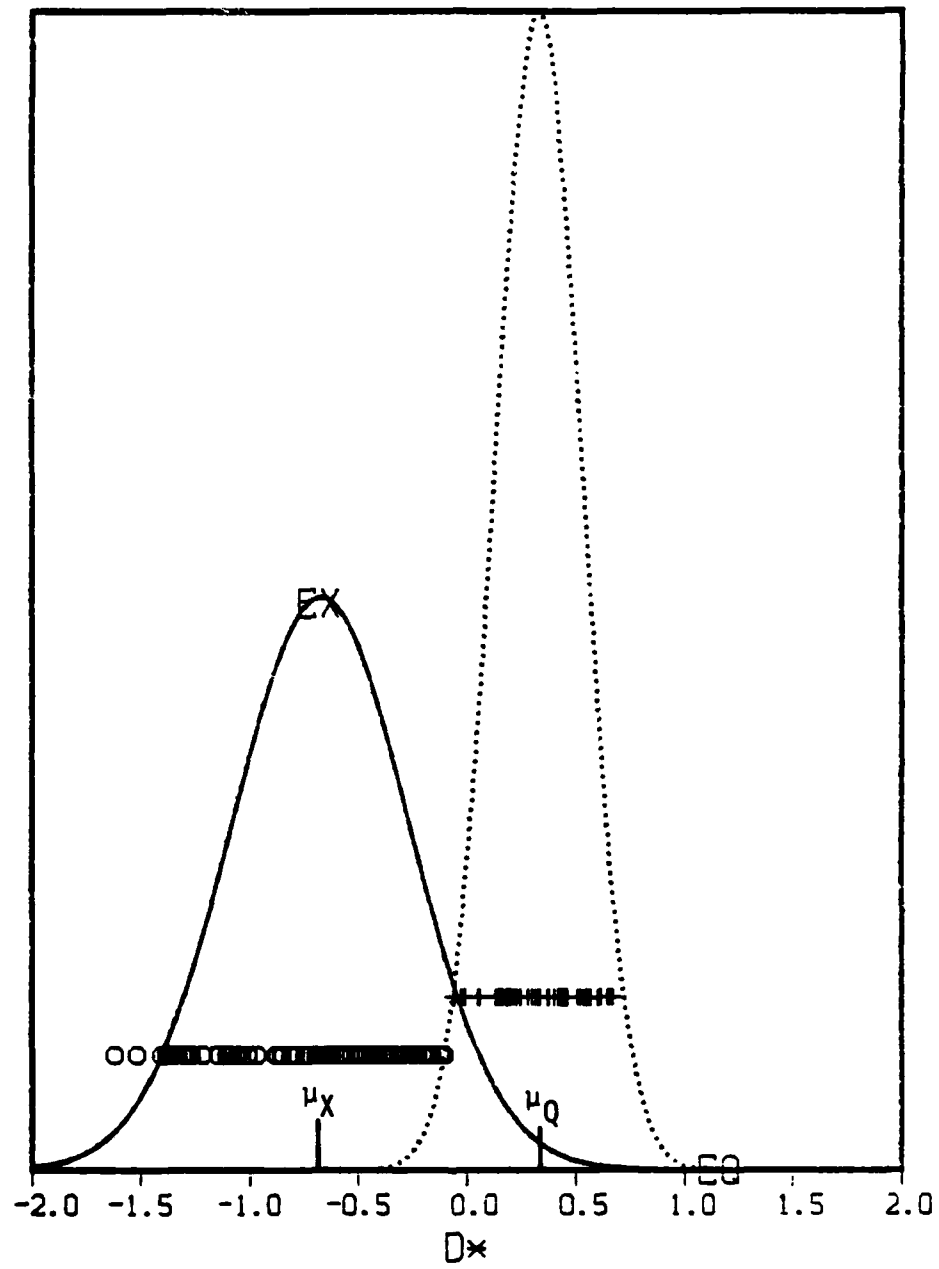


**Figure 28.** When cubic scaling is used, the jackknife produces this discriminant distribution. The explosion grouping is broader and the earthquake grouping is narrower than when quadratic scaling was used (see Figure 27).

We note several curious features on Figure 28. First, the population averages  $\mu_X$  and  $\mu_Q$  are significantly displaced from the reference locations  $\pm 0.5$ , that hold when the algorithm is used on the entire training set. Furthermore, the cubic scaling gives a smaller spread to the earthquake distribution, but a larger spread to the explosion distribution than does the quadratic scaling. This does not conflict with the contention of von Seggern and Rivers (1979) that the cubic model is preferred for earthquakes, but the quadratic for explosions. Finally, it should be noted that the two explosions seen in Figure 27 with most positive  $d^*$  have been gathered into the main cluster, and if the decision rule  $d^* \sim -0.1$  is adopted, there are no misclassified events when the cubic scaling is used.

### 3.2 EFFECT OF ATTENUATION

#### 3.2.1 Constant $t^*$ Model

When deterministic weights are used to classify real (scaled) body wave spectra by direct application of Equation (7), the two populations remain separated, but the scalar discriminant is strongly biased in the positive direction. The effect is schematically illustrated by the idealized plots shown in Figure 29. The direction of the shift, called the discriminant bias, is direct evidence that real spectrums are deficient in high frequency energy relative to the separation spectrum. The size of the bias is too pronounced to be attributable to using a quadratic reference spectrum in preference to the cubic. Both the direction and size of the discriminant bias are entirely consistent with the assumption that it is a consequence of frequency dependent attenuation known to happen due to the combined effects of absorption and scattering in the earth.

One possible way to handle the bias that occurs when deterministic weights are used to classify real data would be simply to measure it (assuming data from both populations are present in the training set), and suitably alter either the scalar constant,  $b$ , in

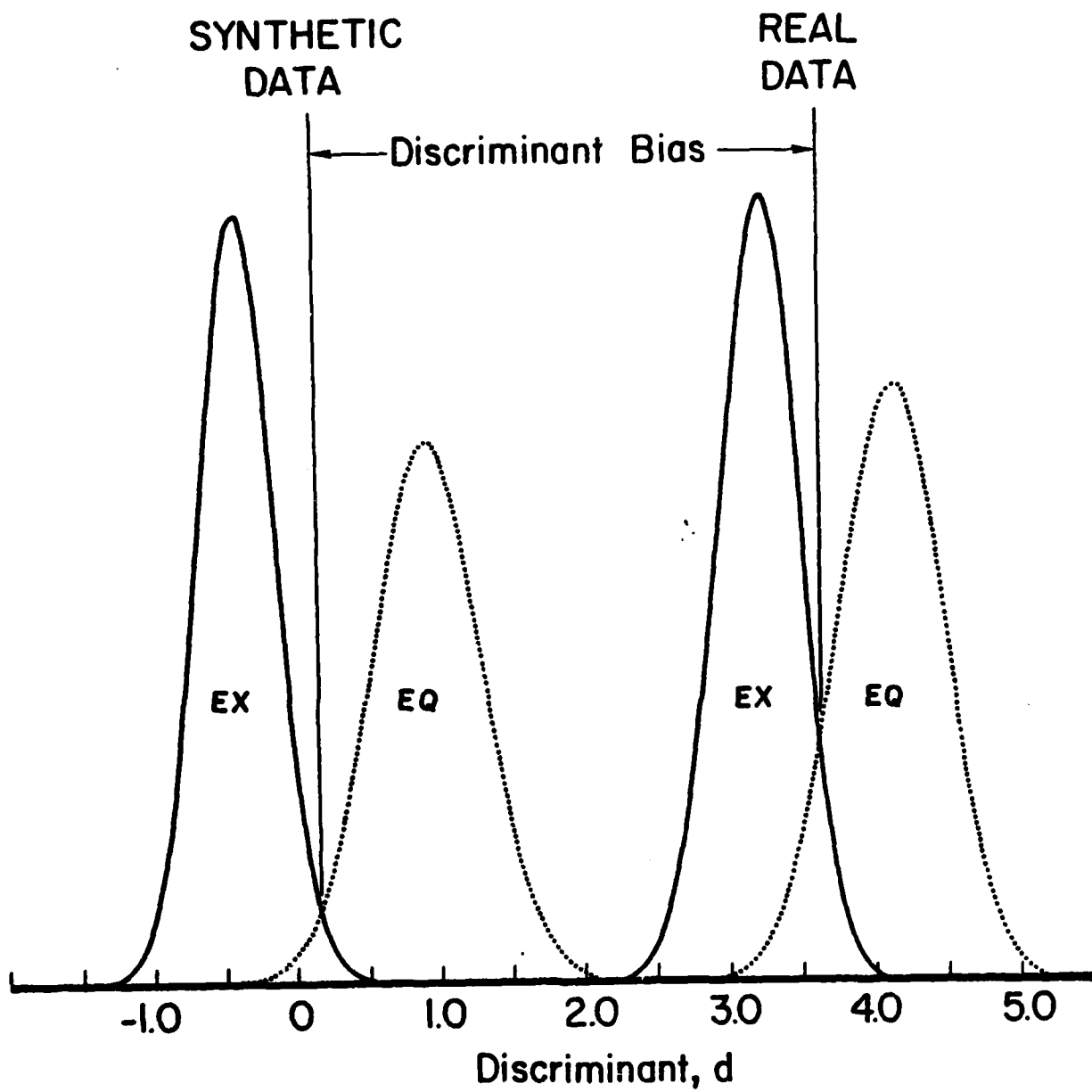


Figure 29. When deterministic weights are applied to real data, the discriminants are shifted towards positive values because of attenuation. The shift shown in this schematic diagram is exaggerated.

Equation (7) or, equivalently, the threshold value of  $d$  used in the classification rule. We instead make a virtue out of necessity and show how the discriminant bias is not only a direct consequence of attenuation, but can, in fact, be used to measure seismic attenuation directly.

There are two points of view that may be adopted, both of which lead to the same result. From the receiving station point of view, the cause of the discriminant bias is to be found in an incorrect choice of reference spectrum; Equation (2), for example, makes no allowance for the path-dependent spectral attenuation due to scattering and absorption.

Alternatively (and, being source modelers, the view we prefer), the cause of the discriminant bias arises because the extrapolation of the far field signal back to the source is incomplete. Instead of allowing just for geometric spreading, the Gutenberg  $B(\Delta)$  term, allowance should be made also for frequency dependent attenuation. Thus, if propagation along the path can be modeled by an operator  $O(f)$ , then the VFM magnitude  $m_b(f)$  ought to be defined by

$$m_b(f) = \log_{10} [fA(f)/O(f)] + B(\Delta) . \quad (12)$$

It is fashionable to posit an absorption band model for explaining seismic attenuation, and Lundquist and Samowitz (1982) have indeed estimated the parameters in such a model from analysis of the same data set we discuss later. We have adopted a more traditional constant  $t^*$  model of the attenuation function (Carpenter, 1967; Der, et al., 1982; see also Lundquist et al., 1980, for a general review), according to which

$$O(f) \sim \exp(-\pi f t^*) . \quad (13)$$

The rule given by Equation (13) cannot hold over all frequencies, but it is a good local approximation over restricted frequency ranges. The range here, of course, is the teleseismic wave band 0.5 to 5.0 hz.

One subtlety must be recognized before Equation (13) can be made an equality and substituted into Equation (12). The distance correction factor  $B(\Delta)$  implicitly combines the effects of attenuation as well as spreading, but it is an earth-averaged attenuation, and it is an attenuation at the frequency of 1.0 hertz, the predominant frequency present in the time domain data from which  $B(\Delta)$  is found. To make this implicit attenuation factor explicit, we write

$$0(f) = \exp(-\pi(ft_p^* - t_e^*)) \quad (14)$$

where  $t_p^*$  is the attenuation coefficient for a particular path and  $t_e^*$  is the earth-averaged, 1.0 hertz attenuation.

Thus, the proper way to define the variable frequency magnitude is

$$m_b(f) = \log_{10}(fA(f)) + 1.36(ft_p^* - t_e^*) + B(\Delta) . \quad (15)$$

It is the middle term on the right hand side that we now relate to the value of the discriminant bias for each station.

### 3.2.2 Effect of $t^*$ on the Deterministic Discriminant

If we scale the spectrum (recall that the deterministic weights apply to scaled spectra, not raw observed spectra), then the equations presented in of Section 3.1.2 lead to a modified spectral magnitude which is to be substituted into the Fisher discriminant given by

$$m'_b(f) = \log_{10}(fA(f)) + B(\Delta) + 1.36(ft_p^* - t_e^*) - \log_{10}\left(\frac{\ell^3 f}{1 + (\ell f)^2}\right) - 5.6 . \quad (16)$$

In this, and subsequent equations, the number 5.6 is simply  $\log_{10}(1/D)$ , as discussed in Section 3.1.2.

A problem now arises -- how is the source parameter  $\ell = f_c^{-1}$  to be chosen? Previously, when the effect of attenuation was ignored,  $\ell$  could be estimated by requiring  $m_b(1.0 \text{ hertz}) = 0.0$  (see Figure 25). Now, the exact value of  $\ell$  is coupled to assumed values for  $t_p^*$  and  $t_e^*$ . That good estimates of source corner frequencies cannot be made independently of estimations of attenuation is well known (Filson and Frasier, 1972). For modest attenuation, the interaction is weak (see Equation (17) below); so a simple iterative analysis method is adequate.

Substituting the scaled spectrum into the Fisher discriminant (Equation (7)), we get,

$$d = a \cdot \left[ \log_{10} \left( \frac{1 + (\ell f)^2}{\ell^3} A(f) \right) + B(\Delta) - 5.6 \right] + b + \underbrace{1.36a \cdot (ft_p^* - t_e^*)}_{\text{discriminant bias term}} \quad (17a)$$

$$= d^R + d_{\text{bias}} \quad (17b)$$

In Equation (17b) we have defined  $d^R$  (R for real data) to be the value of the discriminant scalar that results when the deterministic weights are applied (incorrectly) to the unmodified VFM spectrum, and  $d_{\text{bias}}$  is the shift caused by the  $t^*$  term in Equation (17a).

If  $t_p^*$  and  $t_e^*$  are known quantities, then Equation (17b) shows how the initial discriminant,  $d^R$ , must be modified so as to remove the shift caused by attenuation. With reference to Figure 29, the correction specified by Equation (17b) takes the two Real Data Gaussian functions centered near 3.5 (these are the probability density functions of  $d^R$  for earthquakes and explosions) and shifts them leftwards by amount  $-d_{\text{bias}}$  to get two collections of  $d$ 's centered around zero.

Alternatively, if synthetic spectra are accurate models of real events, then observations of  $d^R$  can be used to estimate  $t_p$  directly from the bias term. This is the notion developed in Section 3.4.

One objection raised during the initial development of the VFM discriminant was that it made no allowance for attenuation. Equation (17b) answers this objection quantitatively. Equation (17b) also furnishes the correct framework for treating data sets containing events recorded over several different paths. For example, most explosions occur in a few compact testing areas. Earthquake epicenters are diffuse and seldom are found near test sites. If independent estimates of  $t_p^*$  can be made for each path, then Equation (17a) can be used to equalize the discriminants. This yields corrected discriminants,  $d$ , which may be averaged together.

### 3.2.3 Definition of the Discriminant Bias

Before applying Equation (17) to estimating attenuation from real data, it is necessary to be more precise in the definition of the discriminant bias. Several plausible meanings are possible. Considering first the synthetic data, define:

$d_1^S$  = the point where the explosion probability density function  $p(d|X)$  equals the earthquake probability density function  $p(d|Q)$ ;

(18a)

$d_2^S$  = the point where the explosion misclassification probability

$$\left( \int_{d_2^S}^{\infty} p(d|X) \right)$$

equals the earthquake misclassification probability

$$\left( \int_{-\infty}^{d_2^S} p(d|Q) \right); \quad (18b)$$

$d_3^S$  = the expected value,  $\mu_X$ , of the explosion population; (18c)

$d_4^S$  = the expected value,  $\mu_Q$ , of the earthquake population; (18d)

$$d_5^S = (d_3^S + d_4^S)/2. \quad (18e)$$

These quantities will be used in the left side of Equation (17b).

Define  $d_i^R$  ( $i = 1, 5$ ) for the real data in a similar manner. Letting  $DB_i$  denote a discriminant bias, then the possible definitions are:

$$DB_1 = d_1^R - d_1^S \quad (19a)$$

(This is the definition illustrated in Figure 29.)

$$DB_2 = d_2^R - d_2^S \quad (19b)$$

$$DB_3 = d_3^R - d_3^S \quad (19c)$$

(This is the definition used in Section 3.3)

$$DB_4 = d_4^R - d_4^S \quad (19d)$$

$$DB_5 = d_5^R - d_5^S. \quad (19e)$$

For any of these definitions, it then follows from Equation (17a) that

$$\begin{aligned} DB &= d^R - d^S \\ &= -1.36a \cdot (ft_p^* - t_e^*) . \end{aligned} \quad (20)$$

Solving Equation (20), we get

$$t_p^* = t_e^* \left( \frac{a \cdot I}{a \cdot f} \right) - \frac{DB}{1.36(a \cdot f)} \quad (21)$$

where

$$a \cdot I = \sum a_i \quad (22a)$$

$$a \cdot f = \sum a_i f_i \quad (22b)$$

are related to the mean and the first moment, respectively, of the deterministic weight coefficients. The expressions given in Equations 22 are defined over the whole frequency range, or any subrange. Evaluating the expressions with the deterministic weights (Appendix A) for two frequency ranges (each is used subsequently) gives

$$\left. \begin{array}{l} a \cdot I = -0.1748 \\ a \cdot f = -1.425 \end{array} \right\} \quad 0.4 \leq f \leq 3.0 \quad (23a)$$

and

$$\left. \begin{array}{l} a \cdot I = -0.828 \\ a \cdot f = -3.92 \end{array} \right\} \quad 0.4 \leq f \leq 5.0 . \quad (23b)$$

As one further refinement, suppose the discrimination constant,  $\log_{10} D$ , is in error by amount  $\delta$ , and suppose there was a first approximation to the path attenuation  $t_{po}^*$  (since evaluation of  $t_p^*$  is affected by choice of  $t_{po}^*$ , this method

requires iterative application), then we get

$$t_p^* = t_{po}^* + \left( \frac{\delta}{1.36} \right) \left( \frac{a}{a \cdot f} \right) - \frac{\delta DB}{1.36(a \cdot f)} . \quad (24)$$

A feeling for the potential resolution of this method for estimating  $t^*$  is formed from consideration of Figure 27. Reading the jackknife discriminant scale at the bottom that the expected values  $u_X$  and  $u_Q$  are separated by about one unit. If we let this be a measure of the uncertainty in the discriminant bias,  $\delta DB$ , then a first variation of Equation (24) yields

$$\delta t_p^* = - \frac{\delta DB}{1.36(a \cdot f)} . \quad (25)$$

Using the first moment of the deterministic weights given in Equation (23), it follows that

$$\delta t_p^* \sim \begin{cases} 0.5 & 0.4 < f < 3.0 \\ 0.2 & 0.4 < f < 5.0 \end{cases} . \quad (26)$$

With a reasonable selection of data it should be possible to do much better than this, particularly if data of both classes are available.

### 3.2.4 Classification of Isolated Events

Suppose body wave spectra are available for an event (?) which is located in a region from which there are no training data. Suppose we are unwilling to fix for certain the attenuation terms  $t^*$  for paths from (?) to the several stations. The situation is bleak, but not hopeless, for it is still possible to make quantitative statements about the likelihood (?) is an explosion or an earthquake. This is done by using synthetic data, and constructing a hypothesis test on  $t_p^*$ .

First, using any additional geophysical information such as source location and depth, tectonic regime, surface wave radiation patterns, etc., synthetic spectra for a collection of sources of

patterns, etc., synthetic spectra for a collection of sources of each type are calculated. These synthetic spectra are used to train the discrimination algorithm, producing coefficients  $\{a, b\}$  which are particularized for the source region. A jackknife procedure is used to get distribution functions for  $d^*$  for each source type. These will look much like Figure 27. The deterministic weights are used to classify each spectrum yielding a set of real data discriminants  $d^R(\cdot)$ . Not knowing whether  $(\cdot)$  is an earthquake or an explosion, the bias term cannot be removed, but we can get a statistical estimate of the bias, conditioned on whether  $(\cdot = X)$ , or  $(\cdot = Q)$ , by using the jackknife results obtained on the synthetics. Thus, for each observation, either

$$DB(\cdot = X) = d^R - d^*(X) \quad (27a)$$

or

$$DB(\cdot = Q) = d^R - d^*(Q) \quad (27b)$$

since the  $d^*$  are random variables and so are the  $DB$ . Equations (27) map the discriminant bias random variable onto a  $t_p^*$  random variable. Either

$$t_p^*(\cdot = X) = t_e^* \left( \frac{a + I}{a \cdot f} \right) - \frac{DB(\cdot = X)}{1.36(a \cdot f)} \quad (28a)$$

or

$$t_p^*(\cdot = Q) = t_e^* \left( \frac{a + I}{a \cdot f} \right) - \frac{DB(\cdot = Q)}{1.36(a \cdot f)} \quad (28b)$$

applies.

Deciding whether  $(\cdot = X)$  or  $(\cdot = Q)$  has now been transformed into deciding whether  $t_p^*(\cdot = X)$  or  $t_p^*(\cdot = Q)$  is most likely. One or the other, but not both are possible, and, clearly, the more paths that are available, the more rigorous the test.

$0 < t_p^* < 1.5$  is a constraint consistent with almost all present data. Other prior information, such as  $\text{AVG}(t_p^*) = 0.5$ ,  $\text{VAR}(t_p^*) = 0.04$  can be used in a goodness of fit test. The same geophysical data used to restrict the range of source models might be used to restrict the limit on  $t_p^*$  or to tailor its mean and variance. One example of this would be the correlation between attenuation and wave velocity used by Marshall, et al. (1979). As attenuation studies mature, we can anticipate soon the partitioning of  $t_p^*$  into a source term and a receiver term (Der, et al., 1982b). If receiver terms are known for all stations recording ( ), then Equation (28) can be corrected for them, yielding equations reflecting just the source attenuation estimate for each seismic recording.

Thus, by rephrasing the problem of discrimination based upon teleseismic body waves into a source modeling, and  $t^*$  problem, it is possible to bring into consideration a variety of ancillary geophysical data.

### 3.3 APPLICATION OF DETERMINISTIC DISCRIMINATION TO SELECTED AI DATA

Deterministic discrimination has been applied to the majority of the VFM spectra calculated by Savino, et al. (1980) during the Area of Interest (AI) experiment. To apply the method to these data, the spectra were taken exactly as archived: no new seismic calculations were made. Subsequent study of the AI experiment has raised certain questions regarding data quality and analysis methodology, but these we have not accounted for. Errors in the data are being corrected and the data are being placed on-line. The availability of on-line data will ultimately allow automatic processing of scores of events per day.

The major reason for discussing these results here is that they illustrate the range of explosion/earthquake separation that occurs when deterministic discrimination is used in practice. The results range from excellent to poor. In some cases (such as for CHT0) better results are obtained in subsequent analysis (see

Section 3.4) which suggests that the problems in the older measurements are indeed severe. In other cases (such as for BFAK), the cause of the imprecision of deterministic discrimination is unclear.

For all the results presented here, the discriminant function has spanned the full frequency range used in the theoretical study, 0.4 hertz to 5.0 hertz. This is now known not to be optimum for those paths where  $t_p^*$  exceeds approximately 0.4. Also we have not performed the iterative improvement required for best  $t_p^*$  calculation.

### 3.3.1 Station KAAO

For Kabul, ten explosion spectrums and 19 earthquake spectrums were used. This collection corresponds to those events lying in the restricted distance range  $15.0 < \Delta < 24.0$  for which Savino, et al. (1980) obtained good separation of the populations using the bivariate ( $m_b(\text{high}):m_b(\text{low})$ ) analysis. Equally satisfactory results are obtained when the method of deterministic discrimination is used: the two populations completely separate, i.e.,  $\{d_X^R\}$  and  $\{d_Q^R\}$  are disjoint sets. Now, however, we can carry the analysis a step farther, turning the discriminant bias into a  $t^*$ .

The VFM (bivariate) method of seismic discrimination, as originally developed, contained two empirical factors, the pair of fiducial frequencies and the equation of the curve separating the two event populations. The first subjective factor was fixed by scanning scatter plots for a range of frequency pairs and selecting that pair which jointly minimized the within-group scatter and maximized the between-group scatter. The second factor, specification of the curve separating the populations, was never actually reduced to an algebraic equation, but decisions were made with reference to an imaginary straight line.

The deterministic extension of VFM discrimination eliminates the first factor (all frequencies are used), and simplifies the second factor. The Fisher discriminant, by projecting the data onto

a one-dimensional subspace ( $d$ ), rather than a two-dimensional subspace ( $m_b(\text{high}):m_b(\text{low})$ ), causes the dimensionality of the separation surface to be reduced from one to zero. Moreover, distance perpendicular to the (point) separation surface has been directly related to a physical quantity,  $t^*$ .

Using the second definition of the discrimination bias (the reference point for each end of the line in Figure 29 is equal misclassification probability) and subtracting it from  $\{d^R\}$ , gives the results shown in Figure 30. Turning the discriminant bias into an attenuation ( $t_e^*$  assumed to be 1.0) gives a  $t_p^*$  of 0.40. This represents an average over all paths represented in the data set.

Comparing the Kabul explosion data with the theoretical explosion data (Figure 27), it is seen that the two population means are nearly identical (-0.4 vs -0.5, respectively) as are the spreads. The near equality between explosion means shows that the  $t^*$  resulting from a match between an average theoretical explosion and an average observed explosion (definition  $DB_3$ ) is nearly the same as that obtained using  $DB_2$  (equal misclassification probabilities for both types of data). By Equations (23a) and (23b),  $DB_3$  yields an attenuation of 0.42.

It is somewhat surprising that the spread of the synthetic explosion data matches so well the spread of the observed explosion data. This is probably fortuitous for the synthetic explosions sampled both a larger yield range and a larger material properties range than likely occurs for the real data. Further understanding requires examination of both results on a case-by-case basis.

Next consider the earthquake data. The assumption that  $t_p^* = 0.40$  shifts the center of the observed earthquake population to a value  $\mu_Q = 0.85$ . For the theoretical earthquakes  $\mu_Q = 0.50$ , and the difference is negated by assuming  $t_p^* = 0.46$  for the explosion data. Both this result and the offset of the explosion means indicates the calculated value of 0.40 using definition  $DB_2$  is a little low, but the difference is less than the error to be assigned to the observation.

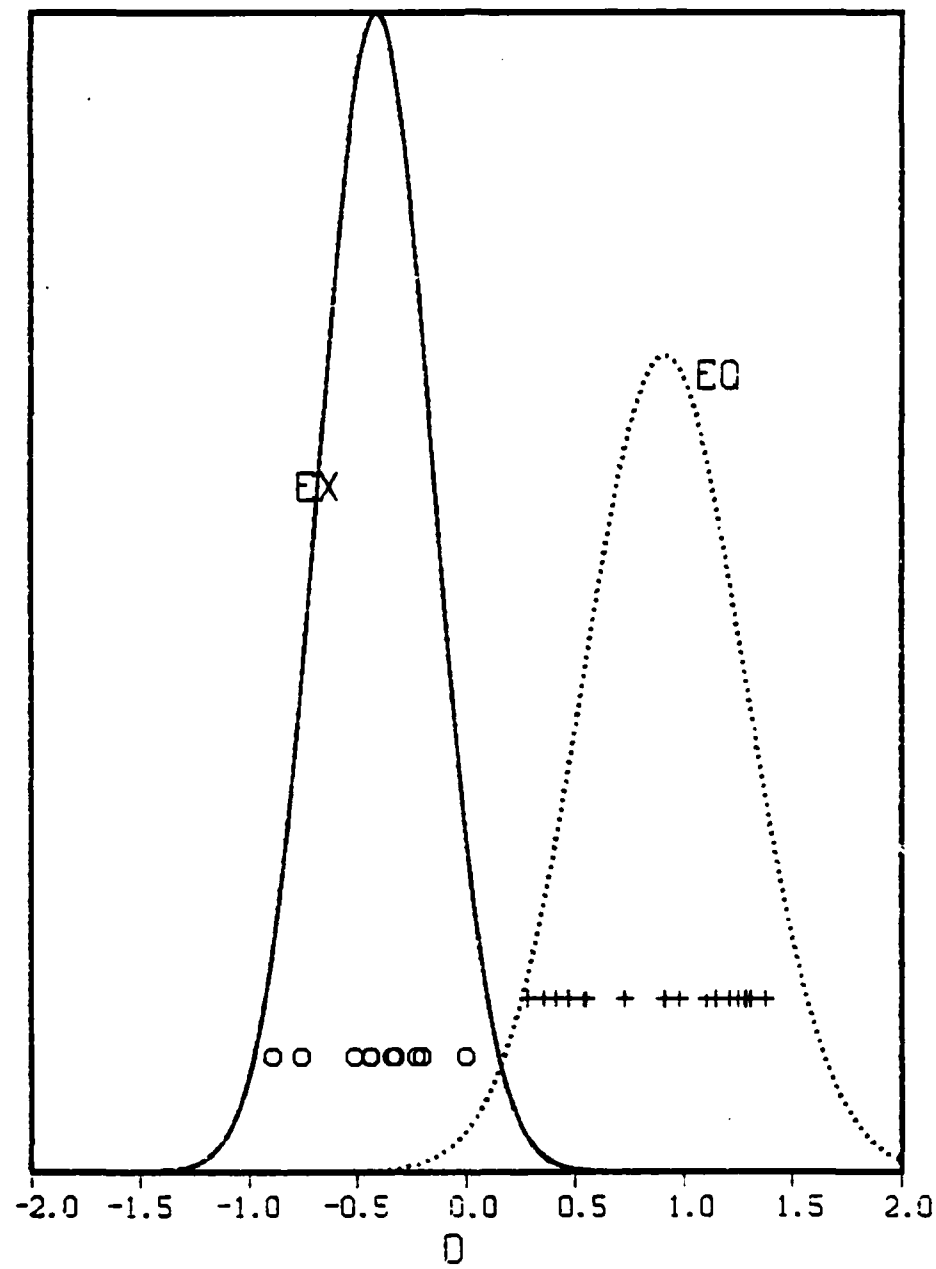


Figure 30. Synthetic weights applied to KAAO spectra effectively separate the two event types. The discriminant bias is equivalent to an attenuation parameter  $t^* = 0.40$ .

The most interesting calculation to be made is to test the hypothesis that the difference  $\mu_Q - \mu_X$  in Figure 30 is entirely due to path differences. It has been suggested that this is a fatal weakness in VFM discrimination since real earthquakes and real explosions are seldom colocated. To cause the earthquake distribution to cover the explosion distribution in Figure 30 requires a shift to the left of 1.4, corresponding to a  $\delta t_p^* = 0.26$ . Thus, supporting the hypothesis that the explosion/earthquake separation is entirely a consequence of differential attenuation requires believing  $t_p^* = 0.40$  for the explosions and  $t_p^* = 0.66$  for the earthquakes. But the inferred earthquake  $t_p^*$  is a conservative lower bound, for attenuation as large as this causes the spectrum to fall below ambient earth noise well below 5.0 hertz. This has the effect of biasing  $t_p^*$  downwards. This effect is accentuated for these data which have a preponderance of small magnitude earthquakes. For this study we have not tested deterministic discrimination for different frequency bands, but from later calculations we estimate the bias might be as large as  $\delta t^* = 0.15$ , pushing the required earthquake attenuation in the region of  $t_p^* = 0.80$ .

Global studies of body wave attenuation do show extremes in  $t^*$  greater than the limits (0.40 to 0.80) required of the hypothesis that earthquakes separate from explosions in these data because of differential attenuation. But analysis of these events for other paths is required before a definite statement can be made. The results in Rivers, et al. (1980) indicate a much smaller differential  $t_p^*$ .

### 3.3.2 Station CHTO

Deterministic discrimination applied to archive VFM spectra for the Thailand station CHTO yields the results plotted in Figure 31. Using criterion  $DB_2$  (equal percentages of misclassified events) gives the estimate  $t_p^* = 0.45$ . Three out of 11 explosions and two out of 20 earthquakes are missed if  $d = 0$  is

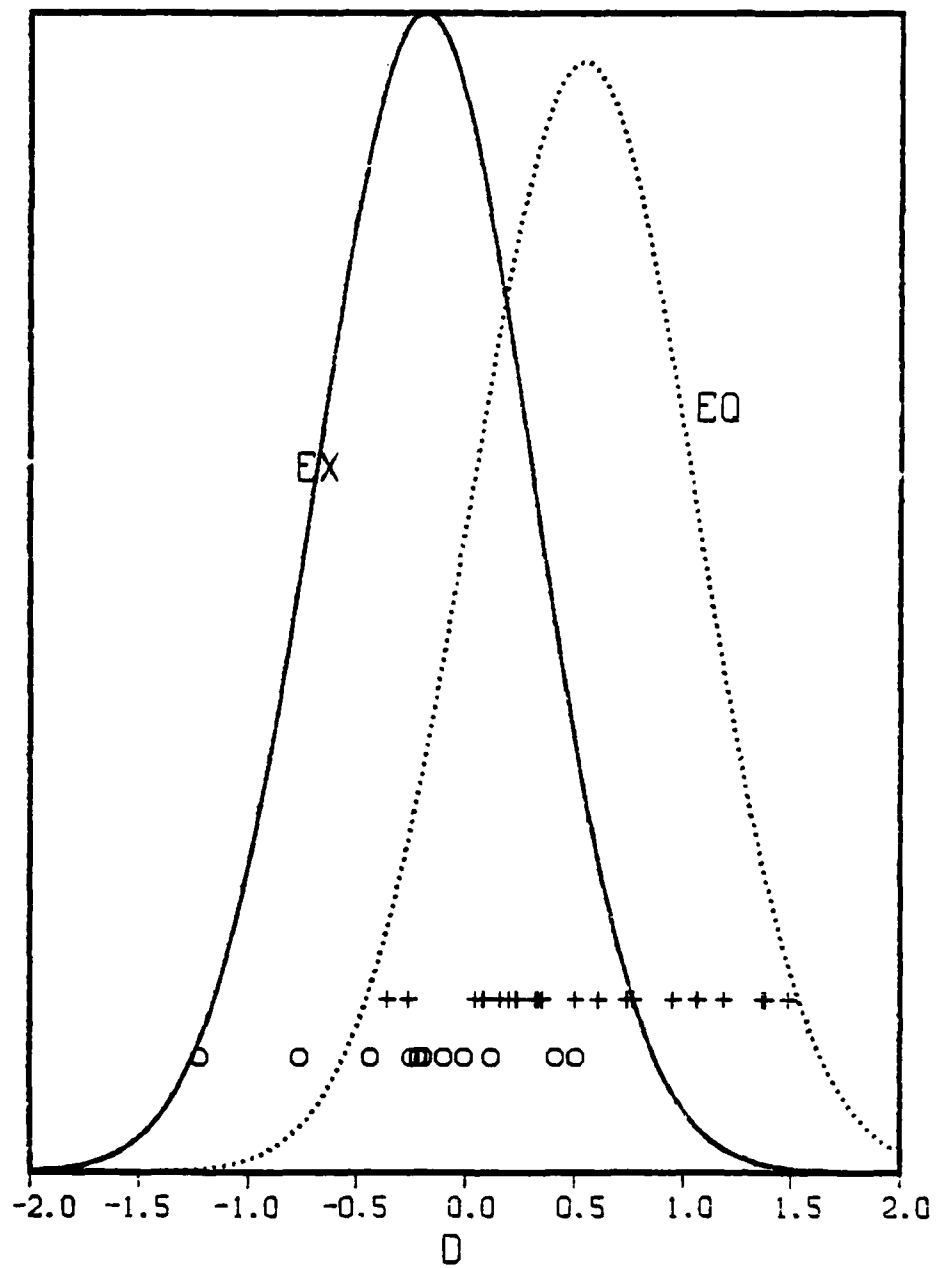


**Figure 31.** Synthetic weights applied to CHT0 spectra give five misclassified events and  $t^* = 0.45$ .

taken as the decision point. The population means are separated by  $\delta d = 0.8$  ( $\delta t^* = 0.15$ ). The spreads are significantly larger than the spreads found for either the synthetic data or the Kabul data. For the explosions, a few prominent outliers are visible. Subsequent analysis of a much larger explosion data set (see Section 3.4) gives smaller scatter, suggesting some of these data are faulty. This may also be the cause for the larger scatter in the earthquake data. To test this supposition would require case-by-case consideration of these data, an examination most effectively performed interactively.

It should also be noted that the inferred value of  $t_p^*$ , 0.45, is considerably greater than a later estimate (among results presented in Section 3.4, is the value  $t_p = .25$  for CHTO), independent indication there are problems in the data.

It is concluded that deterministic discrimination for station CHTO is less than perfect; five events out of 30 are misclassified. Several considerations, however, point to problems in the data, and re-analysis would probably give more dramatic results.

### 3.3.3 Station RKON

Red Lake, Ontario, is an observatory on the Canadian Shield well liked by seismologists because of its high Q and impulse-like crustal transferfunction. Deterministic discrimination produces the results shown in Figure 32. One clear explosion outlier and one possible earthquake outlier are the only misclassified events out of a set containing six explosions and 38 earthquakes. Bias measure  $DB_2$  produces an average path attenuation  $t_p^* = 0.33$ . Requiring the five clustered explosion points to be centered near  $-0.5$ , (the mean of the synthetic explosion data) changes  $t_p^*$  to 0.37. Centering the earthquake population over the explosion population requires a shift in  $d$  of 1.4, equivalent to requiring that the average explosion path has an attenuation constant  $t_p^*$  at least as large as 0.63. The bias in this estimate caused by including the entire 0.4 to 5.0 hertz band is perhaps 0.15, as

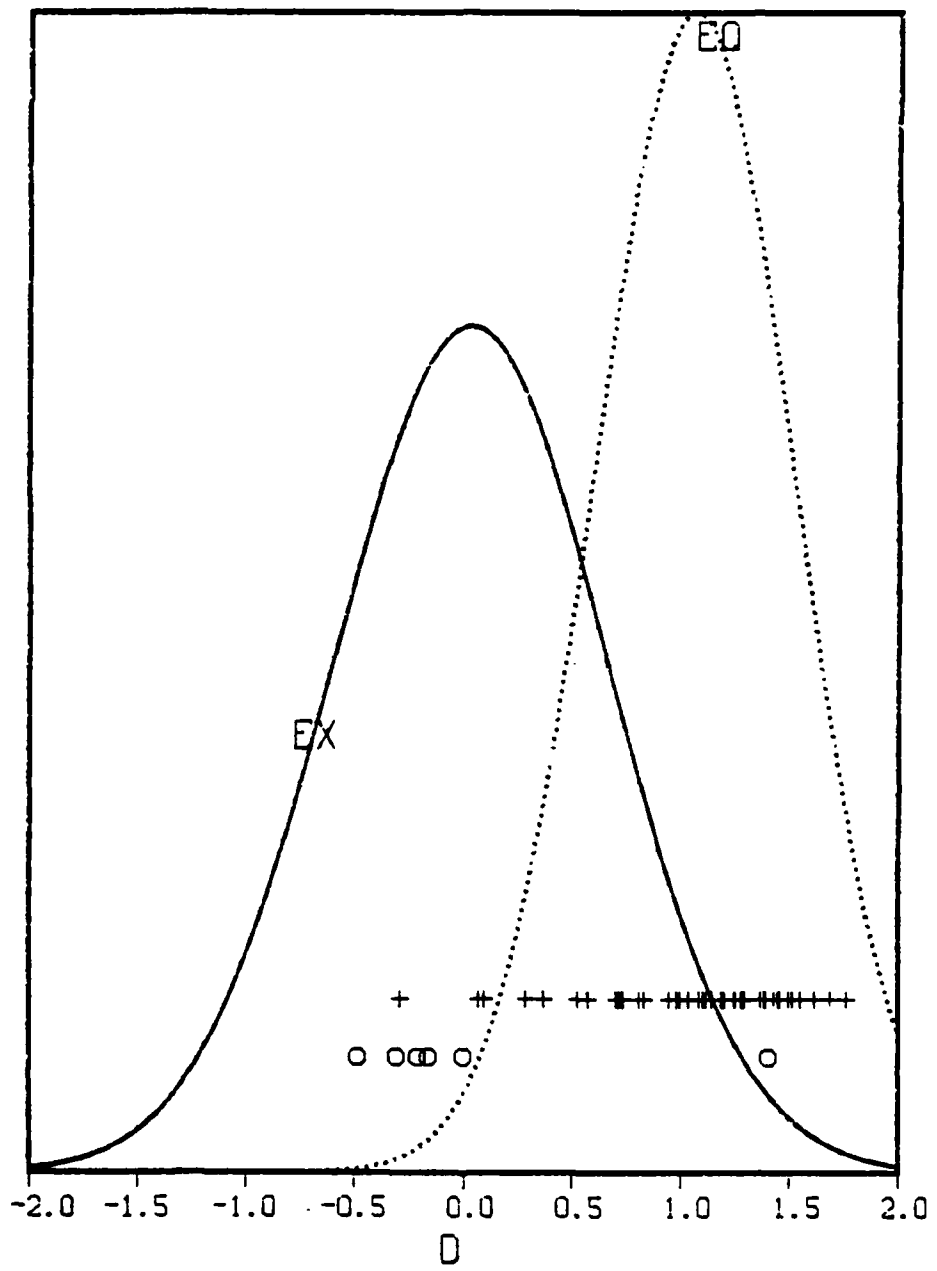


Figure 32. Synthetic weights applied to RKON spectra produce two misclassified events, but the missed explosion is clearly anomalous. The parameter  $t^* = 0.33$ .

discussed above. Such a large differential attenuation is believed unlikely, and, as before, we conclude that deterministic discrimination is an effective means of distinguishing earthquakes from explosions at this station.

### 3.3.4 Station BFAK

The Alaskan station BFAK yielded the poorest results (Figure 33) of the four considered here but some of its neighbors (see Section 3.3.5 and Appendix B) do better. The scatter in the explosion data is particularly pronounced and contrasts sharply with the close agreement between the synthetic data and the three previous examples of real recordings of explosions.

One obvious difficulty in analyzing these data is selecting the appropriate definition of the discriminant bias. Choosing  $DB_4$ , forcing equality between synthetic earthquake mean and real earthquake mean, produces an attenuation,  $t_p^*$ , of 0.58. This clearly means that signals are falling below the noise at the higher frequencies so that not much credence can be placed in these results.

### 3.3.5 Other Stations

Deterministic discrimination works well, often extraordinarily well. This is remarkable because the method, as presently developed, has no adjustable parameters. Results from twelve additional stations from the AI experiment are shown in Appendix B to substantiate this assertion. Not having settled upon a particular method for forming network average classification, we are unable at present to present a consensus answer for each event. Furthermore, network averaging requires regionalized  $t^*$  information for best results (see, for instance, Der, et al., 1982b, and Section 3.4 of this report). More careful selection of analysis bandwidth and, perhaps, better spectrum scaling rules are required as well. Also of great utility would be an interactive way of looking at the data so as to focus quickly on the problem events which should receive special scrutiny.

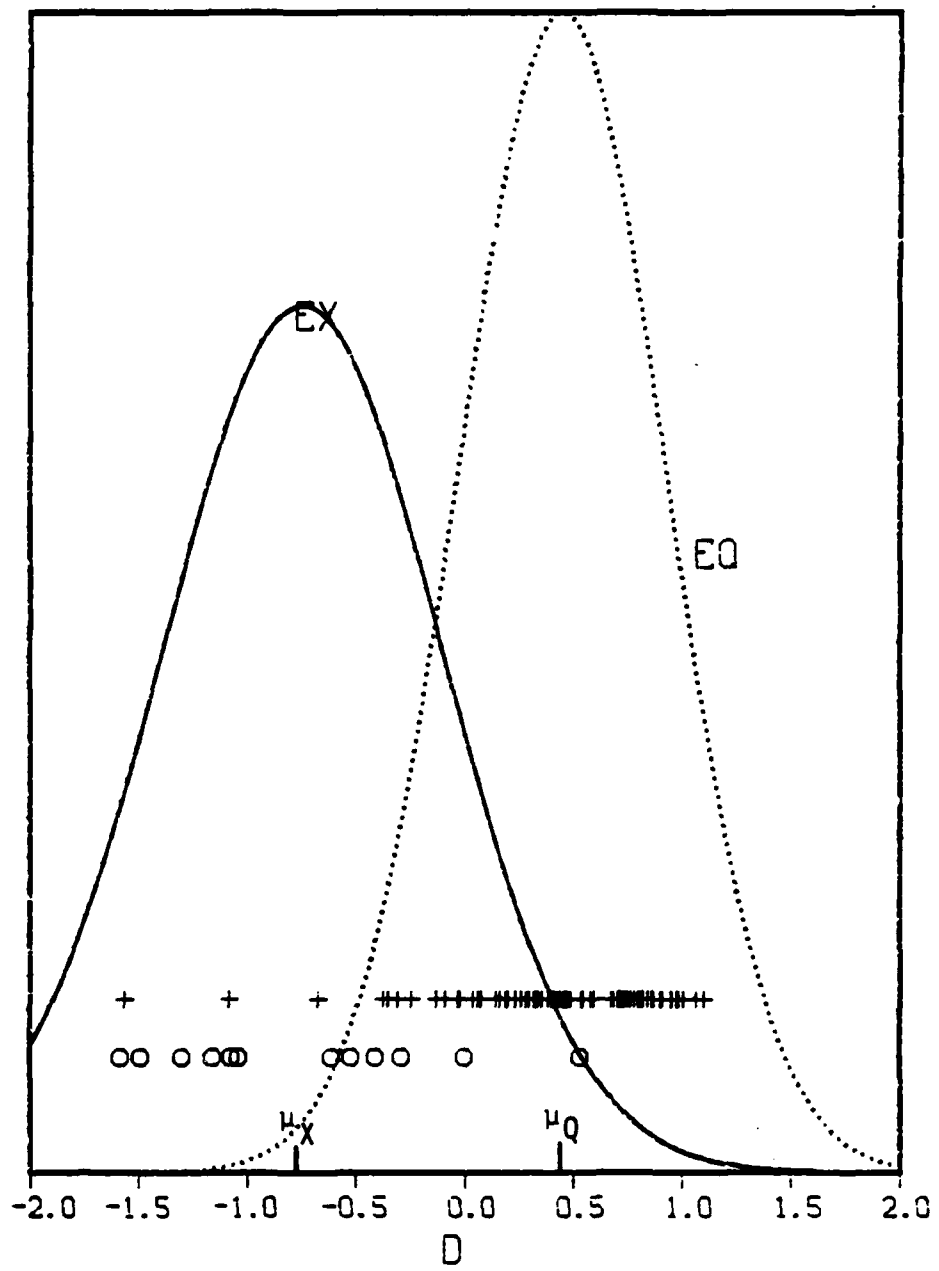


Figure 33. Synthetic weights applied to BFAK spectra give one misclassified explosion and numerous misclassified earthquakes. The large value of the attenuation parameter ( $t^* = 0.58$ ) is evidence that too large a frequency band was utilized. Earth noise at the higher frequencies may account for the relatively large spread in these data.

For each station represented in the set of figures contained in Appendix B, a provisional  $t_p^*$  estimate is given based on the discriminant bias. All data for a given station are plotted with the bias removed. Removing a fixed bias, of course, does not affect the separation between the earthquake and explosion populations. The  $t_p^*$  results have not been assembled into a table because the excessive analysis bandwidth and absence of event selection (deletion of deep events, grouping by source regions) makes them of unverified accuracy. (Neither objection applies to the quantitative results given in Section 3.4.) The important relation to remember is  $\delta t^* = 0.19 \delta d$ , which aids interpretation of the plots shown in the Appendix.

Three SRO stations, ANMO ( $t_p^* = 0.57$ ), CTAO ( $t_p^* = 0.53$ ), and ZOBO ( $t_p^* = 0.45$ ) yielded deterministic discriminants (unbiased) as shown in Figures B-1, B-2, and B-3. These stations are all greater than 90 degrees from Eastern Kazakh, the source of the majority of the explosions; so it is not surprising that the method is unsuccessful. Best results are obtained for CTAO, for if the deep focus earthquake at  $d = -0.6$  is ignored (Event 169), just two explosions (21 and 266) overlap the earthquake population. We note, however, the separation ( $\mu_Q - \mu_X$ ) is 0.5, only half the separation between the means of the theoretical data.

Station HNME (Figure B-4,  $t_p^* = 0.51$ ) shows eight anomalous earthquakes (72, 74, 24, 23, 28, 7, 9, 32), a well-clustered earthquake remainder, and a diffuse spread in the explosion discriminants. Again, the means of the trimmed populations have separation ( $\mu_Q - \mu_X$ )  $\approx 0.5$ .

A succession of Alaskan stations:

1. ATTU,  $t_p^* = 0.29$
2. UCAK,  $t_p^* = 0.51$
3. NJAK,  $t_p^* = 0.52$
4. TNAK,  $t_p^* = 0.55$
5. CNAK,  $t_p^* = 0.49$

are shown in Figures B-5 through B-9. ATTU (B-5) looks dismal, but the others are not as bad as they seem at first glance. Earthquakes 29 and 156 (negative  $d$ ) as well as explosions 273 and 269 (positive  $d$ ) are always grouped in the wrong class for these five stations as they were for BFAK. Ignoring those four events, CNAK (B-6) exhibits no errors although the diffuseness of the explosion population suggests two distinct groupings. NJAK (B-7) is similar in appearance, but a few events (in addition to the four mentioned above) are wrongly situated. Again, earthquakes are bunched, explosions more spread out. For TNAK (B-8) and UCAK (B-9), the earthquake cluster is somewhat broader than it is for CNAK and NJAK, and the number of missed events correspondingly greater.

Three array sites KSRS (B-10,  $t_p^* = 0.53$ ), Norsar (Figure B-11,  $t_p^* = 0.42$ ) and LASA (Figure B-12,  $t_p^* = 0.52$ ) complete the appendix figures. Norsar performs well although the population spreads are larger here than they were for the synthetic results. Explosion 79 ( $d = 1.0$ ), and earthquakes 73 and 159 ( $d \sim -0.7$ ) fail to cluster. There is some overlap of the two populations near  $d = -0.2$ , but the two means are clearly separated.

The results shown in the appendix, in conjunction with the four stations discussed more extensively above, show that at many sites around the world deterministic discrimination separates most earthquake spectra from most explosion spectra. Population variances often exceed the variances in the theoretical spectra, possibly due to the effect of difference in attenuation along the several paths.

If the average attenuation over the paths from all earthquakes to all stations exceeds the average attenuation over the paths from all explosions to all stations by about  $\delta t^* = 0.15$  ( $\delta d^* = 0.75$ ), then deterministic discrimination without an attenuation correction is less reliable. In view of the fact that fully half the explosions were off the Eastern Kazakh test site, this possibility seems unlikely. Clearly, however, the more precise the knowledge of attenuation, the more confidence can be placed on this technique of discrimination.

### 3.3.6 Conclusions

This discussion has highlighted significant advances in the theory and application of seismic discrimination using spectra of seismic body waves. Following on from Stevens and Day (1982), it has been established that an algorithm trained to recognize the differences between synthetic earthquake spectra and synthetic explosion spectra, with no modification, is effective at recognizing the differences between real earthquake spectra and real explosion spectra. This has never been accomplished before, and the key ingredient was the recent development of dynamic models of the earthquake rupture process (Day, 1982a; 1982b). Further work on earthquake modeling is clearly warranted.

The only connection between the learning phase of the algorithm (distinguishing synthetic spectra) and the application phase of the algorithm (distinguishing real spectra) was through a set of spectral weights (the vector  $a$ ) and a rule for spectral scaling (the  $f^{-2}$  model,  $D = 5.6$ ). The weights and scaling law are firmly rooted in the physics of seismic sources and are of universal applicability.

It has been shown that the excess decay of the spectral amplitudes caused by attenuation (a mixture of absorption and scattering) biases the deterministic discriminant. The bias has been interpreted as an attenuation coefficient  $t^*$ , and geophysically plausible results are obtained. Data have been presented which suggest, earlier claims notwithstanding, that differential attenuation does not account for the success of the VFM discriminant.

Deterministic discrimination has been shown effective under the most restrictive of conditions, single station analysis. Application of techniques for combining many single-station results into a network average can only improve the method. This should however be coupled with a network estimation of corner frequency.

Since attenuation so quickly drops signals below noise, an automatic way of truncating the weighted sum ( $a.m_b$ ) should be

developed. This is a particular instance of the more general problem of applying signal/noise weighting to  $(a.m_b)$ , and from the standard error in  $m_b(f)$  at each frequency calculating an unbiased value of the expected value of  $d^R$  and its standard error.

The availability of the universal weights leads to a partial solution of a long standing problem in seismic discrimination: classifying a single body wave recording of an event so small that surface waves are not seen. The classification of such a spectrum can be rephrased into a probability conditioned on  $t^*$ ,  $p(\cdot = X/t^*)$  and  $p(\cdot = Q/t^*)$ . Refined global models of  $Q$  in the crust and upper mantle are producing regionalized estimates of  $t^*$  of constantly improved refinement. These will ineluctably sharpen the method, even if only a general estimate of source location is known. A goal of seismic data analysis should be to tag each Flinn-Engdahl seismic region with a  $t^*$ .

### 3.4 ESTIMATING $t^*$ FROM SRO RECORDINGS OF EXPLOSIONS

Deterministic discrimination has been applied to a collection of SRO explosion recordings, part of a large data set being assembled to study improved methods of yield determination. Discrimination is a misnomer for this portion of the study since only one class of event was processed. It is more properly viewed as a clustering test of the method, for one purpose was to see how effective the deterministic weights were at transforming multidimensional data (VFM spectrums) into compact sets of numbers (discriminants  $d$ ). A second purpose was to estimate the discriminant bias and, from it, infer attenuation parameters  $t_p^*$  on a station-by-station basis for each of the two source regions, NTS and Kazakh. A further purpose was to test the automatic feature selection part of the program (see the upper half of Figure 22) for the analyses discussed in Section 3.3 which were based on archive feature vectors and involved no seismogram processing.

The results are satisfying. Nearly 500 seismograms were analyzed in a few weeks. Deterministic weights are effective at

grouping the majority of the data. Attenuation parameters,  $t^*$ , are found to agree well with other measurements on these data, using entirely different analysis methods.

Some of the cautions mentioned earlier must be remembered. Only the  $f^{-2}$  spectral model, in the form given by Equation (2) has been used to scale the data. The corner frequency and attenuation parameters interact nonlinearly, and we have not ameliorated this coupling by iteration. Since the corner frequency is a property of the seismic source, it should be estimated from all available recordings of each event jointly rather than on an individual basis for each record. Experience gained in this work has indicated how many of these questions might be automated with an improved processing method.

### 3.4.1 Data Set

The data set included 38 explosions on the Kazakh test site and 25 at NTS. The NTS magnitudes for these events range from  $5.2 \leq m_b \leq 6.2$ , and pertinent information is given in Tables 3 and 4. This is an important and much-studied data set, one of the most homogeneous assemblages of digital explosion seismograms yet put together. It is particularly suited to attenuation studies because, in addition to the presumed source simplicity, the uniform well-calibrated instrumentation makes correction to earth motion reliable.

Certain deficiencies should be noted, however. The SRO stations are poorly disposed for recording NTS explosions, but that is partly a consequence of the Pacific Ocean occupying half the interesting surface area. Particularly important stations are KONO and GRFO in Europe and MAJO in Japan, for they pick up both NTS and Kazakh. Data from these three stations should be extremely valuable for differential source studies. It is unfortunate that GRFO appears to lie over a more attenuative mantle than normal, and additional high latitude stations would be useful.

The SRO short-period channel records only vertical component motion. Furthermore, the data is saved only if the signal is strong

Table 3  
EVENT INFORMATION FOR KAZAKH EXPLOSIONS

Code	Date	$m_b$	Remarks
SM1	6/11/78	5.9	
SM2	7/5	5.8	
SM3	8/29	4.9/5.9	Double event
SM4	9/15	6.0	
SM5	11/4	5.6	
SM6	11/29	5.3/6.0	Double event
SM7	6/23/79	6.3	
SM8	7/7	5.8	
SM9	8/4	6.1	
SM10	8/18	6.1	
SM11	10/28	6.0	
SM12	12/2	6.0	
SM13	12/23	6.1	
SM14	9/14/80	6.2	
SM15	10/29/77	5.5/5.6	Same as SM27, double
SM16	3/26/78	5.5	
SM17	4/22	5.3	
SM18	7/28	5.7	
SM19	10/31	5.2	
SM20	5/31/79	5.2	
SM21	5/22/80	5.5	
SM22	7/31/80	5.3	
SM23	12/7/76	5.9	
SM24	5/29/77	5.6	
SM25	6/29/77	5.3	
SM26	9/5/77	5.9	
SM27	10/29/77	5.6	
SM28	11/30/77	5.9	

Table 3 (continued)  
EVENT INFORMATION FOR KAZAKH EXPLOSIONS

Code	Date	$m_b$	Remarks
SM29	2/1/79	5.4	
SM30	4/25/80	5.5	
SM31	6/12/80	5.6	
SM32	6/29/80	5.7	
SM33	10/12/80	5.9	
SM34	12/14/80	5.9	
SM35	12/27/80	5.9	
SM36	3/29/81	5.6	
SM37	4/22/81	5.9	
SM38	5/27/81	5.4	

Table 4  
EVENT INFORMATION FOR NTS EXPLOSIONS

Code	Date	$m_b$	Remarks
PM25	4/11/78	5.3	FONDUTTA
PM26	4/11/78	5.5	BACKBEACH
PM27	8/31/78	5.6	PANIR
PM28	12/16/78	5.5	FARM
PM29	6/11/79	5.5	PEPATO
PM30	9/26/79	5.6	SHEEPSHEAD
PM31	4/26/80	5.4	COLWICK
PM32	6/12/80	5.6	KASH
PM33	7/25/80	5.5	TAFI
PM34	6/6/81	5.5	HARZER
YC16	12/28/76	5.5	RUDDER
YC17	4/5/77	5.6	MARSILLY
YC18	4/27/77	5.4	BULKHEAD
YC19	5/25/77	5.3	CREWLINE
YC20	8/19/77	5.6	SCATLING
YC21	11/9/77	5.7	SANDREEF
YC22	12/14/77	5.7	FARALLONES
YC23	2/23/78	5.6	REBLOCHON
YC24	3/23/78	5.6	ICEBERG
YC25	7/12/78	5.5	LOWBALL
YC26	9/27/78	5.7	RUMMY
YC27	11/18/78	5.1	QUARGEL
YC28	2/8/79	5.5	QUINELLA
YC29	9/6/79	5.8	HEARTS
YC30	4/16/80	5.3	PYRAMID

enough to trigger an automatic detector. This exacerbates gaps in coverage due to maintenance and malfunction. Small magnitude events are under-represented, not only because they often do not trigger the recorder, but also because it has been the recent tendency to test in the intermediate yield range. Even so, these data cover only about a third of all underground shots since the SRO array was deployed starting in 1977.

To show the general data quality, Figure 34 presents a montage of several Kazakh shots with  $m_b \sim 5.5$ . They have been arranged in order of descending  $t^*$  (as derived from the analysis described later). The period lengthening, a consequence of the low pass attenuation filter, is apparent, but the normalized amplitude scale obscures the concomitant decrease in amplitude. SHIO and MAIO show the triplication between 20 degrees and 30 degrees. Most records are simple, but MAJO and TATO have pronounced cudas.

### 3.4.2 Feature Extraction

Data were provided in Lincoln Laboratories waveform data base format, a convenient arrangement which collects the data by event and uses the flexibility of hierarchical directories for organization. Body wave arrivals were picked interactively and automatically written to a marker file for each event. We are grateful to several Geotech analysts for doing this. Some events were repicked, but the review was far from exhaustive. We question a few percent of the time picks at most.

Spectra were calculated using bandpass filtering. This is the VFM analysis technique which has been extensively described (Savino, *et al.*, 1980; Farrell, *et al.*, 1981); it needs little reiteration here. Each seismogram is filtered through a comb of Gaussian filters, and the time domain envelope function found using the Hilbert transform method. Amplitudes and arrival times of envelope extrema are measured and corrected for instrument response. The ground motion amplitudes are converted to magnitudes by the usual relationship.

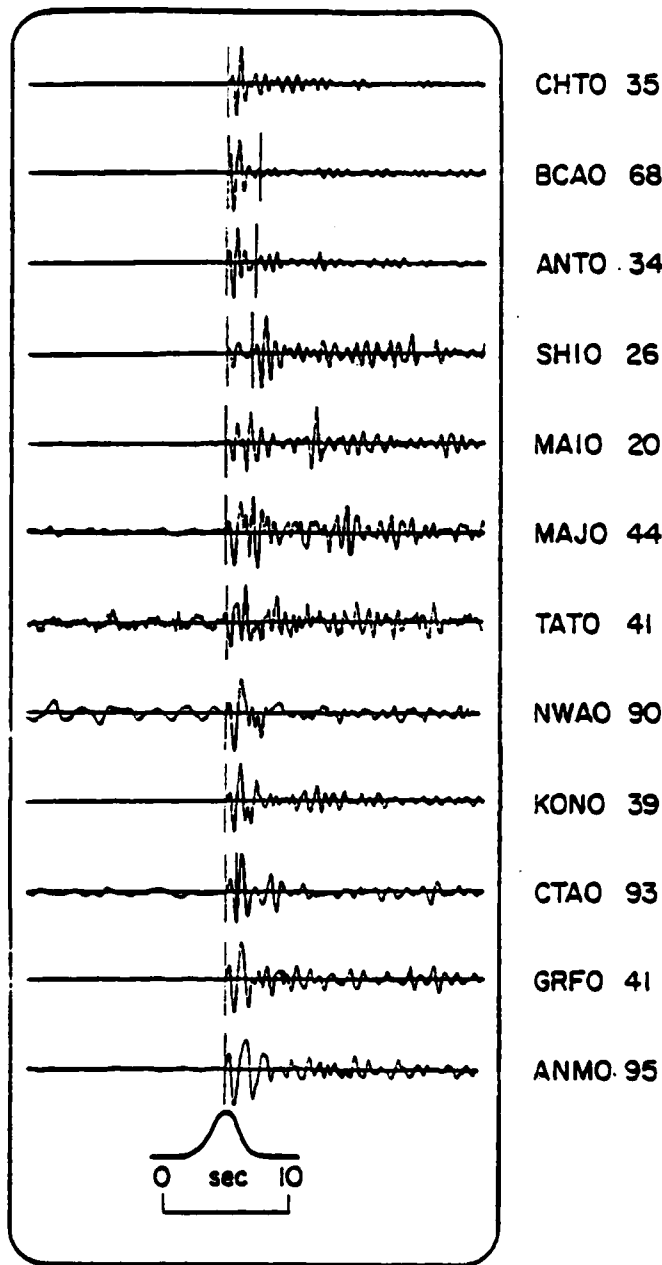


Figure 34. Typical SRO recordings of Kazakh explosions, arranged with smallest apparent  $t^*$  at the top.

$$m_b(f) = \log_{10}(fA(f)) + B(\Delta) \quad (29)$$

where  $f$  is frequency,  $A$  the earth displacement amplitude (nm), and  $B(\Delta)$  the Gutenberg distance correction. Constant bandwidth filters,  $Q = 12f$  were used giving a time resolution of approximately 2.4 seconds and a frequency resolution of approximately 0.13 hertz.

The principal advantage narrow band filtering has over the more usual Fourier analysis is that a finer trade-off between time resolution and frequency resolution is possible through the choice of filter bandwidth. There is no linear filter which gives a smaller  $\Delta t \Delta f$  product. Furthermore, it is not necessary to engage in window carpentry as is required by Fourier analysis. Ultimately one probably wants to tailor the filter comb for particular stations and particular source regions (paths), but this has not yet been done. Since the spectra drop so steeply over a short frequency interval, side lobe contamination is a serious concern. Gaussian filters, however, decay like  $\exp(-(f - f_c)^2)$ ; so the side lobes from a signal falling like  $\exp(-f)$  are at least asymptotically negligible. Other things being equal, side lobe contamination tends to elevate the spectral estimates at high frequencies. This has the effect of biasing  $t^*$  downwards.

Feature selection proceeded as an independent process. Once calculated, VFM spectra were saved for subsequent use.

The well recorded signals permitted a somewhat cavalier attitude towards noise; it was ignored. Obviously bad data were, of course, not used. Moreover, the exponential decay of the earth attenuation operator typically causes the spectral amplitude to plunge from well above earth noise to well below earth noise in a fraction of a hertz. Thus, simply truncating the spectra at a fixed high frequency (we chose 3.0 hertz and 5.0 hertz) achieves most of the objectives lying behind more elaborate testing.

### 3.4.3 $t^*$

A weighted integral of scaled spectra in the form

$$d = a m_b(f) + C \quad (30)$$

was calculated. Since we are pretending this was an assessment of deterministic discrimination, deterministic weights were taken (Section 3.1.3 and Appendix A). The quadratic source model was used for scaling, and the constant  $C$  was the discriminant bias term (Equations (17a) and (17b)). For stations (ANMO, CHT0, CTA0, KAA0), the specific values for  $t^*$  derived from the analysis discussed in Section 3.3 were used to calculate  $C$ . For the remaining SRO stations, an average of the four available station data was taken.

Figure 35 is typical of the results obtained. This figure plots the integral,  $d$ , vertically against event number horizontally. The dotted vertical lines separate the results for KAZAKH (SM1 in the left bin) from the results for Yucca Flats (YC) and Pahute Mesa (PM) PMS4 in the right bin). Thus, the horizontal ordering is simply by sequence number. The horizontal dash line would separate explosion-like from earthquake-like data if the correct value for  $t^*$  were used. This figure is thus exactly like Figure 27 except that it is flipped, turned sideways, and we have used the extra dimension to stretch out the individual data points. This makes it easy to associate the points with a particular seismogram.

Comparing again Figures 27 and 35, it can be seen that we have transferred from the former the zone covered by the numerical explosion models. The zone is centered at  $d = -0.5$ .

That the average of the Kazakh data points for station MAJ0 is more negative than the average of synthetic explosions (separation  $\Delta d$ ) is not evidence that these spectra are even richer in high frequencies than the numerical models. It means that the provisional correction for attenuation, the constant  $C$  in Equation (30), is incorrect. Equations (17) and (21) are combined to give

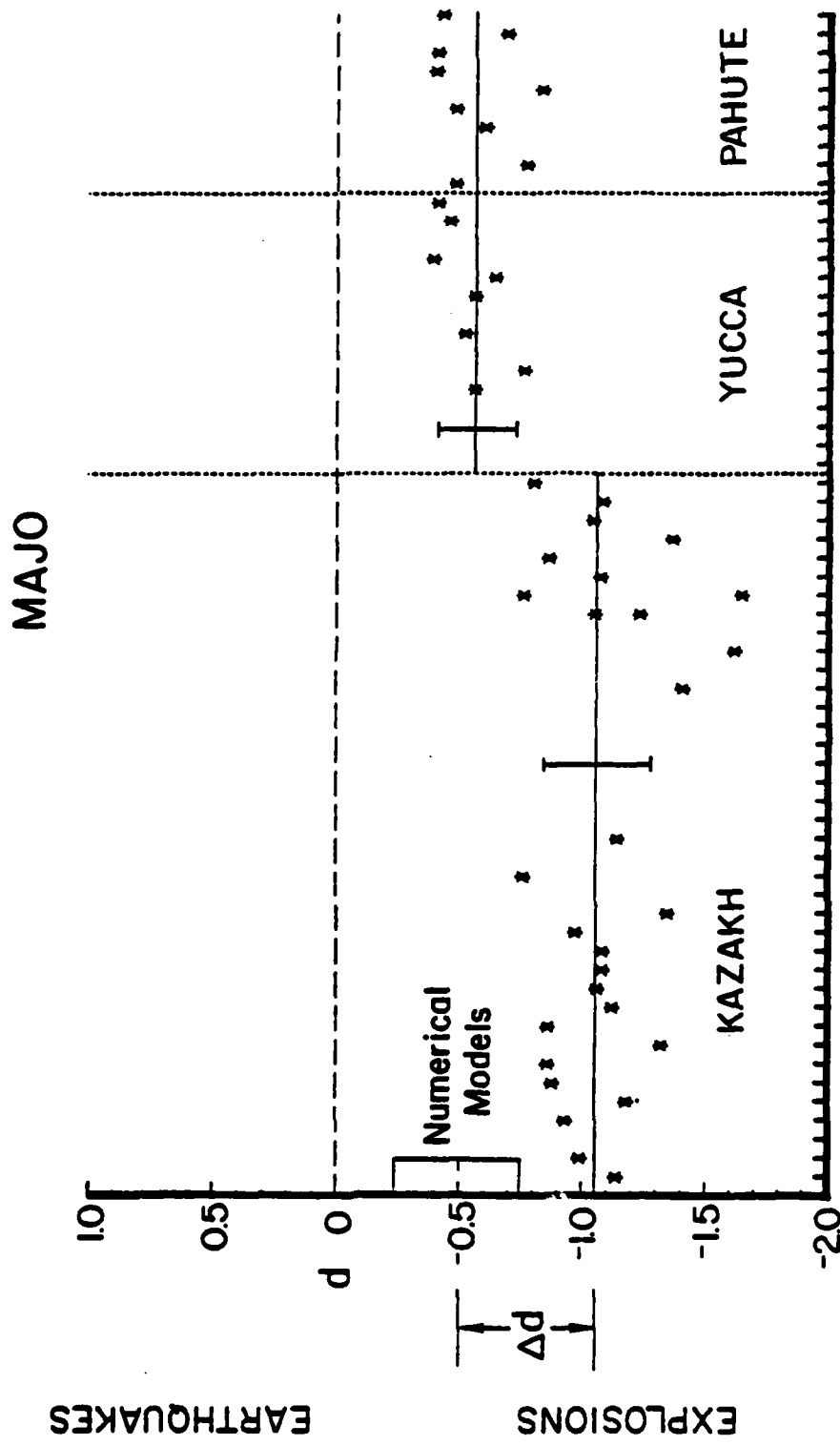


Figure 35. The spectral integral,  $d$ , for a suite of KAZAKH and NTS explosions differs from the values obtained for a collection of numerical explosions because of attenuation. The shift  $\Delta d$  required to make them align is directly proportional to  $t^*$ . In this example, a provisional value of  $t^*$  was assumed in calculating  $d$ . For the NTS data, it was nearly correct since  $\Delta d \approx 0$ . For the KAZAKH data, the provisional value overestimated the actual attenuation as shown by the fact that  $d$  for these data is less than  $-0.5$ .

the correct value for  $t^*$  (the value which reduces  $\Delta d$  to zero)

$$t^* = t_e^* \left( \frac{a \cdot I}{a \cdot f} \right) - \frac{C + d^R - d^S}{1.36(a \cdot f)} \quad (31)$$

where  $d^S = -0.5$  and  $d^R$ , in this case, is about -1.1. This figure makes obvious the well-known fact that seismic waves from NTS are more attenuated (larger  $t^*$ ) than seismic waves from Kazakh. Thus, for each station we make separate calculations for the two regions.

Analyzing all the results in this fashion (Appendix C shows plots for the remaining SRO stations) gives the numbers displayed in Table 5 (Kazakh explosions) and Table 6 (NTS explosions). In calculating the averages  $d^R$ , a small fraction of discordant results were ignored.

The culling and grouping has not been systematic, and it would be extremely valuable to present displays such as those shown in Figure 36 and Appendix C, using a different horizontal index such as event magnitude.

Attenuation causes high frequency energy to be missing in the spectrum. Beyond some high frequency cutoff, the spectra generally reach the level of the to earth noise. This noise enrichment biases the spectral integral negative, yielding an underestimate of  $t^*$ . To explore this effect, Equation (31) has been evaluated both for the full 0.4 to 5.0 hertz bandwidth, as well as a more restricted frequency range from 0.4 to 3.0 hertz. The figures shown here, and the results in the Tables, apply to the restricted interval. (It is probably not true that deterministic weights applied to synthetic spectra yield a mean value  $d^S$  of -0.5 when only the 3.0 hertz bandwidth is utilized. Thus, these results may be systematically biased.) A plot of  $t^*$  (0.4 - 5.0) against  $t^*$  (0.4 - 3.0) is shown in Figure 36. The tendency for the difference between the  $t^*$  produced by the two methods to increase with  $t^*$  is evidence of high frequency noise contamination, we believe.

Table 5  
t\* CALCULATION FOR KAZAKH EVENTS

STA	Δ	Events	C	$\mu$	$d_3^R$	$\sigma$	$\mu$	$t^*$	$\sigma$
ANMO	95	34	1.916	-1.104	0.11	0.80	0.06		
ANTO	34	19	1.478	-1.413	0.13	0.41	0.07		
BCAO	68	15	1.478	-1.552	0.12	0.34	0.06		
BOCO	121	3	1.478	-1.343	0.11	0.45	0.05		
CHTO	35	21	1.275	-1.556	0.12	0.24	0.06		
CTAO	93	25	1.720	-1.188	0.17	0.66	0.09		
GRFO	41	21	1.478	-0.762	0.19	0.75	0.10		
GUMO	64	3	1.478	-1.030	0.17	0.61	0.09		
KAAO	18	31	1.000	-0.646	0.12	0.56	0.06		
KONO	39	20	1.478	-1.023	0.30	0.62	0.16		
MAIO	20	10	1.478	-1.141	0.37	0.56	0.19		
MAJO	44	25	1.478	-1.045	0.18	0.60	0.09		
NWAO	90	19	1.478	-1.044	0.18	0.61	0.09		
SHIO	26	13	1.478	-1.398	0.15	0.42	0.08		
SNZO	123	1	1.478	-1.070		0.59			
TATO	41	5	1.478	-1.098	0.04	0.58	0.02		
ZOBO	137	21	1.478	-0.797	0.15	0.73	0.08		

Table 6  
t\* CALCULATION FOR NTS EVENTS

STA	$\Delta$	Events	C	$\mu$	$\sigma$	$\mu$	$\sigma$
				$d_3^R$	t*		
ANMO	8	20	1.916	-2.015	0.10	0.33	0.03
ANTO	98	3	1.478	-0.890	0.06	0.68	0.03
BCAO	121	5	1.478	-0.380	0.20	0.95	0.10
BOCO	50	12	1.478	-0.520	0.11	0.88	0.05
CHTO	115	6	1.275	-0.135	0.18	0.96	0.09
GRFO	81	9	1.478	-0.540	0.23	0.87	0.12
GUMO	89	2	1.478	-0.830	0.01	0.72	0.01
KONO	73	7	1.478	-0.544	0.20	0.86	0.10
MAJO	79	17	1.478	-0.552	0.14	0.86	0.07
ZOBO	70	18	1.478	-0.744	0.13	0.76	0.07

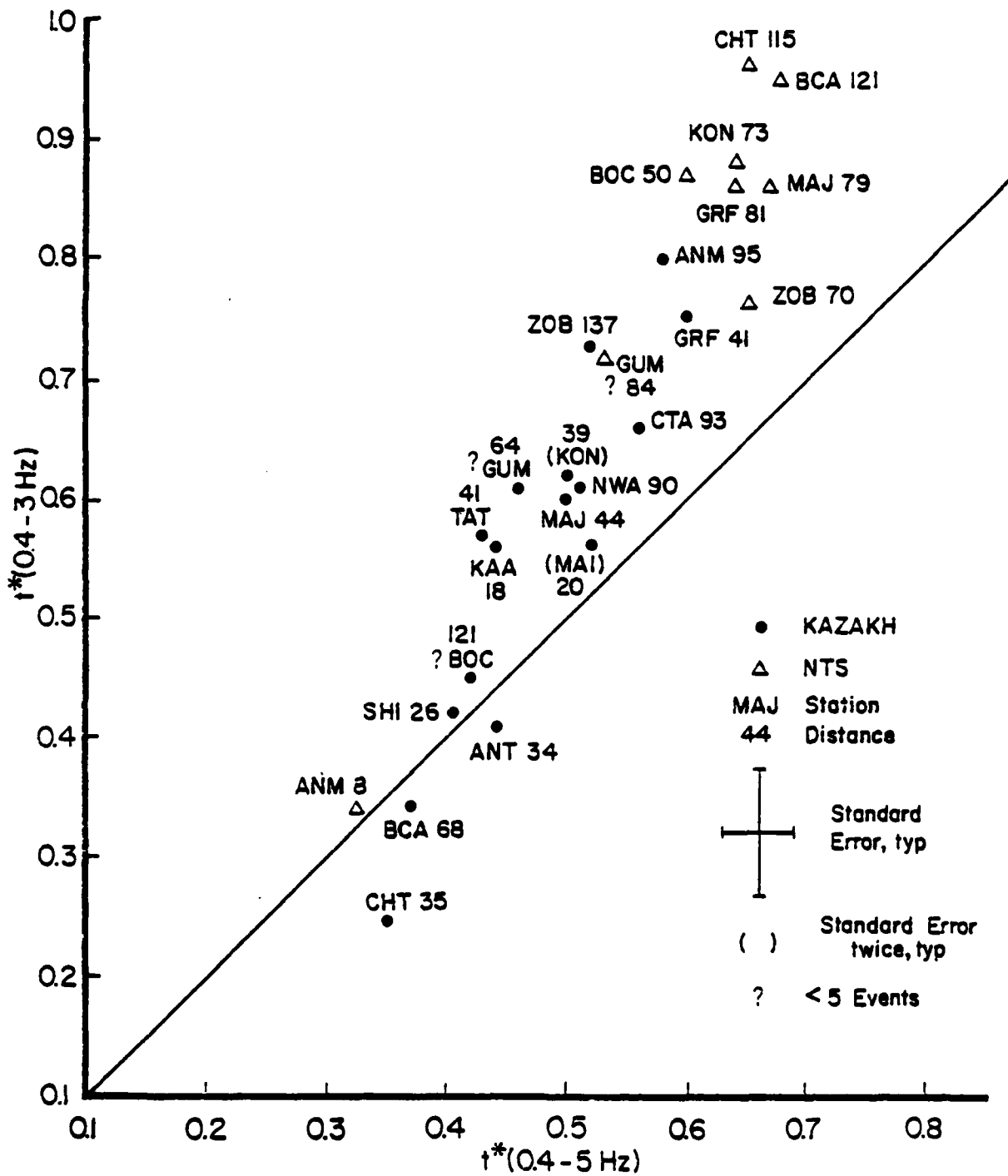


Figure 36.  $t^*$  estimates obtained from body wave spectra spanning two frequency intervals.

In view of the confidence limits attached to the measurements, these data may be grouped as follows:

<u>t*</u>	<u>NTS</u>	<u>KAZAKH</u>
< 0.25		CHTO
0.30 - 0.50		ANTO, BCAO, SHIO
0.55 - 0.65		CTAO, KAAO, KONO, MAIO, MAJO, NWAO, TATO
0.70 - 0.80	ZOBO	ANMO, GRFO
0.85 - 1.00	BOCO, GRFO, KONO, MAJO	

Results for several stations beyond the distance range of P have been included (NTS to BCAO, CHTO; KAZAKH to BOCO, ZOBO); these are more useful for classifying the spectra than studying the earth's absorption. The datum for NTS-ANMO is also suspect because the distance is only eight degrees and the spectrum may be distorted.

The tendencies shown in the above groupings agree well with numerous other studies. More convincing evidence of the accuracy of this procedure can be seen in Figure 37 which compares our Kazakh results with relative attenuation coefficients derived by Lundquist and Samowitz (1982) from substantially the same data.

#### 3.4.4 Conclusions

There are two important advantages to this method of calculating  $t^*$ . The method integrates the spectrum, a robust and stable process and its uses a reference spectrum derived in an explicit manner from statistically combined explosion and earthquake models. Furthermore, it leads to a compact result, one number for each seismogram, which facilitates the search for systematic patterns related to magnitude bias, depth of burial, and regionalization. It is suited to automatic processing, an important consideration when much data must be examined.

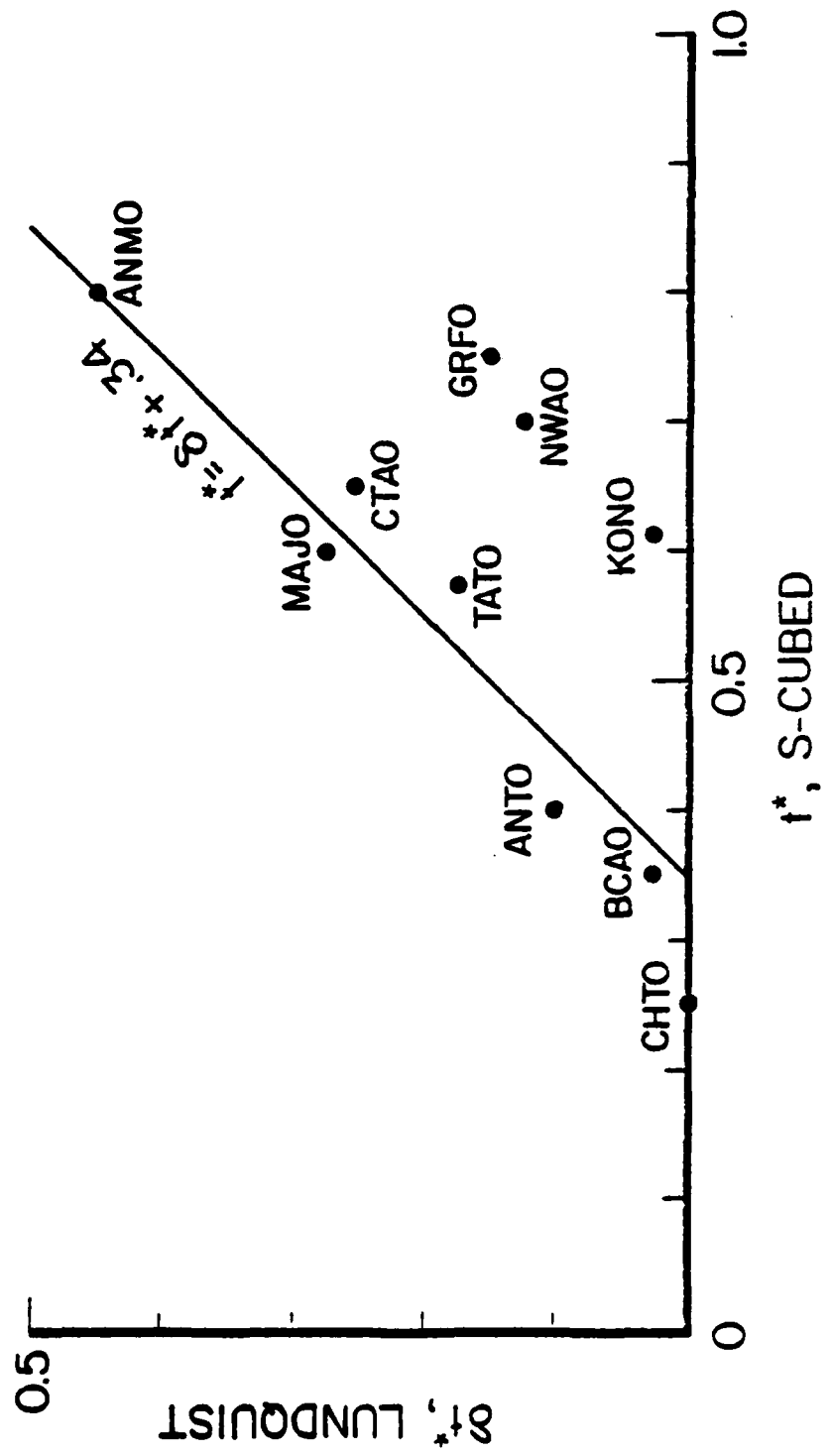


Figure 37. Comparison between  $t^*$  obtained by Lundquist and Samowitz (1982, Figure 7, Page 30) from analysis of the relative receiver function and  $t^*$  obtained in this study for SRO recordings of KAZAKH explosions.

Some weaknesses of the method have been mentioned, the major one, perhaps, being the use of single station corner frequencies. Alternate scaling laws are possible. It would be better to choose a somewhat different set of weight coefficients for this application, a set tuned to explosions alone, rather than one tuned to separating earthquakes for explosions. Also, it may be desirable to form the synthetic explosion data into sets based on similar geologic source media (i.e., sets of explosions in granite, tuff, alluvium and salt) and not mix the sets as was done above. Nevertheless, both as a method of discrimination and as a method of measuring attenuation, the notion of a set of universal, deterministic spectral weights appears promising.

#### IV. REFERENCES

##### 4.1 SECTION II

Bache, T. C., W. L. Rodi, and D. G. Harkrider (1978), "Crustal Structures Inferred from Rayleigh Wave Signatures of NTS Explosions," BSSA, 68, No. 5, pp. 1399-1413.

Ben Menahem, A., M. Rosenman and D. G. Harkrider (1970), "Fast Evaluation of Source Parameters from Isolated Surface Waves Signals," BSSA, 60, pp. 1337-1387.

Harkrider, D. G. (1964), "Surface Waves in Multilayered Media I. Rayleigh and Love Waves from Buried Sources in a Multilayered Elastic Half Space," BSSA, 54, pp. 627-629.

Harkrider, D. G. (1970), "Surface Waves in Multilayered Media II. Higher Mode Spectra and Spectral Ratios from Point Sources in Plane-Layered Earth Models," BSSA, 60, pp. 1937-1987.

Herrin, E., and T. Goforth (1977), "Phase-Matched Filtering: Application to the Study of Rayleigh Waves," BSSA, 67, pp. 1259-1275.

Kanamori, H. and J. W. Given (1981), "Use of Long-Period Surface Waves for Rapid Determination of Earthquake-Source Parameters," Physics of the Earth and Planetary Interiors, 27, pp. 8-31.

Mitchell, B. J., (1975), "Regional Rayleigh Wave Attenuation in North America," JGR, 80, p. 4904-4916.

Schwab, F. and L. Knopoff (1970), "Fast Surface Wave and Free Mode Computations," in Methods in Computational Physics, Vol. II, (B. A. Bolt, ed.), Academic Press, New York.

Takeuchi, H. and M. Saito (1972), "Seismic Surface Waves," in Methods and Computational Physics, Vol. II, (B. A. Bolt, ed.), Academic Press, New York.

Wang, J., J. L. Stevens, W. L. Rodi, J. B. Minster, and B. F. Mason (1981), "Inversion of Surface Waves for Path Structure and Attenuation," Systems, Science and Software Topical Report, SSS-R-82-5232, November.

Stevens, J. L., W. L. Rodi, J. Wang, B. Shkoller, E. Haldi, B. F. Mason, and J. B. Minster (1982), "Surface Wave Analysis Package and Shagan River to SRO Station Path Corrections," S-CUBED Topical Report, SSS-R-82-5518, April.

#### 4.2 SECTION III

Aki, K., and P. G. Richards (1980), Quantitative Seismology, W. H. Freeman, San Francisco.

Archambeau, C. B., D. G. Harkrider and D. V. Helmberger (1974)  
"Studies of Multiple Events", California Institute of Technology Final Report on Contract ACDA/ST-220, prepared for U.S. Arms control and Disarmament Agency.

Burdick, L. J., D. M. Cole, D. V. Helmberger, T. Lay, and T. Wallace (1981), "Effective Source Functions From Local Surface Measurements," Woodward-Clyde Consultants Report, WCCP-R-82-01.

Carpenter, E. W. (1967), "Teleseismic Signals Calculated For Underground, Underwater and Atmospheric Explosions," Geophysics, 32, pp. 17-32.

Day, S. M. (1982a), "Three Dimensional Finite Difference Simulation of Fault Dynamics: Rectangular Faults with Fixed Rupture Velocity," BSSA, 72, pp. 705-727.

Day, S. M. (1982b), "Three Dimensional Simulation of Spontaneous Rupture: the Effect of Non-Uniform Prestress," BSSA, 72, (in the Press).

Der, Z. A., T. W. McElfresh, and A. O'Donnell (1982a), "An Investigation of the Regional Variations and Frequency Dependence of Anelastic Attenuation in the Mantle Under the United States in the 0.5 - 4 Hz Band," Geophys. J. R. astro. Soc., 69, pp. 67-100.

Der, Z. A., W. D. Rivers, T. W. McElfresh, A. O'Donnell, P. J. Klouda, and M. E. Marshall (1982b), "Worldwide Variations in the Attenuative Properties of the Upper Mantle as Determined From Spectral Studies of Short Period Body Waves," (submitted to Physics of the Earth and Planetary Interiors.)

Efron, B. (1979), "Bootstrap Methods: Another Look At the Jackknife," Annals of Statistics, 1, pp. 1-26.

Farrell, W. E., J. R. Murphy, W. L. Rodi, C. B. Archambeau, L. B. Bache, and B. Shkoller (1981), "Automatic Seismic Signal Processing Research," Systems, Science and Software Final Report, VSC-TR-82-17, September.

Filson, J., and C. W. Frasier (1972), "Multisite Estimation of Explosive Source Parameters," JGR, 77, pp. 2045-2061.

Haskell, N. A. (1967), "Analytic Approximation for the Elastic Radiation From a Contained Underground Explosion," JGR, 72, pp. 2583-2587.

Lundquist, G. M., G. R. Mellman, and R. S. Hart (1980), "Review of the Estimation of  $m_b$  and Yield of Underground Explosions," Sierra Geophysics Report to Advanced Research Projects Agency, SGI-R-80-031.

Lundquist, G. M., and I. R. Samowitz (1982), "Relative Attenuation Properties for 12 Paths About the Eastern Kazakh Test Site," Sierra Geophysics Report, SGI-R-82-064.

Marshall, P. D., D. L. Springer, and H. C. Rodean (1979), "Magnitude Corrections for Attenuation in the Upper Mantle," GJR astron. Soc., 57, pp. 609-638.

Mueller, R. A., and J. R. Murphy (1971), "Seismic Characteristics of Underground Nuclear Detonations. Part I, Seismic Scaling Law of Underground Detonations," BSSA, 61, pp. 1675-1692.

Rimer, N., J. T. Cherry, S. M. Day, T. C. Bache, J. R. Murphy, and A. Maewal (1979), "Two-Dimensional Calculations of PILEDRIVER, Analytic Continuation of Finite Difference Source Calculations, Analysis of Free Field Data From Merlin, and Summary of Current Research," Systems, Science and Software Quarterly Technical Report submitted to VELA Seismological Center, SSS-R-79-4121, August. (Not cleared for public distribution.)

Rivers, D. W., D. H. Von Seggern, B. L. Elkins, and H. S. Sproules (1980), "A Statistical Discrimination Experiment For Eurasian Events Using a Twenty-Seven Station Network," Teledyne-Geotech Report, SDAC-TR-79-5.

Savino, J. M., C. B. Archambeau, and J. F. Masso (1980), "VFM Discrimination Results from a Ten Station Network," Systems, Science and Software Technical Report submitted to VELA Seismological Center, VSC-TR-81-29, July.

Shumway, R. and R. Blandford (1970), "Simulation of Discriminant Analysis," Seismic Laboratory Data Report 261, Teledyne Geotech, Alexandria, Virginia.

Stevens, J. L. and S. M. Day (1982), "The Physical Basis of  $m_b:M_s$  and Variable Frequency Magnitude Methods for Earthquake/Explosion Discrimination," Systems, Science and Software Topical Report submitted to VELA Seismological Center, SSS-R-82-5595, June. (Not cleared for public distribution.)

Von Seggern, D. H., and R. R. Blandford (1972), "Source Time Functions and Spectra from Underground Nuclear Explosions," Geophys. J. R. astro. Soc., 31, pp. 83-97.

Von Seggern, D. H. and D. W. Rivers (1979), "Seismic Discrimination of Earthquakes and Explosions with Application to the Southwest United States," SDAC Report No. TR-77-10, Teledyne Geotech, Alexandria, Virginia.

APPENDIX A

TABLE OF SPECTRAL WEIGHTS FOR  
DETERMINISTIC DISCRIMINATION

b-a11		-.015
xmean		-.515
xvar		.286
gmean		.484
gvar		.269
$m_b$	.40	.131
$m_b$	.45	.112
$m_b$	.50	.096
$m_b$	.55	.081
$m_b$	.60	.067
$m_b$	.65	.054
$m_b$	.70	.042
$m_b$	.80	.021
$m_b$	.90	.008
$m_b$	1.00	.000
$m_b$	1.10	-.008
$m_b$	1.20	-.014
$m_b$	1.30	-.021
$m_b$	1.40	-.028
$m_b$	1.50	-.033
$m_b$	1.60	-.036
$m_b$	1.70	-.038
$m_b$	1.80	-.041
$m_b$	1.90	-.043
$m_b$	2.00	-.043
$m_b$	2.10	-.041
$m_b$	2.20	-.041
$m_b$	2.30	-.043
$m_b$	2.40	-.046
$m_b$	2.50	-.048
$m_b$	2.60	-.049
$m_b$	2.70	-.049
$m_b$	2.80	-.051
$m_b$	2.90	-.053
$m_b$	3.00	-.055
$m_b$	3.10	-.057
$m_b$	3.20	-.059
$m_b$	3.30	-.059
$m_b$	3.40	-.058
$m_b$	3.50	-.058
$m_b$	3.60	-.058
$m_b$	3.75	-.062
$m_b$	4.00	-.074
$m_b$	4.50	-.080
$m_b$	5.00	-.083

APPENDIX B

DETERMINISTIC DISCRIMINANT RESULTS FOR THE  
PRIORITY 2 AI STATIONS (ANMO, CTAO, ZOBO, HNME,  
ATTU, CNAK, NJAK, TNAK, UCAK, KSRS, NAO, AND LAO)

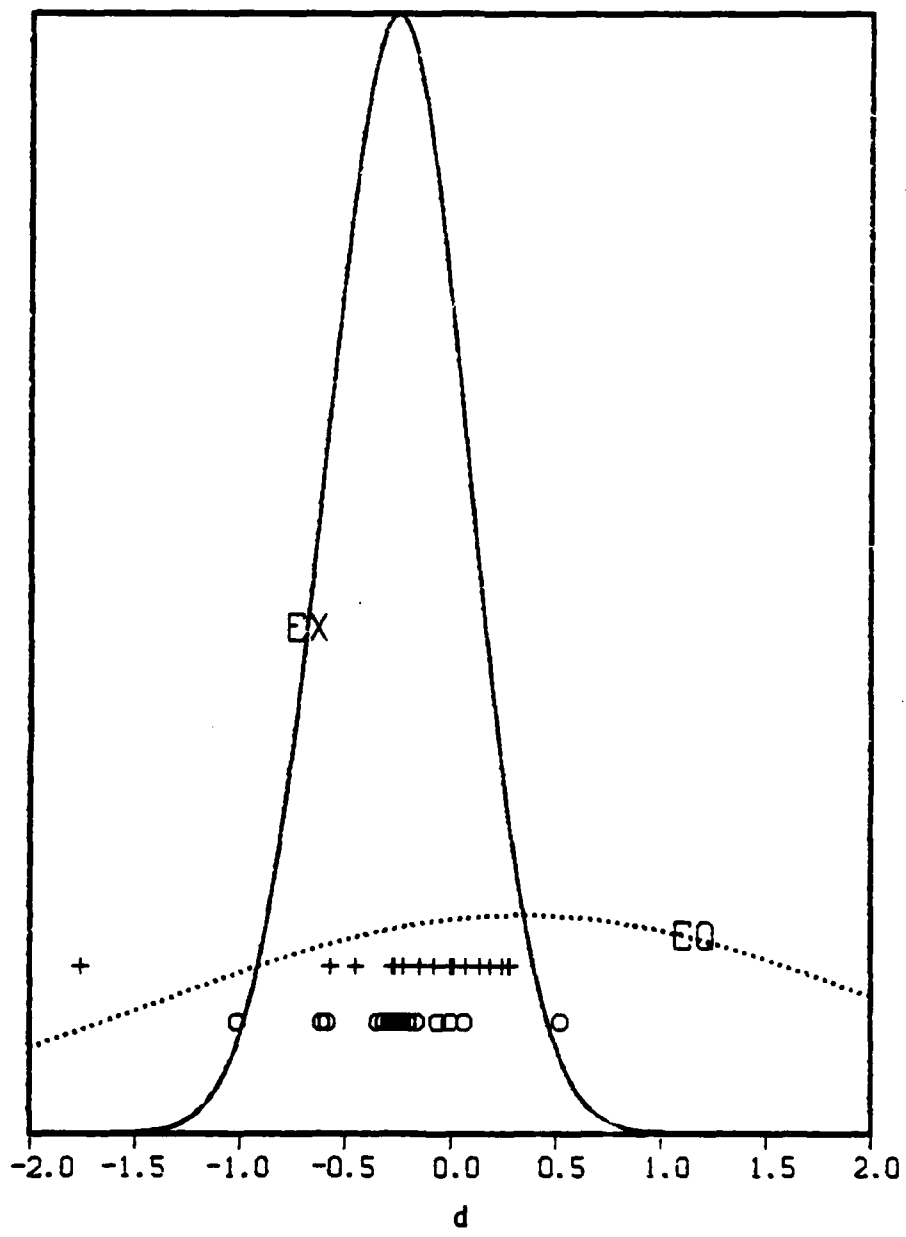


Figure B-1. Deterministic discrimination results for AI data recorded at ANMO.

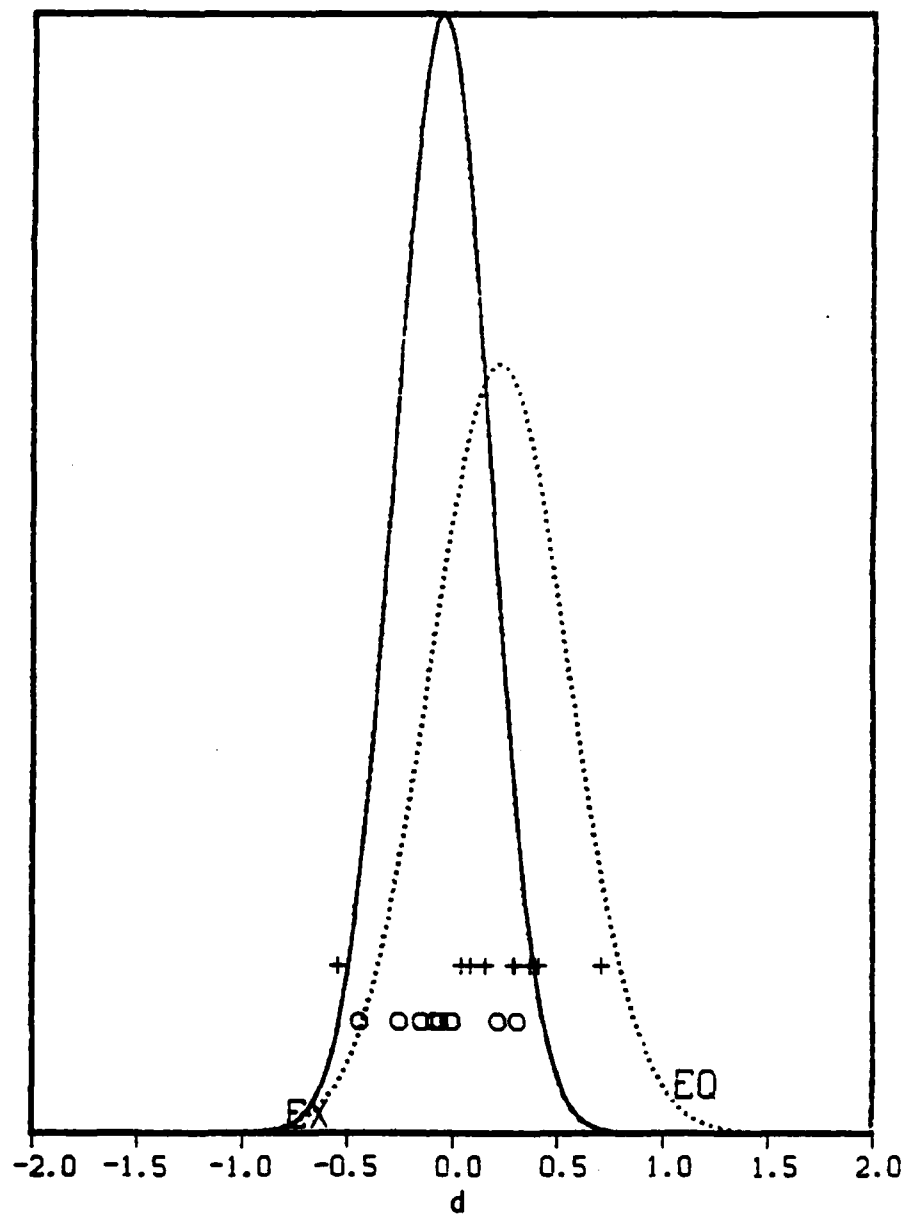
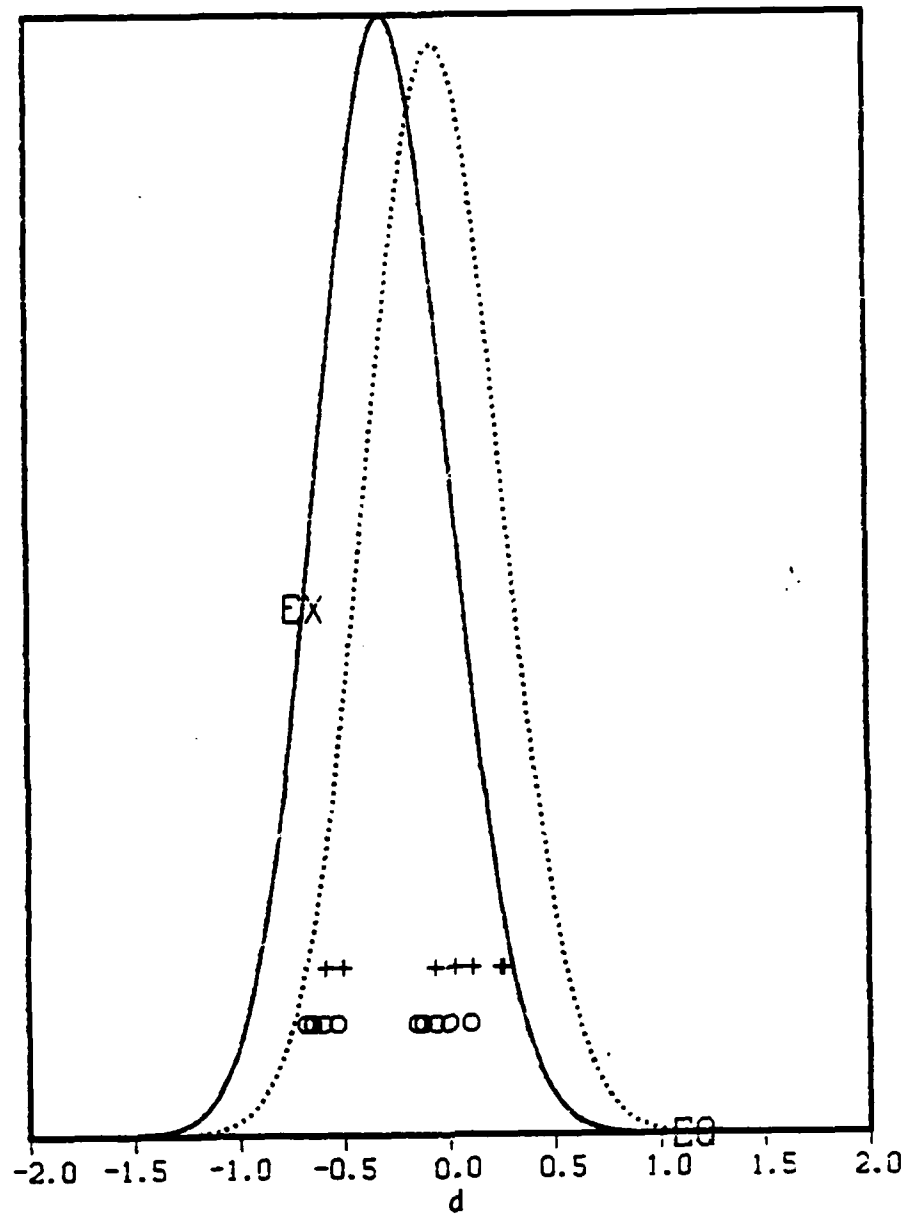


Figure B-2. Deterministic discrimination results for AI data recorded at CTAO.



**Figure B-3. Deterministic discrimination results for AI data recorded at Z0B0.**

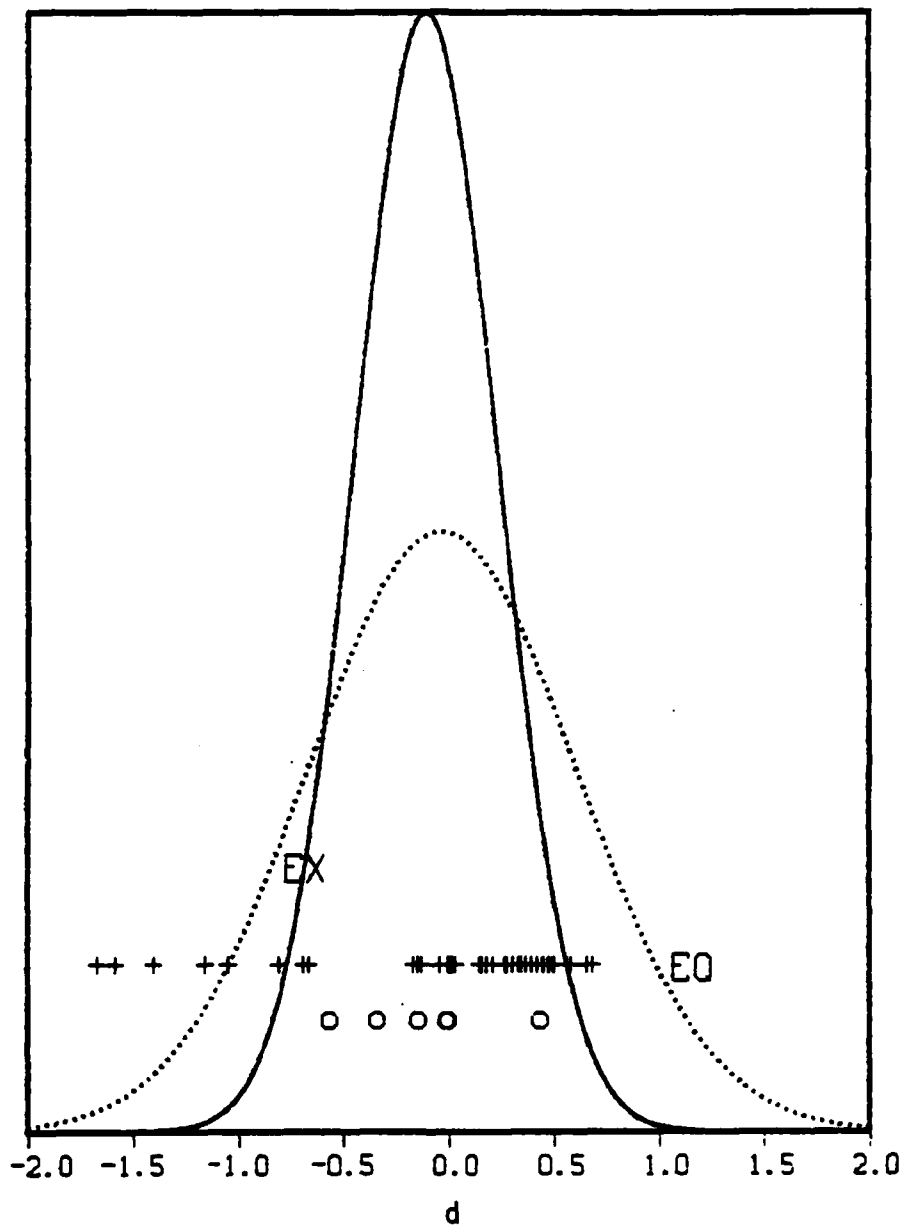
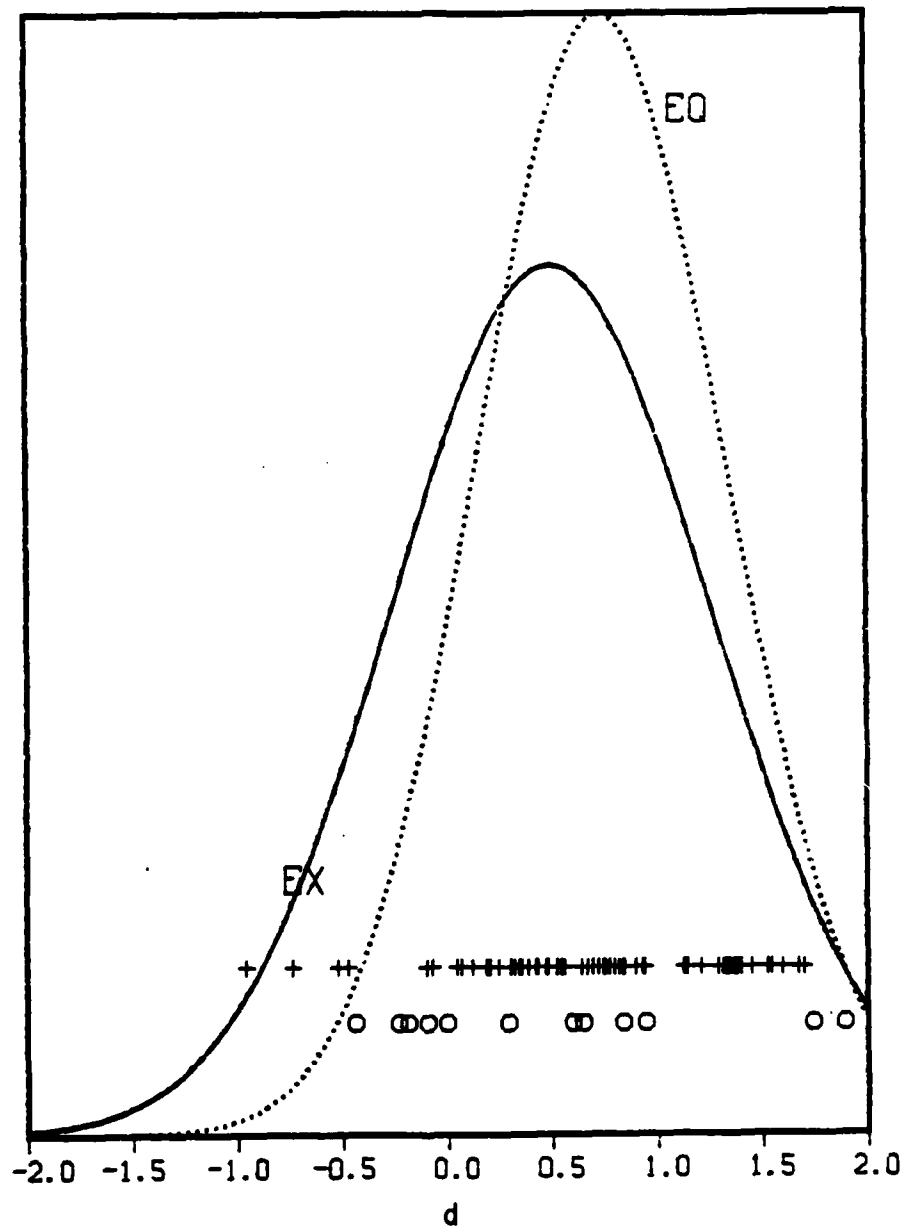
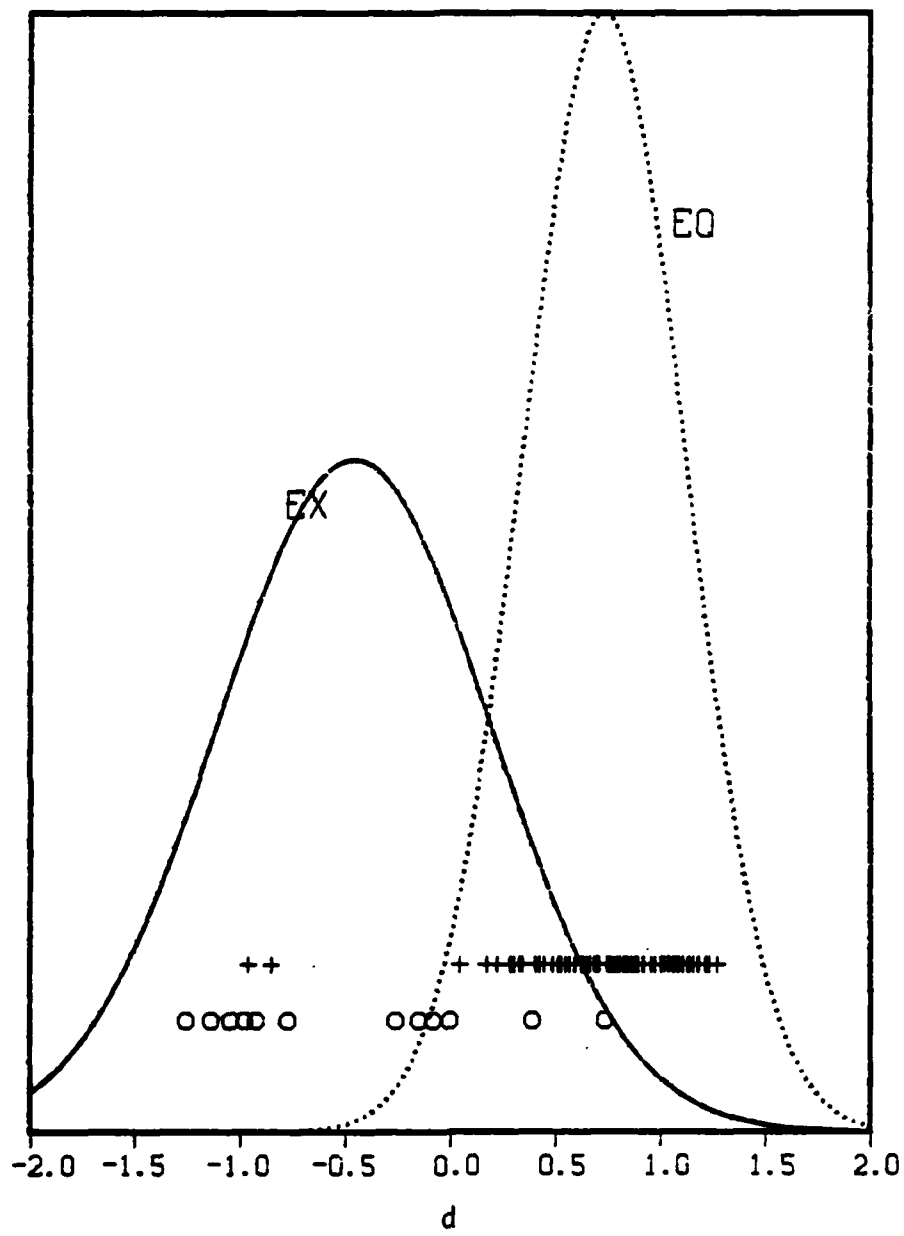


Figure B-4. Deterministic discrimination results for AI data recorded at HNME.



**Figure B-5.** Deterministic discrimination results for AI data recorded at ATTU.



**Figure B-6.** Disterministic discrimination results for AI data recorded at CNAK.

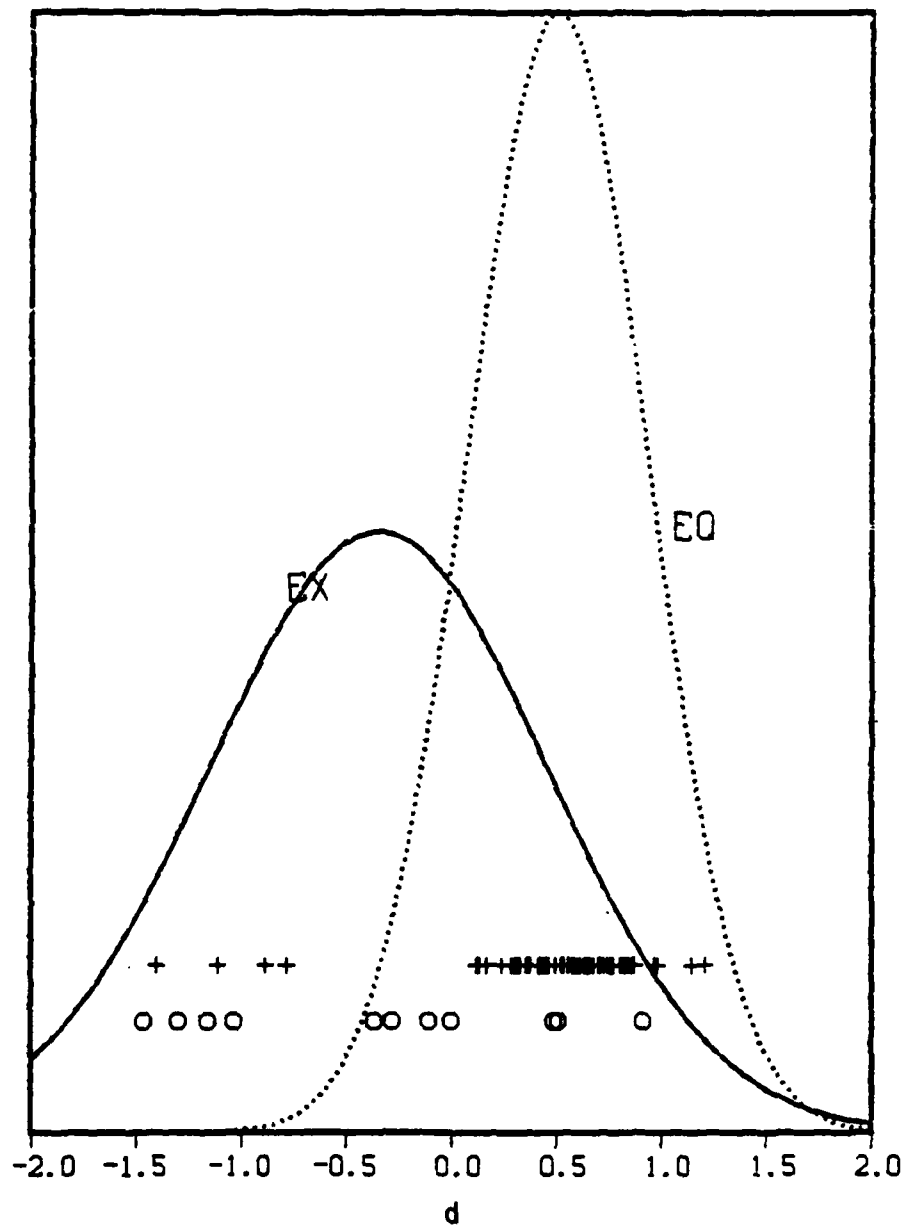


Figure B-7. Deterministic discrimination results for AI data recorded at NJAK.

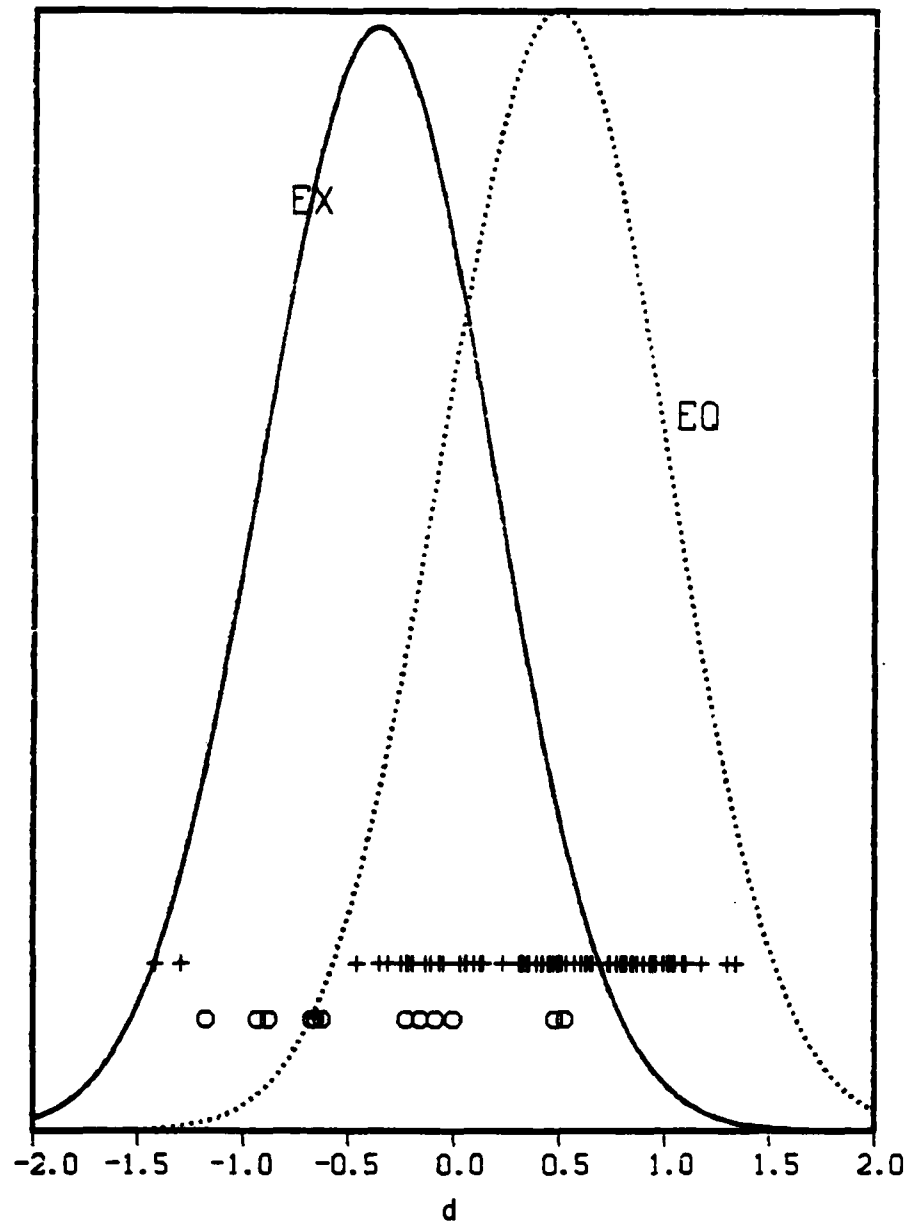
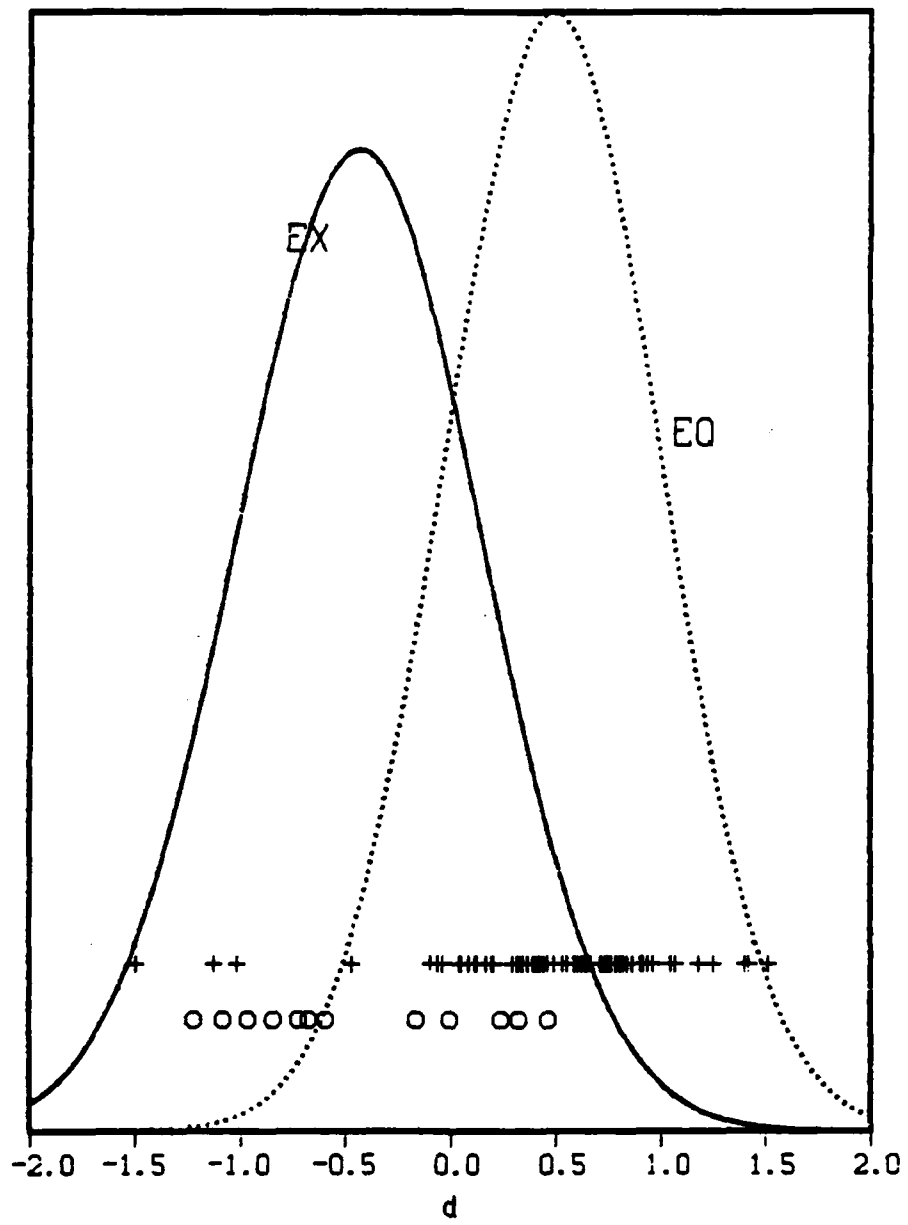


Figure B-8. Deterministic discrimination results for AI data recorded at TNAK.



**Figure B-9. Deterministic discrimination results for AI data recorded at UCAK.**

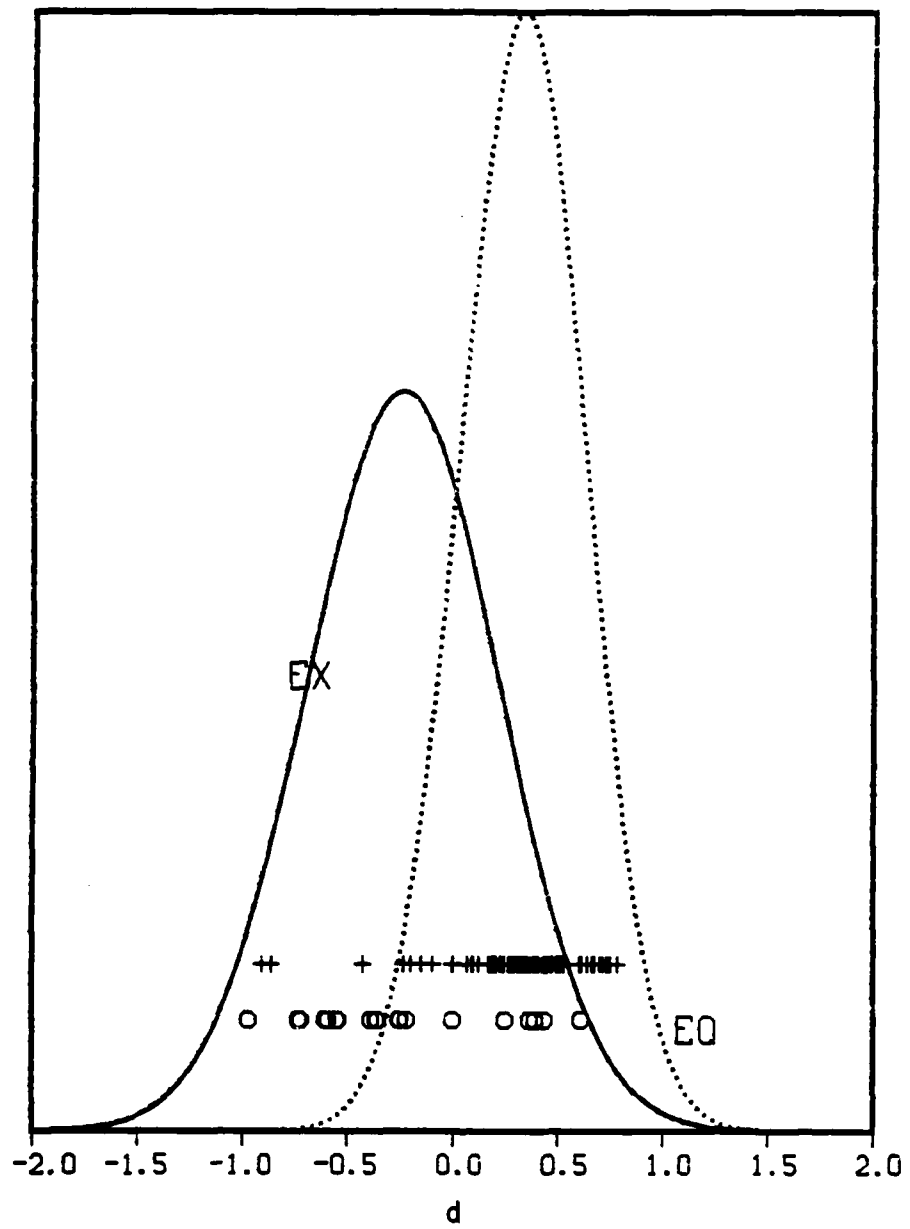


Figure B-10. Deterministic discrimination results for AI data recorded at KSRS.

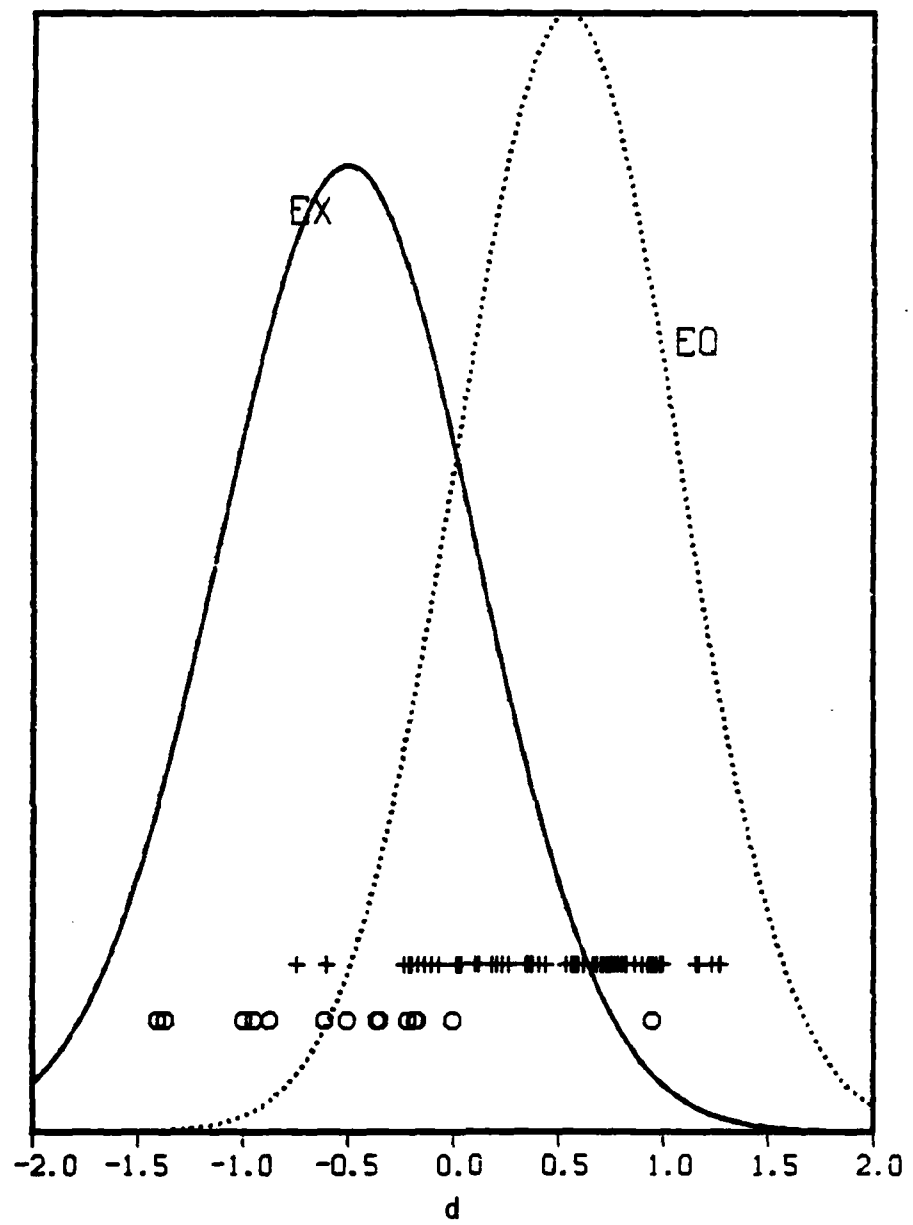
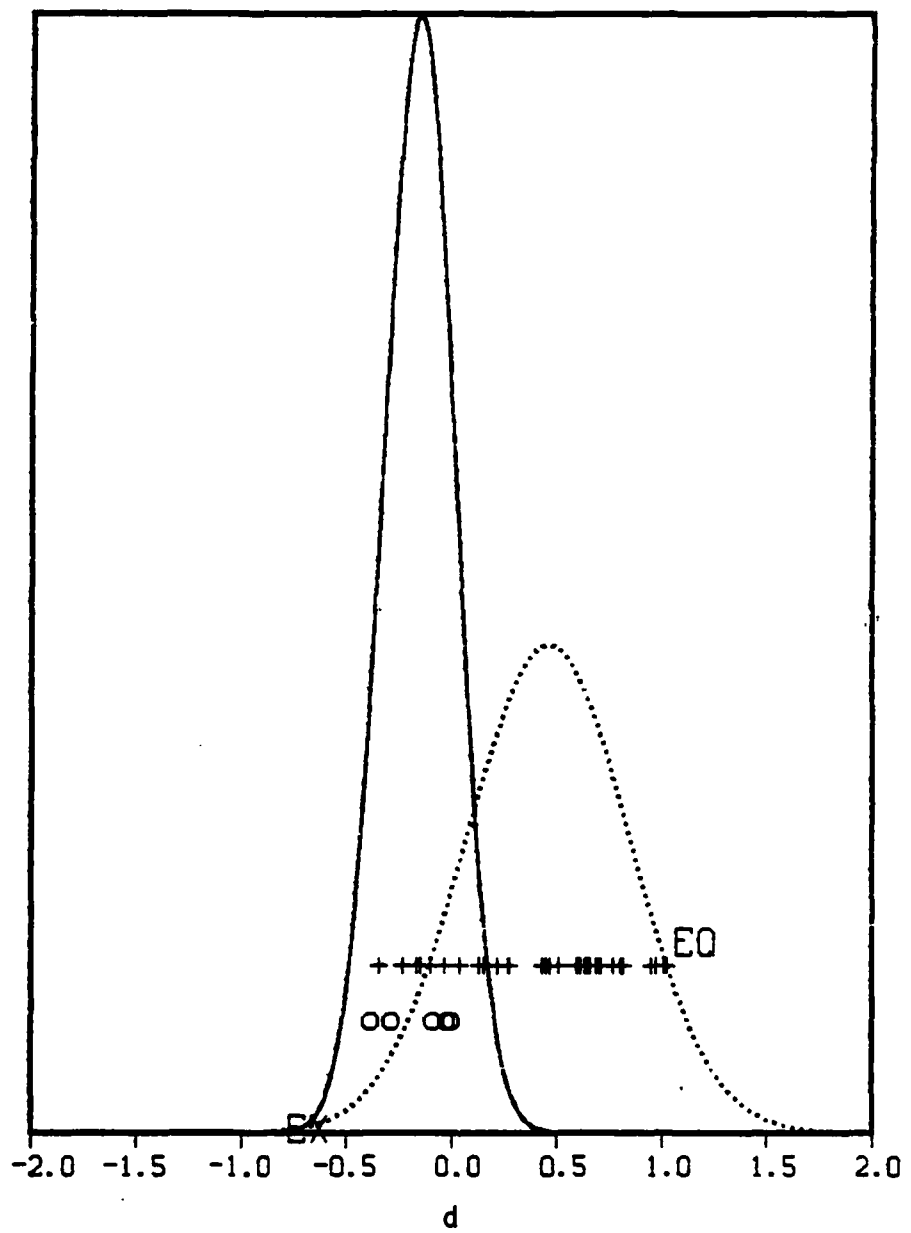


Figure B-11. Deterministic discrimination results for AI data recorded at NAO.



**Figure B-12.** Deterministic discrimination results for AI data recorded at LAO.

APPENDIX C

SPECTRAL INTEGRAL PLOTS FOR  
SELECTED SRO RECORDINGS OF  
NTS AND KAZAKH EXPLOSIONS

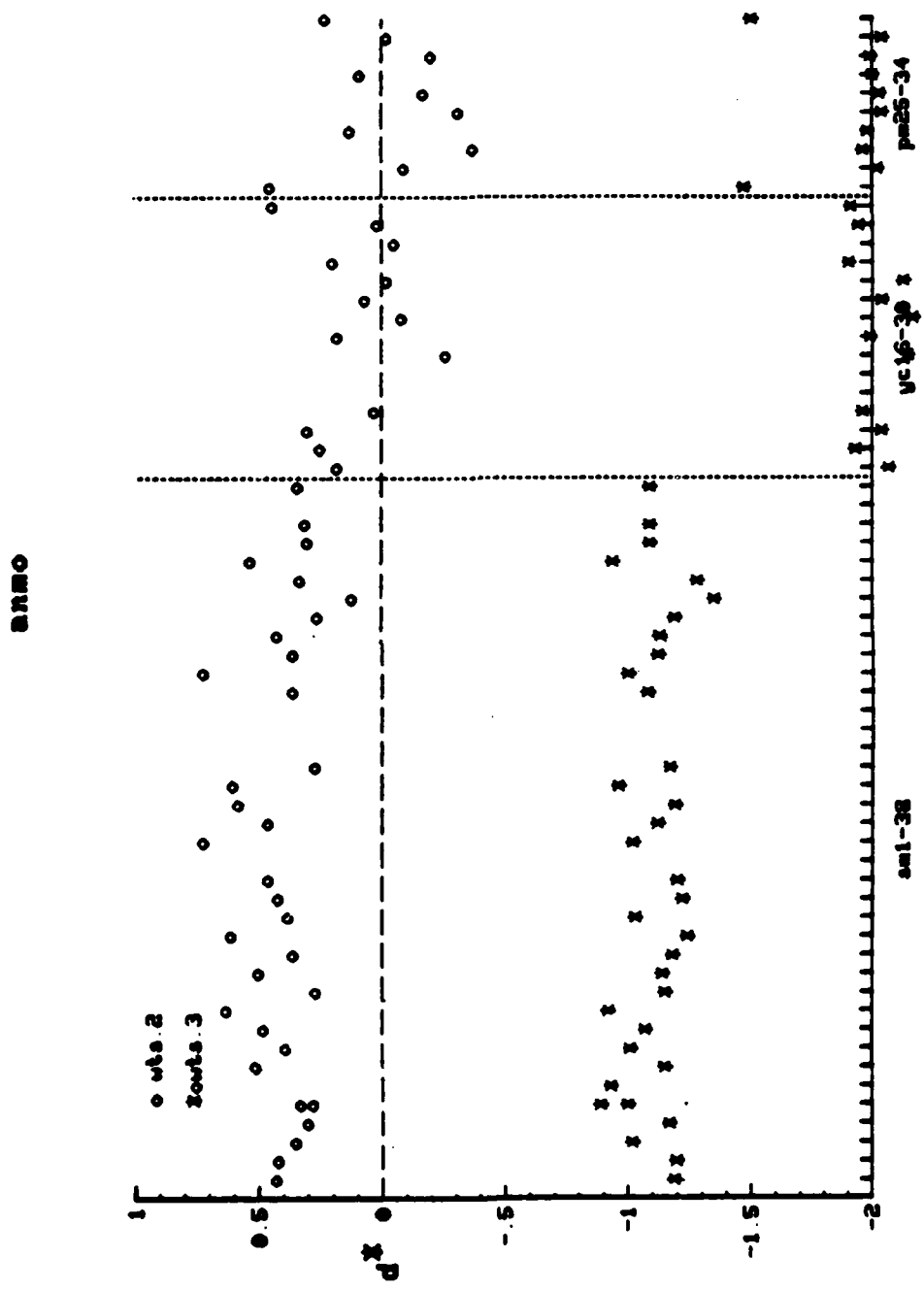


Figure C-1. The spectral integral (Equation 28) obtained using deterministic weights for station ANMO. Only the points denoted by asterisks are meaningful.

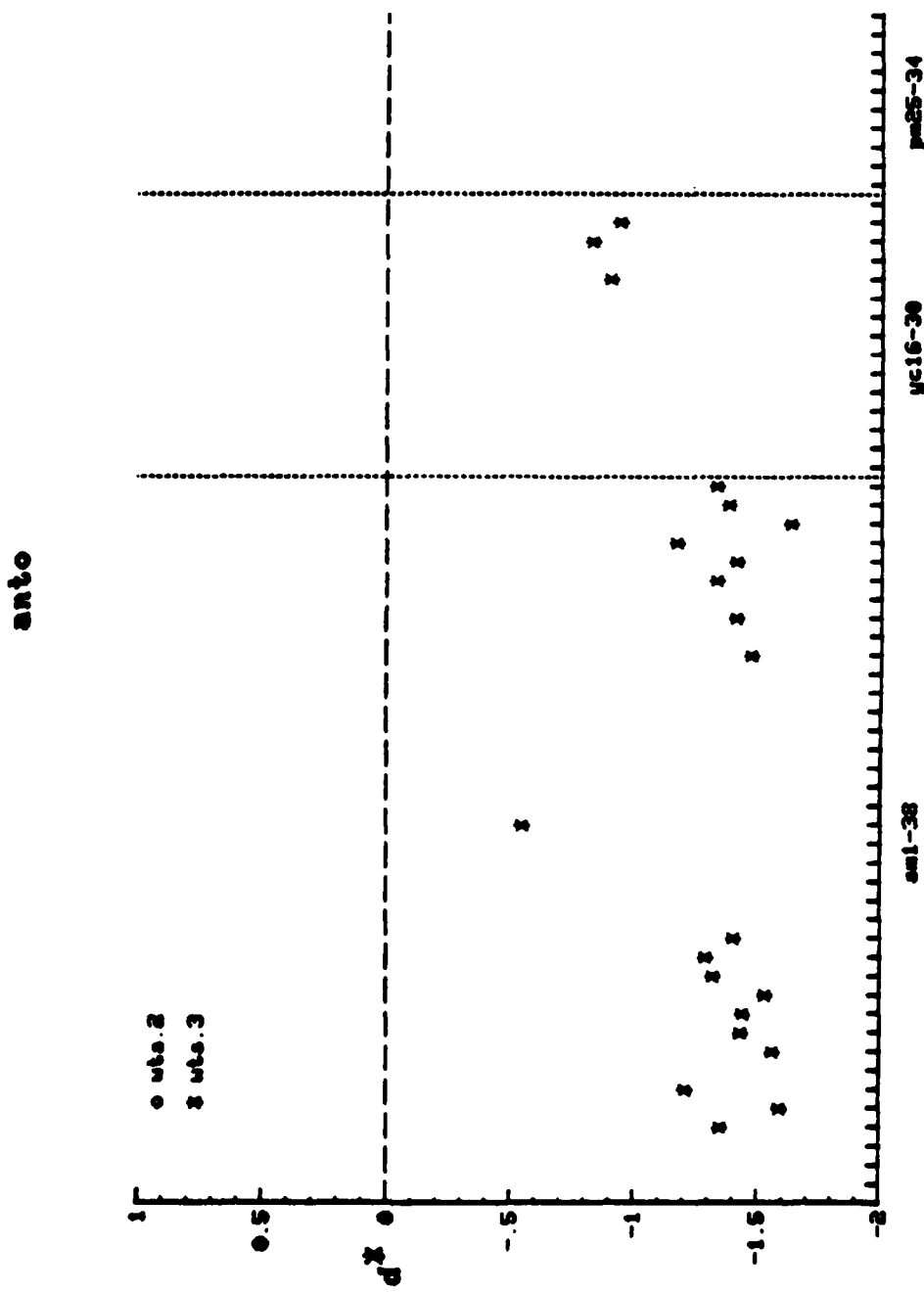


Figure C-2. The spectral integral (Equation 28) obtained using deterministic weights for station ANTO.

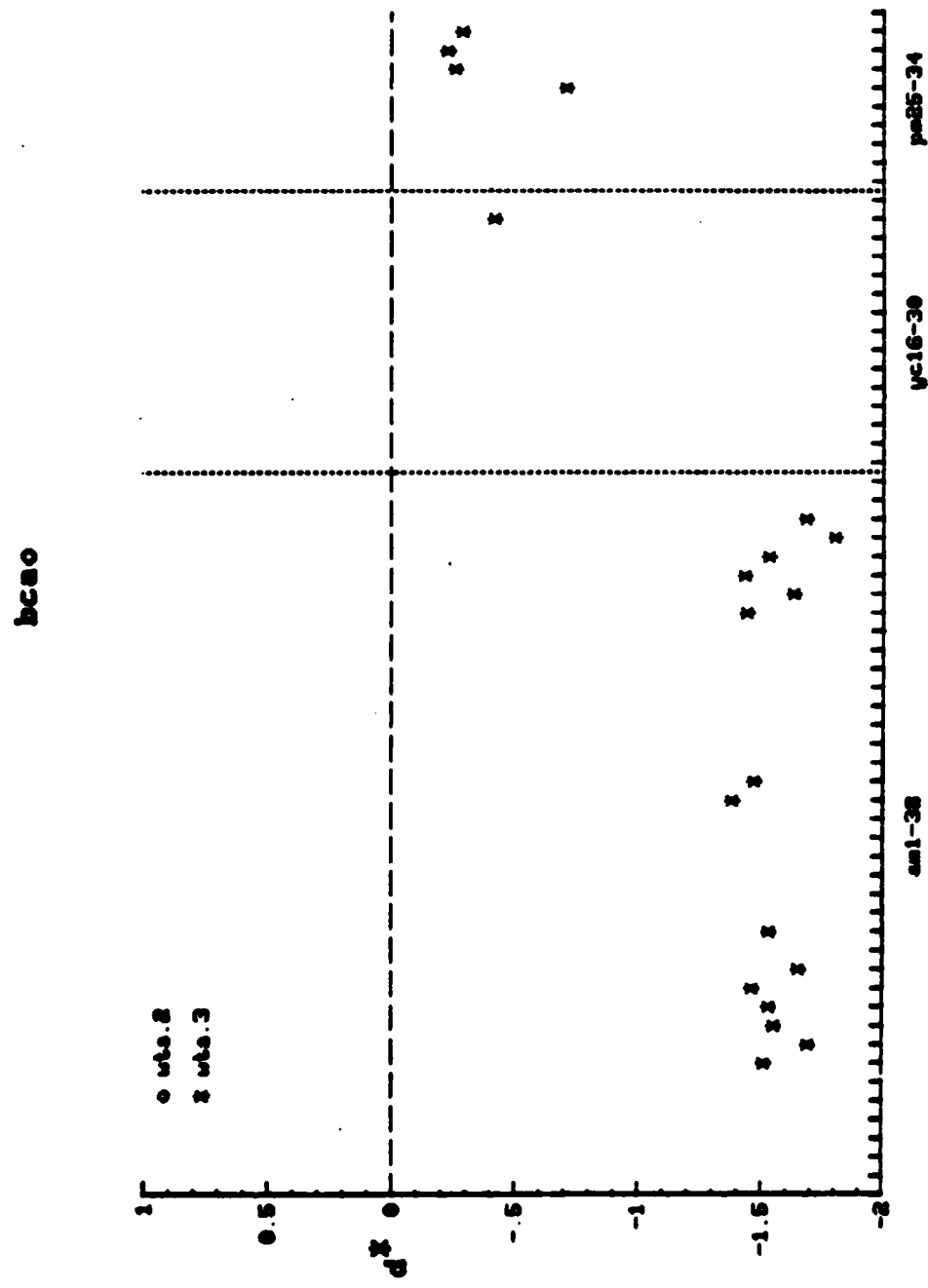


Figure C-3. The spectral integral (Equation 28) obtained using deterministic weights for station BCAO.

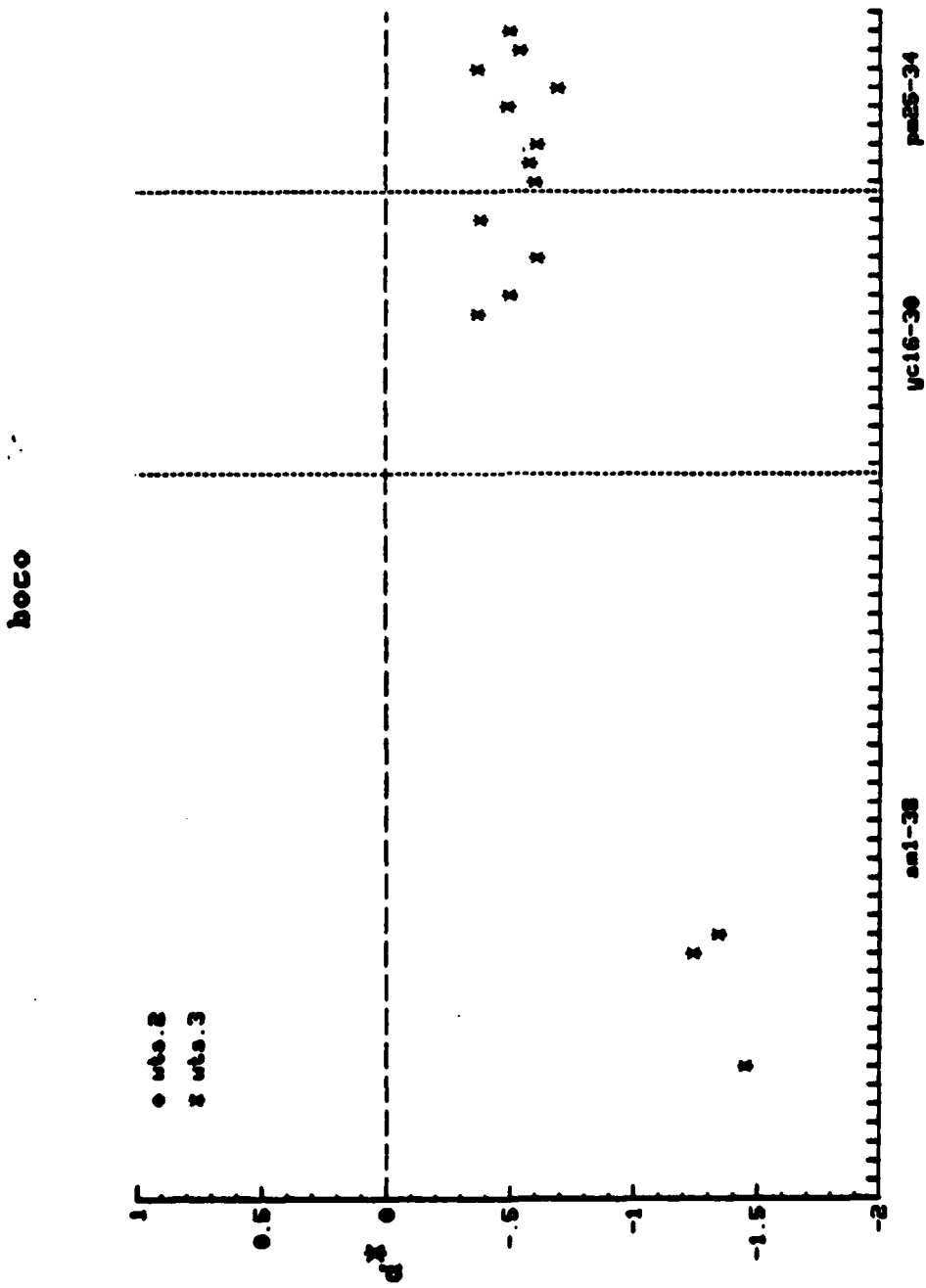


Figure C-4. The spectral integral (Equation 28) obtained using deterministic weights for station B0CO.

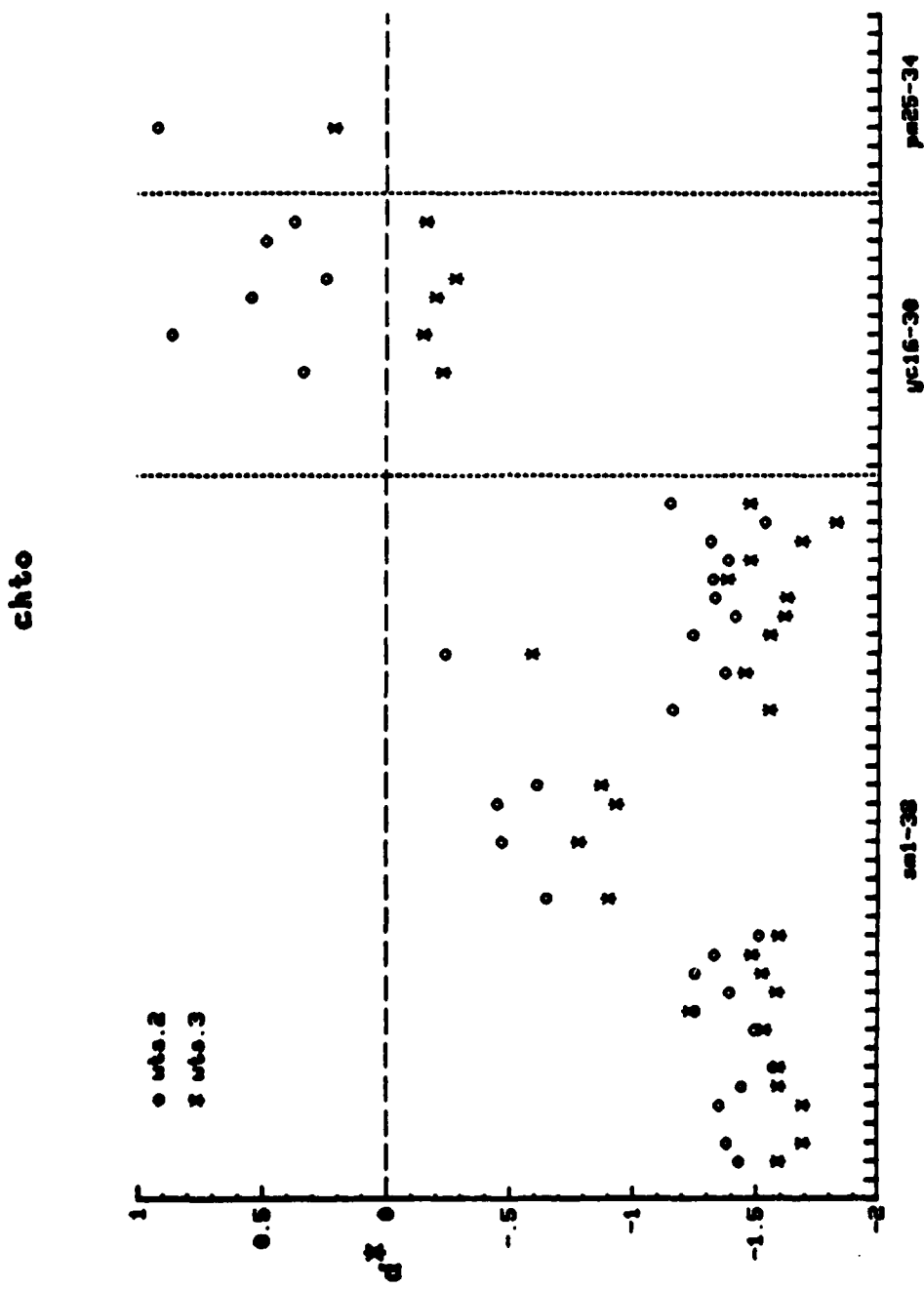


Figure C-5. The spectral integral (Equation 28) obtained using deterministic weights for station CHT0. Only the points denoted by asterisks are meaningful.

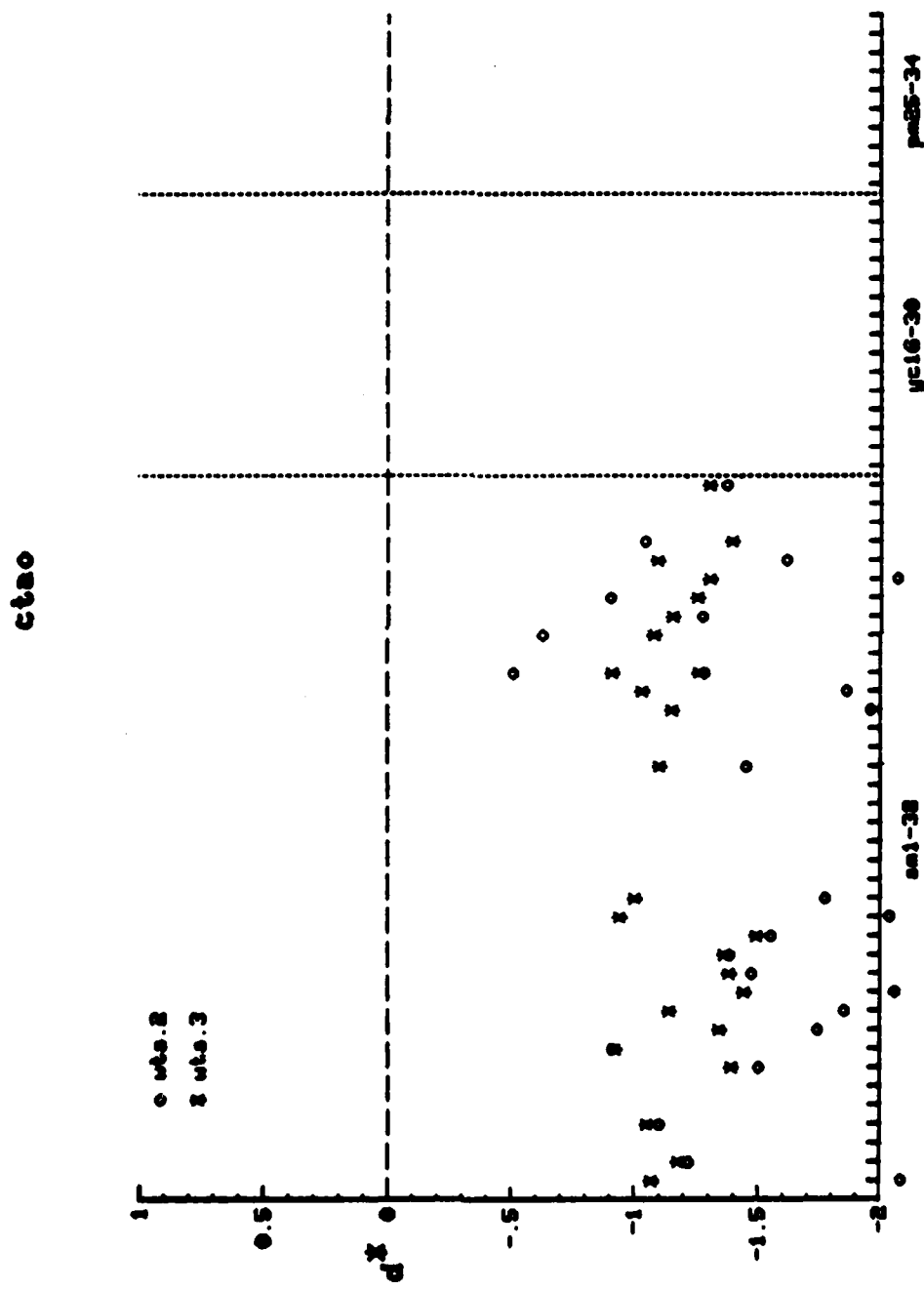


Figure C-6. The spectral integral (Equation 28) obtained using deterministic weights for station CTAO. Only the points denoted by asterisks are meaningful.

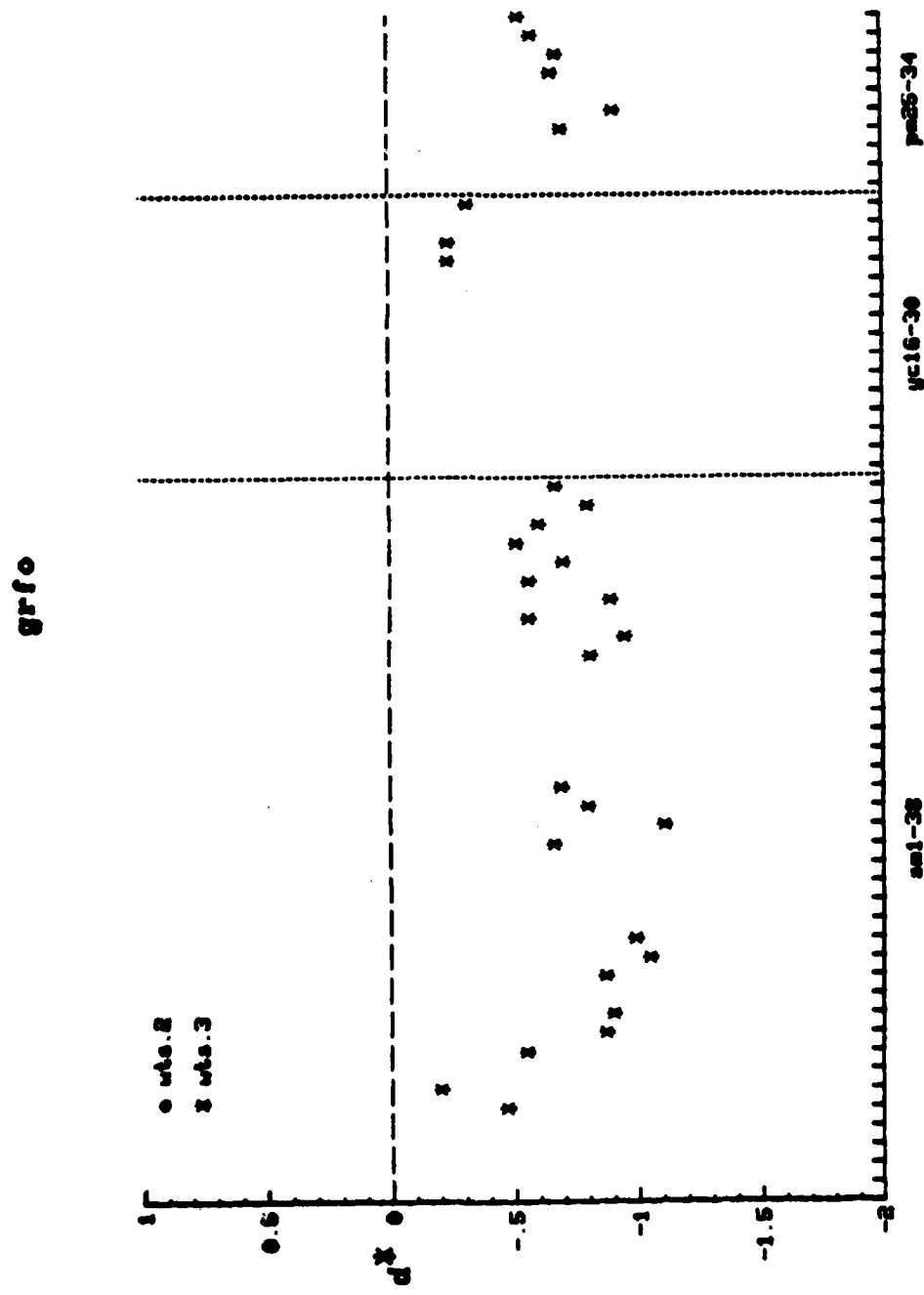


Figure C-7. The spectral integral (Equation 28) obtained using deterministic weights for station GRF0.

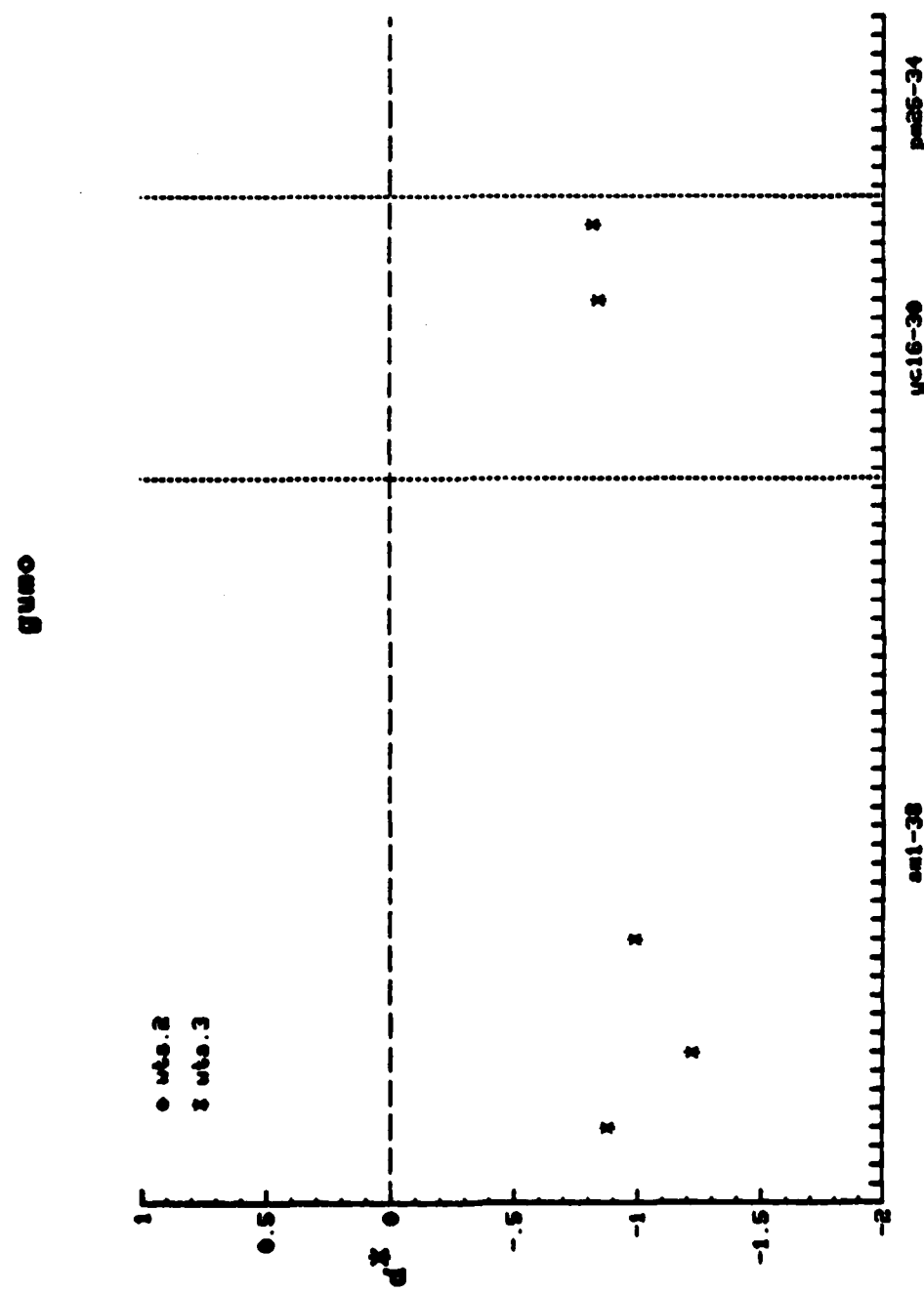
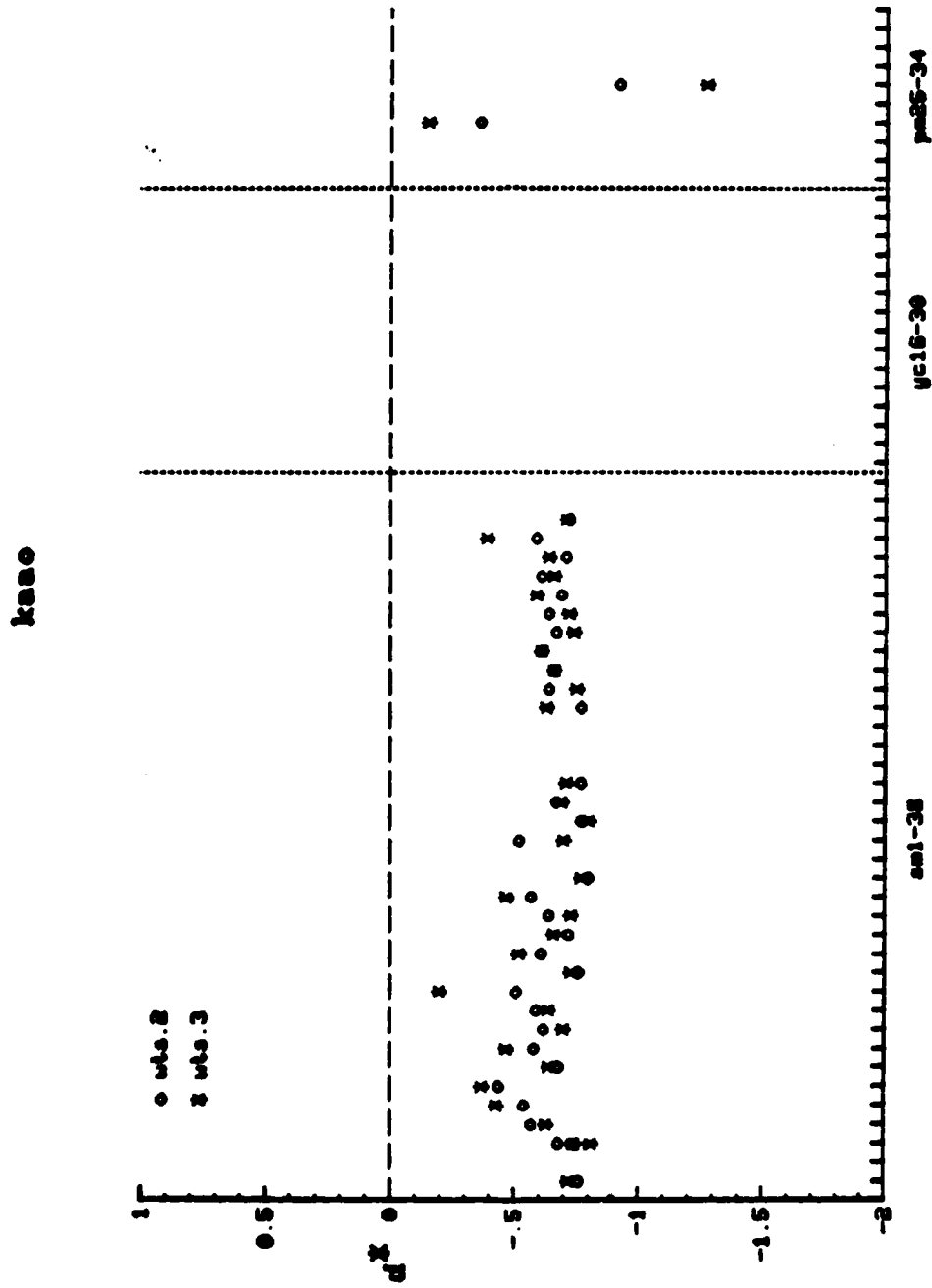


Figure C-8. The spectral integral (Equation 28) obtained using deterministic weights for station GUM0.



**Figure C-9.** The spectral integral (Equation 28) obtained using deterministic weights for station KAA0. Only the points denoted by asterisks are meaningful.

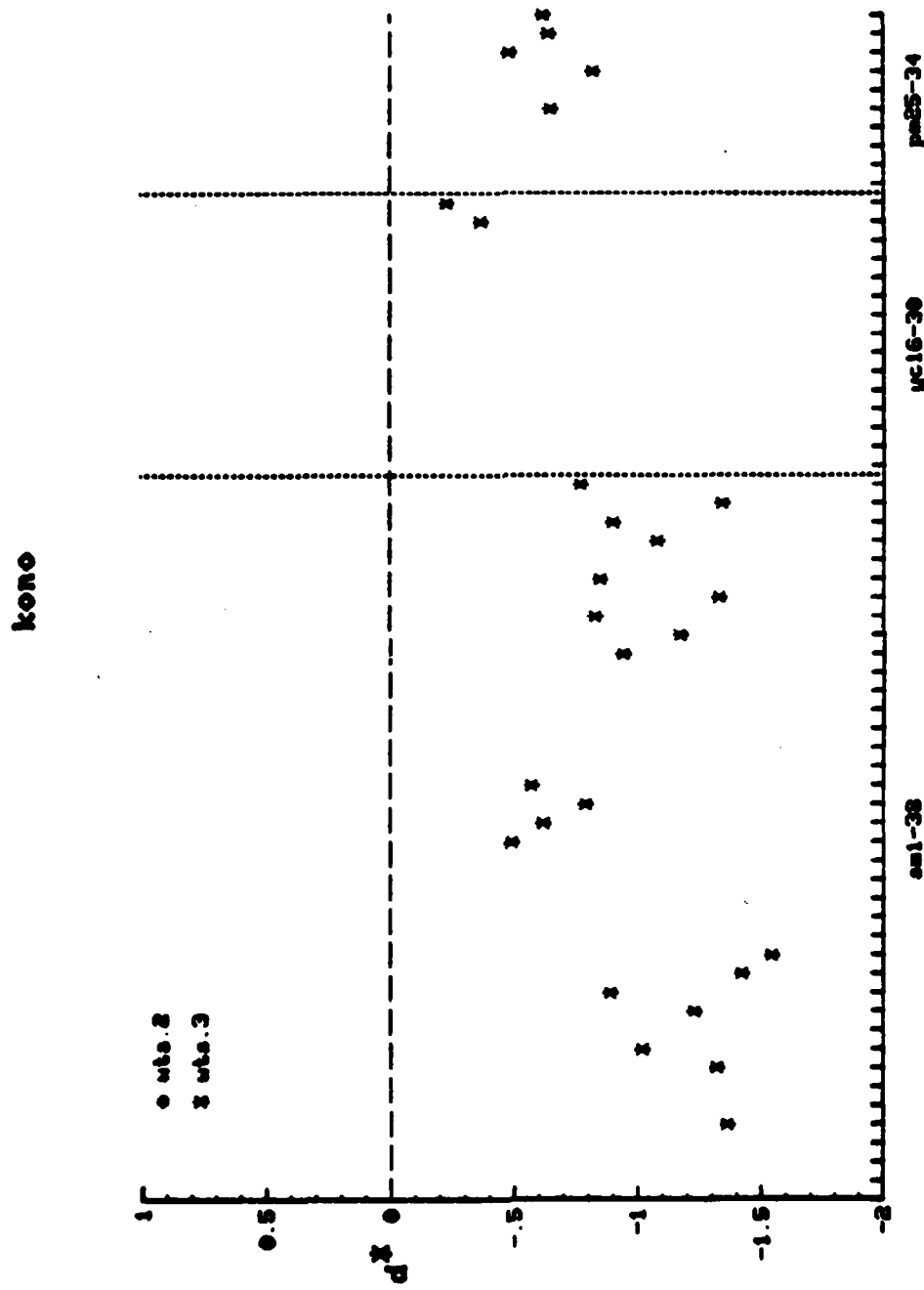


Figure C-10. The spectral integral (Equation 28) obtained using deterministic weights for station KONO.

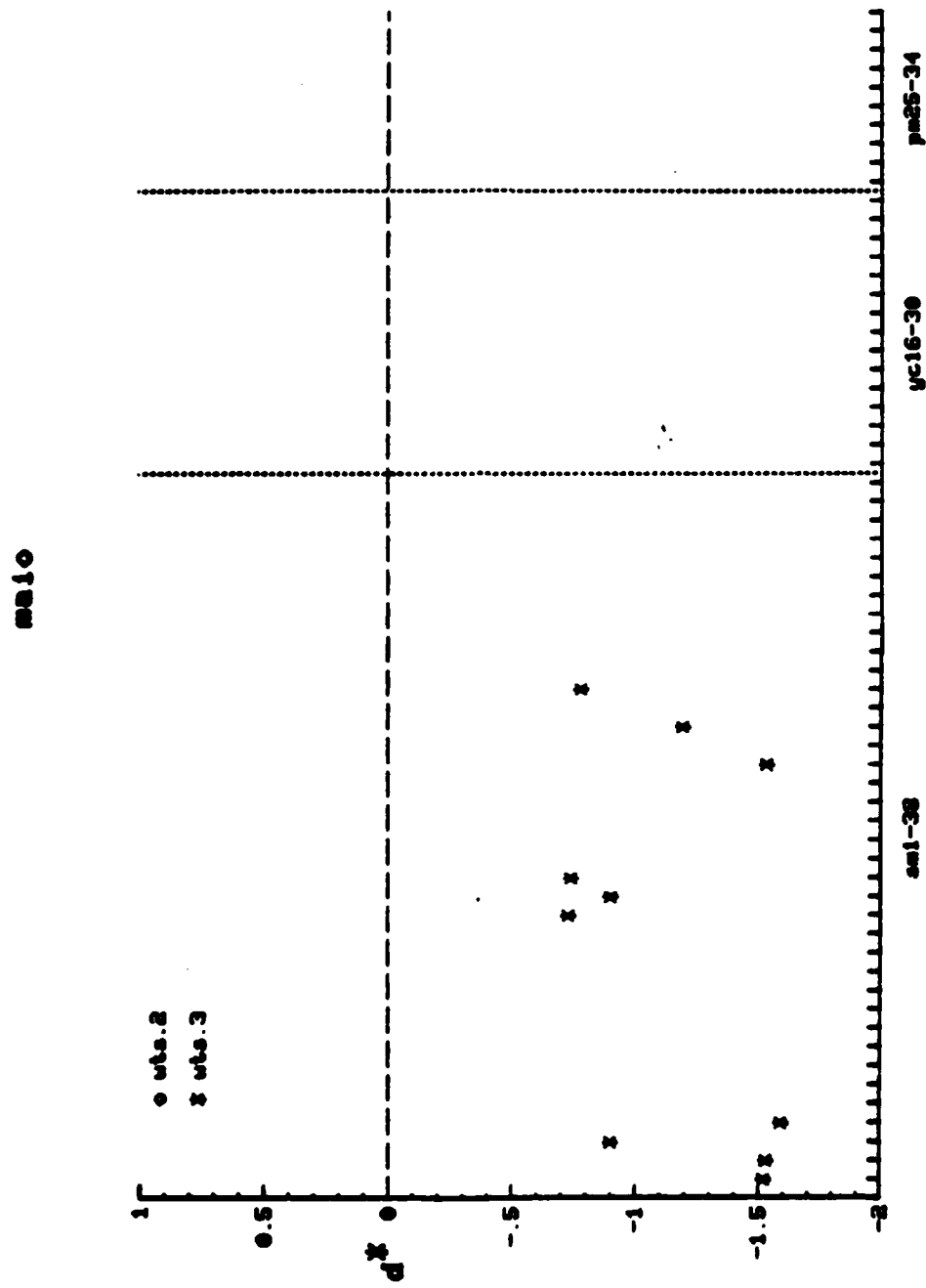


Figure C-11. The spectral integral (Equation 28) obtained using deterministic weights for station MA10.

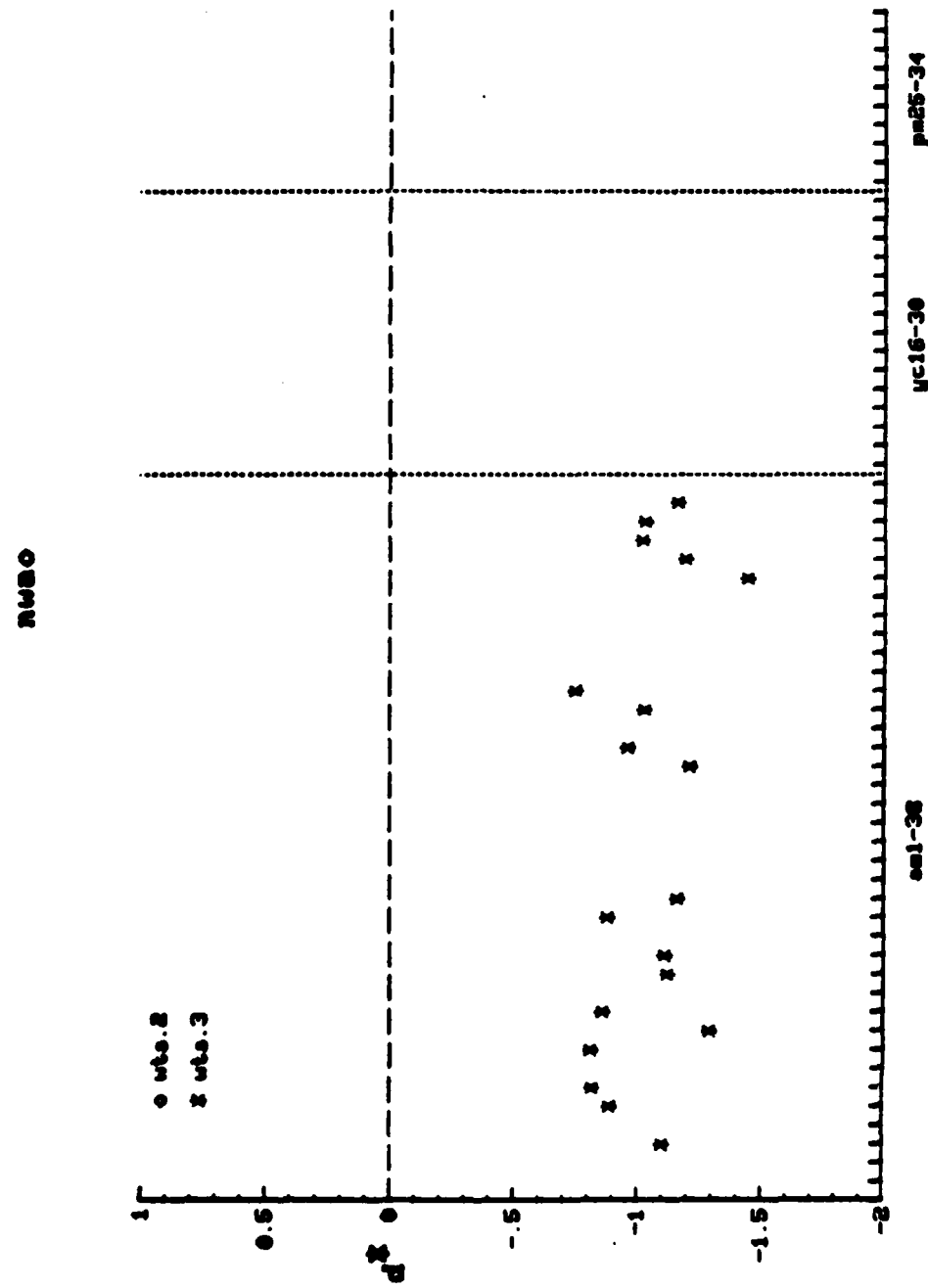


Figure C-12. The spectral integral (Equation 28) obtained using deterministic weights for station NWAO.

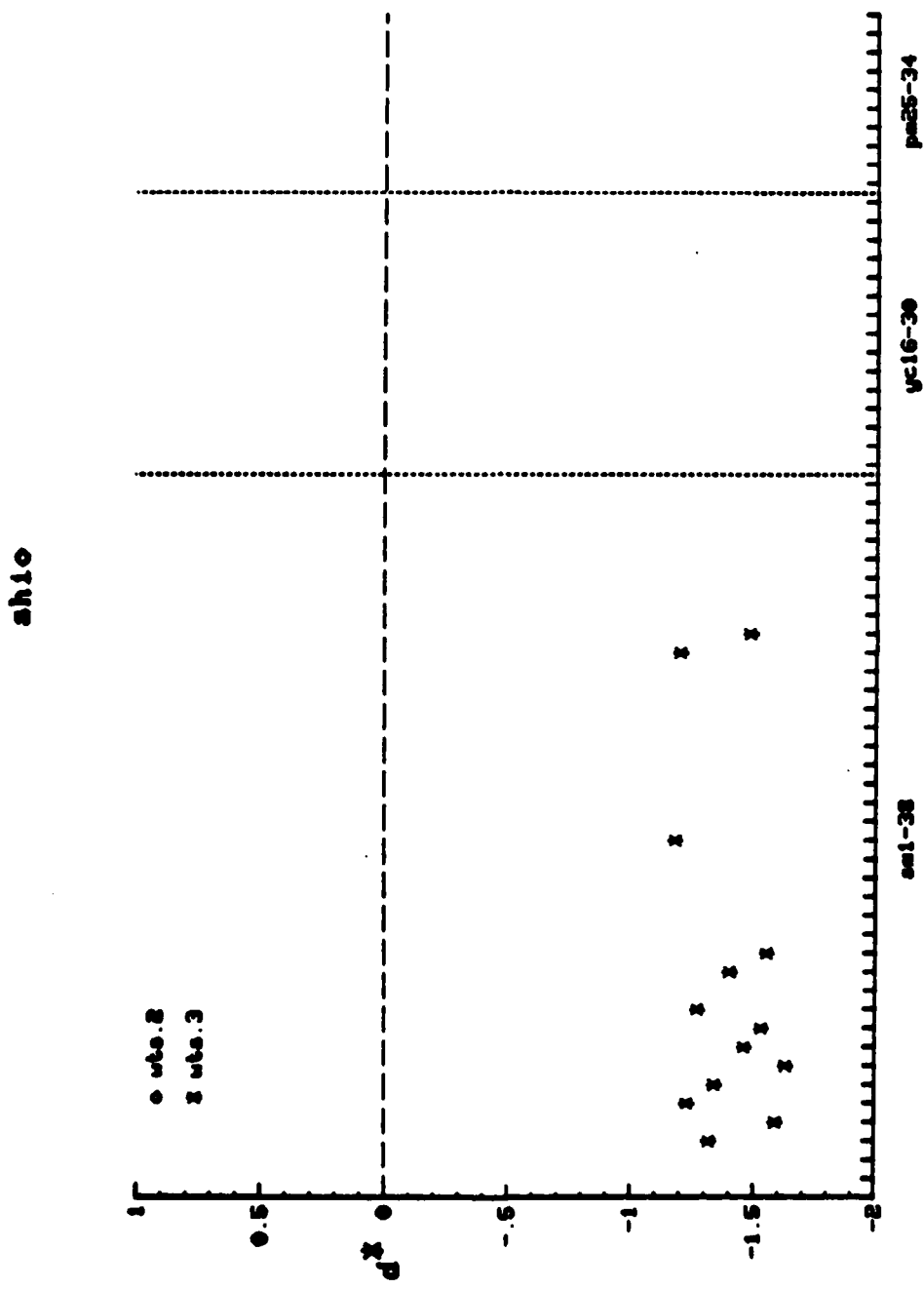


Figure C-13. The spectral integral (Equation 28) obtained using deterministic weights for station SH10.

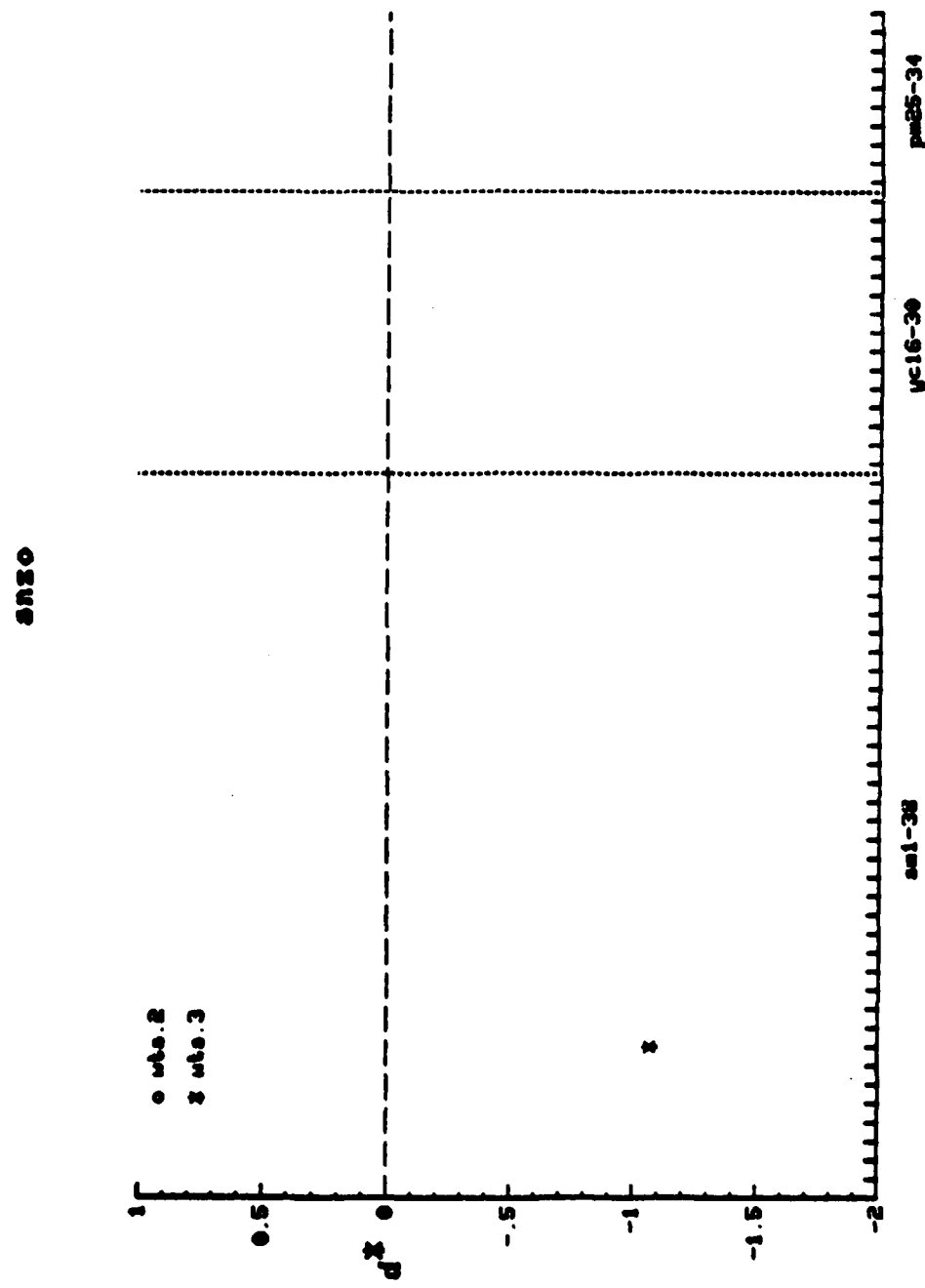


Figure C-14. The spectral integral (Equation 28) obtained using deterministic weights for station SNZ0.

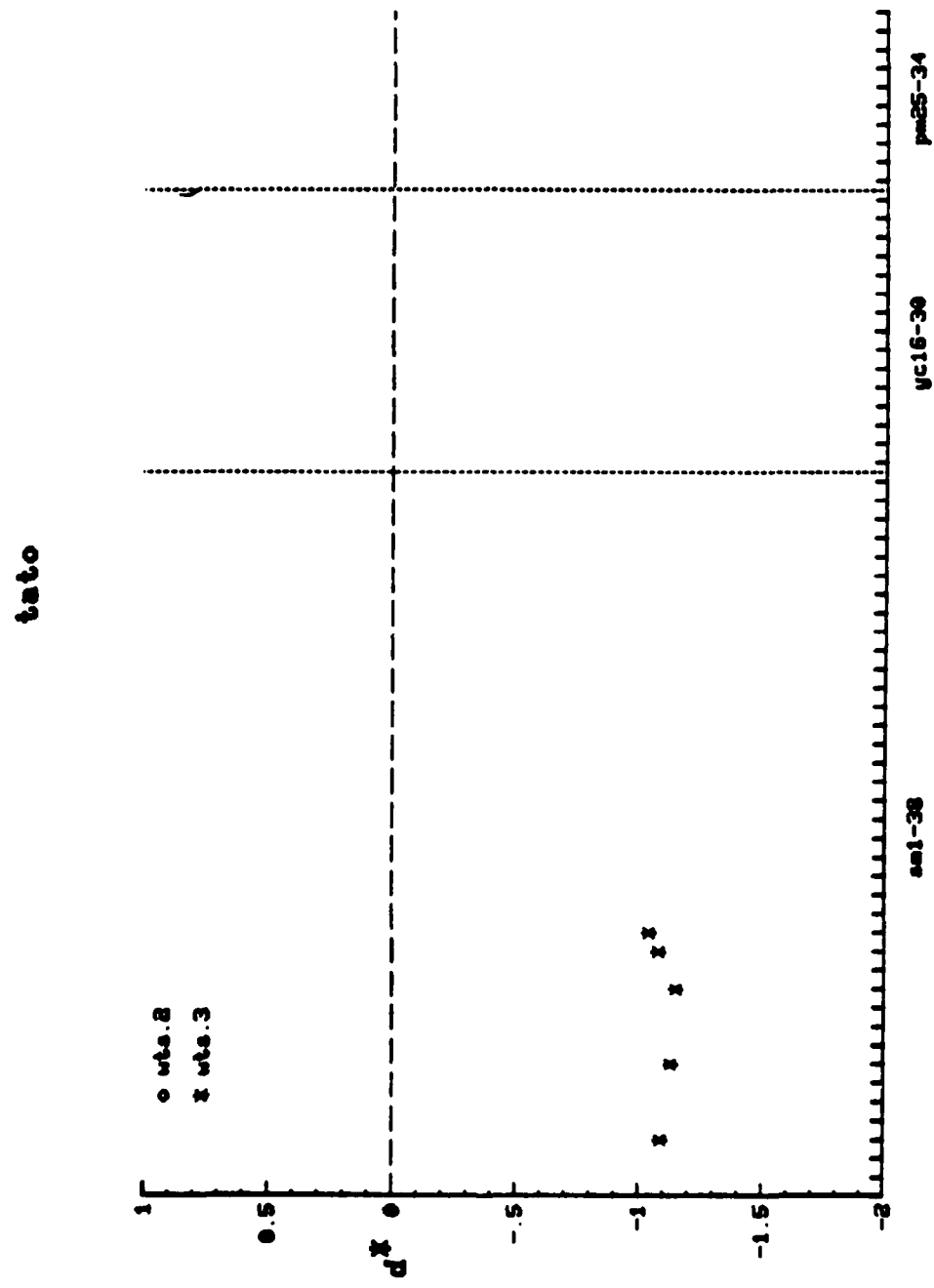


Figure C-15. The spectral integral (Equation 28) obtained using deterministic weights for station TATO.

soho

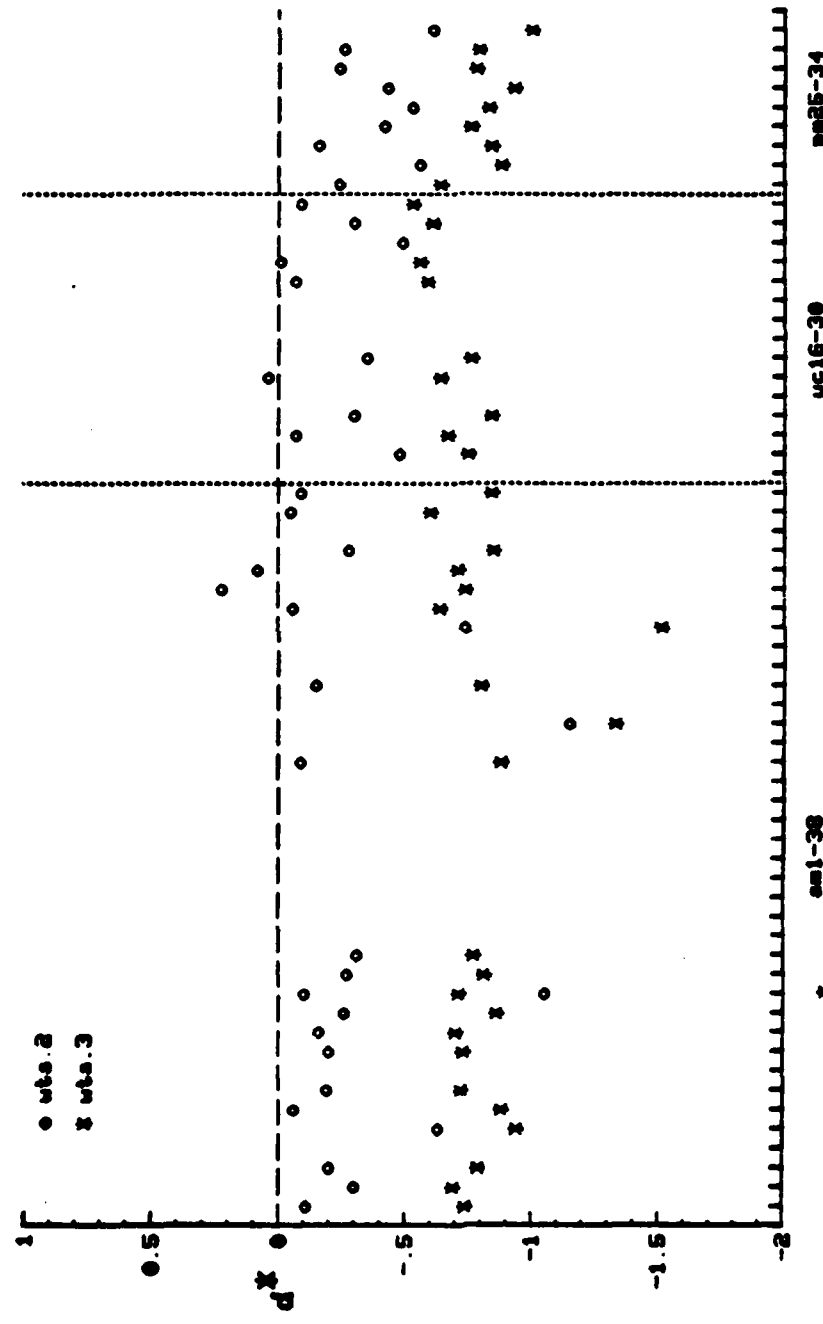


Figure C-16. The spectral integral (Equation 28) obtained using deterministic weights for station ZOBO. Only the points denoted by asterisks are meaningful.